Optimisation Techniques for Combustor Wall Cooling

by

Jason Krawciw

Doctoral Thesis

Submitted in partial fulfillment of the requirements

for the award of

Doctor of Philosophy of Loughborough University

18/05/2017

Department of Aeronautical and Automotive Engineering

Contents

Tables

Figures

Abstract

In a drive to increase the thermal efficiency of modern gas turbine engines, the turbine entry temperature (TET) has been steadily increasing over time to the point where the hot gasses contained within the combustion chamber have temperatures well in excess of the melting point of the materials used in its construction. As a result compressor exit air is widely used to cool these components. However, the use of this air is detrimental to the cycle efficiency. Therefore an important area of study is in optimising the use of this cooling flow in order to minimise the amount of air diverted from the main cycle. Effusion cooling techniques involving the use of a number of holes arrayed on the combustor liner wall are widely used and with additive manufacturing techniques such as direct laser deposition (DLD) gaining maturity, the design space of the cooling passages has become much wider. Therefore methods of assessing the performance of these newly enabled designs must be developed.

This thesis describes a number of methodologies used to evaluate the performance of effusion cooling systems. Experimental methods are employed to determine both overall effectiveness using infrared (IR) thermography and adiabatic film effectiveness using pressure sensitive paint (PSP) and the heat-mass transfer analogy. These measurement techniques are carried out using a single near-ambient conditions wind tunnel and a single set of metal test plates. These methods are used to determine the relative performance of six coolant passage geometries ranging from a simple cylindrical angled effusion design to more exotic helical flow passages. Computational techniques are also used to evaluate the relative film performance of the same six geometries utilising a simplification technique which splits the effusion calculation up and uses a single-passage computation to determine the through-hole flow field then extracts flow properties on a plane near the passage exit. These data are then used as boundary conditions for the effusion array, reducing the mesh size dramatically as only a small region near each hole exit is included in the computation. A conjugate simulation is also carried out on the single-passage geometry to investigate the heat transferred through the passage walls.

These techniques are used to investigate the performance of the six cooling geometries at various conditions of liner pressure drop and freestream turbulence levels. The PSP tests indicate that increasing the momentum ratio beyond 6 has little effect on the adiabatic effectiveness performance for the majority of the designs considered, the only exception being a design which utilises densely packed rows of cooling slots while increasing the distance

between successive rows. These tests also indicated that the main effect of increasing freestream bulk turbulence is to increase the turbulent mixing, resulting in wider coolant traces in the lateral direction while reducing the streamwise trace length. Sensitivity to bulk turbulence levels generally decreases with increasing momentum ratio. IR thermography shows that overall effectiveness is sensitive to freestream turbulence levels with higher turbulence levels showing reduced overall effectiveness for all plates tested. The increased coolant flow associated with higher momentum ratio results in increased overall effectiveness. The computational model struggles to predict the absolute levels of adiabatic film effectiveness accurately. However, the model does show good agreement with experimental data in terms of ranking the six designs tested, with the six designs falling into three main performance bands. The datum cylindrical angled effusion design shows the lowest performance levels in terms of overall and adiabatic effectiveness, with the straight fanned geometries showing significant improvements over the datum. The two helical geometries showed the highest performance of the designs tested combining a strong film with improved internal heat transfer characteristics.

Acknowledgements

I would like to take this opportunity to express what a privilege it has been to be able to continue my studies at Loughborough University and to thank everyone working within the RR UTC for their help and support throughout this process. I would also like to acknowledge Rolls-Royce Plc for providing funding for this research.

Particular thanks are extended to my supervisors, both official and unofficial, Dr Paul Denman and Dr Damian Martin, without whom much of this work would not have been possible. I would also like to thank the technical team for the support and assistance in modifying and developing the wind tunnel.

Additionally, I would like to thank my friends in the B-Team for their advice and entertainment and making sure I was prepared for what was to come while completing a PhD.

Finally, I would like to express my never ending gratitude to both my family and my partner Rea. Your love, encouragement and support have enabled me to pursue this particular dream. Without a doubt any of my successes are attributable to you and would not have been possible without your constant patience and motivation.

Nomenclature

c_p, c_v Specific Heat

d, D Diameter

h Heat transfer coefficient, specific enthalpy

k Thermal Conductivity

$\dot{m}$ Mass Flow Rate

q Heat flux

t Time

y^+ Non-dimensional wall distance

A Area

Bi Biot Number

BR Blowing Ratio

C Concentration

C_d Discharge Coefficient

DR Density Ratio

I Momentum Flux Ratio, Intensity

KR   Thermal Conductivity Ratio

L Length

M Mach number, Mass Flux (Blowing) Ratio

MR Momentum Ratio

Nu Nusselt Number

P Spanwise effusion hole spacing, Pressure

Pr Prandtl Number

R Gas Constant

Re Reynolds Number

S Streamwise effusion hole spacing

St	Stanton Number
T	Temperature
Tu	Turbulence Intensity
U, u, V	Velocity
$\dot{V}$	Volumetric Flow Rate
VR	Velocity Ratio
$\Lambda L, \Lambda_x$	Turbulent Integral Length Scale
γ	Ratio of Specific Heats
η	Adiabatic Film Effectiveness
ρ	Density
τ	Stress
ϕ	Overall Effectiveness

Subscripts

0	No film
∞, g, m	Freestream
ad	Adiabatic
aw	Adiabatic Wall
c	Coolant
f	Film, Fluid
fg	Foreign Gas
j	Jet
ref	Reference
s	Solid body
w	Wall

Acronyms

ALM   Additive Layer Manufacture

CFD   Computational Fluid Dynamics

CTA   Constant Temperature Anemometry

DLD   Direct Laser Deposition

HTC   Heat transfer coefficient

IR   Infrared

PSP   Pressure Sensitive Paint

SFC   Specific Fuel Consumption

TET   Turbine Entry Temperature

1 Introduction

This research looks into the design and assessment of effusion cooling geometries for gas turbine combustor liner applications and the possibilities opened up by the advent of direct laser deposition (DLD) and other additive layer manufacturing (ALM) methods.

Details of effusion cooling and its applications will be covered as well as details of a number of measurement techniques used to assess relative performance of cooling geometries. These methods involve both computational and experimental methods used to model and assess the flow field both through and over the surface of effusion cooled liners.

1.1 History of Gas Turbines

While the gas turbine has only been in use as a practical means of propulsion for the last three quarters of a century, the underlying concept was first demonstrated by Hero of Alexandria in the first century AD. With his aeoliopile, Hero showed that thrust could be generated by heating and pressurising steam and expelling it through a nozzle. The first true gas turbine is accredited to John Barber in 1791, he was granted a patent for an invention which includes the elements of a modern gas turbine, with a compressor, combustion chamber and turbine, designed to power a horseless carriage. This invention was limited by the technology available at the time. Sir Frank Whittle is seen as the father of gas turbines for use in aircraft propulsion. His work in the 1930s and 40s led to the first jet engine powered flight of the W1 powered Gloster E.28/39 in 1941. Since then gas turbine technology has continually developed, with modern turbofan engines producing well in excess of 100 times the thrust of the W1 and powering some of the most advanced aircraft in the world. Currently some of the biggest developmental areas within gas turbine technology revolve around improvements in emissions and efficiency whilst also trying to increase component life and reduce cost and weight.

1.2 Project Motivation

In order to improve specific fuel consumption (SFC) it is beneficial to increase the turbine entry temperature (TET) of the engine. As a result the gas temperatures present in the hot section of a modern gas turbine engine are often greater than the melting temperatures of the nickel super alloys used in the components; this poses a problem both in terms of component efficiency and, in particular, life. Therefore effective cooling methods have been developed allowing these alloys to be used in ever increasing temperature environments.
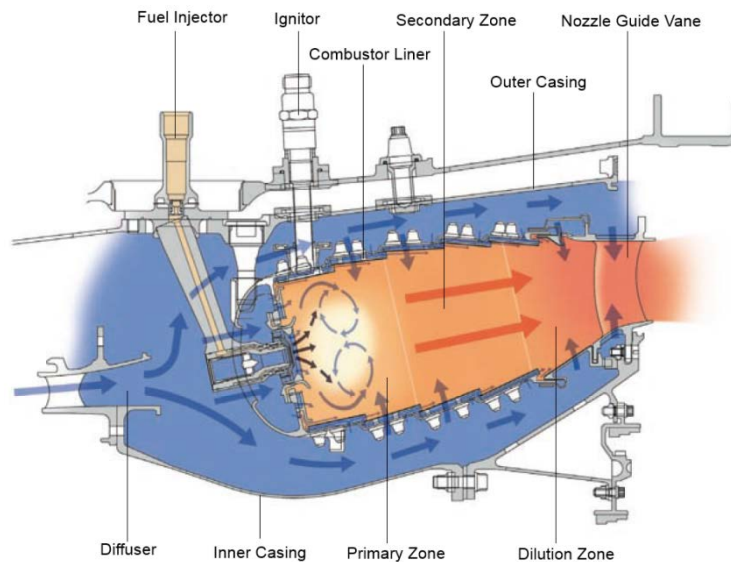
Figure 1 – Example combustion system architecture. (1)

Improvements in SFC can also be realised through a reduction in pressure drop within the combustion system, with a 1% reduction in system pressure drop resulting in a SFC decrease of around 0.3%. Therefore it is important to devise a liner cooling system that functions at low wall pressure drop while expending the available pressure drop energy to extract heat and protect the hot side surface from convective heat transfer.

Traditionally designers were limited to cooling designs that could be manufactured using operation based methods such as mechanical drilling or forging, however new manufacturing methods known as additive manufacture are beginning to become favoured within the aerospace industry as it allows parts to be manufactured to near net shape. One method of doing this is by melting a metallic powder using a precisely targeted laser in order to build up the component layer by layer.

Previously, cooling holes in components such as the combustion chamber liner are laser drilled resulting in a plain circular hole through the skin. However much more complex hole geometries are now offered to designers allowing the performance of these cooling passages to be optimised without incurring a significant cost penalty.

1.2.1 Aims

In capitalizing on the potential of these new additive manufacturing processes, this study aims to develop the techniques necessary to define and assess more advanced liner cooling architectures and therefore satisfying the need to keep components cool in the face of ever increasing gas temperatures within the combustor. This will be done both using a CFD based

approach to rank different passage geometries in terms of heat pickup through the liner wall and film effectiveness on the hot side surface. This modelling approach will also be validated using a number of experimental techniques available on test rigs at Loughborough University to determine the actual performance increases over the standard plain hole cooling arrays regularly used in engine combustor liners today.

1.2.2 Scope

A number of different cooling hole designs are looked at including traditional cylindrical angled effusion holes, current best in class fanned holes, a fanned hole designed to be easier to manufacture using laser drilling methods and three ALM enabled designs which could not be manufactured using traditional methods.

Experiments are carried out on a thermally scaled, near ambient temperature rig using IR thermography to determine overall bulk effectiveness levels for each design. The rig allows tests to be properly scaled both aerodynamically and thermally for the fluid and the liner wall, and has the capability to vary the bulk freestream turbulence levels of the approaching cross flow. Developments to the rig under this study include the addition of a pressure sensitive paint (PSP) measurement technique to determine the adiabatic film effectiveness using the same test plates employed for the conducting tests.

These PSP results are also used to validate a new computational approach to simulating the adiabatic film effectiveness of large cooling arrays using only limited computational resources. Further computational simulations are carried out in order to determine the internal heat removal performance of the test geometries.

1.3 Combustor Cooling Methods

There are two areas within a modern civil gas turbine engine where the gas temperature exceeds the melting temperature of the nickel super alloys used in the 'Hot End' of the engine. These are the combustor flame tube, and the turbine nozzle guide vanes (NGV) and rotors, particularly the first stage of the high pressure turbine. These components are typically manufactured from nickel based super alloys due to the requirement for a high strength, creep resistant, oxidation resistant, and low thermal expansion material with high thermal conductivity. These materials typically have melting points in the region 1500K, but begin to lose strength well before this. Therefore the maximum metal temperature of these

components is typically around 1100K. In a drive to increase engine efficiency, the turbine entry temperature (TET) at maximum take-off (MTO) conditions of engines has been steadily increasing (2) (Figure 2). This is now typically in excess of 1800K in modern engines such as the Rolls-Royce Trent 900 and 1000, and the flame temperature when kerosene is burnt is almost 2400K.
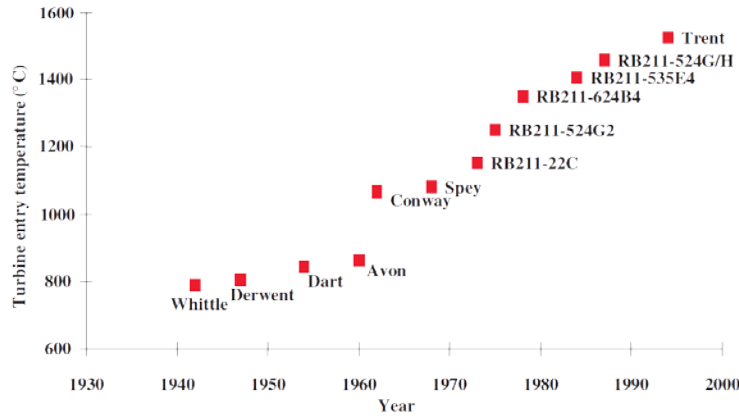
Figure 2 – Development of TET with time. (2)

Use of these materials in such elevated temperature conditions necessitates the use of various cooling technologies such as thermal barrier coatings (TBC), where a ceramic material is placed between the hot gas and the metal surface, and cooling the parts by using the relatively cool (typically 900-1000K at MTO) air from compressor exit and passing it through cavities and effusion holes within the liner wall. Often a combination of these techniques is employed in a successful design. A relatively large amount of cooling air is required, particularly by the high pressure (HP) turbine and the use of this 'cold' compressor exit air is detrimental to the efficiency of the engine. Therefore understanding the most effective and efficient way to deploy the coolant air is a major research area. Combustor flame tubes are designed to introduce this cooling air in various stages in order to cool both the metal chamber itself and the hot air that has been used in the combustion process, reducing the amounts of pollutants such as NO_X and CO_2 generated.

1.3.1 Film Cooling

Traditional film cooling techniques, where a thin film of cool air is passed over the surface of the metal by way of an isolated row of holes (see Figure 3a), effectively shields the metal wall from the hot gas and reduces the amount of heat transferred to the liner by turbulent convection. As the cool air mixes with the hot gas the effectiveness is decreased, resulting in a limited region over which the wall is protected. Due to the combustor mixing, the flow within the combustion

chamber is highly turbulent with large dominant length scales; as a result the protective film created by a single row of cooling holes is quickly degraded. This poor resilience to turbulent flow is a large drawback in this cooling style.

1.3.2 Transpiration Cooling

Transpiration cooling involves passing air through the liner by means of a porous wall (see Figure 3a). This combines two heat exchange effects: convective heat pickup through the wall, and protective film cooling on the hot side where the hot and cooling flow streams mix. However this mixing is a double edged sword inherent to all film cooling type methods; the introduction of coolant reduces the gas temperature on the wall surface, essentially diluting the hot gas near the wall while also causing an increase of the heat exchange coefficient by convection. The net effect of which is a decrease in the heat flux from the hot gas to the component surface. The drawbacks of transpiration cooling include the negative effect porosity has on the wall's thermal and mechanical properties, limiting part life as well as the poor film performance and high manufacturing cost.

1.3.3 Effusion Cooling

Effusion cooling aims to reproduce the cooling features of porous walls while retaining better properties in terms of thermo-mechanical resistance and film performance. (3) Effusive systems consist of metallic nets or walls with discrete holes (see Figure 3a&b). As the cool air is passed through these holes heat is convected from the hotter walls, the air then emerges onto the hot side surface creating a film layer. Through careful design of how the coolant emerges onto the surface this film can act as a protective barrier rather than diluting the hot gas as seen by the transpiration style of cooling. As there are a number of holes in the flow direction the film is repeatedly refreshed and is therefore much more resilient to the highly turbulent nature of the hot gas stream, increasing the effectiveness of the cooling in areas further downstream from the first line of holes. This results in a larger area of metal which is 'shielded' by the film layer. However as many more holes are required the cost of manufacture is higher than the simple film cooling method detailed in 1.3.1 above. As with all film cooling type methods the HTC downstream of the cooling holes is increased.

1.3.4 Impingement Cooling

A number of designs incorporate a dual skin system whereby the air first passes through a cold skin, this creates jets of coolant air which impinge on the hot skin, removing heat locally before

passing through the hot skin usually utilising one of the other cooling methods described or being ejected through a slot at the end of the tile. As a result of first passing through the cold skin the pressure drop available to the hot skin cooling system is reduced. As this is a twin skin system there is a penalty to weight and cost associated with adding a second skin.
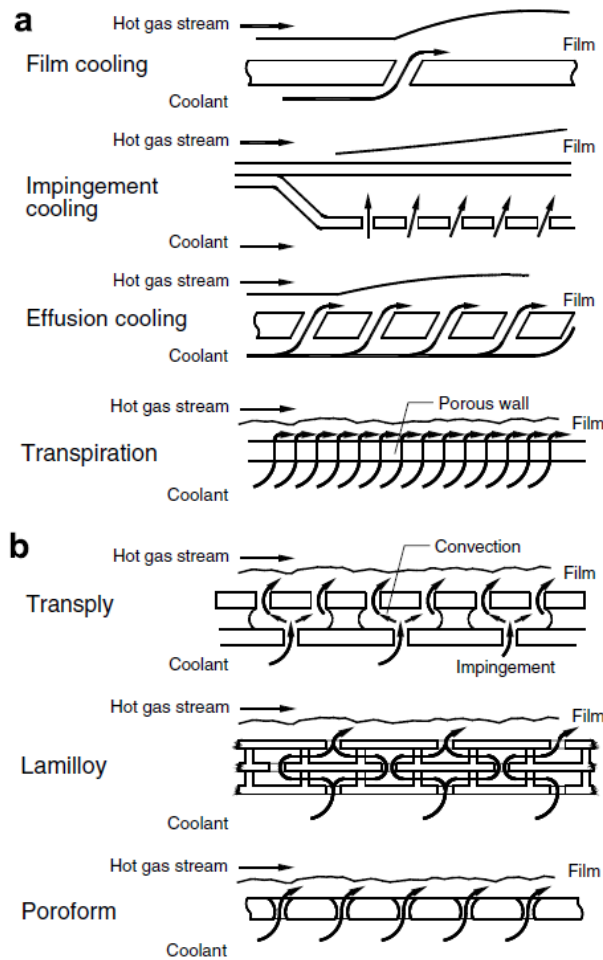
Figure 3 - Main cooling technologies using intermediate fluids.
(a) Cooling schemes; (b) wall manufacturing technologies
suitable for cooling by air effusion (3)

1.3.5   Pedestal Cooling

Pedestal style cooling relies on increasing the heat transfer out of the cold side of the liner through use of pedestals on the cold side greatly increasing surface area exposed to the coolant gas. This allows the coolant air to draw heat away from the liner before it is ejected over the hot side through slots at the end of the tile. These designs rely on a thermal barrier coating (TBC) on the hot side to reduce the amount of heat transferred through the liner and protect the surface from the hot gas as no protective film is produced save at the exit of the previous tile slot, even this is quickly overcome as a result of the highly turbulent hot stream flow.

Figure 3b shows a number of geometries which aim to combine some of the features of the systems described above. The Transply and Lamilloy designs combine multiple skin impingement type designs with effusion cooling holes on the hot skin to create a protective film while also using pedestals to connect the hot and cold skins together, increasing component strength while drawing heat away from the hot skin and into the cold skin. The internal geometry is also designed in such a way as to increase the heat removed within the gap. However this type of design is difficult to manufacture using traditional methods, requiring brazing together two or more laminates of high temperature alloy containing interrelating patterns of impingement and effusion holes while also introducing large thermal gradients.

1.3.6   Hole Geometry

Traditionally the holes used to pass cooling air through the metal were limited in their geometry by the manufacturing methods available; however modern additive manufacturing methods allow designers to drastically change the geometry of these holes with the potential to greatly improve cooling performance. With traditional manufacturing methods the number of individual operations required to create the cooling holes is kept to a minimum in order to minimise costs due to the large number of cooling holes present on the combustor liner skin. As a result the majority of engines utilise simple straight through circular holes, sometimes laid at an angle to the liner surface which require only a single drilling operation. With the introduction of additive manufacturing methods such as direct laser deposition (DLD), part cost is based mainly on part volume due to the parts being built up layer by layer. As a result the geometry of the coolant holes can be much more complex to enhance cooling performance without significantly adding to the manufacturing cost of the part.

1.3.7   Effusion Cooling Parameters

Bogard and Thole (4) comprehensively review film cooling through a discussion of the analysis methodologies, a physical description, and the various influences on film-cooling performance in the application of a turbine blade. In doing so, a number of factors have been identified which influence film cooling performance. These are listed in Table 1.

Coolant/mainstream conditions	Hole geometry and configuration	Surface geometry
Mass flux ratio, M	Shape of the hole	Hole location
Momentum flux ratio, I	Injection angle of the coolant hole	Surface curvature
Mainstream turbulence	Compound angle of the coolant hole	Surface roughness
Coolant density ratio	Spacing between holes, P/d	
Approach boundary layer	Length of the hole, l/d	
Mainstream Mach number	Spacing between rows of holes	
Unsteady mainstream flow	Number of rows	
Rotation		

Table 1 – Factors affecting film-cooling performance (4)

Where;

$$M = \frac{\rho_c U_c}{\rho_\infty U_\infty}, I = \frac{\rho_c U_c^2}{\rho_\infty U_\infty^2}$$

Equation 1(a,b)

Significant influences are the mass flux (blowing) ratio, momentum flux ratio, mainstream turbulence, hole shape, injection and compound angles of the coolant hole and surface curvature. Furthermore these factors are not necessarily independent; therefore it is inherently difficult to predict film-cooling performance.
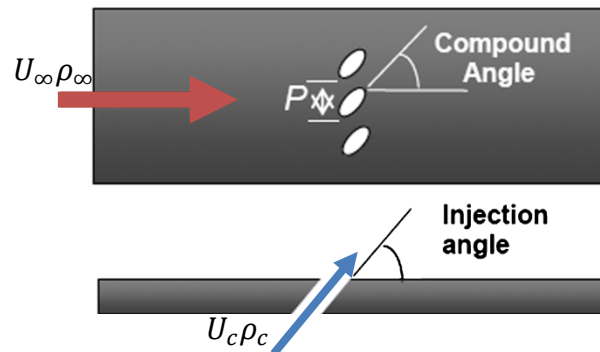
Figure 4 – Schematic of a typical film cooling configuration

The performance of a film-cooling arrangement is closely linked to whether the coolant jet is detached from the surface and factors such as surface curvature, free stream turbulence and the shape of the hole exit can all influence the blowing ratio at which separation occurs.

1.4   Heat Transfer Theory

Heat is transferred to and from the combustor liner through a number of mechanisms. Heat is transferred into the liner through two major mechanisms; radiative heat is transmitted from the high temperature flame and soot particles into the lower temperature wall, while the temperature difference between the hot gas stream and the liner causes heat to be transferred into the wall through the convective mechanism. The heat is conducted through the wall

before leaving the wall through convection into the cooler gas and radiation into the cooler outer casing.

Convective heat transfer into the wall is reduced through the methods described in 1.3.1 - 1.3.3. The conduction through the liner can be reduced by coating the hot side in TBC, however as shown by Greffrath (5), for a range of infrared wavelengths the TBC is effectively transparent to radiation with an emissivity of >0.9 providing no benefits in terms of protection from radiative heat transfer. Convective heat transfer out of the plate can be augmented through methods described in 1.3.4 and 1.3.5.

The following study does not take the radiative heating into account, nor the effects of annulus cross flow on cold side convection. Instead focus is placed on assessing the benefits to metal temperatures realised through optimisation of the convective heat transfer both in terms of limiting the heat transferred into the wall from the hot side through development of a cooling film and increasing the heat transferred from the wall through the internal cooling passages.

Performance of a film-cooling system can be quantified using three parameters: adiabatic film effectiveness (η), heat transfer coefficient (h_f) and net heat flux reduction (Δq_r);

$$\eta = \frac{T_\infty - T_{aw}}{T_\infty - T_{c,exit}}$$

Equation 2

$$q_f'' = h_f(T_{aw} - T_w)$$

Equation 3

$$\Delta q_r = 1 - \frac{q_f''}{q_0''} = 1 - \frac{h_f(T_{aw} - T_w)}{h_0(T_\infty - T_w)}$$

Equation 4

The film effectiveness parameter is the primary measure used to assess film cooling performance. This non-dimensional characteristic allows results to be related to actual temperatures found in the engine. In order to obtain a heat transfer coefficient which is independent of the coolant temperature the reference temperature is set to the adiabatic wall temperature since this is the fluid temperature immediately above the surface for an adiabatic wall. This will vary widely over the surface along with the heat transfer coefficient as the film cooling holes are discreet. Bogard and Thole (4) state that 'Generally, when a cooling jet is injected into a mainstream flow, the shear layers between the coolant jet and/or the wake behind the jet generate higher levels of turbulence within the boundary layer'. This causes the coolant to mix with the hotter mainstream flow, resulting in an increase in local convective heat

transfer coefficient. Therefore by relating the net heat flux both with and without film cooling holes and determining the net reduction in heat flux, the total benefit of placing a cooling hole in a particular location can be evaluated.

Nusselt number is a common measure associated with heat transfer problems. This dimensionless number describes the ratio of conductive to convective heat flux across a boundary. A high Nusselt number indicates a dominant convective heat transfer mechanism and therefore shows heat is being transferred between the fluid and wall more effectively.

$$Nu = \frac{hL}{k_f}$$ Equation 5

Internal heat transfer can also be assessed through use of the Stanton number, this non-dimensional property relates the heat transferred into a fluid to its thermal capacity. Therefore a high Stanton number indicates that more of the cooling capacity of the air flowing through the hole is being utilised.

$$St = \frac{h}{\rho U c_p}$$ Equation 6

Biot number is another useful parameter used in heat transfer problems. This is a dimensionless number which describes the ratio between heat transfer resistances inside of, and at the surface of a body. A low Biot number indicates that the temperature field inside the body does not vary significantly whereas a high Biot number suggests substantial thermal gradients within the solid body.

$$Bi = \frac{hL}{k_b}$$ Equation 7

1.5 Publications

The paper *Measurement and Prediction of Adiabatic Film Cooling Effectiveness of Combustor Representative Effusion Arrays* detailing some of the preliminary work and results on film effectiveness obtained for this project was presented at the 2015 ASME Turbo Expo in Montreal and is included in the appendix of this thesis.

2 Literature Survey

2.1 Introduction

The combustion chamber of a modern gas turbine engine is a hostile environment; the combustor wall is exposed to high temperature loads as well as unsteady flow conditions. As such the requirement to protect and cool the wall is made more complicated by the high turbulence intensity and large length scales produced by the unsteady flow. As a result, turbulent convection and the near wall velocities are increased, enhancing wall heat transfer (6). A large area of study therefore involves generating a film of relatively cool air over the combustor wall surface in order to protect it from the high temperature gas stream while reducing the turbulent mixing with the film layer to limit mixing with the hot combustion gases.

One technology that has significantly improved the cooling performance, resulting in increases in TET and hence SFC, is film cooling. Significant research has been conducted in this area over the last 50 years by a wide range of researchers. An article by Hartnett (7) gives a comprehensive review of some of the early work. While the ideal coolant injection method utilises a two-dimensional slot evenly distributing the coolant over the width of the area to be cooled, this is often not possible due to mechanical limitations. As a result, most recent research looks at an array of discreet cooling holes placed on the surface to be cooled. The resultant hole exit flow interacts with the main stream in a much more complex way than in a slotted design, as a result approximating the ideal of an evenly distributed film and modelling the interaction have become major areas for ongoing research.

In its simplest form, discreet hole film cooling is a series of fundamental jets in cross flow. A detailed review of the interaction of a jet in a cross flow as well as relevant studies is given by Mahesh (8). There are four main structures resulting from the interaction of a jet in crossflow as illustrated in Figure 5; the signature feature is the counter-rotating vortex pair (CVP) which can result in the hot mainstream air being pulled around the coolant jet and onto the surface, reducing the effectiveness (9). The jet shear layer, wake structures and horseshow vortices are also produced when the coolant jet interacts with the mainstream flow, though their influence on the distribution of coolant on the surface is not as pronounced as the CVP.
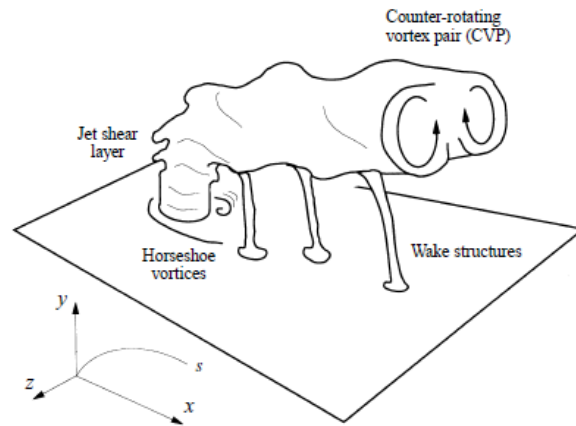
Figure 5 – The known vortical structures of the jet in crossflow (10)

Developments in additive layer manufacturing (ALM) methods have resulted in a great expansion to the design space available for engineers to exploit. Additive layer manufacturing methods such as direct laser deposition (DLD) allow parts to be manufactured with much more complex features, not physically or economically possible using traditional manufacturing techniques. In the realm of film cooling this means the cooling hole can be almost any shape the designer wishes, both internally and at hole inlet and exit. As a result the traditional cylindrical cooling hole is beginning to be replaced with more exotic holes with fanned exits which results in a better cooling film through a number of mechanisms including reducing the jet velocity and hence jet lift off as well as encouraging spanwise spreading the coolant over the surface.

In addition to the benefits of an improved cooling film, ALM allows more efficient use of the coolant air through internal heat removal. The coolant passage can be designed in such a way that more heat is removed from within the wall as the cool air passes through it.

These advances in design space lead to a reinvigoration of research in this area. As such, computational and experimental methods relating to the assessment of film cooling geometries are reviewed in this section alongside some of the conditions and geometric parameters which influence the performance of film cooling systems.

2.2   Film Cooling

Extensive studies have been carried out into the influence of various parameters on the performance of a film cooling system. Bogard and Thole (4) summarise many of these relationships in their application to turbine blade cooling, detailing both the performance measures used when assessing film cooling performance as well as how altering the design and operating conditions affects these measures. An overview of some of the most important parameters is included in the current section.

2.2.1   Adiabatic Film Effectiveness

Adiabatic film effectiveness is a non-dimensional parameter used to relate the temperature of the fluid immediately adjacent to the wall surface between rig and engine conditions through normalising the adiabatic wall temperature by the mainstream and coolant hole exit temperatures. This parameter is important as it defines the driving temperature boundary condition which determines the convective heat transfer into the liner skin. It is used as a means of ranking cooling strategies while also allowing experiments to be scaled to more manageable conditions when appropriate boundary conditions are applied.

$$\eta = \frac{T_\infty - T_{aw}}{T_\infty - T_{c,exit}} \qquad \text{Equation 8}$$

An adiabatic wall condition is defined as one under which there is zero heat transfer into the wall and as such is represented by a perfectly insulating wall. Through use of the adiabatic film effectiveness measure the quality of a cooling film can be rated since T_{aw} is the driving temperature behind the heat flux into the wall. As coolant is ejected from the coolant holes it forms a layer of cool air over the skin surface. The effectiveness of this coolant layer diminishes due to convective processes such as turbulent mixing between the coolant jet and mainstream flow. As a result the adiabatic film effectiveness varies constantly on the cooled surface and is strongly influenced by the coolant system geometry and flow conditions.

2.2.2   Heat Transfer Coefficient

Heat transfer coefficient, h, is the proportionality coefficient between the convective heat flux and the driving temperature difference. This parameter depends on all the variables influencing convection including surface geometry, nature of the fluid motion, fluid properties and fluid velocity. In general form;

$$q'' = h(T_{ref} - T_w)$$

However, as film cooling is a two temperature problem, driven by both coolant and mainstream temperatures, choice of reference temperature is not obvious. As the two flow streams mix the local temperature downstream of the coolant injection hole varies widely   Momentum and heat transfer in the boundary layer is also influenced by the introduction of the coolant flow. Therefore in order to isolate the heat transfer coefficient from the coolant temperature T_{ref} is set to the driving temperature of the fluid above the surface, in this case the adiabatic wall temperature T_{aw}. As a result the heat transfer coefficient with film cooling h_f is defined as;

$$q''_f = h_f(T_{aw} - T_w)$$

Where both h_f and T_{aw} vary widely over the cooled surface.

Injecting a jet of air onto a surface such as is the practice in effusion cooling geometries has the effect of increasing the local surface heat transfer coefficient; as a result the expected performance increase indicated by the film effectiveness measure is reduced.

2.2.3 Overall Effectiveness

Overall effectiveness is a non-dimensional parameter used to relate the actual metal temperature between rig and engine conditions by normalising by the mainstream and coolant flow temperatures. It captures the effects of all heat transfer mechanisms present in the test including both surface and through-hole convection, conduction through the wall and radiation both into and out of the wall.

$$\phi = \frac{T_\infty - T_w}{T_\infty - T_c}$$

2.2.4 Net Heat Flux Reduction

By calculating the heat flux into the wall both with and without film cooling it is possible to assess the benefit of adding a cooling hole in any particular location. This measure is called the net heat flux reduction and is defined as:

$$\Delta q_r = 1 - \frac{q''_f}{q''_0} = 1 - \frac{h_f(T_{aw} - T_w)}{h_0(T_\infty - T_w)}$$

This can then be expressed in terms of heat transfer coefficients with and without film cooling, adiabatic and overall effectiveness values:

$$\Delta q_r = 1 - \frac{h_f}{h_0}\left(\frac{1-\eta}{\phi}\right)$$

<div align="right">Equation 13</div>

2.2.5 Blowing Ratio

Mass flux, or blowing, ratio gives an indication of the proportion of cooling air used relative to the mainstream cross flow. It scales the thermal transport capacity of the coolant because the convective transport is proportional to $c_p \rho_c U_c$.

$$M = \frac{\rho_c U_c}{\rho_\infty U_\infty}$$

<div align="right">Equation 14</div>

It is largely controlled by the liner pressure drop and temperature ratio in a combustor environment. This can vary depending on the cooling geometry used, for example a twin skin impingement-effusion type design uses a large proportion of the available pressure drop over the impingement skin. As a result a lower pressure drop is available for the effusion skin, therefore a lower velocity stream exits the liner and hence a lower blowing ratio in comparison to a single skin system. The internal flow field generated downstream of a swirl-stabilized fuel injector can also cause variations in the local static pressure field as shown by Wurm et al (11); as a result the hole to hole blowing ratio often varies both spatially and temporally. As a result it is important to understand the performance of a given cooling geometry over a range of blowing ratios.

Typically, blowing ratio ranges from $M = 1$ to $M = 4$ in single skin combustor liner applications, with low blowing ratios resulting in better film performance for simple cylindrical angled effusion holes in the near hole region. This is because as blowing ratio increases, the coolant jet starts to 'lift-off' from the liner surface, when the jet is no longer attached the coolant is ejected into the freestream with little of the cooler gas actually producing the desired film on the surface. Even at lower blowing ratios the coolant quickly mixes with the freestream and the effectiveness falls as seen in Figure 6. However, optimization of blowing ratio is limited in combustor liners due to the more dominant requirements of adequate mixing. Therefore, mitigating the influence of the blowing ratio through effusion cooling design is important, with some designs such as fanned effusion holes showing less sensitivity to blowing ratio than established cylindrical hole geometries.
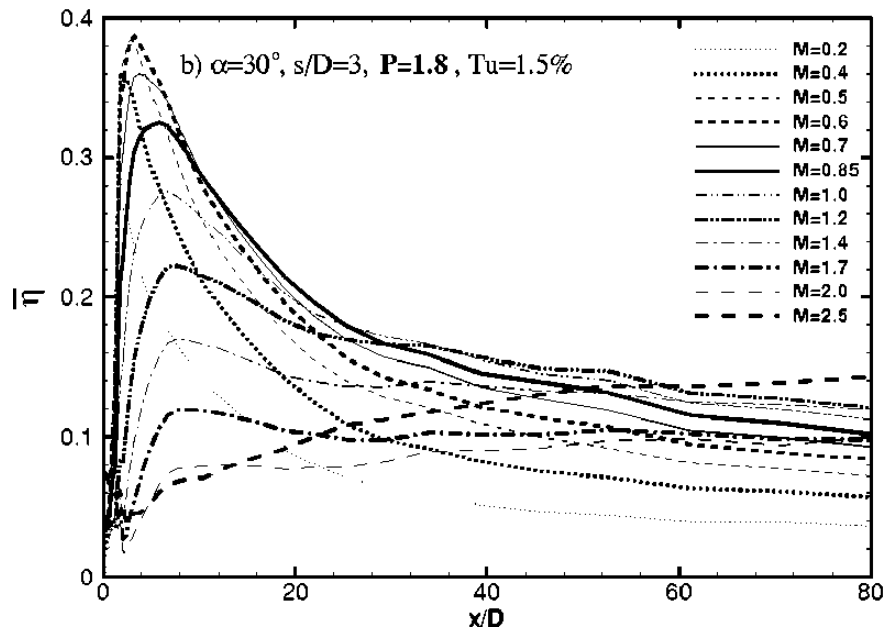
Figure 6 – Effect of variation of the blowing ratio on spanwise average film effectiveness (12)

2.2.6   Momentum Flux Ratio, Velocity Ratio, and Density Ratio

Density ratio is driven mainly by the temperature differences between the coolant and mainstream flows; as such the density ratio in a combustor is typically in the region $DR \approx 2$. However, achieving such a high density ratio in laboratory based experiments is very difficult; therefore it is important to determine how density ratio affects film cooling performance. When testing at DR which do not match engine conditions, only one of the three scaling ratios can be matched, either blowing ratio M, momentum flux ratio I, or velocity ratio V_r.

$$I = \frac{\rho_c U_c{}^2}{\rho_\infty U_\infty{}^2}, V_r = \frac{U_c}{U_\infty} \qquad \text{Equation 15, 16}$$

Momentum flux ratio scales the dynamics of the interaction of the mainstream with the exiting coolant jet because the interaction of the mainstream on the coolant jet causes the coolant jet to turn toward the wall; this turning is a major factor in the cooling performance. The coolant jet must be turned sufficiently that it remains attached to the surface, otherwise the bulk of the coolant will be injected into the mainstream and provide little cooling of the surface. The momentum flux ratio is dependent on the pressure drop over the combustor wall. Velocity ratio scales the shear layer between the coolant and mainstream, scaling the production of turbulence.

Studies conducted by Pederson et al. (13), Baldauf et al. (12; 14) and Sinha et al. (15) evaluate the effects of DR on film effectiveness performance using flat surface, zero pressure gradient

facilities with a single row of coolant holes at 35° inclination angle. Pedersen et al. found that at very low blowing ratio of $M = 0.2$ the spanwise averaged film effectiveness was essentially the same for DR ranging from $DR = 0.8$ to 4. At such low M the coolant jet stays attached at all DRs, as a result the film performance was dependent on M. However, for higher blowing ratios Pedersen found the film performance improved at increased DR. Baldauf et al. (14) tested over a range of blowing ratios and two density conditions, they found that density ratio had little influence on the distribution of the film, but the higher DR resulted in higher peak film effectiveness, attributed to better lateral distribution of the high density coolant as noted by Sinha et al. (15).

2.2.7 Freestream Turbulence

The flow field within the combustor is highly turbulent; as a result eddies within the flow exist at many length scales with large length scale structures containing most of the turbulent kinetic energy. These large length scales are typically an order of magnitude greater than the cooling film thickness.

$$Tu = \frac{u_{rms}}{U}$$

<div align="right">**Equation 17**</div>

Early studies looking into the effects of freestream turbulence were carried out by Launder and York (16) and Kadotani and Goldstein (17; 18; 19). These studies looked at turbulence levels ranging from 3 to 8% with integral length scales around $0.33D$ at the coolant injection location. While these conditions are still very small compared with combustor flows, the conclusion of these studies was that at lower blowing ratios, increasing turbulence levels resulted in as much as 15% reduction in film effectiveness, however at high blowing ratios, a slight increase in film effectiveness is observed.

Turbulent intensity levels within a real combustor are nominally around 20% with various integral length scales, with dilution ports often 10-20 times the size of the film cooling holes injecting jets at high momentum flux ratios ($\sim$50). An investigation into the effects of high free-stream turbulence on the jet-mainstream interaction was carried out by Kohli and Bogard (20). Experiments were conducted at both high $Tu = 20\%$ and low $Tu = 0.5\%$ turbulence conditions with a streamwise integral length scale $\Lambda_x/D = 3$. They found that the process of coolant dispersion is distinctly different at low and high free-stream turbulence conditions. The large shear layer between the mainstream and coolant jet is the primary cause of turbulent

mixing and dispersion of the coolant at low turbulent intensity. At high turbulence levels this shear layer is quickly superseded by large scale turbulent structures from the free-stream, causing free-stream fluid to be thrust through the core of the coolant jet, all the way to the wall.

2.2.8 Hole Shape and Orientation

The orientation of the hole to the surface, or injection angle, is a basic geometrical factor influencing the film cooling performance; studies have shown that film effectiveness generally reduces with increased injection angle. This can be attributed in part to the separation of the jet from the surface at increased injection angles. Kohli and Bogard (21) found that increasing the injection angle from 35° to 55° resulted in a reduction in film effectiveness of 10 and 30% at momentum flux ratios of $I = 0.16$ and 0.63 respectively.
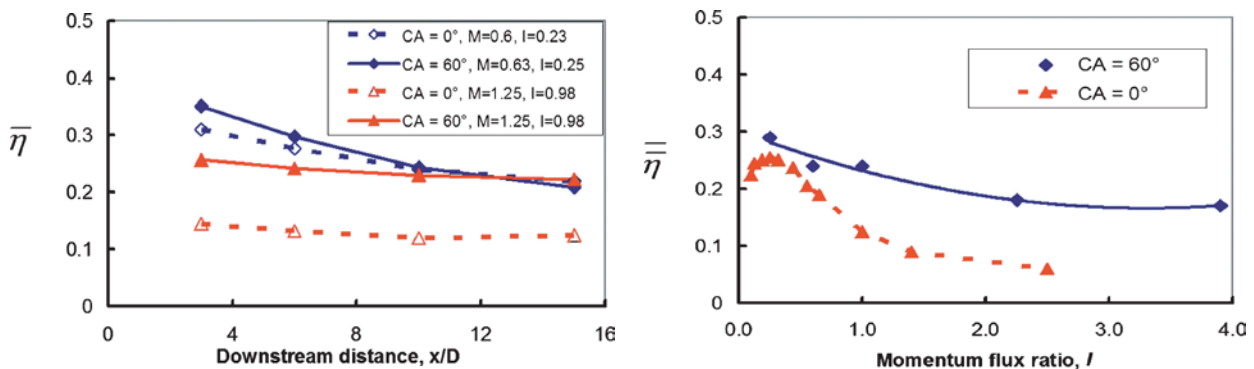
Figure 7 – Film effectiveness for 0- and 60-deg compound angle hole: a) streamwise distribution of laterally averaged cooling effectiveness and b) spatially averaged film effectiveness for varying momentum flux ratios (22)

Orientation of the hole to the main flow direction, known as compound angle, is another geometric factor which can impact the film cooling performance. Schmidt et al. (22) found that at high momentum flux ratios, injecting the flow at 60° to the main flow resulted in around double the film effectiveness while having little effect at a lower mass flux ratio. However, Sen et al. (23) found that the compound angle also increased the heat transfer coefficient by about 15% relative to the aligned case; the resultant net heat flux reduction shows that there is very little difference between 0° and 60° indicating that the increased film effectiveness is offset by the increased heat transfer coefficient. A later study looking at the effects of increased turbulence by Schmidt and Bogard (24) found that at higher levels of free-stream turbulence, $Tu = 17\%$ the film effectiveness performance is essentially the same for angled and aligned holes but the heat transfer coefficients remains higher in the angled case, resulting in reduced net heat flux reduction when a compound angle is included.

Improvements in film cooling performance can be achieved by altering the hole exit geometry, in particular by expanding the flow through a diffuser at exit. This decelerates the coolant jet,

resulting in reduced momentum flux and hence reduced tendency for the jet to separate. In addition, by expanding the flow laterally, a broader jet is introduced to the mainstream resulting in the mainstream having a greater impact in turning the jet towards the wall more effectively.

Figure 8 shows data taken from Saumweber et al (25) who studied the effects of shaped, or fanned, holes on both film effectiveness and heat transfer coefficient. The study used a 30° injection angle and hole spacing $P/d = 4$. A coolant $DR = 1.7$ was used with turbulence ranging from $Tu = 3.1$ to 11%. Effectiveness results were spatially averaged from $x/d = 2$ to 22 for blowing ratios ranging from $M = 0.5$ to 2.5. It can be seen that the shaped hole shows much higher film effectiveness over the range of blowing ratios, as well as performance increasing with blowing ratio where the cylindrical holes performance drops off as blowing ratio increases. This is attributed to the jet separation for the cylindrical hole. This indicates that shaping the hole exit is very effective at reducing the jet separation. Saumweber also found that the heat transfer coefficients were generally similar for shaped and cylindrical holes, but at the highest blowing ratio and turbulence intensity conditions the shaped holes had 50% greater HTC than the cylindrical holes, somewhat offsetting the benefit gained from improved film effectiveness.
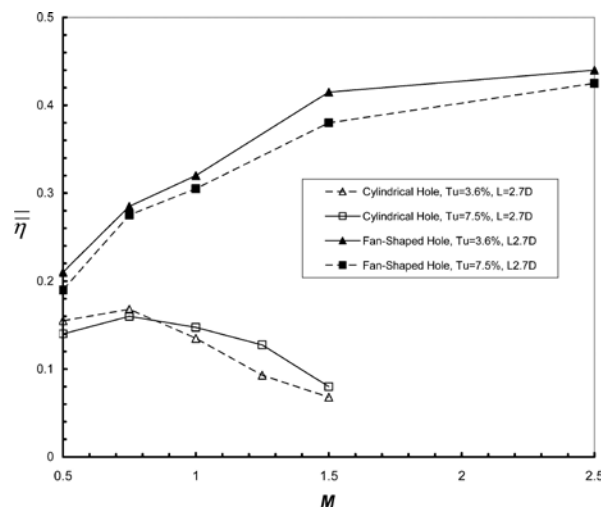
Figure 8 – Spatially averaged film effectiveness for cylindrical and shaped holes (4) (reproduced from (25))

The largest factor limiting the introduction of shaped cooling holes has been the large increase in manufacturing costs relative to simple cylindrical holes. However, with the introduction of ALM the manufacturing cost of such complex designs is similar to that of a simple cylindrical

design. As a result the use of shaped holes, or even more complex geometries, is likely to be introduced into the next generation of engines.

2.3   Measurement Techniques

2.3.1   IR Thermography

Every object emits radiation with a spectral distribution described by Planck's law as shown in Figure 9. Planck's law states that spectral radiation is determined by the objects absolute temperature T and the spectral emissivity $\varepsilon(\lambda)$. Spectral emissivity is the ratio of the spectral emittance of an object to that of a blackbody (one which emits and absorbs all radiation at all wavelengths) and depends on the material the object is made from and its surface quality. This indicates what fraction of radiation is either absorbed, transmitted or reflected. Optically opaque objects have negligible transmissivity, and therefore any radiation which is not absorbed is reflected. When measuring spectral radiation it is therefore important to know the spectral emissivity of the object in order to calculate the surface temperatures. These relations also apply when considering the number of photons rather than spectral radiation and by dividing Planck's formula by the energy of a photon the spectral photon emittance can be found. This is important as most infrared thermography systems use photon detectors as sensing elements.

$$W_{\lambda,b} = \frac{2\pi hc^2}{\lambda^5 \left(e^{hc/\lambda kT} - 1\right)} \quad \text{Planck's law}$$

$$W_{\lambda,o} = \varepsilon(\lambda) \cdot W_{\lambda,b}$$

$W_{\lambda,b}$	blackbody spectral radiant emittance
$W_{\lambda,o}$	object's spectral radiant emittance
$\varepsilon(\lambda)$	object's spectral emissivity
h	Planck's constant
k	Boltzmann's constant
c	velocity of light
T	absolute temperature
λ	wavelength
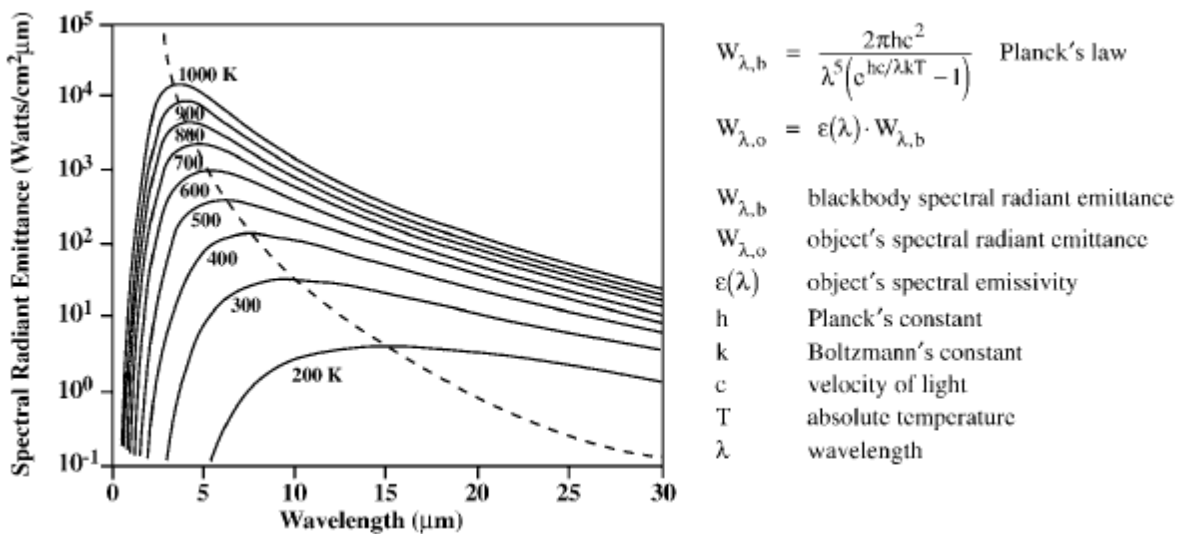
Figure 9 – Spectral distribution according to Planck's law for different temperatures (26)

The infrared band of the electromagnetic spectrum is divided into sub-bands. Due to the air present between the test piece and the sensor and its wavelength dependent transmittance, infrared thermography techniques focus on either the 2-5µm medium infrared or 8-12µm far infrared bands.

There are two principal types of thermography system; scanning and staring systems. Scanning systems, as used by Schulz (26), use prisms and mirrors to direct radiation from individual

'point' locations onto a single sensor by scanning along the surface to be measured. Staring systems, as used by Martin and Thorpe (27), use a sensor array to capture the radiation of a comparatively large area all at once while using an in situ calibration technique to eliminate erroneous reading resulting from viewing through a partially IR transmissive window as well as accounting for background radiation and transmittance of air.

IR thermography can be used to measure both overall effectiveness in conducting materials and adiabatic effectiveness if a very low thermal conductivity material is used.

2.3.2 Adiabatic Effectiveness Measurements Using Pressure Sensitive Paint

Pressure sensitive paint (PSP) and temperature sensitive paint (TSP) are optical sensors used for measuring surface pressure and temperature based on the quenching mechanisms of luminescence. Compared with traditional techniques such as pressure tappings and thermocouples, they offer the capability for non-contact, full field measurements of surface pressure or temperature on a complex aerodynamic model with much higher spatial resolution and at lower cost.

PSP and TSP use luminescent molecules as probes suspended in a polymer binder on the model surface. This mixture can be dissolved in a solvent and sprayed directly onto the model surface. The solvent evaporates leaving a solid polymer coating in which the luminescent molecules are immobilised. When light of the correct wavelength illuminates the paint, the luminescent molecules become excited and emit light of a longer wavelength. The intensity of this emitted luminescence is dependent on a number of physical processes. For PSP, the main photo-physical process is oxygen quenching. This causes a decrease in the luminescent intensity as the partial pressure of oxygen increases. This makes PSP a potential sensor of both pressure when oxygen concentration is constant, and oxygen concentration when the pressure field is known. TSP is insensitive to the effects of oxygen quenching as the binder used is impermeable to oxygen. The second major mechanism affecting the luminescent intensity is thermal quenching, whereby an increase in temperature results in decreased luminescent intensity. A more detailed description of these processes is given in section 3.3.2.

Through the use of a heat-mass transfer analogy, adiabatic effectiveness can be inferred through the measurement of oxygen concentration on the film cooled surface when a coolant simulant containing no oxygen is used. This technique has been used to great effect in helping

to understand film cooling in turbine blades. Zhang et al. (28; 29) use this technique to investigate turbine nozzle and end wall film cooling, with Ahn et al. (30) using PSP to measure the film cooling effectiveness over the leading edge and blade tip region. These studies all use Nitrogen as the coolant gas, allowing the assumption that the gas properties of both coolant and mainstream gasses can be considered equal and molecular mass corrections do not need to be applied. However the requirement that the test be kept isothermal in order to eliminate the temperature sensitivity effects, combined with the use of Nitrogen results in a density ratio of ~ 1. As mentioned previously, density ratio has little effect on film effectiveness results in the attached jet case but influences the blowing ratio at which the jet separates and the peak film effectiveness once separation has occurred. Jonsson (31) chooses to use CO_2 as the coolant gas, this results in a density ratio of ~ 1.7, more in line with engine conditions. However this requires a molecular mass correction documented by Jones (32) to be applied to the results.

$$\eta = \frac{T_{aw} - T_g}{T_c - T_g} = \frac{c_{p,c}\eta_{energetic}}{c_{p,g}(1 - \eta_{energetic}) + c_{p,c}\eta_{energetic}}$$

Equation 18

A complete description of methodology used to determine film effectiveness is given in section 3.3.3.

PSP and TSP must be illuminated using a specific wavelength source which can provide a stable intensity level over the course of the tests. This wavelength differs between paint formulations, with the majority in the UV-blue range of 400-490nm. A number of options exist to provide this illumination; Dhall et al. (33) chose to use a xenon arc lamp passing through a band pass filter. Stability testing revealed no fluctuations in intensity with arc temperature. Facchini et al (34) used high power UV LEDs to illuminate the paint, negating the requirement for a filter as LEDs provide light in a very narrow wavelength band and are stable as long as they are driven at a stable voltage and are mounted to a sufficient heat sink. Other researchers, such as Navarra (35), have used lasers as an illumination source. However, these experiments tend to be performed on rotating platforms requiring very precise phase-locked illumination and image capture well beyond the scope of the current study.

Charge-Coupled Device (CCD) based cameras are almost exclusively used in the measurement of the luminescence intensity of the paint. They provide high sensitivity with a potential dynamic range in excess of 16-bit and low noise, both of which are vital to obtaining accurate results over the range of intensities produced by the concentration gradients often encountered in film

cooling measurements. CCDs used in previous studies include 8-bit (33), 12-bit (30), 14-bit (34)and 16-bit (31) sensors, with higher dynamic range generally resulting in lower frame rates and similar levels of uncertainty reported for 12-, 14- and 16-bit sensors. A filter is placed in front of the camera lens in order to remove any potential light source other than the paint luminescence, the banding of which is dependent on the paint formulation used with most PSPs emitting at >600nm.

A number of paint formulations exist, each with different excitation and luminescent wavelengths, sensitivity to temperature and pressure as well as time response. These properties are strongly influenced by the choice of binder, particularly its permeability, solubility and diffusion coefficient. Details of many of these formulations are given by Liu and Sullivan (36). One of the more common formulations is supplied by ISSI (31; 34; 37). This paint, called UniFIB, contains PtTFPP[1] as the luminophore alongside TiO_2 scatterers suspended in a polymer binding (FIB[2]). This is a bright, single-luminophore paint sprayed as a single component using an airbrush. The paint is excited by light in the range 380-520nm with a peak at 400nm and emits at 620-750nm with a peak at 650nm. Calibration of this paint is stable and repeatable.
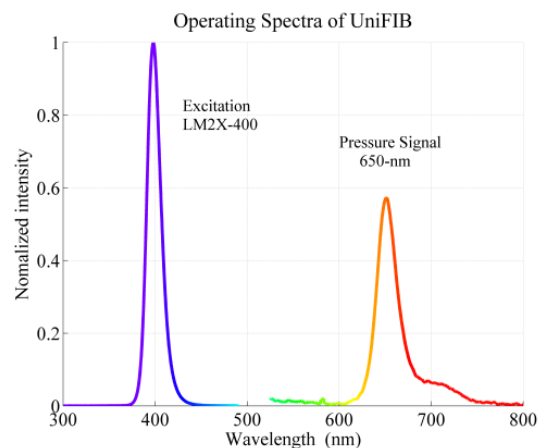
Figure 10 – Emission spectra of UniFIB PSP excited using 400nm LED (38)

In order to determine the sensitivity of the paint to both temperature and pressure/O_2 concentration it is necessary to calibrate the intensity response to these variables. When calibrating against pressure it is advantageous to perform an in situ, pixel-by-pixel calibration. This is often difficult due to the complexities involved in sealing a wind tunnel to pressure

---

[1] Platinum meso-Tetra (pentafluorophenyl) porphine
[2] Fluoro-isopropyl-butyl

variations, without a pixel-by-pixel calibration spatial noise is visible in the absolute pressure measurements made. Fortunately as concentration measurements require taking a ratio of two images at constant pressure; this spatial noise is not a major concern, allowing the use of an a priori calibration in a separate calibration chamber and a bulk average rather than pixel-by-pixel approach.

Jonsson (31) uses a vacuum chamber to calibrate a sample of the paint on a calibration coupon; this coupon is attached to an electronically controlled peltier thermoelectric device allowing temperature to be controlled. The coupon is placed inside the vacuum chamber with optical access provided. The chamber is then cycled through a number of pressure conditions, and the resulting emitted intensity is recorded on the CCD. An average is then taken over a small region of the sample, which is painted at the same time as the model to be tested. This process is then repeated at a number of calibration temperatures. Jonssons calibration results show similar relationships to both temperature and pressure as that provided by the paint datasheet shown in Figure 11 and Facchini et al. (34), who used a similar setup, resulting in a similar calibration curve.
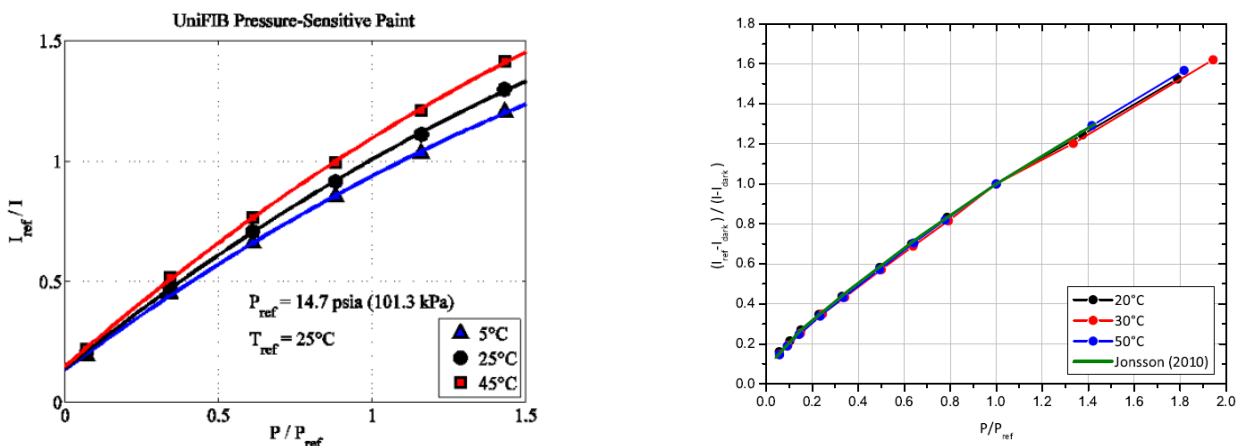
Figure 11 – Calibration of UniFIB PSP a) Manufacturer Data (38), b) Data obtained by Facchini at al. (34)

2.4   Computational Fluid Dynamics

In order to predict accurately the effectiveness of a cooling method and hence the component life, large amounts of data must be collected. Obtaining experimental results is a lengthy and expensive process and ideally would be used very sparingly, often only in the detail design phase of the engine development. An increasingly common practise is to use computational fluid dynamics (CFD) simulations to predict the performance of components.

2.4.1   Governing Equations

Computational fluid dynamics (CFD) simulates a flow field by solving the equations of fluid motion, collectively known as the Navier-Stokes equations. Solving these equations for an infinitesimally small fluid element yields the equations in differential form, while solving for a finite fluid volume results in the integral form of the equations. Derivations for these methods are presented by Anderson (39), Blazek (40) and Versteeg and Malalasekera (41).

The first equation expresses the conservation of mass, known as the continuity equation.

$$\frac{\partial \rho}{\partial t} + \nabla.\left(\rho \vec{V}\right) = 0$$

<div align="right">**Equation 19**</div>

The momentum equations express Newton's second law as applies to a three dimensional fluid element and are expressed as x, y, and z components.

$$\frac{\partial (\rho u)}{\partial t} + \nabla.\left(\rho u \vec{V}\right) = -\frac{\partial p}{\partial x} + \frac{\partial \tau_{xx}}{\partial x} + \frac{\partial \tau_{yx}}{\partial y} + \frac{\partial \tau_{zx}}{\partial z}$$

<div align="right">**Equation 20**</div>

$$\frac{\partial (\rho v)}{\partial t} + \nabla.\left(\rho v \vec{V}\right) = -\frac{\partial p}{\partial y} + \frac{\partial \tau_{xy}}{\partial x} + \frac{\partial \tau_{yy}}{\partial y} + \frac{\partial \tau_{zy}}{\partial z}$$

<div align="right">**Equation 21**</div>

$$\frac{\partial (\rho w)}{\partial t} + \nabla.\left(\rho w \vec{V}\right) = -\frac{\partial p}{\partial z} + \frac{\partial \tau_{xz}}{\partial x} + \frac{\partial \tau_{yz}}{\partial y} + \frac{\partial \tau_{zz}}{\partial z}$$

<div align="right">**Equation 22**</div>

These momentum equations can be combined using Einstein notation.

$$\frac{\partial (\rho u_i)}{\partial t} + \nabla.\left(\rho u_i \vec{V}\right) = -\frac{\partial p}{\partial x_i} + \frac{\partial \tau_{ij}}{\partial x_j}$$

<div align="right">**Equation 23**</div>

The conservation of energy is expressed using the energy equation.

$$\frac{\partial}{\partial t}(\rho E) + \nabla \cdot (\rho E \vec{V})$$
$$= \frac{\partial}{\partial x}\left(k\frac{\partial T}{\partial x}\right) + \frac{\partial}{\partial y}\left(k\frac{\partial T}{\partial y}\right) + \frac{\partial}{\partial z}\left(k\frac{\partial T}{\partial z}\right) - \frac{\partial(up)}{\partial x} - \frac{\partial(vp)}{\partial y}$$
$$- \frac{\partial(wp)}{\partial z} + \frac{\partial(u\tau_{xx})}{\partial x} + \frac{\partial(u\tau_{yx})}{\partial y} + \frac{\partial(u\tau_{zx})}{\partial z} + \frac{\partial(v\tau_{xy})}{\partial x}$$
$$+ \frac{\partial(v\tau_{yy})}{\partial y} + \frac{\partial(v\tau_{zy})}{\partial z} + \frac{\partial(w\tau_{xz})}{\partial x} + \frac{\partial(w\tau_{yz})}{\partial y} + \frac{\partial(w\tau_{zz})}{\partial z}$$

Equation 24

Energy E is given by the sum of the internal and kinetic energies of the fluid element.

$$E = e + \frac{V^2}{2}$$

Equation 25

Again this can be simplified using Einstein notation.

$$\frac{\partial}{\partial t}(\rho E) + \nabla \cdot (\rho E \vec{V}) = \frac{\partial}{\partial x_i}\left(k\frac{\partial T}{\partial x_i}\right) - \frac{\partial(u_i p)}{\partial x_i} + \frac{\partial(u_i \tau_{ij})}{\partial x_j}$$

Equation 26

Where; ρ is the fluid density, p is the pressure acting on the fluid element, t is time and u, v, and w correspond to the fluid velocity in the x, y, and z directions respectively. These velocity components make up the vector $\vec{V}$, with magnitude V and components u_i. τ_{ij} denotes the viscous stress acting on the fluid. When $i = j$ this is the normal stress, otherwise it is shear stress where the stress in the j direction is exerted on a plane perpendicular to the i axis. e is the internal energy per unit mass, k is the thermal conductivity coefficient and T is the temperature. This can also be written in terms of specific total enthalpy h_0.

$$h = e + \frac{p}{\rho}$$

Equation 27

$$h_0 = h + \frac{1}{2}(u^2 + v^2 + w^2)$$

Equation 28

$$\frac{\partial}{\partial t}(\rho h_0) + \nabla \cdot (\rho h_0 \vec{V}) = \frac{\partial}{\partial x_i}\left(k\frac{\partial T}{\partial x_i}\right) + \frac{\partial p}{\partial t} + \frac{\partial(u_i \tau_{ij})}{\partial x_j} + S_h$$

Equation 29

Where S_h represents an enthalpy source term.

For Newtonian fluids, the shear stress τ_{ij} can be related to the velocity gradients, molecular viscosity μ and second viscosity coefficient λ.

$$\tau_{ij} = \tau_{ji} = \mu\left[\frac{\partial u_j}{\partial x_i} + \frac{\partial u_i}{\partial x_j}\right] + \lambda(\nabla \cdot \vec{V})\delta_{ij}$$

Equation 30

By working under the assumption that $\lambda = -\frac{2}{3}\mu$, the shear stresses can be denoted as functions of velocity gradients and the molecular viscosity coefficient only.

From the 5 Navier-Stokes equations there are 7 unknown flow variables. In order to close these it is necessary to make some assumptions about the flow. By assuming that the fluid acts as an ideal gas, a reasonable assumption for many aerodynamic applications, the equation of state can be used to relate pressure, temperature and density, where R is the specific gas constant.

$$p = \rho R T$$

<div align="right">**Equation 31**</div>

Finally, by assuming that the fluid is calorically perfect the system of equations can be closed.

$$e = c_v T$$

<div align="right">**Equation 32**</div>

Here, c_v is the specific heat at constant volume.

2.4.2 Turbulence Modelling

Flows in the laminar regime can be solved using only the equations given above, however many engineering problems involve turbulent flow. The Reynolds number of a flow is a measure of the relative importance of inertial to viscous forces. Below a critical Reynolds number, the flow is smooth and adjacent layers of fluid slide past each other in an orderly fashion. If the flow is steady, i.e. the applied boundary conditions do not change with time, the flow is in the laminar regime. However, at Reynolds numbers above this critical value the flow characteristics begin to change, eventually resulting in a random and chaotic state in which the flow becomes intrinsically unsteady even with constant boundary conditions.
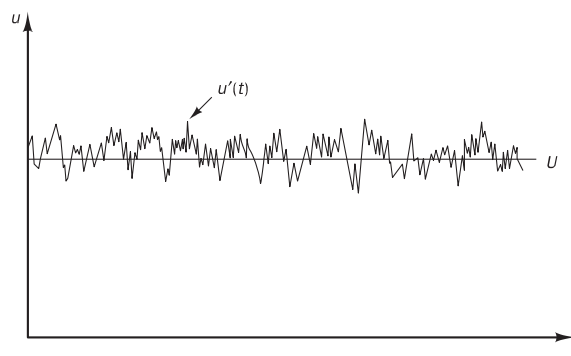
Figure 12 – Typical point velocity measurement in turbulent flow (41)

When all flow properties including velocity vary in a random and chaotic way the flow is said to be turbulent. In this regime the properties can be expressed as a time averaged value indicated by an over bar e.g. $\bar{u}$, and a fluctuation about that mean denoted by a prime e.g. u'. This is known as Reynolds decomposition, an example of this decomposition for velocity is given in Equation 33.

$$u_i(t) = \bar{u_i} + u_i'(t)$$

These fluctuations can be attributed to turbulent eddies within the flow field and these eddies can exist at a range of different length scales. The result of these eddies is the effective mixing of heat, mass and momentum. Capturing these complex and dynamic interactions is therefore important as over- or under-predicting the effects of turbulence often results in poor accuracy. Extensive research has been carried out by the CFD community into the development of numerical methods to capture the important effects due to turbulence. These methods can be grouped into three categories; DNS, LES and RANS.

2.4.2.1 DNS

Direct numerical simulation (DNS) computes the mean flow and all turbulence velocity fluctuations. The unsteady Navier-Stokes equations are solved on spatial grids that are fine enough that they can resolve the Kolmogorov length scales ($N \propto Re^{9/4}$). The Kolmogorov length scales can be defined as the eddies with a characteristic length, characteristic velocity and kinematic viscosity, η, υ and ν respectively, such that the Reynolds number based on these properties is equal to unity, $Re_\eta = \frac{\upsilon\eta}{\nu} = 1$. This signifies that the inertial and viscous forces are equal and is considered to be the finest scale in the energy cascade, after which kinetic energy is converted into thermal energy. Time steps must also be sufficiently small as to resolve the fastest fluctuations. As a result these kinds of simulations require huge computational resources that are costly in both time and computational power, therefore DNS studies are generally restricted to research of fundamental type problems or 'numerical experiments' and are often employed in order to develop less costly turbulence models.

2.4.2.2 LES

Large eddy simulation (LES) exploits the difference in behaviour between large and small eddies. Smaller eddies are nearly isotropic and have a universal behaviour for turbulent flows at

sufficiently high Reynolds numbers. Large eddies are more anisotropic and their behaviour is dictated by the geometry of the domain, the boundary conditions and body forces. The LES approach solves for these larger scale eddies while using a model to predict the effects of the smaller eddies. The larger and smaller eddies are separated through the use of a special filter. A filtering function is selected along with a certain cut off width with the aim of resolving all eddies with a length scale greater than this width in an unsteady flow calculation. The spatial filtering operation is then performed on the time dependent flow equations, during which information relating to the smaller, filtered out eddies is destroyed. This and interaction between the resolved and unresolved eddies gives rise to sub-grid-scale (SGS) stresses. The effect of these stresses on the resolved flow is described through use of an SGS model. While LES type simulations are gaining popularity, the computational requirements are still restrictive to the majority of applications requiring the use of computational clusters and weeks or months of continuous running time to solve.

2.4.2.3 RANS

For a large number of engineering applications it is unnecessary to resolve details of the turbulent fluctuations. For these applications engineers are satisfied with time averaged properties of the flow. Therefore many engineering simulations are based on the Reynolds Averaged Navier-Stokes (RANS) equations. Reynolds averaging involves first applying Reynolds decomposition as in Equation 33, then using one of three averaging schemes: Time averaging, as given by Equation 34, for statistically steady turbulence, spatial averaging for homogeneous turbulence or ensemble averaging for general turbulence. For all three schemes the average of the fluctuating part is zero, i.e. $\overline{u_i'} = 0$. However, both $\overline{u_i'u_i'}$ and $\overline{u_i'u_j'} \neq 0$.

$$\overline{u_i} = \lim_{T \to \infty} \frac{1}{T} \int_t^{t+T} u_i \, dt \qquad \text{Equation 34}$$

In cases where density is not constant, a density weighted or Favre decomposition of certain quantities is used instead of Reynolds averaging in order to avoid complications due to additional correlations involving density fluctuations. An example of Favre averaging is given in Equation 35 where $\bar{\rho}$ denotes the Reynolds averaged density.

$$\widetilde{u_i} = \frac{1}{\bar{\rho}} \lim_{T \to \infty} \frac{1}{T} \int_t^{t+T} \rho u_i \, dt \qquad \text{Equation 35}$$

Favre decomposition is denoted

$$u_i = \widetilde{u_\iota} + u_i''$$

Where $\widetilde{u_\iota}$ represents the density weighted mean value and u_i'' is the fluctuating part of the velocity u_i. Again the average of the fluctuating part is zero, i.e. $\widetilde{u_\iota''} = 0$ but the product of two fluctuating quantities is not zero, $\widetilde{u_\iota'' u_\iota''} \neq 0$ and $\widetilde{u_\iota'' u_j''} \neq 0$. It is also worth noting that the Reynolds-average of the fluctuating part of the velocity $\overline{u_\iota''} \neq 0$, but $\overline{\rho u_\iota''} = 0$.

By applying the Reynolds averaging technique to the Navier-Stokes equations, the aptly named RANS equations are given. For example, applying the technique to the incompressible Navier-Stokes equations, the following relations for mass and momentum conservation are obtained.

$$\frac{\partial \overline{u_\iota}}{\partial x_i} = 0$$

$$\rho \frac{\partial \overline{u_\iota}}{\partial t} + \rho \overline{u_j} \frac{\partial \overline{u_\iota}}{\partial x_j} = -\frac{\partial \overline{p}}{\partial x_i} + \frac{\partial}{\partial x_j}\left(\overline{\tau_{\iota J}} - \rho \overline{u_\iota' u_j'}\right)$$

These equations are identical to the Navier-Stokes equations with the exception of the additional term

$$\tau_{ij}^R = -\rho \overline{u_\iota' u_j'} = -\rho(\overline{u_\iota u_j} - \overline{u_\iota}\,\overline{u_j})$$

This is known as the Reynolds-stress tensor and represents the transfer of momentum due to turbulent fluctuations.

Similarly, applying Reynolds averaging to density and pressure and Favre averaging to the remaining flow variables results to the compressible Navier-Stokes equations yields the Favre- and Reynolds-Averaged Navier-Stokes equations.

$$\frac{\partial \overline{\rho}}{\partial t} + \frac{\partial}{\partial x_i}(\overline{\rho}\widetilde{u_\iota}) = 0$$

$$\frac{\partial}{\partial t}(\overline{\rho}\widetilde{u_\iota}) + \frac{\partial}{\partial x_j}(\overline{\rho}\widetilde{u_j}\widetilde{u_\iota}) = -\frac{\partial \overline{p}}{\partial x_i} + \frac{\partial}{\partial x_j}\left(\overline{\tau_{\iota J}} - \overline{\rho}\widetilde{u_\iota'' u_j''}\right)$$

$$\frac{\partial}{\partial t}(\bar{\rho}\tilde{E}) + \frac{\partial}{\partial x_j}(\bar{\rho}\tilde{u}_j\tilde{H})$$

$$= \frac{\partial}{\partial x_j}\left(k\frac{\partial\tilde{T}}{\partial x_j} - \bar{\rho}\widetilde{u_j''h''} + \widetilde{\tau_{ij}u_i''} - \bar{\rho}\widetilde{u_j''K}\right)$$

$$+ \frac{\partial}{\partial x_j}\left[\tilde{u}_i\left(\widetilde{\tau_{ij}} - \bar{\rho}\widetilde{u_i''u_j''}\right)\right]$$

Equation 42

As with Reynolds averaging, the momentum (and energy) equations are extended by the Favre-averaged stress tensor.

$$\tau_{ij}^F = -\bar{\rho}\widetilde{u_i''u_j''}$$

Equation 43

Both Reynolds- and Favre-averaged stress tensors result in six extra stresses in the momentum equation, in order to solve for these added stresses a turbulence model is employed. These models use tuned constants based on empirical data, as a result, turbulence models which work well for one application often provide poor results for other flow regimes. There are a number of turbulence models available, with a summary of some of the most popular given below.

- Spalart-Allmaras (SA) – 1-equation model which employs a transport equation for an eddy-viscosity variable, $\tilde{v}$. Developed based on empiricism, dimensional analysis and Galilean invariance. Easy to implement into an unstructured solver, best results for attached boundary layers and flows with mild separation, not suited to flows involving jet-like free-shear regions, complex recirculation and body forces. Often used to predict blade flows in axial compressors where separation and unsteadiness are avoided.

- K-Epsilon – 2-equation model, most widely used model in industrial applications, wall function must be used to resolve the viscous sublayer. Based on the solution of equations for the turbulent kinetic energy, k, and the turbulent dissipation rate, ε. Accuracy degrades for flows with adverse pressure gradients and flow with extreme flow curvature.

- K-Omega – 2-equation model, improved performance for boundary layers under adverse pressure gradients relative to the K-Epsilon model. Solves transport equations for the turbulent kinetic energy, k, and the specific dissipation rate, ω, where $\omega \propto \varepsilon/k$. Boundary layer computations are very sensitive to values of omega in the free stream.

- Reynolds Stress Transport (RST) – 7-equation model which derives exact equations for the Reynolds stresses using a second-order closure, these are solved along with model

equations for the scalar dissipation rate, ε. This imposes a significant computational overhead as well as requiring more iterations to reach a converged solution. (42)

These models have been in development for a number of years, as a result there are a number of variations based on suggested improvements made to the basic models tuned for specific flow regimes.

Alongside the turbulence model, a wall treatment is used. This is a set of assumptions for each turbulence model and determines how the flow is treated in the near wall boundary layer region. This directly influences the mesh used to define the simulation. There are three types of wall treatment commonly used.

- The high y^+ wall treatment implies the wall-function type approach in which it is assumed that the near-wall cell lies within the logarithmic region of the boundary layer. Wall functions use empirical laws to circumvent the inability of a turbulence model to predict the logarithmic velocity profile near a wall.
- The low y^+ wall treatment is suitable only for low Reynolds number turbulence models in which it is assumed that the viscous sublayer is properly resolved.
- The all y^+ wall treatment is a hybrid treatment employed by StarCCM+ that attempts to emulate high y^+ wall treatment for coarse meshes and the low y^+ wall treatment for fine meshes. It is also formulated to produce reasonable results for meshes of intermediate resolution where the wall-cell centroid falls within the buffer region of the boundary layer.

The k-Epsilon and Reynolds Stress Transport models use a two-layer wall treatment, where the computation is split into two layers. In the layer adjacent to the wall, turbulent dissipation rate ε and turbulent viscosity μ_t are specified as functions of wall distance. The values of ε specified in the near wall region are blended smoothly with the values computed from solving the transport equation far from the wall. The equation for the turbulent kinetic energy is solved in the entire flow. (42)
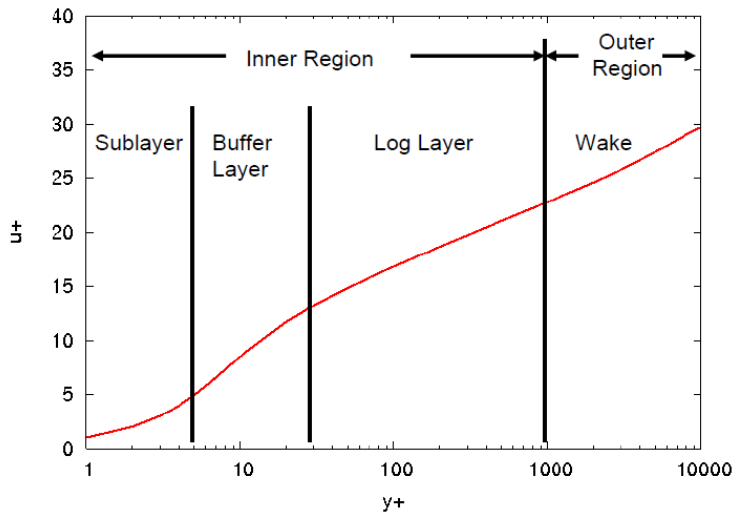
Figure 13 – Boundary layer regions (43)

The high y^+ wall treatment requires a y^+ value which is typically greater than 30 for the first cell centroid above a wall which lies in the logarithmic region of the boundary layer. The low y^+ wall treatment requires a y+ value of 1 or less for the first cell above the wall, placing it in the sublayer of the boundary layer. (42) The all y^+ wall treatment is designed to give results similar to the low y^+ treatment as $y^+ \rightarrow 0$ and the high y^+ treatment for $y^+>30$, whilst giving reasonable results where the centroid falls in the buffer layer.

2.4.3   Grids

There are a number of different grid types commonly used in CFD applications and as an object has an effect on the flow field both in the local region of the object and often the far field as well, the domain needs to be much larger than the object being analysed. Therefore a large volume is used, typically spanning around 50 diameters in each direction for external flow over a sphere. For internal flows such as in the cases considered, it is necessary to ensure that there is sufficient distance both up- and down- stream of the cooling holes, as well as above the wall surface for the flow to fully develop.

This entire domain must be split into cells and nodes, these cells and nodes are the locations at which the code calculates and stores fluid properties such as temperature, density, velocity etc. Therefore, to reduce the storage and computational time required to run the calculation it is important to keep the grid as coarse as possible in a given area. However, in order to resolve high gradients in the fluid properties, cells need to be very small in regions of high spatial gradient. These conflicting requirements form the basis for grid generation techniques as a good grid is paramount to obtaining a good computational solution.

Figure 14 shows the major grid categories; structured and unstructured, with hybrid and composite meshes mixing the two (44), and a number of sub categories. A structured mesh is characterised by regular connectivity that can be expressed as a 2- or 3-D array with cell locations stored as regular points in a coordinate system, this coordinate system can be Cartesian, but may also be curvilinear. Structured grids offer good solutions for fairly simple geometry and have relatively low memory requirements.
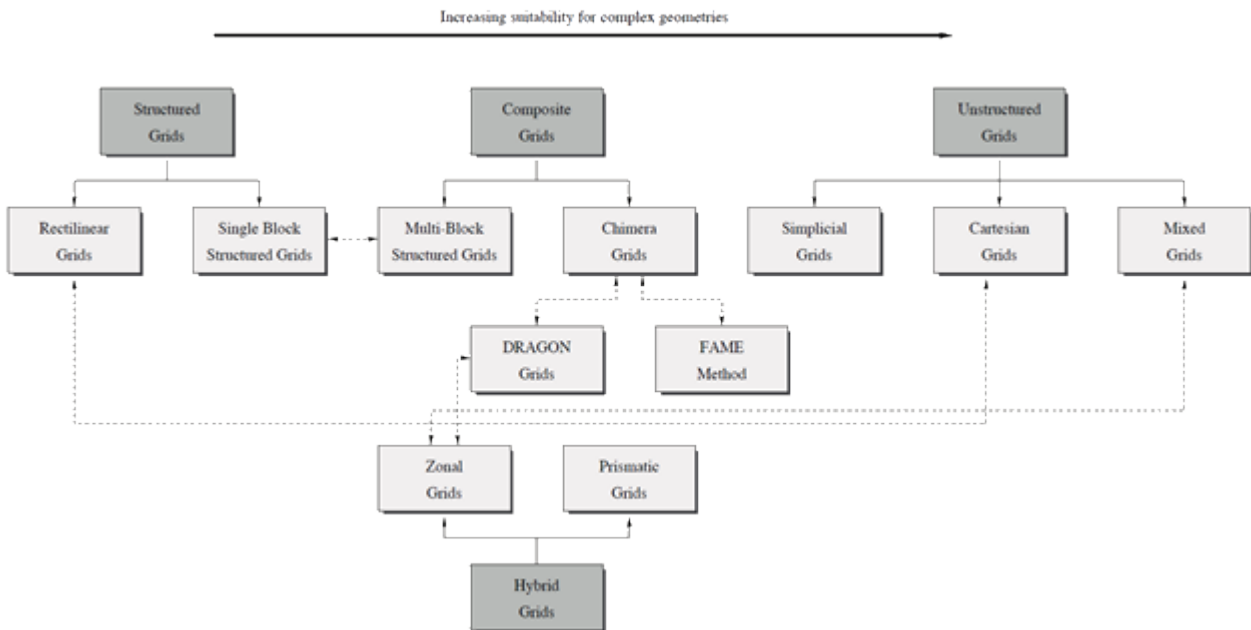
Figure 14 – Major grid categories (grey) and sub-categories (white) (45)

However, for more complex geometry a structured grid must be adapted to account for curved surfaces. One method of doing this is to create an adaptive grid which decreases cell size for areas close to the geometry as shown in Figure 15. Curvilinear grids can be set up to curve around simple shapes such as an aerofoil (Figure 16), but are unsuitable for complex geometries.
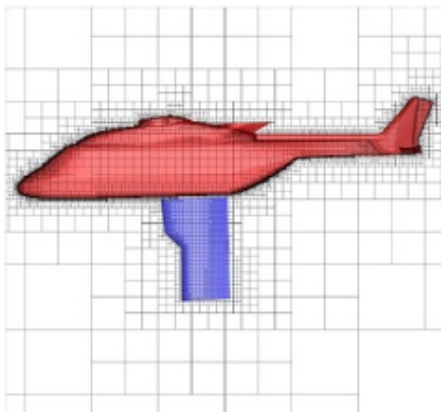
Figure 15 – Adaptive Cartesian grid (46)
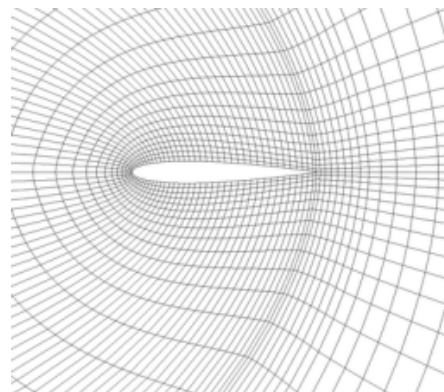
Figure 16 – Curvilinear grid around an aerofoil (47)

Unstructured grids, such as illustrated in Figure 17, are often created from polygons of varying size, shape and orientation with irregular connectivity that cannot be readily expressed in a 2- or 3-D array. Volumes, edges and vertices are numbered and their connectivity is stored in a look-up table. This significantly adds to the memory requirement for the grid. A major advantage of this grid type however is the ease with which it can be adapted to complex geometry and regions of interest within the flow, where smaller polygons can be used to obtain the required resolutions in areas with high curvatures/gradients and larger polygons can be used to fill in the space up to the far field, optimising the memory usage.
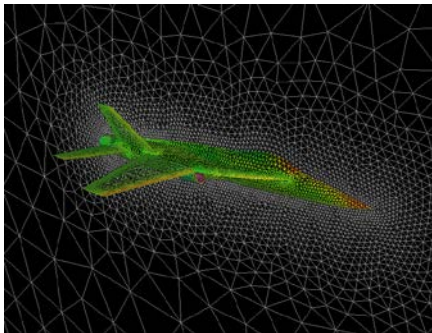
Figure 17 – Unstructured grid (48)
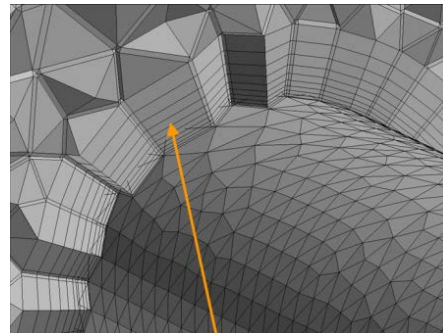
Figure 18 – Unstructured grid with prism layer in near wall region (49)

For regions close to a solid wall where there are high gradients it is often beneficial to use a prism layer grid as illustrated in Figure 18, where the 2D polyhedral mesh on the surface is extruded to create a number of prisms with increasing thickness. This is particularly useful when attempting to resolve the boundary layer as the cells nearest the wall can be very slender allowing more of the velocity profile to be captured and the cell growth and overall thickness can be tailored as necessary. A regular unstructured grid is then often used to fill the space to the far field. However, there are some numerical issues associated with unstructured meshes that must be considered, such as where cell volumes increase too quickly.

2.4.4 CFD Applied to Film Cooling Problems

Mendez and Nicoud (50) conducted a study using LES to generate detailed data numerically and to reach a better understanding of turbulent flows with effusion; a first step towards the development of appropriate wall models for Full-Coverage Film-Cooling (FCFC) or effusion cooling.

They use a computational domain which is periodic in both stream-wise and span-wise directions around a single hole to simulate an infinite plate (Figure 19). This represents the

interaction between a large number of jets and the mainstream flow. Both sides of the plate are computed to avoid any erroneous assumption regarding flow through the hole.
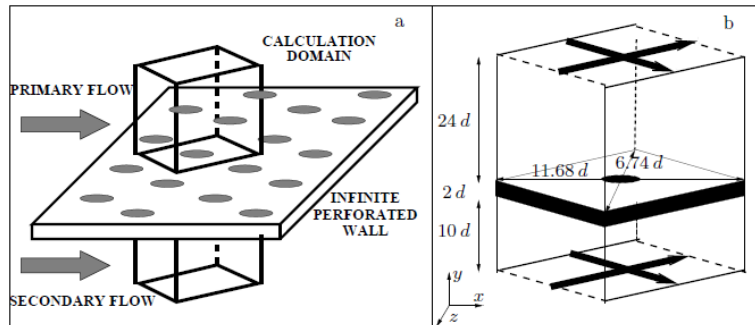
Figure 19 – (a) Geometry of the infinite perforated wall. (b) Calculation domain centred on a perforation with bold arrows corresponding to the periodic directions (50)

A plate thickness of 10mm was considered, with the 5mmØ hole at an angle of 30° to the plate in the stream-wise direction and a hole length to diameter ratio of 4. This test plate is based on a 10:1 scaled model with respect to a real perforated plate of combustor walls (51). Three meshes were considered, consisting of 150,000, 1,500,000 and 25,000,000 tetrahedral cells respectively. The simulations were carried out on the LES code AVBP developed at CERFACS. This is based on a fully explicit cell-vertex formulation and solves the compressible Navier-Stokes equations on unstructured meshes for mass density, momentum and total energy. The WALE sub-grid scale model was used, providing the appropriate damping of the sub-grid scale viscosity on the solid walls region. This sub-grid scale uses an algebraic formulation to model the sub-grid scale stresses. The TTGC numerical scheme was used which was specifically developed to handle unsteady turbulent flows on unstructured meshes. This scheme is third order accurate in both space and time. An adiabatic, non-slip wall boundary was used for the plate, with free stream boundaries used for the upper and lower limits of the domain.

The influence of the computational domain is discussed with simulations of 1-hole and 4-hole configurations showing no major differences in either time-averaged or root mean square velocity profiles. Comparisons are then made with experimental results to determine similarities and differences between a bi-periodic effusion flow and a spatially evolving flow as seen in real applications, with the simulations showing good general agreement. The main difference between spatially evolving experimental results and the synthetic computational flow is in the stream-wise velocity, which changes from one row to the next in the experiment. The simulation therefore best describes the asymptotic case where the turbulent flow is fully developed and the flow is independent of the hole considered.

Using this methodology, the authors were able to capture a number of the main flow features characteristic of a film cooling flow regime including the counter-rotating vortical structures both inside and outside the hole, a horseshow vortex upstream of the jet and spiral separation node vortices downstream, separation at hole entry and exit due to high blowing ratio and the entrainment phenomenon in the jet wake. However, as this is a LES study, the simulation was carried out on a supercomputer.

Ceccherini et. al. (52; 53) have carried out both experimental and computational analysis of the cooling effectiveness contributions of slot and effusion arrays. Effusion testing is carried out over a number of velocity ratios in order to cover a range of engine operating conditions and measurements of heat transfer coefficients were taken on a scale model using a steady-state technique and thermo-chromatic liquid crystals. A RANS based CFD calculation is also conducted over the first 16 rows of effusion cooling holes using the ANSYS® CFX package.
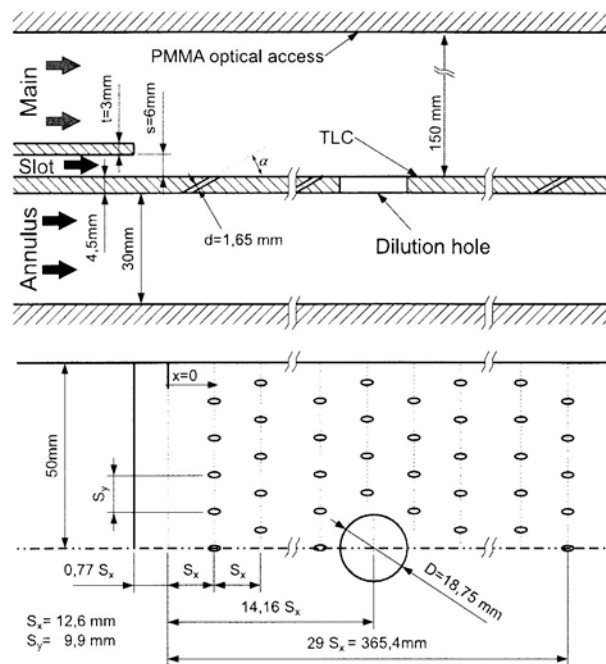
Figure 20 – Test rig geometry (53)

In this CFD solution the fluid is modelled as an ideal gas with constant specific heat capacity, thermal conductivity and molecular viscosity, with the energy equations solved in terms of total energy including viscous heating effects. A K-ω based Shear Stress Transport (SST) turbulence model is used with high resolution advection scheme built into CFX. A fully hexahedral multi-block numerical grid is used throughout the domain, with a correct O-grid meshing approach applied to the effusion holes. Automatic wall functions ensure a consistent near wall treatment of $y^+ \approx 1$. A total of about 2 million mesh elements are used. Inlet turbulence level and

macroscopic length scale are set in order to replicate experimental test conditions. Adiabatic boundary conditions were imposed on all walls, with symmetry conditions set on the lateral sides.

This study was focused on the interactions between the slot flow and the effusion cooling jets. In this experiment cooling air is drawn through the cooling chamber with the use of a pump on the outlet. The addition of the slot injector has the characteristics of a backwards facing step when it is not in use, this inevitably has an effect on the turbulence levels in the flow downstream inducing a region of recirculating flow.

It is noted in (52) that the CFD calculations overestimated the heat transfer coefficients with respect to the experimental results obtained. This is put down to a reduction in the thermal boundary layer due to the mass additions performed by the effusion jets as well as the induced three dimensional vortical structures originating from the jets in cross flow. It is also found that the scaling factor for increased HTC due to effusion jets in this experiment is the velocity ratio (V_r) rather than the blowing ratio (M) which is usually considered for adiabatic effectiveness, where;

$$V_r = \frac{V_{effusion}}{V_{main}}, M = \frac{\dot{m}_{effusion}/A_{effusion}}{\dot{m}_{main}/A_{main}}$$

<div align="right">**Equation 44a,b**</div>

With $\dot{m}, A$ and V representing mass flow rate, cross section area and velocity respectively. This implies that the density ratio of the cooling and main flows is more important when considering HTC than blowing ratio. In an engine the density ratio is typically in the range 1.5-3. Ceccherini et al. initially conducted analysis at a density ratio of 1, and then moved onto 1.51 through the use of CO_2 as the coolant gas.

Harrison and Bogard (54) compare the realizable k-ε, standard k-ω and Reynolds Stress Model (RSM) turbulence models in simulating a flat plate film cooling experiment. Simulations are run to determine the adiabatic effectiveness (η) and heat transfer coefficient augmentation distributions on a flat plate.

The geometry and hexahedral mesh are generated using GAMBIT and cases solved using FLUENT 6.3. The mesh is developed for all simulations with y^+ =1 so that near wall treatment could be used. Symmetry planes are used at the hole centre plane and half pitch plane to simulate a row of film cooling holes. A symmetry plane is also used on the top face of the

domain at a distance of 6*D*. Adiabatic walls are used for all walls for the adiabatic effectiveness case, and all but the top face of the flat plate for the heat transfer case. Blowing ratios of M=0.5 and M=1 are used in both cases, and for the adiabatic effectiveness case density ratios of 1.5 and 1.8 are analysed. Heat transfer cases are run with a density ratio of 1 to reflect experimental conditions. The final mesh consisted of approximately 1.36 million cells. The hole is angled at 30° with a 5mm diameter.
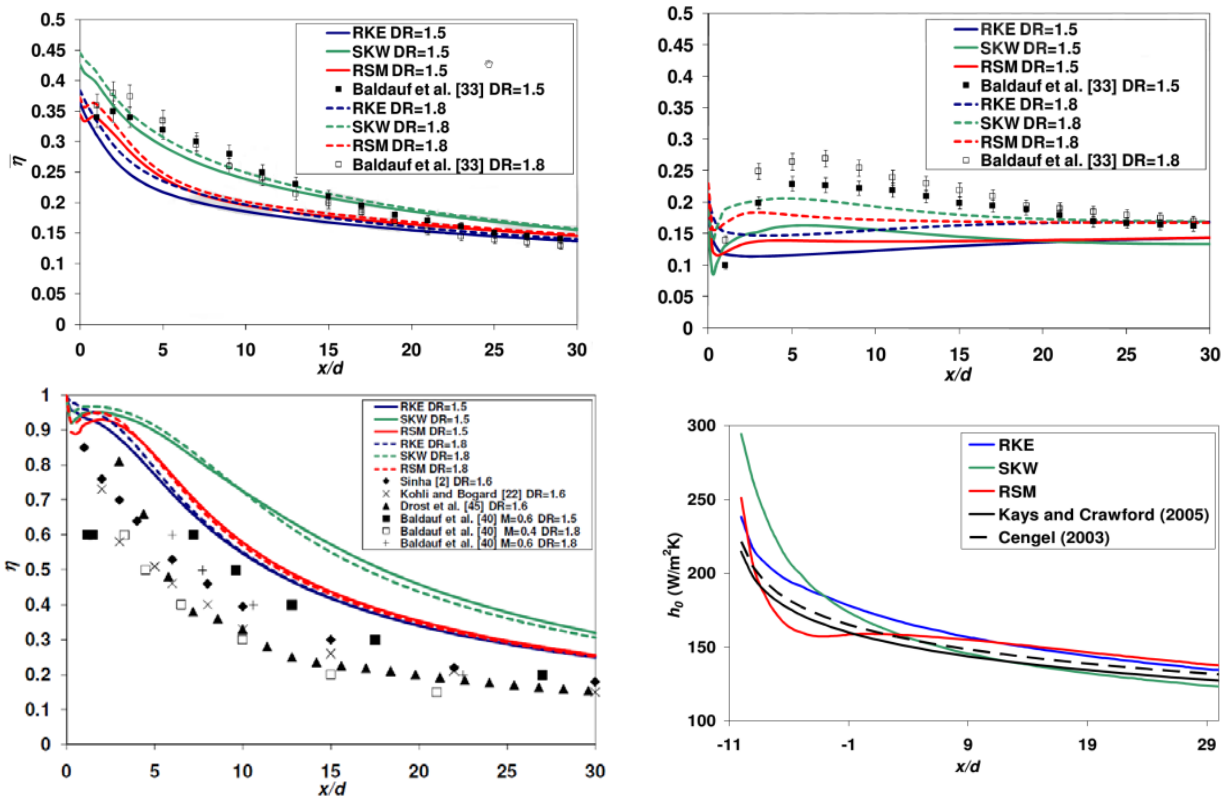
Figure 21 – Average span-wise effectiveness at a) M=0.5 and b) M=1, c) Centreline effectiveness distribution at M=0.5 d) Predictions of h_0 (54)

Results show that the *k-ω* predicts *η* most accurately near the hole, with the RSM model agreeing with experiment slightly better than *k-ε* but not as well as *k-ω*. Far from the hole, all turbulence models predict similar *η* levels and predict experimental values accurately as shown in Figure 21. However, the *k-ω* model is the worst at predicting centreline *η* with the *k-ε* model showing slightly better results than RSM. All three models provide poor predictions of lateral distributions. All three models predict reasonable results for heat transfer coefficients. Density ratio is shown to have a much greater effect at the higher blowing ratio condition when the jet is detached from the surface, with lower DR causing a higher VR at a given blowing ratio, increasing the jet separation from the wall.

Bacci and Fachinni (55) try to improve on the standard RANS based turbulence models by using a modified version of the *k-ε* turbulence model specifically designed for film cooling flows, based on an anisotropic eddy viscosity assumption. Comparison of computed adiabatic effectiveness profiles with experimental measurements is provided in order to validate the model quantitatively, along with results obtained from a standard *k-ε* model.

The modified model (KEA) introduces an anisotropy factor to correct the eddy viscosity relative to the cross Reynolds stresses. This factor varies from a value of 4.5 in the log-layer to 1.0 at the outer edge of the boundary layer. This is based on experimental data and DNS simulations which show the overall effect of flow anisotropy on the main flow field is a larger turbulent transport in the jet lateral direction, especially with respect to the wall-normal direction. This correction is applied in the momentum equations only, with the continuity and energy equations remaining unchanged. A wall function approach is used to model turbulence in the near wall region.

The model is validated against a test case consisting of a flat plate with a single row of stream-wise inclined round jets. The hole of diameter (*D*) 12.7mm, has a length to diameter ratio (l/d) of 1.75 and is inclined at 35°. A hole near the centre of the plate is considered, allowing edge effects to be neglected. The flow field is then assumed to be symmetric about a plane dissecting the hole under consideration and its neighbour in either direction. The flow domain inlet is extended 18*D* upstream of the hole leading edge, allowing a fully turbulent boundary layer to develop on the plate wall. The upper boundary of the domain is 10*D* away from the plate so that it is embedded in the free-stream and a symmetry boundary applied. The constant pressure outflow boundary is located at 18*D* downstream of the hole trailing edge. A block structured mesh is used, containing 556,018 elements with y$^+$ below one for all computations and at least 10 elements are embedded in the boundary layer on the plate. Simulations were run at DR=2 and M=0.5 and 1.

The numerical results obtained with the anisotropic model showed a much better agreement with experiments than the standard *k-ε* model as shown in Figure 22.
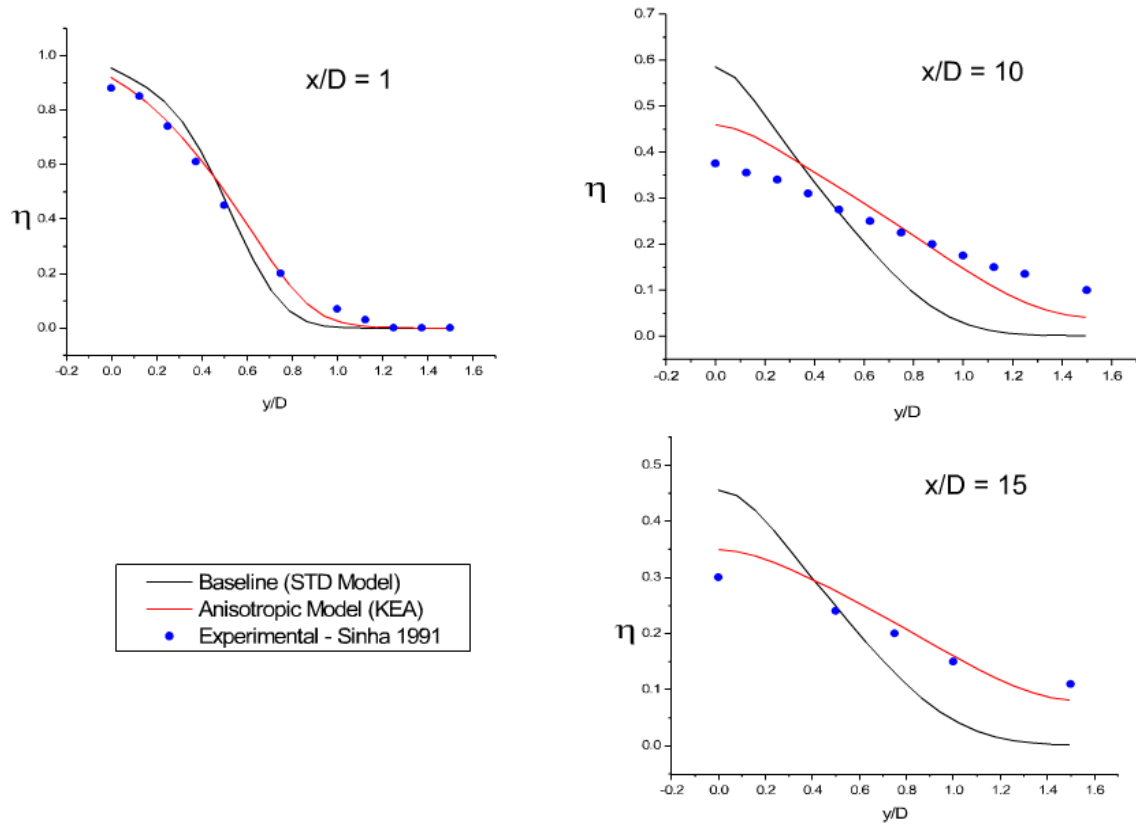
Figure 22 – Span-wise adiabatic effectiveness at different stream-wise locations for M=0.5 (55)

Roy et. al. (56) consider a Detached Eddy Simulation (DES) based on the Spalart-Allmaras turbulence model for a film cooled plate. DES is a hybrid modelling approach that combines features of RANS simulation in some parts of the flow and LES in others. DES turbulence models are set up so that boundary layers and irrotational flow regions are solved using a base RANS closure model. However, the turbulence model is intrinsically modified so that, if the grid is fine enough, it will emulate a basic LES SGS model in detached flow regions.

An unstructured grid is used to resolve the dynamic flow structures on both sides of a plate containing a single row of ∅2.54mm holes angled at 35° at a blowing ratio of 1.0 and density ratio of 2.0. This model is compared to a standard RANS based simulation and provides a more realistic description of the dynamic mixing process.

A grid size of 899,584 cells is used for this analysis with a y^+ value less than 1.0 at all locations. Stretching ratios less than 1.2 are used normal to the viscous walls and convergence judged to be reached once all residuals reduce below four orders of magnitude and there is no observable change in surface temperature prediction for an additional 30 iterations. The inlet is located 19D upstream of the hole and the outlet is 30D downstream. Symmetry planes are located on

the hole centreline and on the y/D=10 plane. It is noted that placing a symmetry plane through the hole centreline introduces a limitation in the simulation, preventing the possibility of capturing the unsteady asymmetric vertical flow patterns. Fixed mass flow rate and stagnation temperature inlet conditions are applied to both free stream and plenum inlets to control the density and blowing ratios. A fixed static pressure outlet boundary is used. No-slip wall conditions are applied to all solid walls including the hole and plenum. Turbulence intensity of 0.5% and length scale of 3% of inlet height are used. The Reynolds number based on the hole diameter and inlet conditions is 16,100. Experimental geometry used for comparison is scaled by a factor of 5 based on this Reynolds number in order to reduce the maximum flow velocity below Mach 0.3, minimising the effects of compressibility and allowing the use of a density based numerical solver.

From Figure 23 the span-wise averaged effectiveness distributions show good matching between RANS and DES solutions up to about 2D downstream of the hole, with RANS showing comparable results to experiment at x=5D, and DES results becoming more reasonable as x>12D.
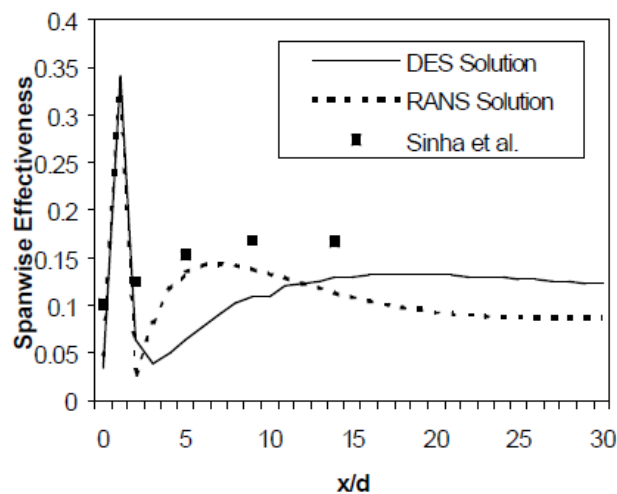
Figure 23 – Comparison between experimental and numerical
(DES and RANS) values of span-wise effectiveness (56)

Roy et al conclude that the mixing processes downstream of the hole are highly anisotropic as the turbulent diffusion is stronger in the span-wise direction. It is also noted that DES should provide a better description of the time-dependant flow structures than RANS, but the use of a symmetry boundary condition might have inhibited the growth of three-dimensional asymmetric instabilities, constraining further mixing. It is suggested that two improvements are

key for future DES simulation of film cooling applications; grid independence study and removal of symmetrical boundary conditions.

3   Experimental Setup and Test Rigs

Two experimental techniques have been developed to assess the performance of various cooling geometries in terms of adiabatic film effectiveness and overall effectiveness utilising the same test rig with modifications. Firstly, by using infra-red thermography on a conducting test piece, the overall effectiveness of a design can be determined by recording the metal temperature. Secondly, by making use of pressure sensitive paint (PSP) and a heat-mass transfer analogy, the adiabatic film effectiveness of each design can be determined.

Estimating metal temperatures from adiabatic effectiveness and heat transfer coefficient data is difficult due to the effect of conductive heat transfer through the metal. This is because the ratio of convective to conductive heat transfer (Biot number) has a strong influence on overall cooling performance. By matching the Biot number at engine and test rig conditions, the normalised metal temperature ϕ, (and therefore overall effectiveness) is maintained. Using this methodology in combination with adiabatic testing it is possible to infer quantitative information about the relative contributions of internal convection, internal conduction and film cooling on the net surface temperature.

$$Bi = \frac{hL}{k_{wall}}, \phi = \frac{T_\infty - T_w}{T_\infty - T_c} \qquad \text{Equation 45a,b}$$

3.1   Experimental Facilities

Experiments are run on the 'Biot-Scale Rig' at Loughborough University, designed and developed by Martin (57). This rig was developed with the intention of running Biot number matched experiments in order to replicate the overall effectiveness of combustor representative cooling geometries using IR thermography. Beginning with the original design concept, a number of modifications have been made in order to expand the capability and enhance the fidelity of the rig. These include the addition of a bulk free-stream turbulence generator, test section and plenum mounting modifications allowing a range of geometric scale factors and modifications enabling use of the PSP measurement technique to capture adiabatic film effectiveness. The modifications regarding the use of the PSP techniques were developed as part of this study.

In-line Heater

Air

Flow Controllers

Vent to
atmosphere

Coolant
Plenum

Test
Plate

Turbul
ence
Fan

Main
Flow
Fan

Viewing
Window

Turbulence
Generator

IR
Camera

Figure 24 – Wind Tunnel Schematic – IR Configuration

Test section flow is provided through a recirculating wind tunnel with a 20kW inline heater allowing working temperatures in the region of 600K, a schematic of which is illustrated in Figure 24. Air is circulated around the tunnel circuit by a 37kW centrifugal fan located downstream of the test section. The mainstream air is conditioned through a series of flow straightening grids and screens before entering a jets-in-crossflow type turbulence generator and on to the 150x150mm cross section test section. The turbulence generator draws air through an offtake in the vertical section of the tunnel downstream of the heater, passes it through another centrifugal fan and into a pair of plenums located on either side of the mainstream. Boosted in pressure by the centrifugal fan, this air then re-enters the mainstream flow through a set of holes of differing diameters just upstream of the test section, allowing the bulk turbulence levels in the test section to be controlled. This arrangement provides turbulence intensity levels of around 5% when the generator is not active, increasing to 20% when the generator is enabled. Coolant flow fed from the main laboratory air system at around 6bar is scheduled by a pair of Alicat^{TM} flow controllers which pass air at a desired flow rate into a plenum and through a pair of grids in an effort to ensure the flow is delivered to the test plate as evenly as possible. The plenum is mounted to the test section with a 15mm thick Monolux® gasket to limit heat conduction from the hot walls of the test section into the coolant. Rubber gaskets are also used where necessary to eliminate coolant leaks. The tunnel is vented to atmosphere just downstream of the test section and before the fan to maintain atmospheric

pressure conditions in the mainstream flow. Fresh air is circulated through the room from a ceiling vent located at one end of the room and into a variable speed ventilation fan pushing air through a second ventilation duct at the opposite end. This prevents the build-up of heat and ambient Nitrogen concentration in the IR and PSP experiments respectively.
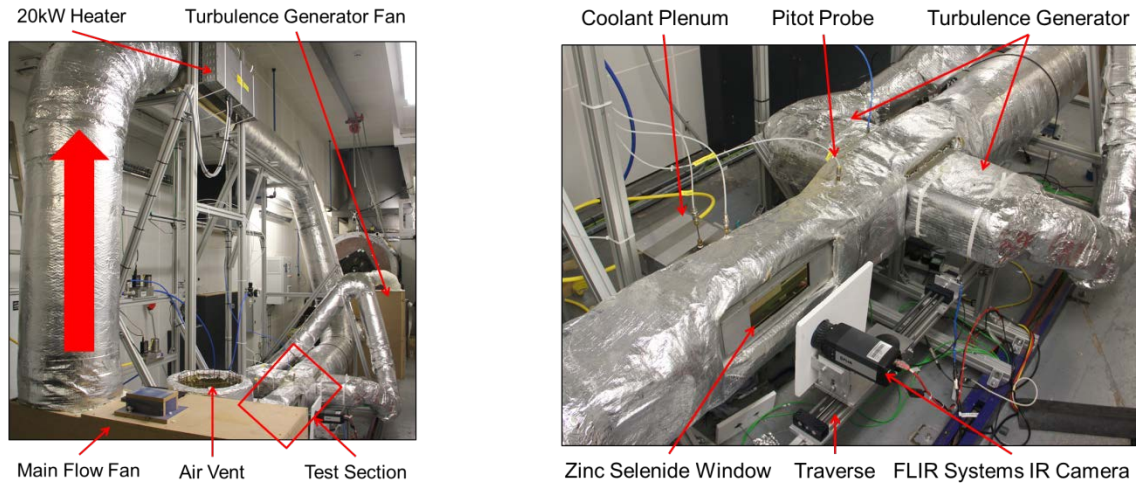
Figure 25 – Picture of Biot scale rig and test section

3.1.1 Instrumentation

Pressure tappings, Furness™ and SensorTechnics™ transducers and K-type thermocouples are used to measure pressure and temperature information at key locations such as the coolant feed plenum, main flow section and test section wall. Main flow velocity is measured using a pitot probe located between the turbulence generator and test section. Signals are conditioned using a National Instruments CompactDAQ module-based measurement system consisting of a 16-channel thermocouple module and two 4-channel voltage measuring analogue input modules, data is captured and displayed in the custom Labview™ rig monitoring and control software. The main flow temperature is controlled using a 20kW electric heater and PID controller monitoring the temperature immediately upstream of the test section. The two Alicat^{TM} flow controllers are used to control and measure coolant flow rates into the plenum section up to 2000l/min (STP) each and the pressure differential over the test plate is measured with a SensorTechnics™ BTE5000 350mbar series pressure transducer. A window aperture is located on the opposite wall to the test plate to allow optical access for the imaging systems. Cameras are mounted on a stepper motor driven linear traverse in order to enable precise incremental imaging of the entire test plate with a limited field of view. Figure 25 shows several key components of the test rig.

3.1.1.1 IR Thermography

 A FLIR A600 series infra-red camera is trained directly onto the test plate through a specially coated zinc selenide window which is semi-transparent to IR wavelengths (3.5-12µm) allowing the capture of temperature data on the metal plate surface once the entire system has been calibrated. This camera uses an uncooled micro-bolometer with a spectral range of 7.5-14µm and a focal plane array to image the surface with a resolution of 640x480 pixels. Due to the limited field of view provided by the fixed lens, the camera is mounted on a stepper motor driven linear traverse, allowing images to be acquired at incremental locations along the plate surface and then digitally stitched together to form an image of the complete plate. The body of the IR camera is shielded from the radiative heat generated by the elevated temperature of the tunnel with a sheet of Monolux®. In this IR bulk effectiveness measurement configuration, the flow controllers are fed with high pressure air from the main lab air system, at or near ambient temperature conditions.
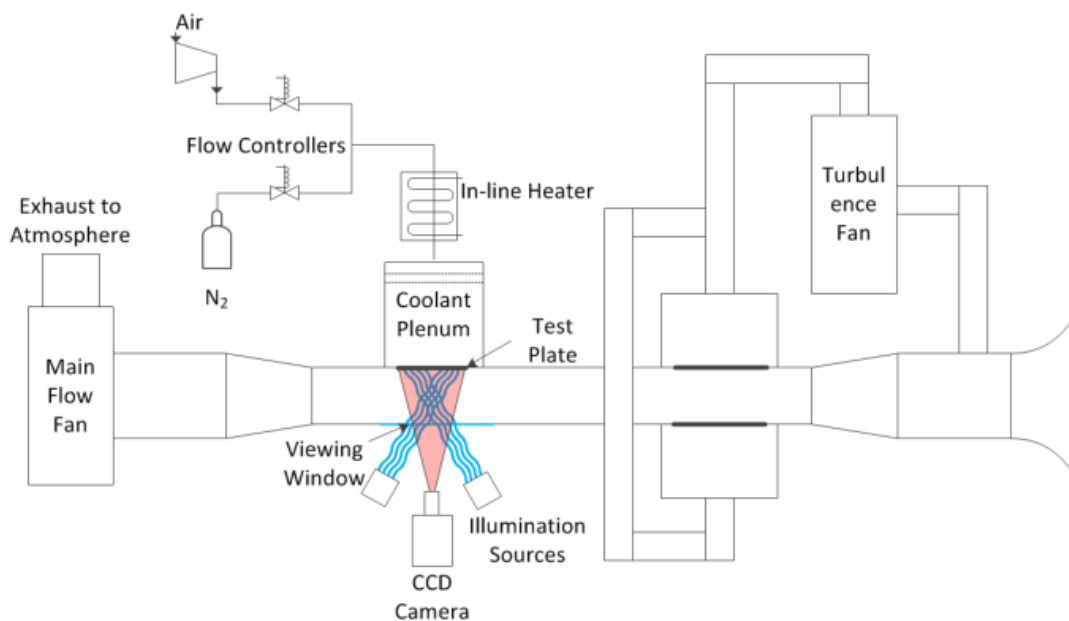
Figure 26 – Wind Tunnel Schematic – PSP Configuration

3.1.1.2 Pressure Sensitive Paint (PSP) Technique

Application of the pressure sensitive paint (PSP) technique described in section 3.3 requires a number of modifications to be made to the rig as shown in Figure 26 and 27. A section of the tunnel is removed upstream of the heater, resulting in an open-loop configuration. Without this modification, the concentration of Oxygen within the recirculating flow reduces as the test proceeds and more Nitrogen is added. This results in the leading edge of the test plate

measuring an adiabatic effectiveness greater than zero, compromising the results. The main flow heater is no longer used and instead an inline heating element has been added into the coolant delivery line to ensure isothermal running conditions using the existing PID controller set-up. The window is replaced with float glass to allow imaging at visible wavelengths and the IR camera is replaced with a PointGrey Grasshopper2 with 16mm wide angle lens allowing an image to be taken of the entire test plate at once. This monochrome camera contains a Sony ICX625 CCD sensor allowing a maximum resolution of 2448x2048 pixels at up to 15fps with a 14-bit ADC. The sensor has a full well depth of $7300e^-$ and SNR of 57dB. Illumination is provided by a pair of Luxeonstar Royal Blue Tristar LED clusters providing light at 445nm. These LEDs are mounted onto the camera, ensuring the illumination field cannot move relative to the camera field of view. Figure 27 also shows an alternative lighting setup where the LEDs are mounted to the inside of the window frame. Although not employed in gathering the data described here, this modification represents a design improvement evolved from this study. The actual lighting is similar to the setup shown in Figure 40. The LEDs are controlled through the NI CompactDAQ chassis allowing the rig software to switch them on and off as required. A 660±30nm bandpass filter is fitted to the front of the camera lens to filter light that is not in the emission range of the paint. The air supply to one of the coolant flow controllers is also switched to a regulated Nitrogen supply fed from a cylinder reservoir outside the laborotory.
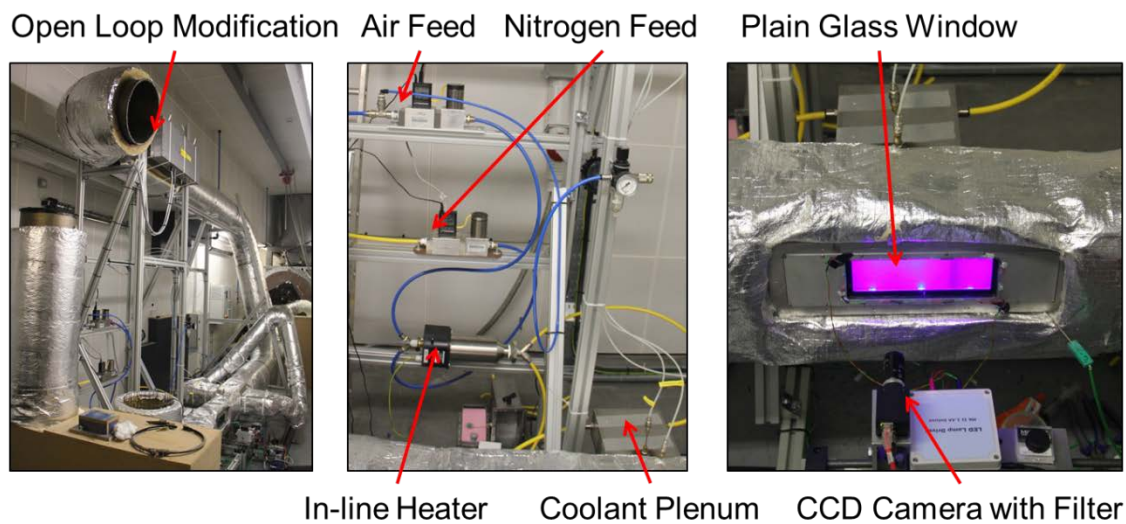
Figure 27 – PSP Specific Modifications

3.1.2 Turbulence Generator

A jets in crossflow type turbulence generator is used in this wind tunnel in order to vary the bulk freestream turbulence level and set its scale. This was developed in the same way as described

by Martin. (57) A second centrifugal fan is used to feed high pressure air into a pair of plenums located upstream of the test section, this fan removes air from downstream of the heater in order to minimise the temperature difference between freestream and injected air. Perforated plates are fitted to the wall of the tunnel and fed with air via the plenums. A number of perforated plate designs are tested in order to obtain a highly turbulent yet uniform flow field. The target intensity was given by combustor turbulence data gathered on annular rigs operated within the Combustion Aerodynamics UTC research group of around 20%. The turbulent flow characteristics are measured at two locations just up- and down-stream of the test section. These measurements are carried out using Dantec™ Dynamics Streamline constant temperature anemometer. This technique relies on the cooling effect of a flow on a heated fine wire gauge to determine the time-dependent variation of velocity at a point in the flow. Statistics such as mean velocity, turbulence intensity, integral length scale and power spectra can be extracted from the resulting CTA velocity time histories.

Figure 28 –Turbulence Generator prior to installation of insulation
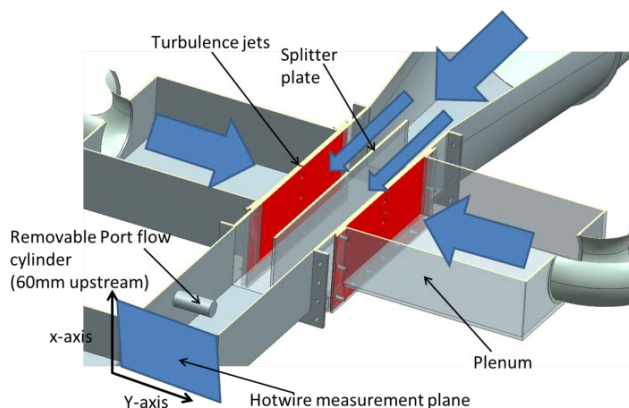
Figure 29 – Turbulence Generator Schematic

The turbulence generator, as illustrated in Figures 28 and 29, employs high velocity cross flow jets to manipulate the freestream turbulence conditions; these jets create high levels of shear, augmenting the turbulence levels. In order to obtain as uniform a flow field as possible, a range of different diameter holes are used in the turbulence plates. This approach results in jets with different levels of penetration into the freestream as shown in Figure 30, with correlations used to guide the design of the turbulent jets.
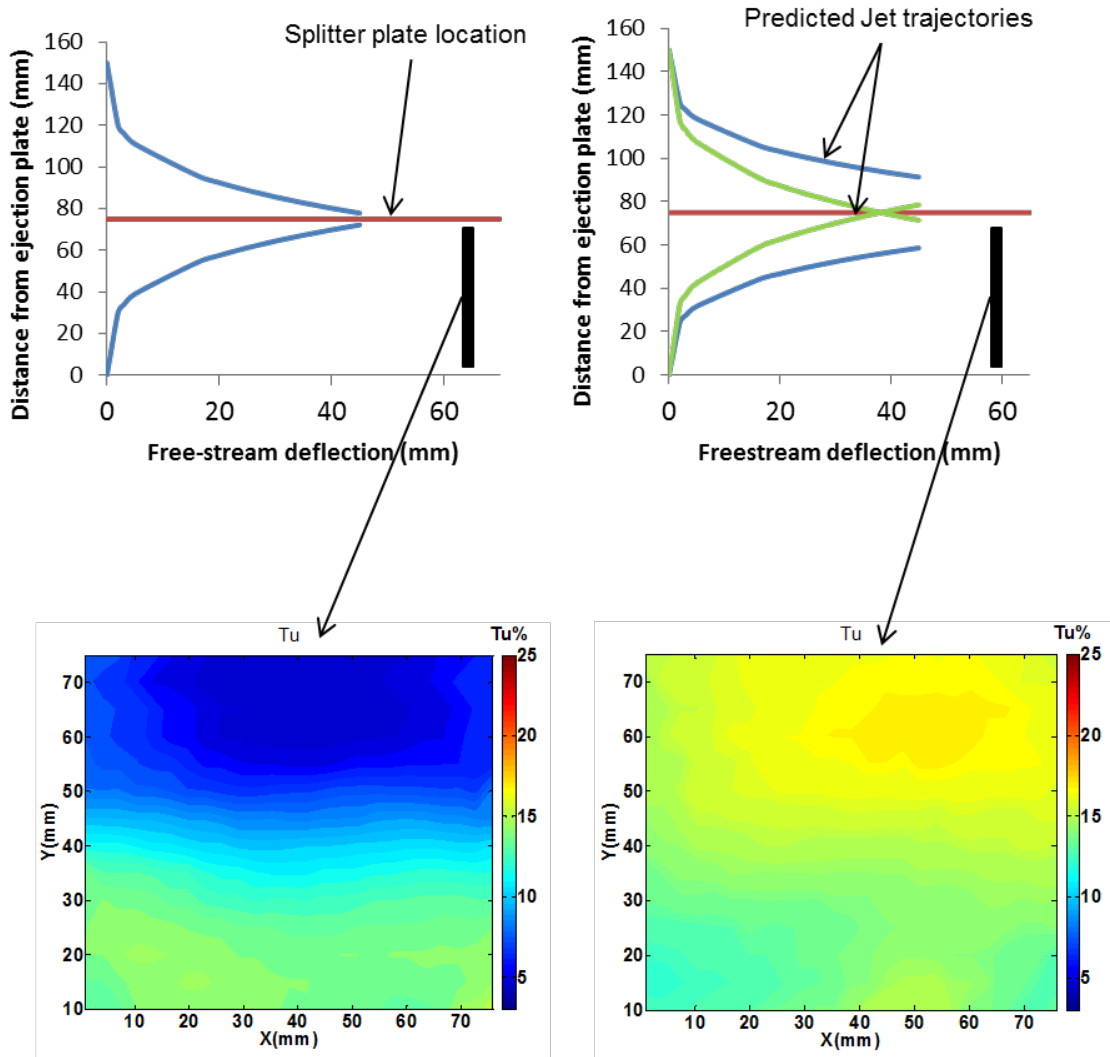
Turbulence flow profiles

Figure 30 – Using multiple jets to improve freestream turbulence uniformity

Turbulence levels are first measured without the turbulence generator to establish the baseline conditions, results for mean velocity, turbulence intensity and length scales are illustrated in Figure 31. All tests are carried out at ambient temperature and pressure conditions due to limitations on running the CTA probe at elevated freestream temperatures. The baseline tests resulted in an average turbulence intensity of 4.4% and length scale of 16mm just upstream of the test section.
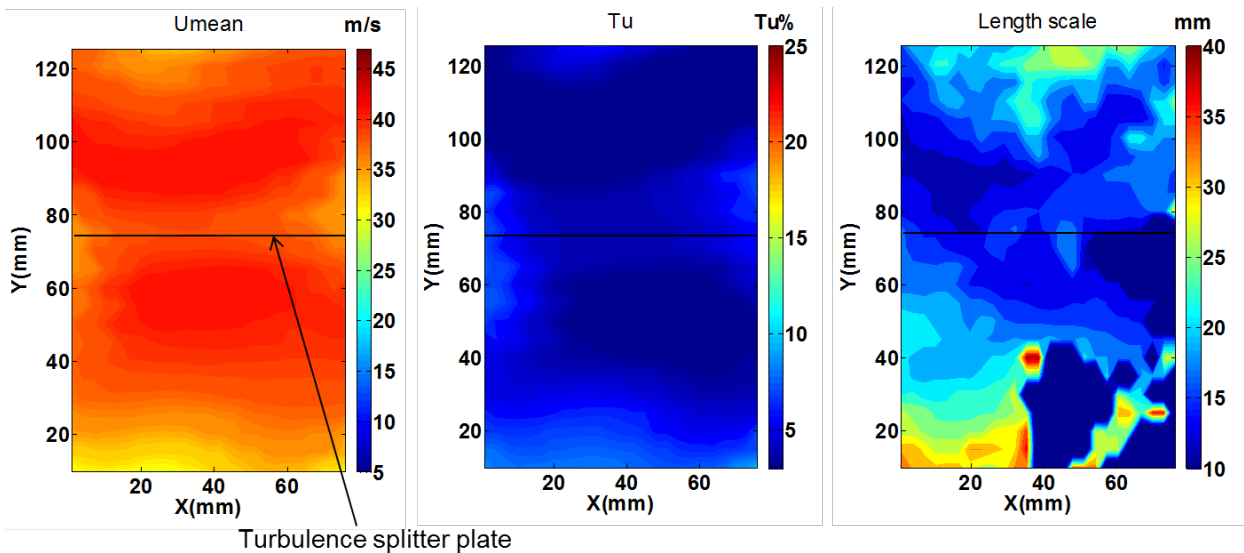
Figure 31 – Baseline turbulence conditions
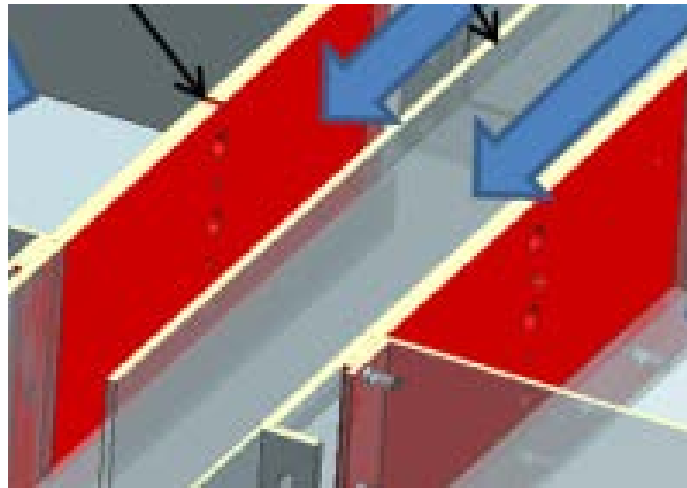
Figure 32 – Close up of perforated plates

A number of perforated plates and pressure drops were tested, with the combination resulting in the highest and most uniform turbulence condition consisting of a plate containing 6x8mm and 5x12mm diameter holes alternately placed similar to the example plate shown in Figure 32 but with the holes placed on the trailing edge of the plate, locating them closer to the test section. By running this plate at a velocity ratio of 4.1, an average turbulent intensity of 19.1% and length scale of around 13D is measured just upstream of the test section as illustrated in Figure 33. Measurements taken just downstream of the test section show an average turbulent intensity of 12.1% and length scale of 13.6D as shown in Figure 34. The two configurations described are then used as the low and high turbulence conditions during both IR and PSP tests.

Figure 33 – High turbulence conditions upstream location
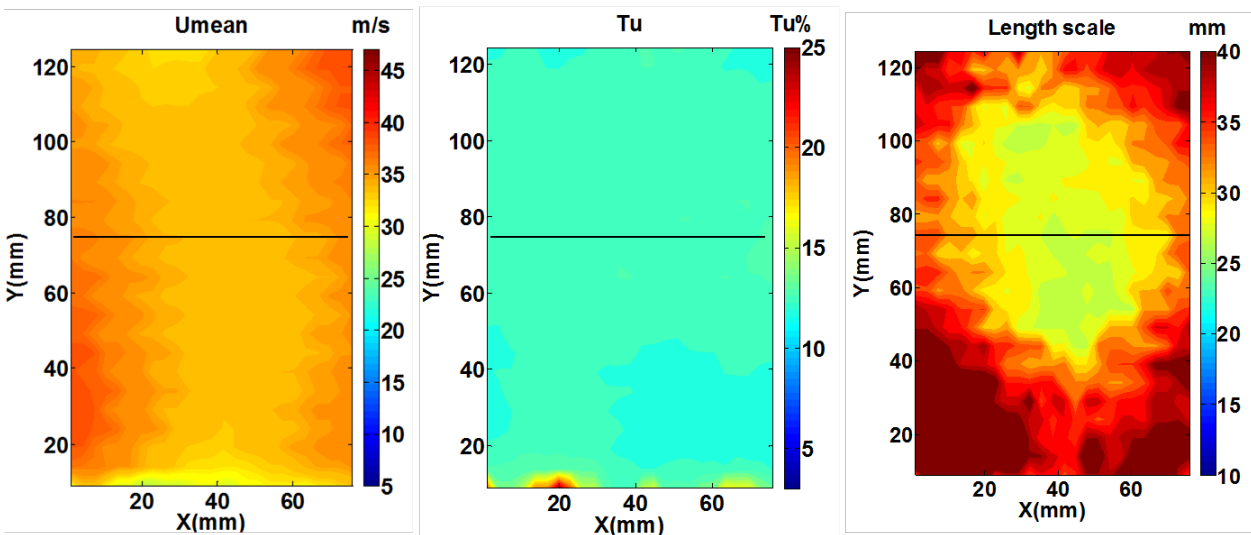
Figure 34 – High turbulence conditions downstream location

3.2 Overall Effectiveness Measurements - Infra-Red Thermography

Overall effectiveness is a non-dimensional temperature used to relate the surface metal temperature to the coolant and freestream gas temperatures and is defined by Equation 47.

Using this measure it is possible to relate metal temperatures obtained through rig testing to an equivalent metal temperature at engine running conditions by appropriately scaling the experiment. This overall temperature accounts for the effects of conduction through the metal as well as convective heat transfer between the gas and metal surface and therefore gives a more representative indication of the actual temperatures the metal is exposed to in the engine environment. This experiment relies on IR thermography to measure the surface metal temperature.

3.2.1 Introduction to IR thermography

As previously discussed in section 2.3.1, all objects emit radiation with a spectral distribution according to Plank's law based on their absolute temperature and spectral emissivity. Infrared thermography uses the energy emitted at infrared wavelengths to determine this temperature. The technique involves use of an IR camera which consists of a micro bolometer to measure the power of incident electromagnetic radiation through a change in electrical resistance of a detector material when it is heated by the radiation emitted by the target. Real physical bodies can reflect and absorb fractions of the incident radiation, therefore careful calibration is required in order to minimise the effects of any radiation from sources other than the test plate, such as atmospheric and viewing window transmittance or ambient radiation from the test section walls. The in-situ calibration technique also reduces the impact of optical effects such as reflection of the lens in the window, which can be seen as a halo in the recorded image.

3.2.2 Biot Scaling Philosophy

Due to the requirement to extract engine equivalent metal temperatures from the data obtained on this rig, it has to be correctly aero-thermally scaled. The Reynolds number must be matched to ensure the flow field is correct. Nusselt number is matched to scale the boundary between the fluid and the wall and Biot number reproduces the conduction of heat away from the surface and into the wall. Therefore, both the fluid properties, in order to match engine Nusselt number, and hence convective heat transfer, as well as the solid properties, to match engine Biot number and hence conductive heat transfer, must be scaled.

$$Re = \frac{\rho U L}{\mu}, Nu = \frac{hL}{k_{gas}}, Bi = \frac{hL}{k_{wall}}$$

<div align="right">**Equation 46a,b,c**</div>

As a result, both fluid properties, as in conventional adiabatic cooling flow experiments (i.e. Re, M, I and k_c), as well as the wall conductivity k_w must be considered. As such, the conductivity ratio k_w/k_c must be matched correctly by choosing an appropriate material from which to manufacture the test plates. The 'Biot Scale' test rig was conceived and developed by Steve Thorpe and Damian Martin alongside this scaling methodology. Martiny et al. (58) show the importance of Biot number on heat transfer in effusion cooling problems through the development of a mathematical model.
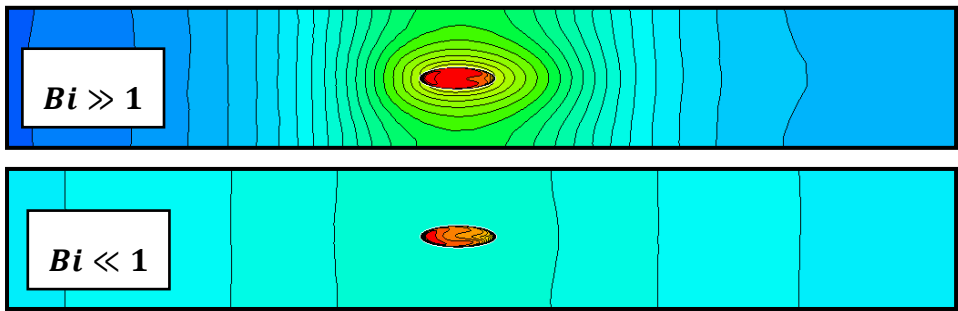
Figure 35 – Biot number effect on normalised metal temperature

Figure 35 shows the influence changing Biot number has on the normalised metal temperature distribution around a single cylindrical hole through a wall. It shows that in order to correctly capture the thermal gradients within the metal, the conductivity ratio between metal and air at test conditions must be matched to those at engine conditions. A computational study was carried out as a preliminary part of this study to ensure the material choice for the test plates is appropriate by scaling the calculated overall effectiveness taken on a line through the centre of the test plate back up to engine scale conditions and subtracting the resultant metal temperature from those obtained from a simulation carried out at engine conditions, the result of which is illustrated in Figure 36. From this plot it can be seen that using the correct material is important to get the correct temperature field, particularly in the area around the cooling hole. Figure 37 shows typical engine running conditions and properties for an example engine cycle, along with equivalent test conditions once scaling to rig appropriate conditions has been applied.
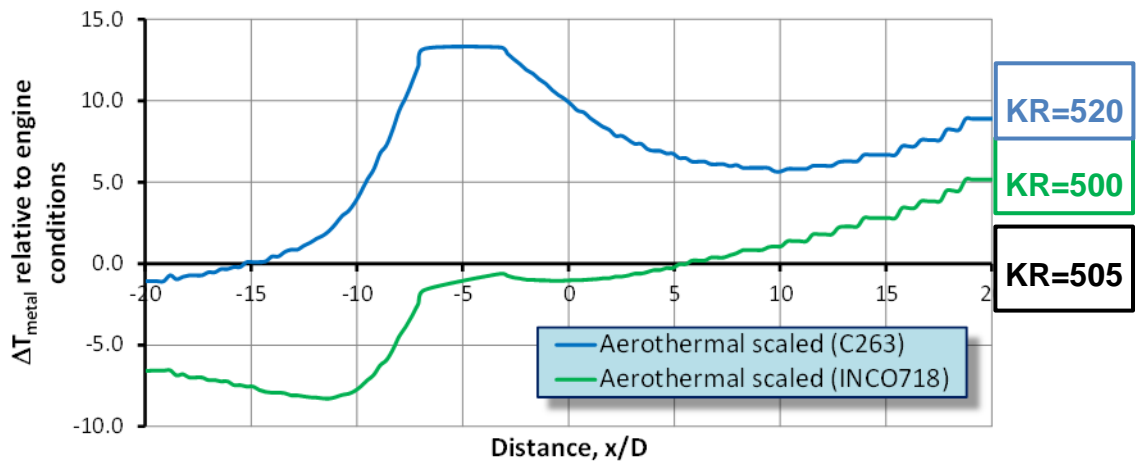
Figure 36 – Comparison of experimental scale results to engine scale temperature

Engine cycle entaps

$Po\infty = 29.1$ Bar
$To\infty = 1900K$
$\rho\infty = 5.5$ kg/m3
$U\infty = 50\text{-}60$m/s

$Poc = 30$ Bar
$Toc = 900K$
$\rho c = 11.6$ kg/m3
$Kc = 6.3x10^{-2}$ w/mk

$Re\infty = 4500\text{-}5500$

$Kwall = 26$w/mk @ $Tw = 1200K$, $\phi = 0.7$

$Red = 2.23x10^4$ ($d = \emptyset$ 0.6mm)
$Uj = 125$.m/s

$Dr \approx \dfrac{T_g}{T_c} = \dfrac{1900}{900} = 2$

$DP/P \approx 3\%$
$\Delta P = 90$Kpa

$\dfrac{T_w}{T_c} = \dfrac{1200}{900} = 1.3$

Br = 5.6, I=14.64, Dr = 2

Biot Rig

$Po\infty = 0.94685$ Bar
$To\infty = 600K$
$\rho\infty = 0.581$ kg/m3
$U\infty = 55\text{-}62$(max) m/s

$Poc = 1$ Bar
$Toc = 300K$
$\rho c = 1.16$ kg/m3
$Kc = 2.62x10^{-2}$ w/mk

$Re\infty = 3400\text{-}4700$

$Kwall = 10.7$w/mk @ $Tw = 378.9K$

$Red = 2.23x10^4$ ($d = \emptyset$ 2.4mm)
$Uj = 147$m/s

$Dr = \dfrac{T_g}{T_c} = \dfrac{600}{300} = 2$

$DP/P \approx 12.6\%$
@ SF 4
$\Delta P = 12.6$Kpa

$\dfrac{T_w}{T_c} = \dfrac{378.9}{300} = 1.2$

Br = 5.6, I=14.64, Dr = 2
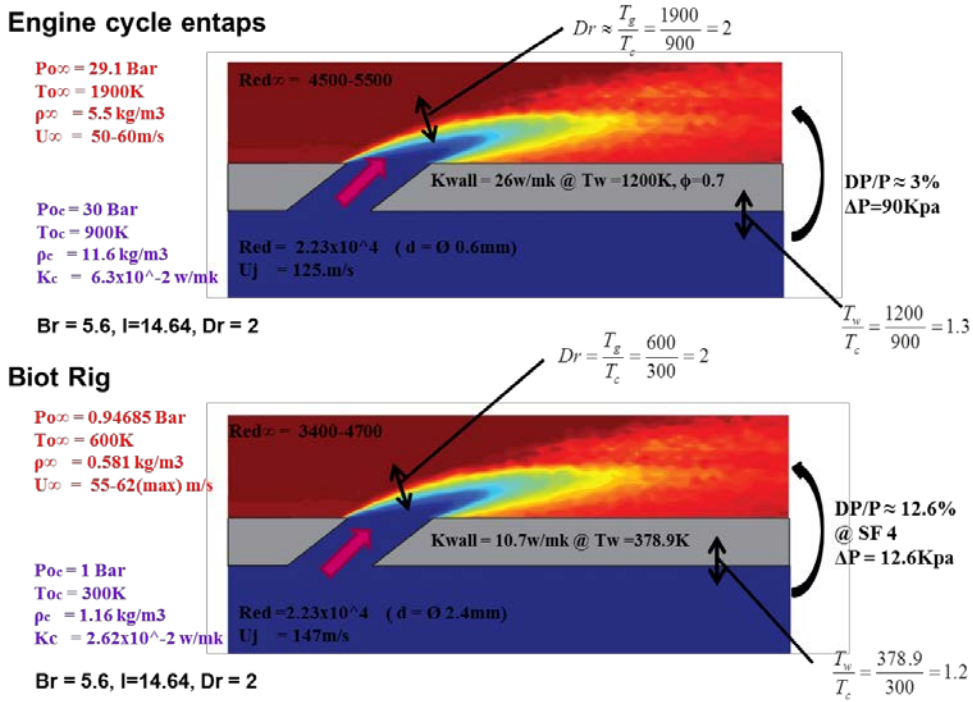
Figure 37 –Aero and thermal scaling for an example engine cycle

However, the scaling process is constrained by the operating limitations of the test rig; the coolant delivery temperature is limited to a near ambient condition due to the lack of any pre-cooling of the coolant flow. The freestream temperature is limited to roughly 550K due to the occurrence of thermal degradation of the zinc-selenide window coating above this temperature. Fan power limits the freestream velocity to around 38m/s. Nitrogen feed pressure limits the maximum coolant mass flow rate to around 1000l/min restricting the maximum coolant pressure drop to around 10,000Pa and the rig is not pressurised limiting the freestream pressure to ambient.

A scale factor of 4.2 is chosen for these tests as it allows for a sufficient number of cooling holes to be placed in the test plate area available whilst allowing the rig to be run at atmospheric pressure conditions when scaling is applied. As outlined earlier, the experiment must first be scaled aerodynamically, the first step of which is to match the flow Reynolds number, in particular in relation to the coolant hole flow. This is constrained by the pressure drop available to drive the cooling air through the hole as the coolant temperature is limited to near-atmospheric conditions. Once this flow rate is determined, the freestream conditions are set to match the momentum flux ratio. Due to the limited freestream velocity and temperature available it is not possible to match both momentum flux and density ratios, but as noted in section 2.2.6 density ratio has only a second order effect on the cooling film. Momentum ratio is chosen over blowing ratio or velocity ratio as it provides the best agreement when it is not

possible to match density ratio as shown by Martin (57). Momentum ratio describes how the jet is deflected by the mainstream flow where blowing ratio describes the relative mass of air in each stream, therefore by scaling on momentum ratio the shape of the cooling patch is better captured, this is important as in the geometries tested all rely on the coolant stream remaining attached to the wall. The shape of this coolant patch will have a larger impact on the cooling performance than the mass of coolant used, particularly as this is a single skin problem where the blowing ratio is high. The maximum running speed of the fan dictates the freestream velocity and matching the momentum flux ratio then determines the freestream temperature completing the selection of running conditions. The thermal conductivity must then be considered; this is characterised by the Nusselt and Biot numbers. As the thermal conductivity of the gas is known, the only remaining variable is the conductivity of the material the test plate is made from. In order to match the conductivity ratio between air and wall as closely as possible to engine conditions, the test plates are manufactured from Inconel718. Running conditions and the equivalent engine conditions for the experiments described here are given in Table 4.

3.2.3   Plate Preparation

The hot-side surfaces of the plates are cleaned, primed and then spray-painted with high temperature matt black high temperature paint that has a known emissivity value. The plate is allowed to dry at ambient conditions and then placed in an oven to cure at 300°C for an hour. The paint is applied in such a way as to keep the finish as even and consistent as possible.

The plates are mounted into a Tufnol frame; this helps to thermally isolate the plate from the walls of the test rig as much as possible. The plate is sealed to the frame with a bead of high temperature silicon and held in place using four grub screws.

3.2.4   IR Calibration

The IR camera is calibrated using an in-situ technique. A flat calibration plate made of 10mm thick aluminium is painted in the same way as the test plates and has two thermocouples embedded just beneath the surface, one slightly upstream and one slightly downstream of the plate centre, to measure the plate temperature. The plate is mounted on a Monolux® backing to reduce heat transfer out of the back of the plate. Due to the high thermal conductivity and thickness of the plate, a near isothermal surface is presented to the IR camera optics. The rig is brought up to temperature with a blanking plate over the plate mounting hole until thermal

equilibrium is achieved. This helps to ensure the surrounding wall temperatures are consistent with those present during the experiment. The calibration plate is then mounted and IR images taken as the plate slowly warms up ensuring the entire range of expected plate temperatures are captured. Care is taken to ensure that the plate temperature remains as close to isothermal as possible by ensuring the flow velocity is sufficiently low and monitoring the two thermocouples for parity. The IR images and simultaneous thermocouple readings are captured at regular set plate temperature intervals with 10 images captured every time the measured temperature increases by 1 degree. These data are then used to create a unique third order polynomial calibration curve for each pixel over the range of temperatures expected as shown in Figure 38. This is derived using a Matlab script to describe the relationship between temperature and intensity for each pixel in the image. This calibration data is then stored in a matrix for converting raw IR images into temperature maps for each of the test plates. Due to the fixed focal length and resolution of the IR camera, two camera positions are required to capture the entire plate and to account for possible transmission anomalies in the IR window, calibration data is captured at each unique camera location. This process has been repeated a number of times and the calibration has been found to be stable, therefore repeat calibrations are only carried out once for each testing series. Calibrating in a pixel by pixel fashion removes any effects such as reflections in the window or edge effects. Each pixel maps to roughly 0.05mm^2 on the surface of the test plates.
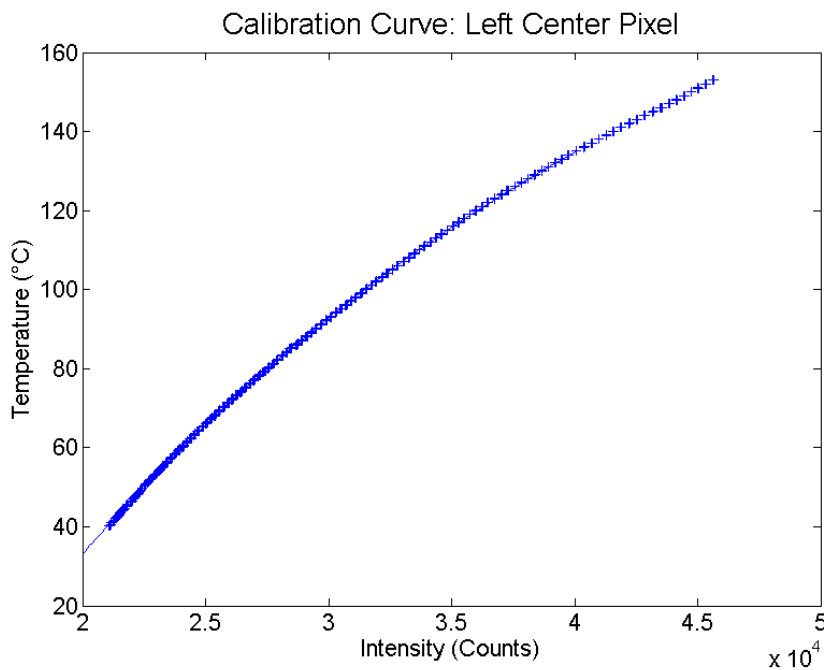
Figure 38 –Typical IR calibration curve for a single pixel

3.2.5   Test Procedure

Once the test plate has been fitted and the rig is up to the required main flow temperature, the coolant mass flow is altered until the desired pressure drop is achieved. These values are entered into the Labview code designed to operate the rig along with traverse positions required to create a composite image of the entire plate. The software will set the required flow rate and wait for the system to stabilise before recording sensor data and taking IR snapshots simultaneously. 30 data points are recorded at each traverse position before the next flow rate is set, allowed to stabilise and again recorded. A stabilisation period of 10 minutes is used to ensure thermal equilibrium is reached within the system; this is validated as sufficient by monitoring the time history of the area average plate temperature as seen by the IR camera for convergence.

3.2.6   Post Processing

Once the data has been obtained, it is input into a Matlab data reduction script which averages the 30 data points and images to obtain a time average. Intensity readings from the camera are converted into temperature using the calibration data and then in turn into normalised temperature images using the measured freestream and coolant delivery temperatures and Equation 47. These images are then stitched together to give an image for the entire plate. A span-wise effectiveness plot is also created by taking the data from a central strip, eliminating edge effects, and splitting it into slices to obtain an average for each slice.

$$\phi = \frac{T_\infty - T_{w(hotside)}}{T_\infty - T_c}$$

<div align="right">**Equation 47**</div>

3.3   Adiabatic Effectiveness Measurement – PSP Technique

In order to separate the film effectiveness from the overall effectiveness measured from the Biot scaled experiments, a technique is implemented utilising Pressure Sensitive Paint (PSP). Conventionally, 2D or surface mapped adiabatic film effectiveness of candidate cooling geometries is captured using the IR thermography technique on a low conductivity test plate to approximate an adiabatic wall. However, as cooling designs become more complex through the use of enabling technology such as the DLD manufacture technique, it becomes ever more difficult to replicate cooling geometries within test pieces using conventional manufacturing techniques. As a result, a technique involving the use of PSP and the heat-mass transfer analogy is utilised to allow existing metal test plates manufactured using the DLD process and

created for the overall effectiveness tests to be used to also determine the adiabatic film effectiveness. In this way, both bulk and adiabatic film effectiveness data are collected from the same test piece.

3.3.1 Introduction to the PSP technique

Pressure sensitive paint contains a luminescent molecule suspended in a polymer binder. When light of a specific wavelength illuminates the paint the luminophore becomes excited and emits light of a longer wavelength. This emission is affected by a number of physical processes. The most prevalent of these is oxygen quenching, whereby an increase in the partial pressure of oxygen at the paint surface results in a decreased intensity of emitted light. Another important process influencing the intensity of emitted light is temperature. As the paint temperature increases, the energy in the system increases, increasing the rate at which the dynamic quenching processes occur and therefore reducing the intensity of the emitted light.

3.3.2 Photophysics: Kinetics of Luminescence

The luminescent molecules in PSP are based on the oxygen quenching process of luminescence which is a reversible process in molecular photoluminescence. The Jablonski energy level diagram, illustrated in Figure 39, clearly describes the different energy levels and photophysical processes of luminescence. The ground-state energy of the molecule is represented by the lowest horizontal line, normally a singlet state denoted by S_0. The upper lines are energy levels for the vibrational states of excited electronic states with the excited singlet, denoted by S_1 and S_2, and triplet, denoted by T_1, states.

Singlet Excited States
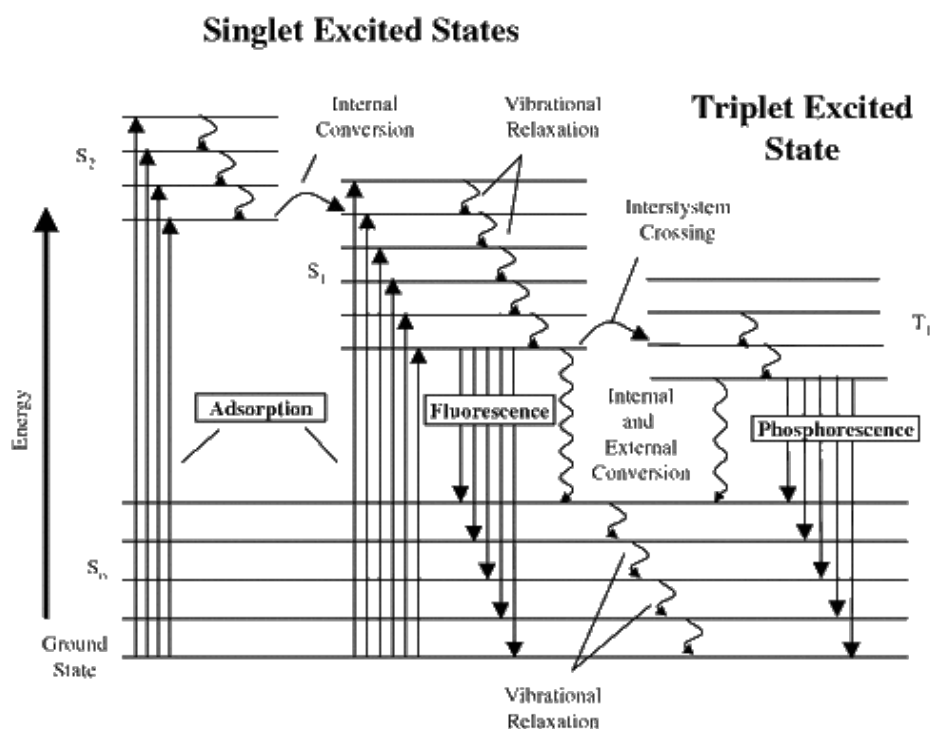
Figure 39 –Jablonski energy-level diagram, reproduced from (36)

When a photon is absorbed, the luminophore becomes excited from the ground electronic state to the excited electronic states ($S_0 \rightarrow S_1$ and $S_0 \rightarrow S_2$). Each electronic state has different vibrational states and each vibrational state has different rotational states. The excited electron returns to the unexcited ground state by a combination of radiative and radiationless processes with emission occurring through the radiative process luminescence, where luminescence is a general term for both fluorescence and phosphorescence. Fluorescence occurs when the electron transitions between the lowest singlet state (S_1) to the ground state (S_0). This is a spin-allowed radiative transition between two states of the same multiplicity. The radiative transition from the triplet state (T_1) to the ground state is called phosphorescence and is a spin-forbidden radiative transition between two states of different multiplicity. The lowest excited triplet state is formed through a radiationless transition from S_1 by intersystem crossing. Since phosphorescence is a forbidden transition, the phosphorescent lifetime is longer than the fluorescent lifetime.

The excited singlet and triplet states can be deactivated through interaction of the excited molecules with the components of a system; these processes are known as quenching processes. PSP relies on the oxygen quenching of luminescence in order to relate the air pressure (or oxygen concentration) on the model surface to the luminescent intensity of the paint. Thermal quenching also influences the luminescent intensity as the quantum efficiency

of luminescence decreases with increasing temperature due to the increased frequency of collisions improving the possibility for deactivation by external conversion.

After the luminescent molecules in the PSP absorb the energy from the excitation light of wavelength λ_1 they emit luminescence of longer wavelength λ_2 due to the Stokes shift. A CCD camera can be used to capture this emitted luminescence using a filter to remove the excitation light signal.

3.3.3 Application of PSP

In order to use the PSP technique to quantitatively measure the adiabatic film effectiveness of the various film cooling designs, the oxygen quenching behaviour of the preparation is utilised. By using nitrogen as a coolant gas and air as the main flow gas, a heat-mass transfer analogy can be applied as described by Jones (32), replacing the temperature scalar with a gas species. For a binary mixture of inert, foreign gas coolant in a freestream gas the mass concentration equation is;

$$G_x \frac{\partial C}{\partial x} + G_y \frac{\partial C}{\partial y} - \frac{\partial}{\partial y}\left(\lambda \frac{\partial C}{\partial y}\right) = 0 \qquad \text{Equation 48}$$

The energy equation, expressed in terms of enthalpy, is;

$$G_x \frac{\partial h}{\partial x} + G_y \frac{\partial h}{\partial y} - \frac{\partial}{\partial y}\left(\zeta \frac{\partial h}{\partial y}\right) = 0 \qquad \text{Equation 49}$$

Where C is the mass concentration of the coolant and h is the specific enthalpy of the mixture,

$$h = h_{main}(1 - C) + h_{cool}C \qquad \text{Equation 50}$$

The local mass flux is G with λ and ζ referring to the mass and thermal diffusion constants respectively. It is assumed that the molecular diffusivity between the gasses is similar to the thermal diffusivity. In the context of the present turbulent flow, this refers to the turbulent quantities and their equality results in the turbulent Lewis number being unity, a reasonable assumption for gasses. (59) The adiabatic wall case corresponds to an impermeable wall for the concentration equation, therefore at the wall;

$$\left(\frac{\partial C}{\partial y}\right)_w \equiv \left(\frac{\partial T}{\partial y}\right)_w = 0 \qquad \text{Equation 51}$$

With the concentration field corresponding to the temperature field,

$$\frac{C}{C_{cool}} \equiv \frac{T_{main} - T}{T_{main} - T_{cool}}$$

Therefore adiabatic effectiveness is given as;

$$\frac{C_w}{C_{cool}} \equiv \frac{T_{main} - T_{aw}}{T_{main} - T_{cool}}$$

A map of the coolant distribution over the surface is obtained by measuring the local intensity of the emitted light and therefore the local concentration of oxygen while using an oxygen free gas (in this case nitrogen) as the coolant. This map is then used to infer the equivalent temperature at the surface of an adiabatic plate and hence the adiabatic film effectiveness.

$$\eta = \frac{T_{main} - T_{aw}}{T_{main} - T_{cool}} \equiv \frac{C_{O_2\,main} - C_{O_2\,w}}{C_{O_2\,main}}$$
$$= 1 - \frac{1}{\left(1 + \left(\frac{P_{O_2:air}/P_{O_2:ref}}{P_{O_2:fg}/P_{O_2:ref}} - 1\right)\frac{M_{fg}}{M_{air}}\right)}$$

Nitrogen and air have a similar molecular mass, therefore $M_{fg}/M_{air} \cong 1$;

$$\eta \equiv \frac{C_{O_2\,main} - C_{O_2\,w}}{C_{O_2\,main}} = 1 - \frac{P_{O_2:fg}/P_{O_2:ref}}{P_{O_2:air}/P_{O_2:ref}}$$

As partial pressure varies with both concentration and pressure, the relationship $P_{O_2:air}/P_{O_2:ref}$ corrects the results for variation in static pressure over the surface due to aerodynamic features of the flow. The intensity response of the paint to the partial pressure of oxygen is related through the modified Stern-Volmer relation, Equation 56. The coefficients A, B and C are determined through a calibration procedure each time a set of test plates is sprayed with PSP.

3.3.4 Scaling

The emitted light from PSP is dependent on both the partial pressure of oxygen and the local temperature, therefore in order to avoid determining the local temperature field, it is necessary to run the test under isothermal conditions. As a result an in-line heater is added to the coolant feed line. This heater is set to match the measured freestream temperature ensuring the coolant and freestream flows are the same temperature. As previously described, the density ratio has only a second order effect on the cooling film and so is considered to have little impact

on the ranking of the designs tested. In order to match the momentum flux ratio between the two different types of experiment however, the freestream velocity must be reduced from the value used in the overall effectiveness experiments to compensate for the reduced temperature. Coolant flow properties do not change significantly from the overall effectiveness experiments, with only a slight change in feed pressure and hence mass flow rate, due to the small difference in molecular mass between nitrogen and air. This change is within the measurement resolution of the mass flow controllers. Test conditions are given in Table 4 at the end of this chapter.

3.3.5 Plate Preparation

For PSP testing the 'hot' surface is cleaned then the PSP is airbrushed directly onto the metal surface in a very thin layer and allowed to dry, this is repeated until a good surface coverage has been obtained, usually requiring around 8 layers. All test plates are sprayed at the same time alongside a calibration coupon to enable the batch to be calibrated. The sprayed plates are then placed in an oven at 65°C for an hour to cure. Once painted, exposure to light must be limited as the paint photo-degrades. Therefore when not in use, the plates are stored in a sealed box away from ambient light sources.

The plates are mounted in a Tufnol frame and sealed using a bead of silicon. It is important to ensure the plates are completely sealed before testing as any leaks will show up as areas of high effectiveness in the post-processed images. This can impact severely on the results downstream of the leak as the Nitrogen diffuses into the mainstream air. Grub screws are used to secure the plates against the frame.

3.3.6 Calibration

After painting, each batch must be calibrated so that the intensity response at a certain partial pressure condition is known. This is done using a modified version of the Stern-Volmer equation, Equation 56 below. Since partial pressure is a function of the total pressure and gas concentration, by calibrating at a constant atmospheric pressure and altering the oxygen concentration at the surface, the paint response can be calibrated against gas concentration;

$$\frac{C_{O_2}}{C_{O_{2_{ref}}}} \equiv \frac{P_{O_2}}{P_{O_{2_{ref}}}} = A(T)\left(\frac{I_{ref}}{I}\right)^2 + B(T)\frac{I_{ref}}{I} + C(T) \qquad \text{Equation 56}$$

$$A = a_1 T^3 + a_2 T^2 + a_3 T + a_4$$
$$B = b_1 T^3 + b_2 T^2 + b_3 T + b_4$$
$$C = c_1 T^3 + c_2 T^2 + c_3 T + c_4$$

The intensity of the luminescence is also a function of the temperature and therefore the paint must also be calibrated to account for temperature effects. This is done through relating the calibration coefficients A, B and C to temperature as shown in Equation 57. The calibration chamber setup is illustrated in Figure 40 with a schematic shown in Figure 41.
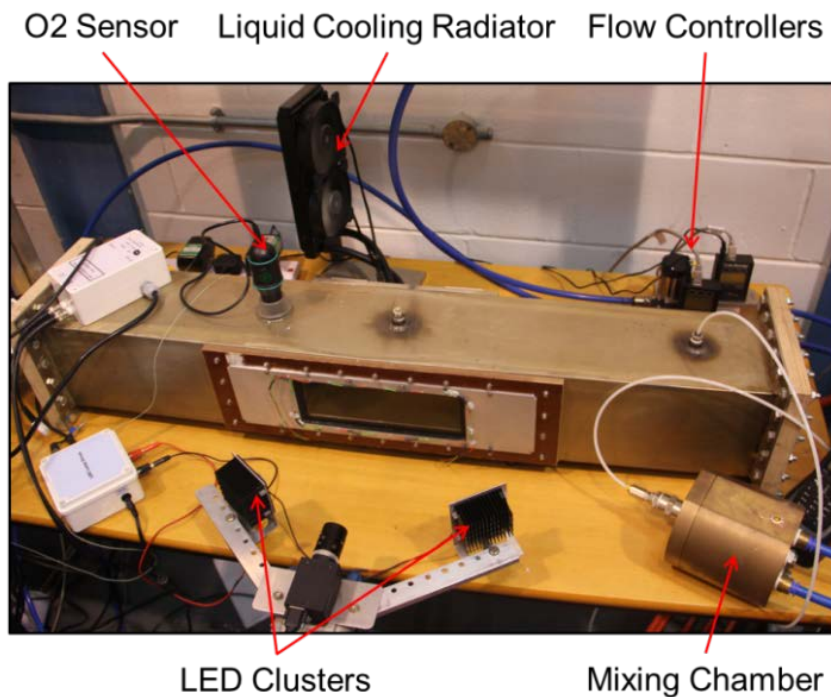
Figure 40 - Calibration Chamber Photo
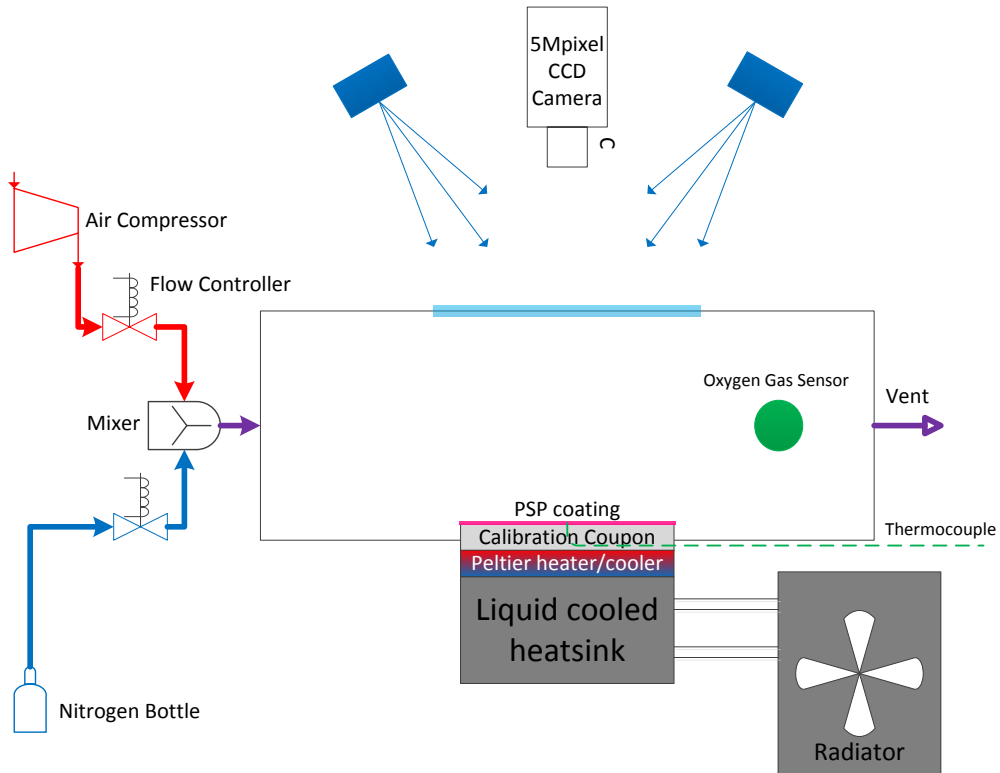
Figure 41 – Calibration Chamber schematic

Calibration is carried out a priori using a dedicated calibration rig consisting of a modified version of the test section with the same dimensions as the main rig; closed at both ends and with a vent to atmosphere. The chamber is flooded with a range of oxygen concentrations ranging from 0% to ambient air by mixing atmospheric air with nitrogen through a mixing chamber. The flow mixture is controlled by a pair of Alicat^{TM} flow controllers and a Vernier^{TM} O_2 gas sensor is used to monitor the concentration within the chamber. The calibration coupon is mounted to a liquid cooled Peltier thermoelectric heater with an embedded thermocouple close to the coupon surface, allowing the temperature of the coupon to be altered. The optical access window and LED lighting source is the same as used in the testing environment as is the CCD camera although a longer 24mm lens is used due to the smaller required field of view. A thick curtain surrounds the calibration rig, isolating it from any outside light sources whilst in operation. 200 images are captured at each condition and a further 200 are captured with the light source turned off to act as a dark field correction.

The temperature of the calibration coupon and concentration within the chamber are cycled in order to build up data points for the calibration; typically data is captured in 2% concentration and 5°C intervals from 0% to atmospheric (~21%) oxygen concentration and 10-35°C plate temperature. Concentration and temperature measurements are recorded at the start and end

of each acquisition phase and an average of the two readings used as part of the calibration condition. The resultant images are averaged and the dark field correction applied by subtraction. The images are then cropped to cut out any pixels that are not imaging the painted surface and a mean intensity value of this region is calculated. The intensity and concentration ratios relative to the reference condition are then calculated for each temperature and concentration condition. This data is then used to determine the constants A, B and C in Equation 56 for each temperature using a second order polynomial fit. The temperature dependence of these constants is then determined as in Equation 57 using a third order polynomial fit. An example of the resulting calibration curves are shown in Figure 42 for a reference condition of ~21% C_{O_2} and 15°C. The calibration coefficients are determined using each of the temperature settings as the reference to allow the experiments to be conducted with varying atmospheric temperatures and an appropriate calibration to be applied.
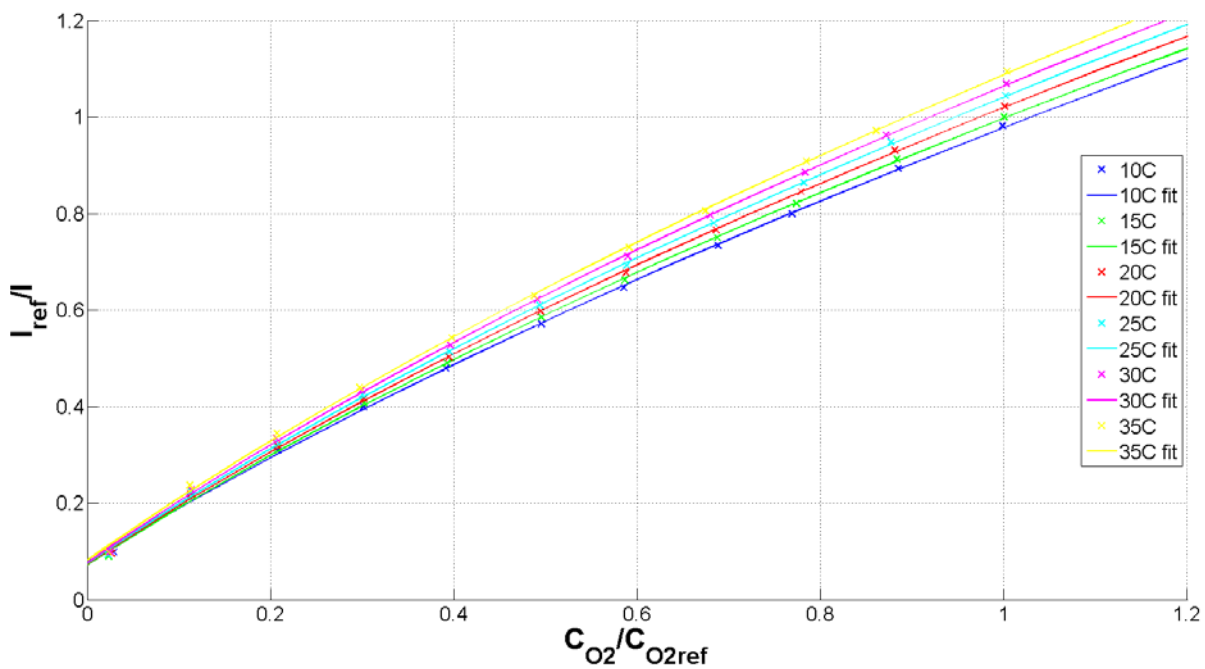
Figure 42 – PSP Calibration Curve

3.3.7   Test Procedure

In order to determine the two partial pressure ratios required to calculate the adiabatic film effectiveness, images must be captured at 4 conditions;

1) Dark Image: I_{dark}. Acquired with no illumination source. Corrects for background noise due to the camera CCD.

2) Reference Image: I_{ref}. Acquired using no flow, also referred to as wind-off, represents the reference intensity field.

3) Air Image: I_{air}. Acquired using air as both the coolant and main stream flows. Serves to both set the flow condition and corrects for static pressure variation over the surface.

4) Tracer N₂ Image: I_{fg}. Coolant is switched to Nitrogen at the same flow conditions. Represents oxygen partial pressure field.

The tests must be carried out in isothermal conditions to negate the thermal sensitivity of the paint. Therefore once the plate has been fitted, the main flow and turbulence fans are run up to speed and coolant air is injected. As air passes through the turbulence fan its temperature increases, as a result the mainstream air temperature is higher than ambient. The coolant air is heated to match the main stream air temperature and the whole system is allowed to thermally soak before testing begins. While this is happening the lights within the test cell are switched off as are the LEDs and the camera captures the required dark images, which provides a background noise correction to remove any error associated with CCD dark current within the camera sensor. Once the system temperature has reached equilibrium, both fans and coolant air are switched off and the LEDs are switched on in order to capture a set of reference or wind off images. Once this image set is captured, the fans are again switched on and allowed to reach the required set points. The coolant is set to air and the flow rate is set to give the desired pressure drop. The system is allowed to settle before images are again captured to give the wind-on (air) condition. The coolant source is switched to nitrogen at the desired flow rate then again allowed to settle before images are captured to give the wind-on (N₂) condition. The coolant is then switched back to air at the next flow set point and the process repeated switching between air and nitrogen until all required flow conditions are completed. All flow is then switched off again and another set of reference images are captured to ensure there have been no significant change in reference conditions throughout the duration of the test.

Data from thermocouples, pressure transducers and flow meters are recorded at the start and end of each image acquisition phase and an average of the two readings used for post processing.

3.3.8 Post Processing

A Matlab script has been created to carry out the post processing required to obtain surface effectiveness from PSP experiments. This script reads in the images and calculates a time

average image for each image type and flow condition. The mean dark image is then subtracted from each of the other mean images to correct for CCD dark current.

$$I = I_{illuminated} - I_{dark}$$

The reference images are then divided by the wind on images to obtain the intensity ratio I_{ref}/I. The calibration can then be applied to determine concentration ratios $C_{O_2 air}/C_{O_2 ref}$ and $C_{O_2 fg}/C_{O_2 ref}$. Concentration ratio is equivalent to partial pressure ratio, enabling the use of Equation 55 to determine surface effectiveness. This is presented as surface maps of adiabatic film effectiveness with the spanwise averaged value calculated over a central strip in the same way as the overall effectiveness results.

3.4 Uncertainty

Uncertainty is calculated according to the method outlined by Kline and McClintock (60) for both overall and adiabatic film effectiveness measurements.

3.4.1 Overall Effectiveness

From Equation 47;

$$\phi = \frac{T_\infty - T_{w(hotside)}}{T_\infty - T_c}$$

$$\delta\phi = \left[\left(\frac{(T_w - T_c)}{(T_\infty - T_c)^2} \delta T_\infty \right)^2 + \left(\frac{(T_\infty - T_w)}{(T_\infty - T_c)^2} \delta T_c \right)^2 + \left(\frac{1}{(T_c - T_\infty)} \delta T_w \right)^2 \right]^{\frac{1}{2}}$$

Wall temperature is determined through the use of an Infrared camera. This camera is calibrated to determine the relationship between temperature and recorded intensity. This is done through the use of a pair of thermocouples embedded close to the surface of a calibration plate. As calibration is carried out in-situ with the test section at the same temperature conditions as seen during the test the sources of background radiation such as transmissivity of the air and reflectivity of the window and test section walls which could influence the results are accounted for. The uncertainty associated with the thermocouples used to carry out this calibration is ±1.5K. As these thermocouples are not measuring the temperature of the surface exposed to the IR camera but instead at a location just below the surface a source of bias uncertainty is introduced. This uncertainty is estimated to be of order 1K from subsequent calibration plate designs containing both surface mounted and embedded thermocouples. The

resulting uncertainty in wall temperature is therefore ±1.8K. The random uncertainty in wall temperature is estimated to be 0.4K, this accounts for the contributions to the measured temperature of both calibration (through use of repeat calibrations) and intensity sensitivities (through a standard deviation of the gathered samples). This results in an overall uncertainty in measured wall temperature of ±1.85K. Thermocouple readings for the mainstream and coolant temperatures have accuracy of ±1.5K. Using freestream and coolant temperatures of 455K and 300K respectively and wall temperatures of 325K and 430K the relative uncertainty is therefore $\delta\phi/\phi = \pm 1.78\%$ at an overall effectiveness of 0.8 and $\pm 7.13\%$ at an overall effectiveness of 0.2.

3.4.2 Adiabatic Film Effectiveness

From Equation 55 and Equation 56 and denoting $C_1 = P_{O_2:fg}/P_{O_2:ref}$ and $C_2 = P_{O_2:air}/P_{O_2:ref}$;

$$\eta = 1 - \frac{C_1}{C_2}, \quad \delta\eta = \left[\left(\frac{\delta C_1}{C_2}\right)^2 + \left(\frac{C_1 \delta C_2}{C_2^2}\right)^2\right]^{\frac{1}{2}}$$

<div align="right">Equation 60</div>

$$C_1 = A\left(\frac{I_{ref}}{I_{fg}}\right)^2 + B\frac{I_{ref}}{I_{fg}} + C$$

$$\delta C_1 = \left[\left(\left(\frac{I_{ref}}{I_{fg}}\right)^2 \delta A\right)^2 + \left(\frac{I_{ref}}{I_{fg}}\delta B\right)^2 + \delta C^2\right.$$

<div align="right">Equation 61</div>

$$\left. + \left(\left(2A\frac{I_{ref}}{I_{fg}} \delta\frac{I_{ref}}{I_{fg}}\right) + B\delta\frac{I_{ref}}{I_{fg}}\right)^2\right]^{\frac{1}{2}}$$

Similar for C_2 replacing I_{fg} with I_{air}. Where;

$$\delta\frac{I_{ref}}{I} = \left[\left(\frac{\delta I_{ref}}{I}\right)^2 + \left(\frac{I_{ref}\delta I}{I^2}\right)^2\right]^{\frac{1}{2}}$$

<div align="right">Equation 62</div>

Calibration coefficient random uncertainties are determined through repeat calibration tests to be $\delta A = 0.0384, \delta B = 0.0476, \delta C = 0.0064$ with a 95% confidence level. There are three potential sources of uncertainty in the calibration of the PSP. First the thermocouple used to measure the temperature of the calibration plate. As the thermocouple is not calibrated separately this is assumed to be the standard uncertainty for a class 1 K-type thermocouple at ±1.5K. Installation also impacts the bias uncertainty of the thermocouple measurement. As the

thermocouple is embedded within the calibration plate it is not measuring the surface temperature, this is a source of bias uncertainty. Second, the Oxygen concentration sensor has a quoted accuracy of ±1% volume O_2, however, the oxygen sensor is calibrated prior to each test by taking a reading in atmospheric air where the concentration of Oxygen is 20.95% and another when the calibration chamber has been filled with Nitrogen and hence the Oxygen concentration is 0%. Finally, the intensity as measured by the CCD camera makes up the third source of bias uncertainty. This error source is eliminated through the subtraction of the 'Dark frame' image whereby frames are captured when no light source is present, any measurements taken from the camera at this point are as a result of the bias of the camera and by subtracting this signal from the other images the bias is corrected.

200 images are captured at each test condition to ensure that the samples are statistically independent. Therefore, the error for the mean intensity recorded can be expressed by;

$$\delta I = \frac{1.96 \times \sigma_I}{\sqrt{200}}$$

<div align="right">**Equation 63**</div>

This relation is applied to each of the image types and, along with the calibration coefficient uncertainties, the uncertainty propagation to the surface effectiveness can be calculated. This results in mean surface effectiveness errors $\delta\eta/\eta$ of ±35% at $\eta = 0.20 \rightarrow 0.25$ and ±3% at $\eta = 0.75 \rightarrow 0.80$.

The main uncertainty source in these readings is the sensitivity of the camera. Due to the inverse relationship between O_2 concentration and emitted intensity from the PSP, the majority of the measurement range of the camera is only utilised to capture the lowest concentration regions (i.e 65% of the range relates to effectiveness regions >0.8). As a result, any noise in the signal results in a larger uncertainty at lower effectiveness regions. This, combined with the low full well capacity of the CCD used (the amount of charge in individual pixel can hole before saturating), results in a relatively low SNR and therefore presents a significant source of uncertainty. Other uncertainty sources attributable to PSP are detailed by Liu and Sullivan (36) including illumination stability, photodegradation and spectral leakage. Due to the process of taking the ratio of images, and their low contribution to overall uncertainty, many of the error sources inherent to PSP testing can be negated.

3.4.3 Flow Properties

Flow properties are calculated using the flow rate of coolant air, as measured by the flow controllers, and the pressures and temperatures of both mainstream and coolant air streams. The Alicat™ flow controllers used set the volumetric flow rate with an accuracy of 0.8% of reading plus 0.2% of full scale. Temperature is measured using K-type thermocouples with an accuracy of ±1.5K. Atmospheric pressure is measured using a resonant sensor barometer with accuracy ±0.15mbar. Differential pressure measurements are made using Sensor Technics™ and Furness™ pressure transducers providing an accuracy of ±0.25% full scale and ±0.5% of reading respectively. The Furness transducers are used to measure the mainstream dynamic and static pressure while the Sensor Technics are used to record static pressure in the plenum and the pressure difference between the mainstream and the coolant in the plenum. All pressure transducers are calibrated in-situ using a PACE™ 6000 series pressure controller with a precision of up to 0.005% reading ±0.005% full scale.

Coolant mass flow rate is calculated from the flow rate measured by the flow controllers and the density of the air stream as determined by the ideal gas law;

$$\dot{m} = \dot{V} \times \rho, \rho = \frac{P}{RT} \qquad \text{Equation 64}$$

Uncertainty of Sensor Technics pressure measurements;

$P_c = 102270 Pa, \delta P_c = 88.8 Pa, \delta P_c / P_c = 0.087\%$ (worst case)

$\Delta P_c = 1850 Pa, \delta P_c = 87.5 Pa, \delta P_c / P_c = 4.73\%$ (worst case)

Uncertainty of mainstream static temperature measurement;

$T_c = 300K, \delta T_c = 1.5K, \delta T_c / T_c = 0.5\%$

$$\delta \rho_c = \left[\left(\frac{\partial \rho_c}{\partial P_c} \right)^2 (\delta P_c)^2 + \left(\frac{\partial \rho_c}{\partial T_c} \right)^2 (\delta T_c)^2 + \left(\frac{\partial \rho_c}{\partial R} \right)^2 (\delta R)^2 \right]^{\frac{1}{2}} \qquad \text{Equation 65}$$

$$\delta \rho_c = \left[\left(\frac{1}{RT_c} \right)^2 (\delta P_c)^2 + \left(\frac{-P_c}{RT_c^2} \right)^2 (\delta T_c)^2 \right]^{\frac{1}{2}} \qquad \text{Equation 66}$$

$$\delta \rho_c = \left[\left(\frac{1}{287 \times 300} \right)^2 (88.8)^2 + \left(\frac{-102270}{287 \times 300^2} \right)^2 (1.5)^2 \right]^{\frac{1}{2}} \qquad \text{Equation 67}$$

Giving $\delta \rho_c = \pm 6.03 \times 10^{-3} kg/m^3$ or $\delta \rho_c / \rho_c = \pm 0.5075\%$ (worst case)

$$\delta\dot{m} = \left[\left(\frac{\partial\dot{m}}{\partial\dot{V}}\right)^2(\delta\dot{V})^2 + \left(\frac{\partial\dot{m}}{\partial\rho_c}\right)^2(\delta\rho_c)^2\right]^{\frac{1}{2}}$$

Equation 68

$$\delta\dot{m} = \left[(\rho_c)^2(\delta\dot{V})^2 + (\dot{V})^2(\delta\rho_c)^2\right]^{\frac{1}{2}}$$

Equation 69

$$\delta\dot{m} = [(1.188)^2(6.67\times10^{-5})^2 + (5.83\times10^{-3})^2(6.03\times10^{-3})^2]^{\frac{1}{2}}$$

Equation 70

Giving $\delta\dot{m} = \pm1.44\times10^{-4}kg/s$ or $\delta\dot{m}/\dot{m} = 0.63\%$ at the highest flow rates of 1090slpm and $\delta\dot{m} = \pm8.66\times10^{-5}kg/s$ or $\delta\dot{m}/\dot{m} = 1.25\%$ at the lower flow rates of 350slpm.

Similarly for the coolant jet velocity;

$$V_j = \sqrt{\frac{2\Delta P_c}{\rho_c}}$$

Equation 71

$$\delta V_j = \left[\left(\frac{\partial V_j}{\partial\Delta P_c}\right)^2(\delta\Delta P_c)^2 + \left(\frac{\partial V_j}{\partial\rho_c}\right)^2(\delta\rho_c)^2\right]^{\frac{1}{2}}$$

Equation 72

$$\delta V_j = \left[\left(0.5\sqrt{\frac{2}{\Delta P_c\rho_c}}\right)^2(\delta\Delta P_c)^2 + \left(-\frac{0.5}{\rho_c}\sqrt{\frac{2\Delta P_c}{\rho_c}}\right)^2(\delta\rho_c)^2\right]^{\frac{1}{2}}$$

Equation 73

$$\delta V_j = \left[\left(0.5\sqrt{\frac{2}{1850\times1.188}}\right)^2(87.5)^2\right.$$

$$\left. + \left(-\frac{0.5}{1.188}\sqrt{\frac{2\times1850}{1.188}}\right)^2(6.03\times10^{-3})^2\right]^{\frac{1}{2}}$$

Equation 74

Giving $\delta V_j = 1.57m/s$ or $\delta V_j/V_j = 2.82\%$ at the lowest pressure differential and $\delta V_j = 0.80m/s$ or $\delta V_j/V_j = 0.67\%$ at the highest pressure differential.

Uncertainty in mainstream parameters during hot tests is given below.

Uncertainty of Furness pressure measurement;

$P_m = 100740Pa, \delta P_m = 18Pa, \delta P_m/P_m = 0.02\%$

$\Delta P_m = 570Pa, \delta\Delta P_m = 3Pa, \delta P_m/P_m = 0.5\%$

Uncertainty of mainstream static temperature measurement;

$T_m = 455K, \delta T_m = 1.5K, \delta T_m / T_m = 0.33\%$

$$\delta \rho_m = \left[\left(\frac{\partial \rho_m}{\partial P_m} \right)^2 (\delta P_m)^2 + \left(\frac{\partial \rho_m}{\partial T_m} \right)^2 (\delta T_m)^2 + \left(\frac{\partial \rho_m}{\partial R} \right)^2 (\delta R)^2 \right]^{\frac{1}{2}}$$

<div style="text-align:right">**Equation 75**</div>

$$\delta \rho_m = \left[\left(\frac{1}{RT_m} \right)^2 (\delta P_m)^2 + \left(\frac{-P_m}{RT_m^2} \right)^2 (\delta T_m)^2 \right]^{\frac{1}{2}}$$

<div style="text-align:right">**Equation 76**</div>

$$\delta \rho_m = \left[\left(\frac{1}{287 \times 455} \right)^2 (18)^2 + \left(\frac{-100740}{287 \times 455^2} \right)^2 (1.5)^2 \right]^{\frac{1}{2}}$$

<div style="text-align:right">**Equation 77**</div>

Giving $\delta \rho_m = \pm 2.55 \times 10^{-3} kg/m^3$ or $\delta \rho_m / \rho_m = \pm 0.33\%$

$$\delta V_m = \left[\left(\frac{\partial V_m}{\partial \Delta P_m} \right)^2 (\delta \Delta P_m)^2 + \left(\frac{\partial V_m}{\partial \rho_m} \right)^2 (\delta \rho_m)^2 \right]^{\frac{1}{2}}$$

<div style="text-align:right">**Equation 78**</div>

$$\delta V_m = \left[\left(0.5 \sqrt{\frac{2}{\Delta P_m \rho_m}} \right)^2 (\delta \Delta P_m)^2 + \left(-\frac{0.5}{\rho_m} \sqrt{\frac{2\Delta P_m}{\rho_m}} \right)^2 (\delta \rho_m)^2 \right]^{\frac{1}{2}}$$

<div style="text-align:right">**Equation 79**</div>

$$\delta V_m = \left[\left(0.5 \sqrt{\frac{2}{570 \times 0.771}} \right)^2 (3)^2 \right.$$

<div style="text-align:right">**Equation 80**</div>

$$\left. + \left(-\frac{0.5}{0.771} \sqrt{\frac{2 \times 570}{0.771}} \right)^2 (2.55 \times 10^{-3})^2 \right]^{\frac{1}{2}}$$

Giving $\delta V_m = 0.10/s$ or $\delta V_m / V_m = 0.26\%$

3.5 Test Plate Geometry

All test plates are manufactured from Inconel 718 using DLD techniques with base dimensions shown in Figure 43. They are designed to have the same porosity through scaling the hole diameter, with effective porosity given by;

$$Effective\ Porosity = \frac{C_d \times A_{hole} \times No_{holes}}{Effusion\ Surface\ Area}$$

<div style="text-align:right">**Equation 81**</div>

Discharge coefficient is estimated from previous experience and preliminary CFD data. Manufacturing tolerances result in hole diameters that differ slightly from the CAD model used to define the geometry. However, as the internal geometries are complex, it is difficult to measure the actual cross sectional area with confidence and therefore the nominal design diameter is used to estimate both effective area and C_d values. This issue is particularly apparent in the Spey fan test plate (as described in Section 3.5.2) which was designed to have a metering diameter of 2.40mm but due to the immaturity of the manufacturing technique a flat spot is visible in the metering section, resulting in an actual minimum cross-section of around 2.05mm.

The rectilinear helix test plate was designed and manufactured based on earlier CFD data which indicated a lower Cd than the circular helix geometry, however under experimental conditions and in subsequent simulations the Cd is found to be higher at the test conditions considered in this study resulting in a higher flow rate of coolant at the pressure drops considered.

All test plates share the same basic dimensions ensuring the measurement area is the same for each test and all plates are the same thickness. An overview of the test plate geometry can be found in Table 2, this lists the discharge coefficients measured during testing. Although care was taken to minimise the leakage of coolant around the periphery of each test plate using a high-temperature sealant, it was often difficult to provide a perfect seal. This is particularly apparent for the rectilinear helix case which did not fit perfectly into the supporting frame. As a result, evidence of a small leakage of coolant passed the plate seal is apparent from the adiabatic film cooling effectiveness data gathered for this geometry. The designs tested are all 'single wall' cooling solutions and, as a result, bear the full system pressure drop across the effusion array.
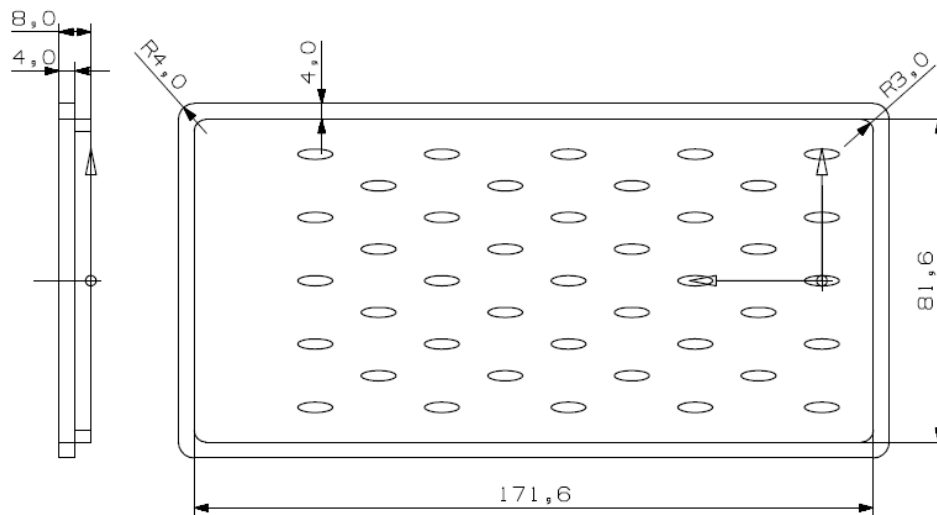
Figure 43 –Cycle-scaled test plate geometry
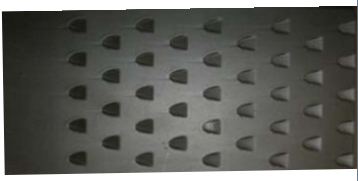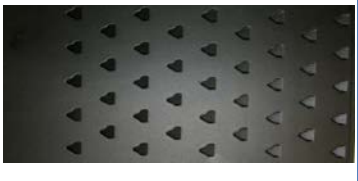
		Cd	d	α	p/d	s/d	No.
Cylindrical hole		0.67	$\phi 2.58mm$	17° (main)	6.2	6.2	41
Spey fan		0.79	$\phi 2.4(2.05)mm$	17° (main)	6.7	6.7	41
Modified fan		0.89	$\phi 2.11mm$	21° (main)	7	7	41
Slotted		0.79	$\phi_{eqiv} 2.26mm$	17° (main)	3.7	12.4	43
Circular Helix		0.43	$\phi 2.90mm$	20° (exit)	5.51	5.51	41
Rectilinear Helix		0.46	$\phi_{eqiv} 3.02mm$	20 °(exit)	5.3	5.3	41

Table 2 – Cycle-scaled test plates

3.5.1 Cylindrical

The Cylindrical hole geometry is the datum case against which the remaining test cases summarised in Table 2 are evaluated and is shown in Figure 44. Variations of this type of geometry are currently the most widely used method for combustor wall effusion cooling due to their simplicity of manufacture. The specific geometry considered in this test involves a simple straight-through cylindrical hole aligned with the main flow velocity vector at an inclination angle of 17° to the wall surface. In the engine combustor liner or tile, a single percussion or laser drilling operation is used to create a cylindrical hole through the wall and 17° is considered to be the minimum inclination angle currently possible using a laser drilling technique. However, since all test plates are made using a DLD process, the hole feature is created as the plate is built, as a result the definition and surface roughness within the hole are subject to the accuracy of the DLD process. The holes are staggered over the surface and the pitch and spacing of the holes is chosen based on representative engine geometry.
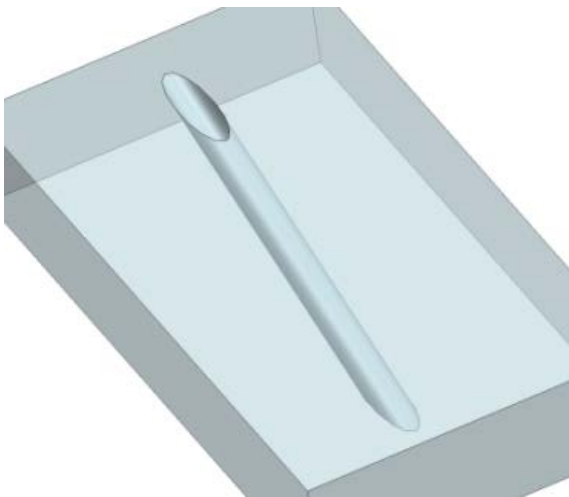
Figure 44 – Cylindrical passage geometry
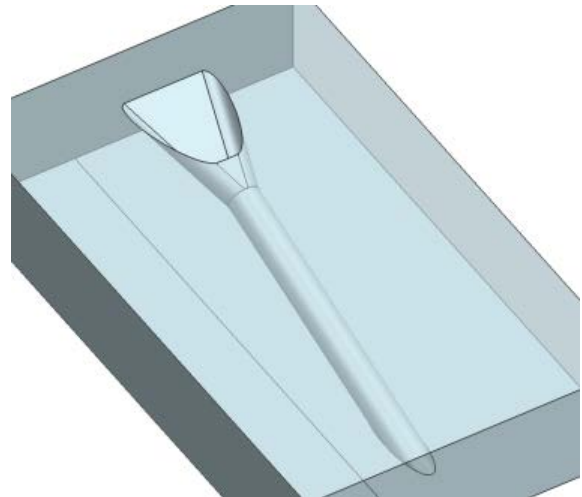
Figure 45 – Spey Fan passage geometry

3.5.2 Spey Fan

In terms of cooling performance, the Spey fanned geometry is currently considered to be close to the optimum achievable for single-skin arrangements manufactured using conventional manufacturing processes. This design originated from a demonstration of an advanced liner cooling geometry which employed the Rolls-Royce Spey engines as its host. The major difference from the cylindrical geometry is the fanned exit to the passage as shown in Figure 45; this decelerates the flow as it exits the hole, reducing the tendency of the cooling air to 'lift off' from the combustor skin at high blowing ratios whilst spreading the coolant in the spanwise direction. The resultant film covers a much larger area and develops much faster than the

cylindrical design. Due to the fanned exit, this geometry cannot be created by a single laser drilling operation. This results in a high manufacturing cost in terms of both time and complexity compared to the datum, and is often prohibitively expensive to apply over the entire surface of the liner wall. Conventional diffuser designs rules would suggest the included fan angle of this particular design to be greater than that required to maintain flow attachment. As a result, the fan is over-expanded and leads to the tendency of the flow to attach itself to one side of the fan and create a separation on the opposing side. By reducing the fan angle from 16° to 12°, it is possible to keep the flow attached throughout and further increase the film performance.

3.5.3 Modified Fan

The Modified design aims to recreate the performance of the Spey fanned design without the significant increase to manufacturing cost associated with forming the exit fan. This is done by approximating the fan shape using three laser drilling operations slightly off axis to create the diffusing section. All three operations share the same entry point but are inclined slightly with respect to the main central hole resulting in the shape shown in Figure 46. The fan of this design results in a more gradual area increase when compared to the Spey design resulting in the flow remaining attached throughout the length. This geometry was developed by Damian Martin (57).
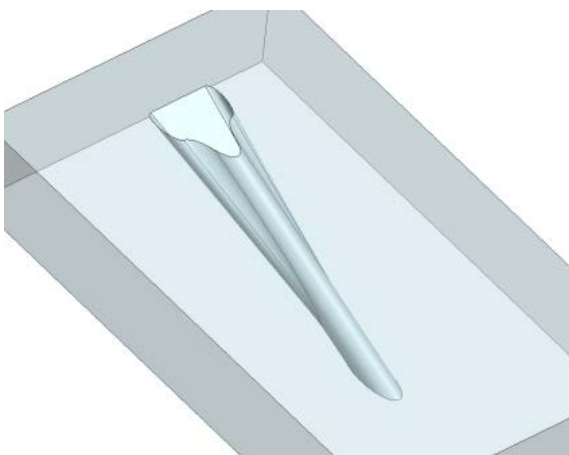
Figure 46 – Modified Fan passage geometry
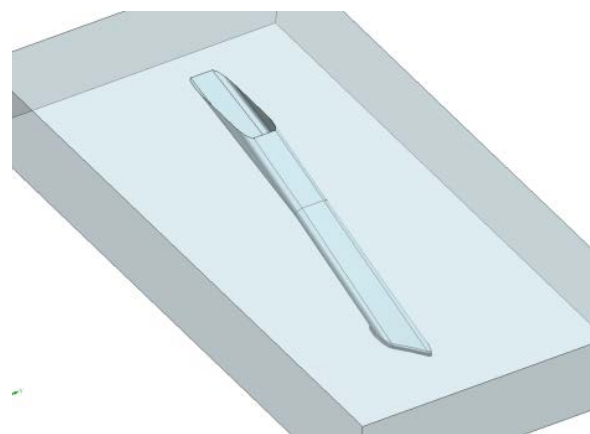
Figure 47 – Slotted passage geometry

3.5.4 Slotted

The Slotted design is the first geometry designed with DLD based manufacturing methods in mind. A thin, wide slot is used instead of a traditional cylindrical hole as illustrated in Figure 47. The exit of the slot is fanned in the normal direction, whereas the other fanned geometries are fanned in the spanwise direction. The inlet is shaped in order to ease the DLD manufacturing

process and although porosity matched, the effusion spacing pattern departs from the conventional alternatives described so far. Roughly twice as many holes are placed in the span-wise direction with almost half the number in the stream-wise direction. This geometry was developed by the combustion group at Rolls-Royce Bristol.

3.5.5 Circular helix

The Circular helix design aims to improve the overall cooling performance by increasing the removal of heat within the effusion passage whilst maintaining a strong film generated by fanning the exit as shown in Figure 48. Internal heat removal is enhanced by both increasing the internal surface area through coiling the passage and increasing the wall shear stress and hence heat transfer coefficient at the wall (61). The internal surface area is further increased as the discharge coefficient of this design is much lower than previously tested geometries, requiring a larger diameter passage to pass the same amount of air for a given pressure drop. Due to the small size and helical nature of the design, it would be impossible to create this geometry using conventional manufacturing techniques. As a result, this is a truly DLD enabled design. The helix arrangement employed in this study is defined using a minimum ligament distance between coils of 0.75mm at engine scale. Due to the extended axial length of this design, care has been taken when defining the inter-passage spacing in order to attain the required porosity whilst still ensuring a minimum ligament distance between passages of 0.75mm at engine scale. As a result, three coils are used, increasing the overall passage length but limiting the increase in axial length. The other tuneable parameter is the helix diameter, this is set to $D_{helix} = 1.1 \times D_{hole}$. The helix diameter must be large enough to prevent the flow from simply passing unhindered through the centre of the passage, whilst remaining small enough to keep the thickness of the plate minimal to reduce the thermal mass whilst again adhering to the minimum ligament distance. The exit is aerodynamically fanned to promote the spanwise spreading of coolant over the surface. This design utilises a larger proportion of the pressure drop available to drive the coolant through the internal passages, resulting in a lower momentum flow exiting the passage. This encourages the coolant to remain attached and close to the surface rather than being ejected into the freestream. This combination of helical and fanned geometry was developed as part of this project.
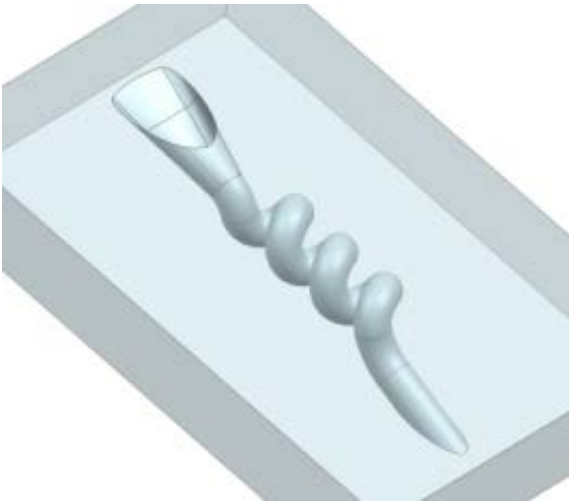
Figure 48 – Circular Helix passage geometry
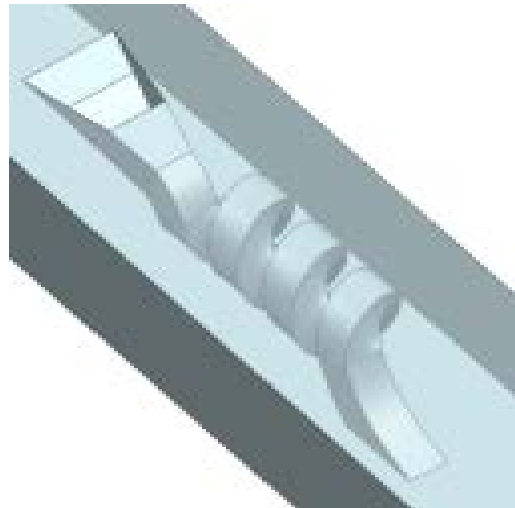
Figure 49 – Rectilinear Helix passage geometry

3.5.6 Rectilinear helix

The Rectilinear helical design builds upon the circular helix by further increasing the internal surface area through use of a square cross section as shown in Figure 49. This has the added benefit of increasing the passage blockage through the generation of secondary flows by the confluent boundary layers, resulting in low discharge coefficient and therefore larger cross-sectional area required to give the same effective area. It also aims to use the secondary flow generated in the corners to further drive up the heat transfer coefficient and the relative contribution of internal heat removal (62). Due to the angular nature of the internal geometry, this design challenges what is currently possible even with DLD manufacture. All governing dimensions are defined in the same way as for the circular helix design, using an effective diameter derived from the cross sectional area and the exit is fanned to promote spreading of the coolant film over the hot-side surface. As with the circular helical design, the effusion exit flow has a lower momentum relative to the conventional designs, resulting in the coolant remaining attached to the surface at much higher overall blowing ratios. The development of the circular helical geometry into this rectilinear variant was carried out as part of this project.

3.6 Test Matrix

Chapter 5 contains the results obtained for both the adiabatic and overall effectiveness experiments conducted under this study. These experiments identify how the six test plates compare at various freestream turbulence levels and engine equivalent liner pressure drop conditions with experimental conditions scaled from representative engine cycle conditions provided in Table 3. Due to the temperature difference required for the overall effectiveness study and the requirement for isothermal running conditions for the adiabatic tests, the

experimental conditions between the two regimes must differ and it is not possible to match both density and velocity ratios. Therefore, for both sets of conditions the momentum flux ratios are matched, allowing a degree of similarity for comparison.

DR	~ 2.16	T_c	$\sim 900K$
P_0	$\sim 3 \times 10^6 \, Pa$	T_{main}	$\sim 1900K$
U_{main}	$\sim 42m/s$	$\varnothing_{hole}$	$\sim 0.6mm$

Table 3 – Representative engine conditions

Two different turbulence conditions are tested in order to determine the effects of freestream turbulence on both adiabatic and overall effectiveness as well as to validate the CFD code at different turbulence levels. The higher condition relates to turbulence intensity of around 20% and length scales of 13D as illustrated in Figure 33, and the low turbulence condition relates to around 5% turbulence intensity and 6.3D length scale as shown by Figure 31. These turbulence conditions are also used as the boundary conditions for the computational simulations carried out.

Experimental results are collected at a number of liner pressure drop conditions, ranging from an engine equivalent $\Delta P/P = 0.5\%$ to 2.5% in 0.5% steps, this equates to momentum ratios ranging from 3.11 to 15.86. This provides a sample of potential engine liner pressure drops expected from a single skin combustor operating at a representative engine cycle. The corresponding momentum flux ratios are determined and used to set the pressure drop for the two scaled experiments. Table 4 contains details of the experimental test conditions for the two testing regimes as well as the equivalent engine condition. The difference in coolant pressure drops occur as a result of the use of Nitrogen as the coolant gas for the adiabatic film effectiveness measurements. When switching from Air to Nitrogen the associated molecular mass and hence density changes when Reynolds matching the through hole flows requiring the altered pressure drop. The difference in experimental freestream velocity occurs as a result of momentum flux matching between conditions at different density ratios.

	Momentum Ratio	Engine	Overall Effectiveness (IR)	Adiabatic Film Effectiveness (PSP)
Freestream Temperature, T_∞		1900K	455K	300K
Coolant Temperature, T_c		900K	300K	300K
Density Ratio		2.16	1.65	1.05
Coolant Pressure, P_{0_c}		30bar	1.03:1.1bar	1.03:1.1bar
Liner Pressure drop as a percentage of coolant Pressure, $\frac{\Delta P}{P}$	3.11	0.5%	1.8%	1.9%
	6.25	1.0%	3.5%	3.6%
	9.42	1.5%	5.0%	5.2%
	12.62	2.0%	6.5%	6.7%
	15.86	2.5%	7.9%	8.2%
Freestream Velocity, U_∞		42m/s	37.5m/s	32m/s

Table 4 – Engine equivalent and test conditions for both overall and adiabatic film effectiveness measurements

Liner pressure drop is controlled by altering the mass flow rate of coolant entering the plenum and monitoring the measured test plate pressure difference. Due to the setting accuracy of the flow meters it was not possible to set the desired pressure drop exactly so experimental pressure drop is allowed to vary by ±10% and the actual pressure drop recorded. The test plates are designed to have the same porosity and therefore should all exhibit similar pressure drop characteristics for a given coolant mass flow rate. However, due to immaturity in the DLD manufacturing technique available to produce the plates, this is not true in all cases. The Spey Fan plate has a slight distortion at its entry caused as a result of the build direction. This anomaly reduces the cross-sectional area of the holes, reducing the mass flow at a given pressure drop. Other plates show slight variation in the mass flow required to achieve a given pressure drop, though this is minor and likely caused in part by inaccuracies of discharge coefficient estimated from CFD modelling of each design prior to manufacture.

4   Computational Techniques

This section describes a RANS based approach used to develop a method of quickly ranking a number of combustor liner cooling geometries.   The technique is used to assess the performance of various cooling geometries in terms of adiabatic film effectiveness for a full cooling array using a split computational approach whereby the flow field for a single cooling hole is solved and used as the inlet boundary conditions at passage exit for a multiple hole array.   Internal heat transfer performance of a single passage is also assessed for each of the six geometries.   These tools are developed to aid the down-select and optimisation stages of combustor liner cooling designs and as such, they have been developed with an emphasis on relative performance rather than producing absolute numbers.   In this way, combustion system designers are able to quickly appraise and rank candidate cooling architectures to which more rigorous computational techniques can be applied.   This section first covers the features of the numerical solver as used to solve the Reynolds Averaged Navier-Stokes equations; this is followed by a review of the different numerical experiments including information on the domain geometry, mesh generation process, application of boundary conditions and post processing procedure.

4.1   Simulation Modelling Approach

Computational Fluid Dynamics (CFD) is a tool used to simulate the flow of fluids over a range of geometrical and flow conditions.   This is accomplished by splitting a given flow domain up into small control volumes or cells and solving the Navier-Stokes equations using an iterative approach and a set of boundary conditions.   A large number of approaches to solving these equations exist, each with a computational cost associated with the nature and level of complexity of the flow and the methodology used to either model or solve the turbulent structures.

4.1.1   Solver Features

The numerical solver used for this project is Star-CCM+® developed by CD-adapco. Star CCM+ is more than just a CFD solver, it is an entire engineering process for solving problems including flow (of fluids or solids), heat transfer and stress. Star CCM+ is a more complete package than a typical CFD solver as it contains the functionality to define, mesh, solve and visualise solutions in a single package. It is a very powerful tool with physics modelling capabilities including;

- Solvers
    - Segregated or coupled
- Time
    - Steady, implicit and explicit unsteady
- Turbulence
    - RANS, LES and DES
- Compressibility
    - Ideal or real gas
- Heat Transfer
    - Conjugate heat transfer and radiation

Star-CCM+ also contains an automated meshing tool. This tool can 'shrink-wrap' a high quality triangulated surface mesh onto the geometrical model, closing holes in the geometry and joining disconnected or overlapping surfaces to create a single, manifold surface which can be used to generate the computational mesh without user intervention. From this either a polyhedral or hexahedral mesh can be automatically created with user defined control volumes allowing increased mesh control. A high quality prism-layer mesh is automatically extruded from solid walls within the domain with conformal meshes created on interfaces between multiple physical domains.

In order to create a mesh, the domain geometry has to be defined. This is done using Siemens NX CAD software. Once the flow passage has been defined, the flow domain is tailored parametrically based on the diameter of the passage profile and a constant plate thickness which is taken from the test plate geometry. This solid model is exported from NX as a parasolid file, which is then imported into Star-CCM+ as a part and each face is assigned to a particular boundary.

A powerful analysis suite is also available within Star-CCM+, with scalars, vectors, streamlines and other data all updated live as the solution iterates. Data can also be exported for further analysis using other tools.

4.1.2   Turbulence Model

A RANS based turbulence approach is used for this study. Details of the Reynolds Averaging process as applied to the Navier-Stokes equations are covered in section 2.4.2.3. As the goal of

this study is to develop a tool allowing the quick assessment and down-selection of a large number of candidate designs in terms of their relative performance, the choice of this relatively simple approach to turbulence modelling is an attractive one. In this case the k-ε model is chosen in the two-layer realizable formulation. Details of the realizable k-ε turbulent model can be found in a paper by Shih et al (63). Described in detail by the authors, the two layer approach allows the k-ε model to be applied in the viscous sublayer and divides the computation into two layers. In the layer next to the wall, the turbulent dissipation rate ε and the turbulent viscosity μ_t are specified as functions of wall distance while k is solved in the entire flow. This two layer formulation blends this one-equation model with the two-equation k-ε model smoothly. This explicit specification of ε and μ_t is arguably no less empirical than the traditional damping function approach and the results are often as good or better.

4.1.3   Flow, Energy and Species Models

The solver used in this study is the coupled model; this solves the conservation equations for mass, momentum and energy simultaneously using a pseudo-time marching approach, driving the unsteady form of the governing equations to a steady state. A pseudo-transient term replaces the physical time derivative and the solution advances in pseudo-time to drive this term to zero. The discretized equations are solved implicitly; this results in a wider stability margin permitting Courant numbers greater than unity. As a result the pseudo-time steps can be larger providing relatively fast convergence rates over an explicit spatial integration scheme but requiring more storage space. A 2nd order accurate upwind discretisation scheme is also employed here.

$$Courant\ number = \Delta t \sum_{i=1}^{n} \frac{u_{x_i}}{\Delta x_i} \qquad \text{Equation 82}$$

The coupled species model introduces an extra transport equation which, along with global mass continuity, provides a means of updating the mass fraction field and defining the mixture composition of nitrogen and air where applicable. This is required to ensure the method used to calculate adiabatic effectiveness is consistent with the experiment in which the heat-mass transfer analogy is employed, drawing a parallel between gas concentration and temperature distribution and allowing the PSP technique to be employed.

The coupled flow model is chosen for this study since the solutions are generally more robust and accurate than the segregated model and whilst more memory is required for this model, the computational resources available are sufficient to run a coupled case (42).

4.1.4 Initial Conditions

The simulation is initialised using the 'expert initialisation' functionality built into StarCCM+. This procedure steps through a number of grid densities (typically 10) from very coarse to the full resolution defined by the meshing procedure and solves an inviscid calculation for each using the solution of the previous grid resolution as a starting point. This provides a good first approximation of the flow field, reducing the number of iterations required to reach a converged solution compared to initialising from uniform initial conditions.

The turbulence model is then applied with main stream flow turbulence intensity and length scale set to match the experimental conditions and the solution is run until convergence is reached.

4.2 Numerical Solver Implementation

This section describes the numerical experiments performed in order to estimate cooling film distribution and internal heat pickup. A description of the procedure used to estimate the discharge coefficient of a new design, a required property to ensure test plates are porosity matched, is also included.

4.2.1 Initial Design & Discharge Coefficient

The coolant passage must be designed such that the pressure drop across and mass flow through the combustor liner are matched between designs, when this is true the design is said to be porosity matched. In order to achieve this condition the hole discharge coefficient (C_d) must be determined to allow the effective area of each design to be calculated, the passage diameter is then scaled based on the calculated C_d such that the resulting effective area is matched with the existing datum geometry.

4.2.1.1 Simulation Topology

The initial study is carried out for a single passage system based on the experimental test conditions given in section 3.6. Key dimensions of the flow domain are given in Figure 50. This has to be of sufficient size that the extents have no influence on the flow through the passage. Therefore the height of the hot side flow domain is 18 times the hole profile diameter (D) to

ensure it is well within the free-stream and away from the jet, with periodic planes used to make up the side walls which are placed at half the pitch (P) away from the hole, mimicking an infinite row of holes. The inlet for the hot side flow is placed 15D upstream of the hole inlet and the outlet is 35D downstream of the exit plane of the passage, this allows the boundary layer to develop upstream of the exit while preventing the presence of the outlet and wall boundaries influencing the flow around the entry and exit of the flow passage. The coolant plenum has a depth of 8D with the domain extending the full length of the mainstream as the same domain is used for both adiabatic and conjugate models. The size of the coolant plenum region is dictated by the conjugate requirement and therefore must stretch the entire length of the hot side domain.
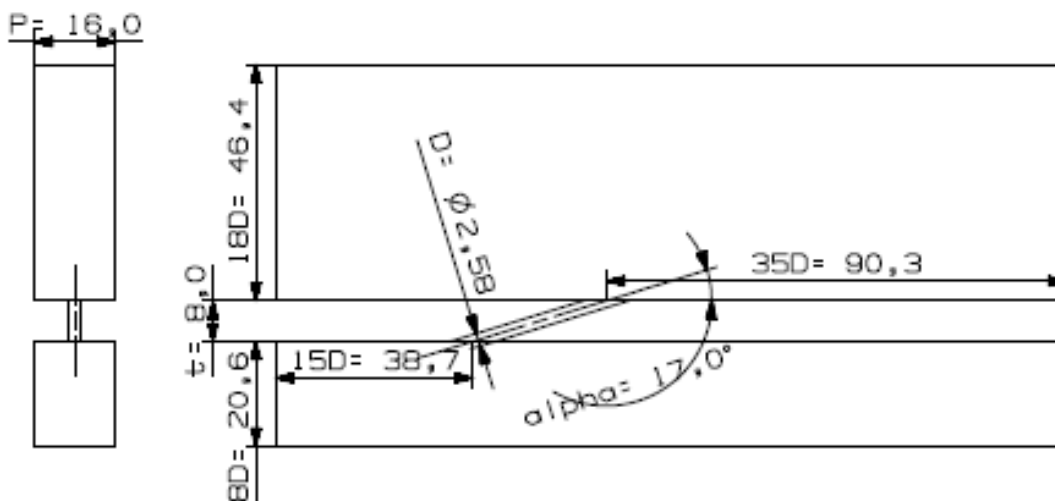
Figure 50 – Drawing of example single passage flow domain, dimensions in mm
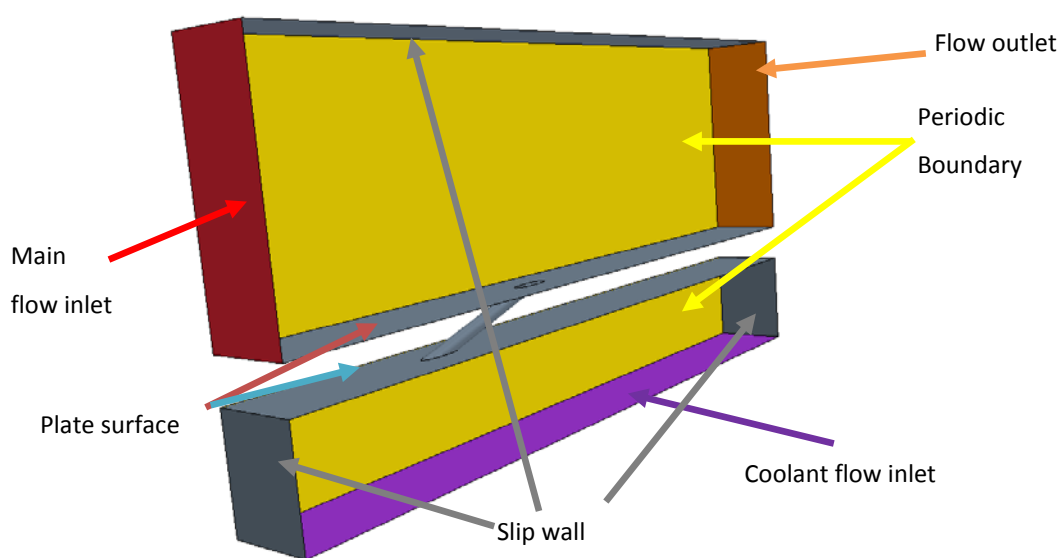
Figure 51 – Boundary conditions

The boundary types are set for each face as shown in Figure 51, with;

- Non-slip, adiabatic walls used for the hole, hot and cold plate surfaces (grey). These walls use a non-slip condition which models the shear stresses in the near wall region forming a boundary layer by setting the tangential velocity to zero. Boundary face pressure and temperature are extrapolated from the adjacent cell using reconstruction gradients.

- Slip wall applied to the top face of the domain and the front and back walls of the coolant chamber (grey), the slip wall does not model the shear stress on the wall, allowing the flow to pass freely with the velocity computed by extrapolating the parallel component of velocity in the adjacent cell using reconstruction gradients. This is used as the experimental domain is actually much larger than the computational domain, which has been reduced in order to decrease the number of cells and hence computational overhead. The flow outside of the area captured by the computational domain is assumed to have no effect on the flow inside.

- Periodic planes for the side walls (yellow). This allows the code to do one set of calculations for a regular, effectively repeating row of holes. The boundaries are separated in space but conditions are mapped from one to the other through a constant translation.

- Velocity inlet for the main flow inlet plane (red). This is used to simulate the 'hot' flow delivered to the test section in the experiment. Inlet velocity, temperature and turbulence properties are specified while pressure is extrapolated from the adjacent cell using reconstruction gradients.

- Pressure outlet for the outlet plane (orange). Flow exits the domain through this boundary, with pressure drop over the test plate measured relative to the pressure on this boundary. In the computational simulation, the pressure is specified as zero with respect to the reference pressure to reduce numerical round off error. The reference pressure is set to ambient.

- Stagnation inlet for the coolant flow inlet plane (purple). Total pressure on this face is specified and kept constant, simulating a far upstream plenum in which the flow is completely at rest. Total temperature and turbulence conditions are also specified as in

Table 5. As the flow is incompressible, Bernoulli's equation is used to relate total pressure, static pressure and velocity magnitude on this boundary.

4.2.1.2 Meshing

The next step is to apply a surface mesh; this creates a mesh on the surfaces of the solid model and forms the basis of the volume mesh over the whole domain by triangulating the initial CAD surface. This surface mesh needs to be fine in the region around the hole in order to resolve the high gradients in flow properties such as velocity likely to occur in this area, while being coarse in other regions in order to reduce the computational time necessary to resolve areas where the flow is unaffected by the introduction of the coolant air through the hole.

The automatic meshing tools built into Star CCM+ cluster cells around geometrically complex surfaces, such as the flow passage, where geometry is curved and so flow gradients are likely to be high. The cells are then allowed to grow in size as distance from these features increases based on selected rules. This allows a good surface mesh to be created without the need for the user to manually define it. This grid can then be tailored afterwards to add cells in particular areas as required.

The mesh shown in Figure 52 uses a base size equal to the diameter of the passage, forming the basis on which other grid controls are scaled. A mesh sensitivity study was conducted on the cylindrical hole domain indicating little benefit to refining grid density below the 4% minimum. Therefore a relative minimum size of 4% of base is used to set the smallest cell size in the main domain, and a target size of 225% of base is used to set the target size in areas far away from the passage. These parameters control the cell sizes within the surface and volume meshes, clustering the cells where necessary and allowing them to grow elsewhere. The surface growth rate is set at 1.1 to control the increase in cell size. The surface mesher splits surfaces up into smaller triangles, while this is accurate on flat surfaces, curved surfaces require infinitely small triangles to accurately capture the true curvature. The mesher splits a curved surface into a number of points based on the parts per circle basic curvature parameter. The higher this parameter, the more triangles will be placed on the surface and, along with the minimum cell size, this controls the cells on the curved surface. The basic curvature is set to 108pts/circle ensuring the outer circumference of the passage is defined with enough resolution.
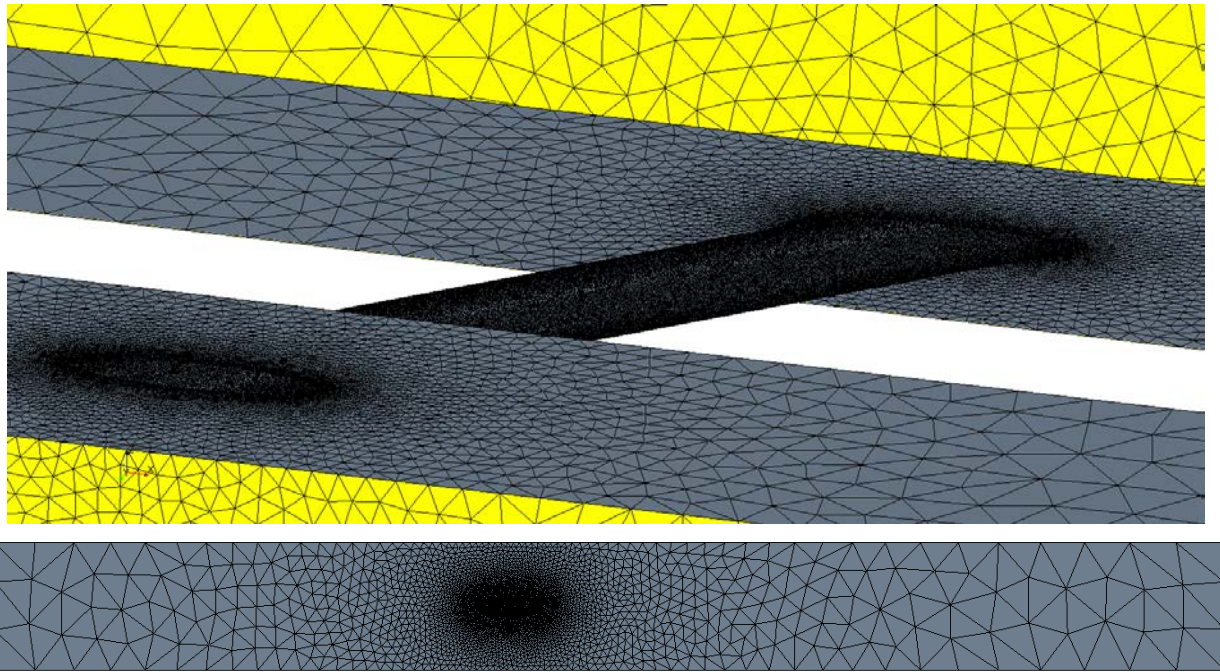
Figure 52 – Surface mesh of a) passage exit region; b) Hot plate surface. Darker areas indicate higher cell clustering

As can be seen in Figure 52, the surface mesh generated has a greater mesh density in the region surrounding and through the passage as desired and the cells grow larger as distance from the hole increases.

The next stage is to generate the volume mesh from this surface mesh. In near wall areas it is beneficial to use a prism layer mesh in order to resolve the high gradients present within a boundary layer. Hence, prism layer meshes have been generated on the non-slip wall boundaries i.e. on the plate surfaces and on the cooling hole inner wall. The boundary layer should be completely contained within the prism layer with enough cell layers to resolve the velocity gradient in the near wall region, and the smallest cell will have a height such that $y^+<1$ in order to satisfy the low y+ wall treatment as described in section 2.4.2.3. This is accomplished using a total prism layer thickness of 7.5% of base, near wall prism layer thickness of 1.7μm, and 18 prism layers with the cells expanding according to a hyperbolic tangent relationship. The y+ values are then checked using the calculation built into Star CCM+ once the first prediction is completed. A polyhedral mesh is used as polyhedral cells have an advantage over tetrahedral in allowing accurate solutions to be obtained with fewer cells, requiring less computing time (64).

The meshing procedure is automatic, using the surface mesh as a basis. 4 optimisation cycles are carried out in order to improve the quality of the volume mesh to a tetrahedral mean ratio

of 0.8, consistent with the recommendation within the Star user manual for a high quality mesh. (42)

$$Tetrahedral\ Mean\ Ratio = \frac{12 \times (3v)^{\frac{2}{3}}}{\sum_i l_i^2}$$

<div align="right">**Equation 83**</div>

Where v is the cell volume and l is the edge length.

Figure 53 shows a cross section through the centre of the domain in order to show the distribution of the volume mesh sizes through the hole. It can be seen that the cell density through the passage is much higher than the regions away from the entrance and exit. The growth of prism layer cells covering the wall can also be seen.

The cell count of the mesh for the plain hole geometry is around 810,000, which is higher than most of the studies considered in section2.4.4, but low enough to be run on the available machines as detailed in section 4.3.

A brief mesh independence study is carried out on the plain hole geometry with minimum cell sizes of 8%, 4% and 2% of base resulting in meshes containing roughly 290,000, 810,000 and 2,080,000 cells respectively. The medium mesh is found to be sufficient for these simulations, with variation in measured C_d between medium and fine of 0.35% and between coarse and fine of 1.6%.
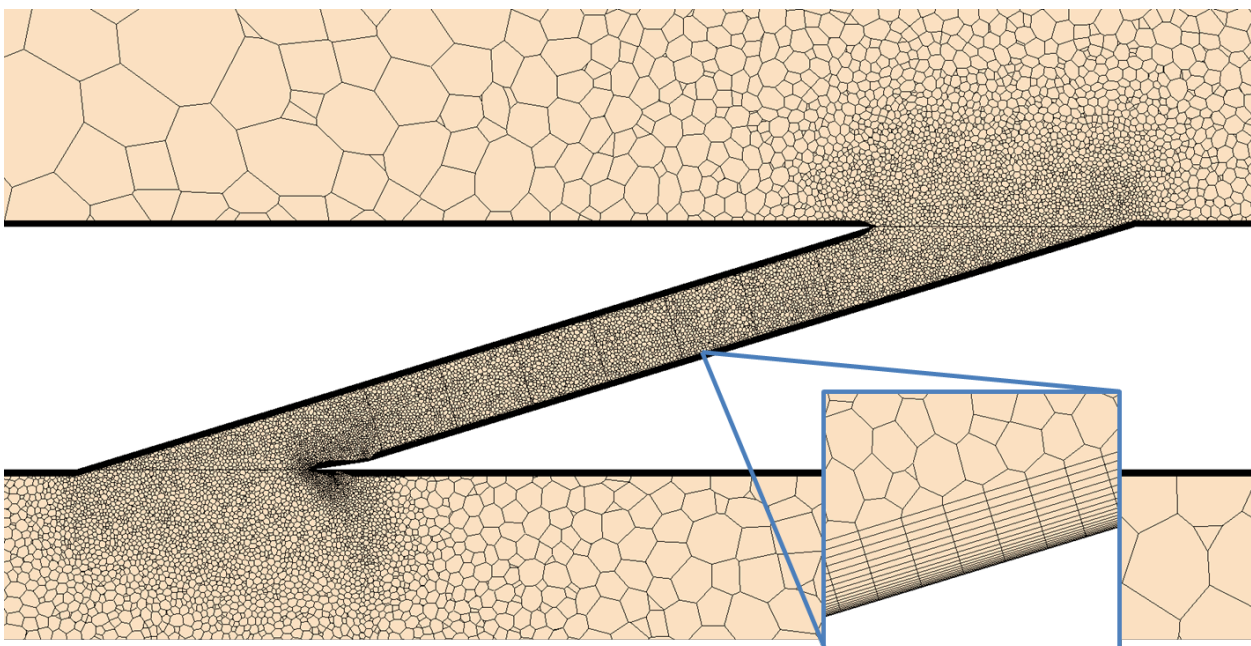
<div align="center">**Figure 53 – Volume mesh at cross section dissecting passage, flow from left to right**</div>

4.2.1.3 Physics & Boundary Conditions

Calculations are completed at conditions consistent with the Biot scaled cycle given in Table 5. The steady, 3-dimensional flow case is treated as an ideal gas.

T_{0_c}	$300K$	T_∞	$455K$
ΔP_{plate}	$9000Pa$	U_∞	$37.5m/s$
Tu_∞	0.05	ΛL_∞	$16.0mm$

Table 5 – CFD inlet boundary conditions – Discharge Coefficient

Preliminary simulations show that the realizable k-ε turbulence model with two-layer wall treatment shows the best agreement with experimental results when predicting discharge coefficient with the initial geometry considered; therefore subsequent simulations use this model.

The reference pressure for the simulation is set to an ambient condition of 101325Pa with all other boundary condition pressures set as offset values to this reference pressure. By subtracting the reference pressure, a working pressure is obtained for use within all calculations which is less prone to numerical round off errors (42).

The inlet boundary pressure for the coolant flow channel is set in line with experimental conditions to match the scaled liner pressure drop and the resultant mass flow rate is extracted from the solution using a constrained plane section typically located 2.4D upstream of the passage exit. This is the location of the start of the fanned section of the Spey fan design and represents the location at which data is extracted as part of the domain simplification technique detailed in section 4.2.2.6. The plenum inlet pressure is set to the same value for all cases. At a given cooling hole diameter, differing geometries will result in a different mass flow rate through the passage as a result of different discharge coefficients. Therefore the passage diameter must be altered in order to match both mass flow rate and pressure drop between cases.

Main flow conditions including temperature, velocity and turbulence conditions are set on a velocity inlet plane in order to mimic the hot-side flow in the experiment.

The outlet pressure is set to zero with respect to the reference pressure. Inlet temperatures are set to match experimental conditions.

4.2.1.4 Stopping Criteria and Post Processing

Simulations are run until all residuals asymptote to a minimum and are below at least 10^{-3}. In the majority of cases residuals are below 10^{-4}. The discharge coefficient is monitored for convergence along with net mass flow across the coolant system where the mass flow rate through the passage is measured using a constrained plane section normal to the passage axis just upstream of the exit. This plane is also used to extract data in later simulations. This should match the plenum inlet mass flow; although some small difference is expected due to numerical error and convergence level. Solution convergence is considered adequate once the difference is below 10^{-7} kg/s.

The pressure is extracted from the face of the inlet plenum and the outlet face on the hot-side to determine the pressure drop through the coolant passage. Coolant temperature is set as a boundary condition and mass flow rate through the cooling hole cross section is extracted. Knowing these quantities and the passage cross-sectional area derived from the CAD model, the discharge coefficient can be calculated using Equation 84. (65)

$$C_d = \frac{\dot{m}}{P_{0_c} \left(\frac{P_m}{P_{0_c}}\right)^{\frac{\gamma+1}{2\gamma}} \sqrt{\frac{2\gamma}{(\gamma-1)RT_{0_c}}\left(\left(\frac{P_{0_c}}{P_m}\right)^{\frac{\gamma-1}{\gamma}} - 1\right) A}}$$

Equation 84

A comparison of discharge coefficients obtained through simulation and experimentation are given in Table 6 below.

Geometry Tested	Simulation	Experimental	Error	Re
Plain Hole	0.612	0.67	8.7%	12,440
Spey Fan	0.737	0.79	6.7%	13,040
Modified Fan	0.917	0.89	3.0%	7,935
Slotted	0.843	0.79	6.7%	13,570
Circular Helix	0.468	0.43	8.8%	11,590
Rectilinear Helix	0.495	0.46	7.6%	12,930

Table 6 – Discharge coefficient measurements

It should be noted that the experimental values have uncertainty associated with the inability to measure the area of the flow passages, with variation seen between holes limited by the resolution of the DLD process. Simulations also look at a single hole in isolation whereas the experimental results are run on a full array, therefore any effects of hole to hole interaction and variability between holes caused by the manufacture process on the discharge coefficient will

be present. As a result a difference between computational and experimental results is expected. Notwithstanding these observations, the simulations appear to closely approximate the measured results in the majority of cases.

4.2.2 Adiabatic Film Effectiveness Calculation

With the geometry finalised, another set of simulations is carried out in order to determine the adiabatic film effectiveness performance of each design. Due to the high computational requirements involved in carrying out a complete simulation of an entire hole pattern array, this computation is accomplished by splitting the problem up into two parts. First a single passage is simulated using the same domain and mesh definitions as described above. The aim of this simulation is to determine the flow properties through the hole, particularly the velocity distribution. Once the through hole properties are known they are used as inlet boundary conditions for the second part of the computation. This simulation contains the hole pattern array, but only simulates a small region of the flow near the exit of the cooling hole, reducing the number of cells required within each individual hole and allowing more cells to be clustered on the plate surface resulting in better resolution of the coolant film. As a result an array containing multiple rows of coolant holes can be approximated using a much reduced number of grid cells.

These simulations are run with conditions mimicking the experimental adiabatic film effectiveness tests described in section 3.6. In keeping with the experimental film effectiveness methodology, these simulations are resolved using an inert gas scalar mixing based approach where the flow is kept at isothermal conditions throughout. Air is used as the mainstream gas and nitrogen gas is chosen as the coolant simulant. This involves using the multi-component gas model and setting gas properties such as molecular weight, dynamic viscosity and specific heat for each gas component.

4.2.2.1 Single Hole Simulation

The aim of this simulation is to find the flow conditions near the exit of the passage. These conditions will then be used as an inlet boundary for the multi-hole type simulations in order to compare with the results obtained through experimental rig testing (see section 5.1). This is achieved by creating a constrained plane at a distance of 2.4D upstream of the passage exit, as can be seen in Figure 54, and extracting data for the velocity vectors, static temperature, turbulent kinetic energy, turbulent dissipation rate and mass fractions of air and N_2. These

properties are stored in a table and exported for use in the multi-hole calculation to be applied as an inlet boundary. The location of this extraction plane is selected to be far enough upstream of the exit that it is largely isolated from the influence of any external features such as adjacent jet flows or turbulence.

The domain geometry and mesh used in these simulations share the same design rules and similar controlling parameters as used for the initial discharge coefficient study. The main difference between the two sets of prediction is the switch to isothermal conditions throughout the entire computational domain together with the substitution of a Nitrogen gas as the coolant in line with the experiment. This requires the addition of the coupled species model in order to calculate the interaction of the two gasses.

Velocity (m/s)

| 0.00000 | 18.400 | 36.800 | 55.200 | 73.600 | 92.000 |
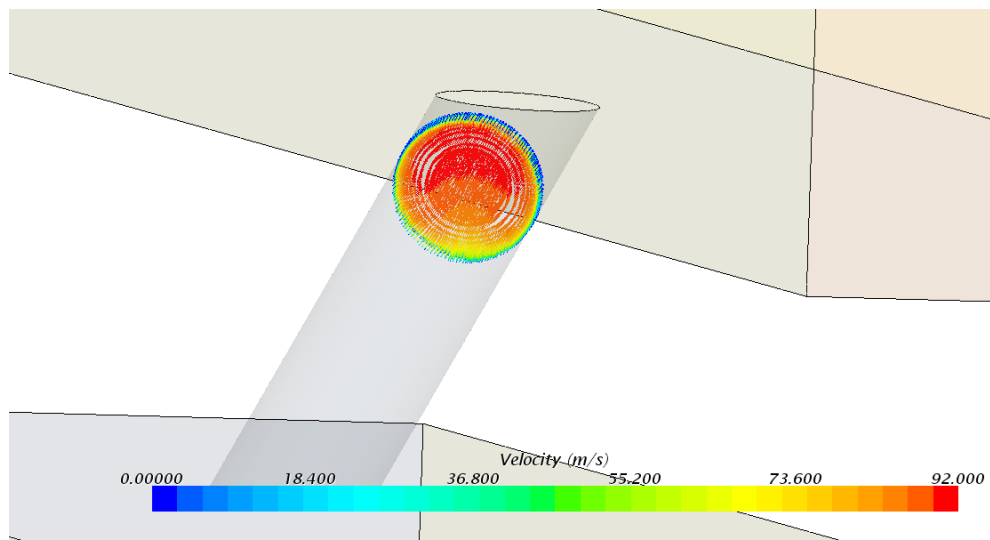
Figure 54 – Extracted constrained plane section data

4.2.2.2 Multiple Hole Simulation

Once flow conditions near the passage exit have been calculated, they are used as the velocity and species inlet boundary conditions for a calculation on a plate involving multiple hole passages. This reduces the size of the computational domain, allowing a detailed calculation of the flow properties through a single hole and then applying those conditions to form a detailed simulation of the adiabatic flow over the plate surface containing an array of cooling holes.

4.2.2.3 Simulation Topology

The single hole domain is the same as that used in the initial C_d study scaled to the correct effective area. The multi-hole geometry is defined based on that of the experiment as with the single passage case; this is used to define the flow domain parametrically. This flow domain only contains a small portion of the coolant hole passages, with only the final 2.4D modelled.

However, the exit flow region of multiple holes is captured, with typically 8 rows of coolant holes included for all but one of the designs considered based on the hole pattern. As a result this model simulates the interaction between the coolant jets as they exit the cooling holes and mix with each other and the mainstream over the surface. While this approach does not completely capture the more global effects of the array structure on the coolant flow through the holes, in particular the velocity profile, the local effects of the interactions are captured. As a result care must be taken when applying this technique that the effect of the array on the through hole velocity profile is considered.

Inlet and outlet length as well as domain height are kept constant with the single hole model and the domain width is the hole pitch as shown in Figure 55. Periodic repeating boundaries are used for the side walls; as a result flow properties are transferred from one boundary to the other, simulating an infinite width plate with regular cooling passages using an interface. This boundary is shown in yellow in Figure 56. Velocity inlet boundaries are shown in red, these are placed at the same 2.4D distance upstream of the cooling hole exit plane as the extracted plane from the single passage. All other boundaries are the same type as with the single-passage case, in this image the main flow velocity inlet is coloured cream.

Figure 55 – Drawing of example multiple passage flow domain, dimensions in mm
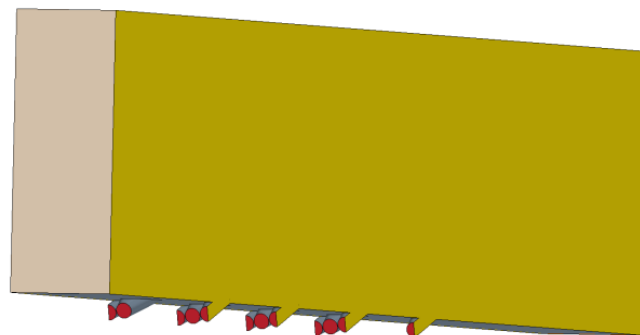
Figure 56 – Drawing of example multi-passage flow domain, dimensions in mm

4.2.2.4 Meshing

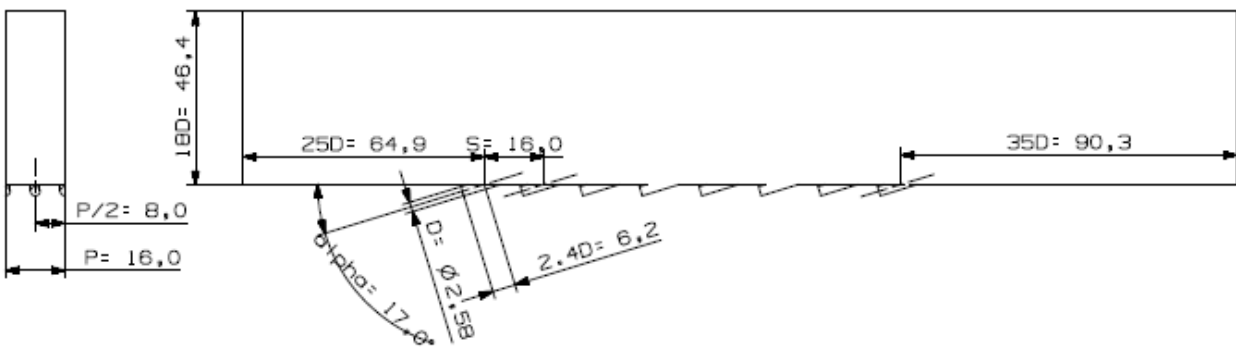As a result of using the periodic boundary, the mesh generator automatically creates a conformal grid which is exactly the same on both 'walls'. There are three major differences in the mesh controls between the single- and multi-passage cases. First the surface curvature is reduced from 108 to 72pts/circle with the higher value used to resolve the definition in the sensitive area at the passage entry which is not present in the multi-passage case. The maximum cell size on the plate surface is limited to a target size of 10% of base in order to ensure cells cluster close to this surface and capture the film distribution in the multi hole array. The global target cell size is also reduced to 100% of base; limiting the cell size in the domain and ensuring the exit flow is sufficiently resolved. The resulting multi-hole domains typically contain around 3-5million cells.

4.2.2.5 Physics & Boundary Conditions

Similar physics models are used in both single- and multi-passage cases as described in section 4.2.1.3, the only difference being that the flow is isothermal with the coupled species model used to simulate the mixing of mainstream air with the Nitrogen coolant in order to determine the adiabatic film effectiveness in line with the experimental tests. The main difference between the single- and multi-passage cases is the velocity inlet boundaries used to map the inlet conditions for each passage exit in the multi-hole array; flow properties such as velocity, temperature, and turbulence properties are imported from the data extracted in the single hole simulation for use on these boundaries. The inlet boundary conditions are given in Table 7 below. Two pressure drop conditions are tested similar to the highest and lowest conditions used for the experimental film effectiveness tests as well as high and low freestream turbulence conditions. Other flow properties are kept the same for all simulations in line with the experimental conditions.

T_{0_c}	$300K$	T_∞	$300K$
ΔP_{plate}	$2000, 9000Pa$	U_∞	$32.0m/s$
Tu_∞	$0.05, 0.20$	ΛL_∞	$16.0, 32.9mm$

Table 7 – CFD inlet boundary conditions – Adiabatic Film Effectiveness

4.2.2.6 Inlet mapping

Data consisting of velocity components, static temperature, turbulent dissipation rate, turbulent kinetic energy, species mass fraction and position is required to form the inlet boundary condition for the multi-hole array simulation. The data is extracted from a

constrained plane in the single-passage case using a table; this table can then be imported into a different simulation to form a boundary condition. In order to map the solution from the single-passage case onto each of the inlets simulated in the multi-passage case, it is necessary to define a local coordinate system for each individual boundary. This ensures that the solver is mapping the profiles correctly, particularly for the side passages which only contain half of the inlet as can be seen in Figure 57. Each boundary has the origin for the associated coordinate system located at the passage centre, equivalent to the centre of the constrained plane section where the origin of the extracted data is located.

Both the extraction plane in the single-hole simulation and the inlet planes on the multi-hole simulation are located 2.4D upstream of the centreline of the coolant passage exit plane in order to capture any upstream flow effects that may be imposed as the coolant leaves the passage and enters the mainstream.
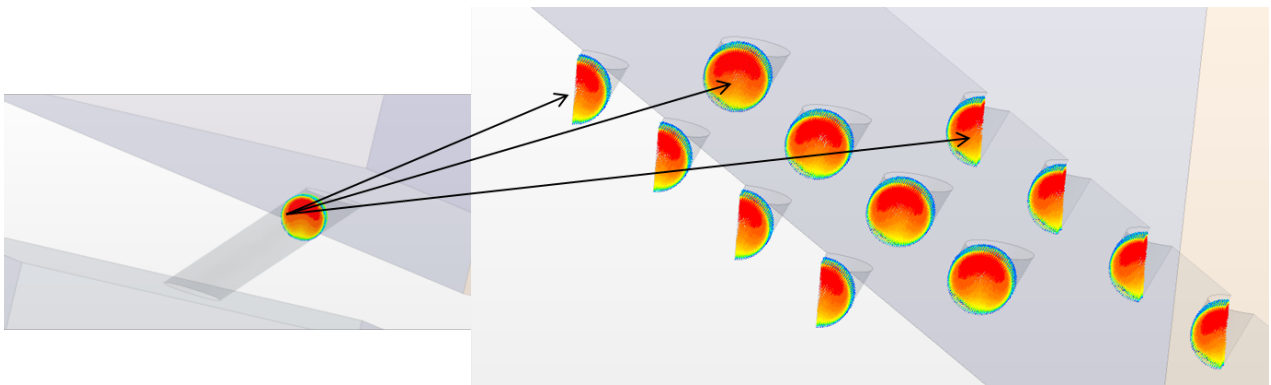
Figure 57 – Inlet condition mapping

4.2.2.7 Stopping Criteria and Post Processing

Simulations are run until the momentum, energy, continuity, turbulence and species residuals have asymptoted to a minimum. Both the discharge coefficient and mass flow balance between the plenum inlet and the constrained plane at the cooling hole exit are monitored for convergence in both simulations. The surface average film effectiveness on the plate is also monitored alongside the mass flow balance in the entire domain for the multi-hole simulation.

Comparison with experiments is drawn between both the span-wise averaged surface effectiveness as well as the qualitative surface effectiveness map. In order to make this comparison, the data from the simulation is extracted and imported into a Matlab script which splits the surface effectiveness data into thin slices in the streamwise direction and calculates the area averaged surface effectiveness in each slice. The results are then plotted against

distance from the passage exit plane. Effectiveness for the simulations is visualised by means of a field function and this is defined as;

$$\eta_{xy} = \frac{C_{air_\infty} - C_{air_{xy}}}{C_{air_\infty}}$$

The subscript ∞ refers to the surface average at the main flow inlet plane.

4.2.3 Internal Conjugate Heat Transfer

A conjugate heat transfer type calculation is carried out on a single passage in order to simulate the heat transfer between the metal and air within the passage. This allows the internal heat removal performance of the various designs to be assessed. It is difficult to obtain this information from an experimental test rig due to the problems encountered when trying to obtain optical access required for a number of measurement techniques, particularly as internal cooling designs become more complex in shape.

The governing equation for energy transport in a solid as used by StarCCM+ is;

$$\frac{d}{dt}\int_V \rho c_p T dV = -\oint_A \boldsymbol{q}'' \cdot d\boldsymbol{a} + \int_V s dV$$

Equation 86

Where $\boldsymbol{q}''$ is the heat flux vector and s represents entropy.

4.2.3.1 Simulation Topology

For the conjugate model, the same basic geometry is used as in the single passage calculation with the addition of a solid domain to act as the plate. A contact interface is created between the solid surfaces and the fluid on the top and bottom exposed plate surfaces as well as the cooling hole surface. This allows the heat to transfer between the fluid and the wall, setting up and capturing the thermal gradient through the solid material (cross-hatched in Figure 58) between the hot main flow and the cold plenum. Figure 59 shows the boundary types used for this simulation; the main boundaries are the same as for the adiabatic effectiveness calculations where red indicates the main flow velocity inlet, purple shows the plenum stagnation inlet, orange is the pressure outlet, grey are slip walls in the fluid domain and two faces in the solid domain are modelled as adiabatic boundaries, yellow are periodic interfaces and green indicates a direct contact interface between the solid plate and the fluid air domains.
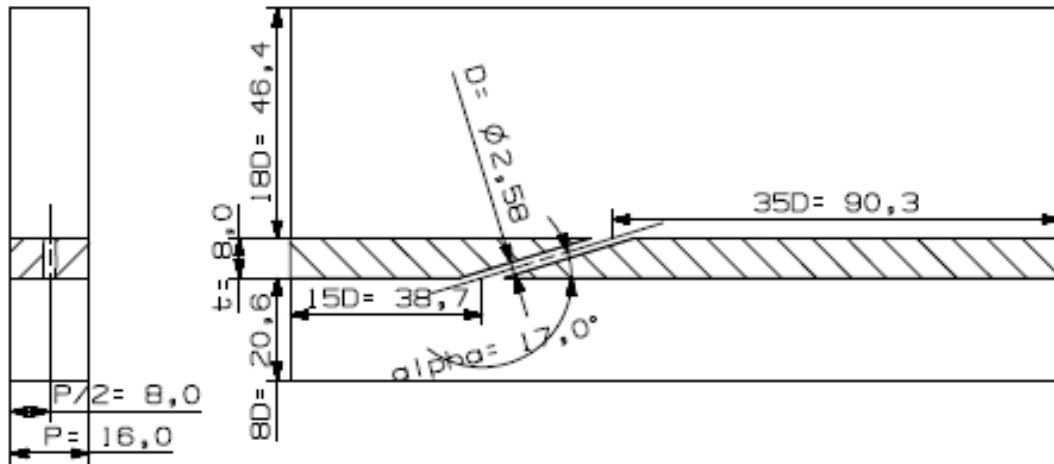
Figure 58 – Drawing of example single passage conjugate flow domain, dimensions in mm
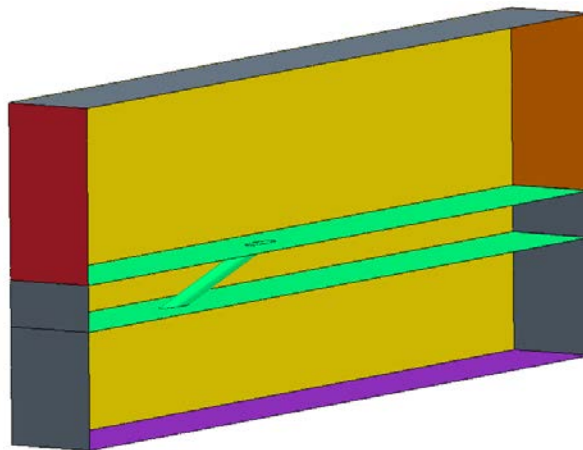
Figure 59 –Side views of domain

4.2.3.2 Meshing

The meshing parameters used for the conjugate model are similar to those used for the single-passage case; a mesh is now needed to define the solid liner wall through which the coolant passage passes. This additional requirement increases the number of cells necessary in this region of high cell density where prism layers grow in both directions from the boundary as seen in Figure 60, the boundary interface is shown in blue. As there is no flow to resolve within the solid region the number of prism layers is decreased to 8, with the overall and near wall thicknesses increased to 15% of base and 0.01mm respectively. A conformal mesh is created on the interface between solid and fluid regions ensuring properties are correctly transferred between the two. Cell counts for these conjugate computations range between 1- and 2-million.
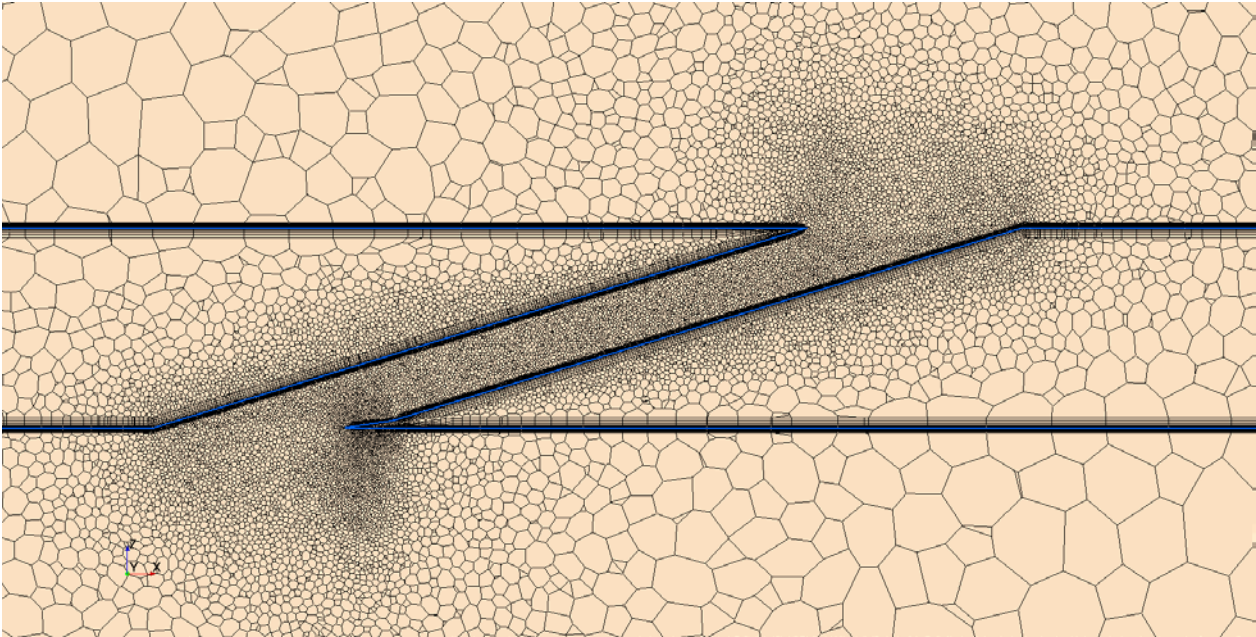
Figure 60 – Example volume mesh for conjugate case

4.2.3.3 Physical & Boundary Conditions

The physical model and boundary conditions for this model are set to reflect the conditions used for the hot experimental tests at the highest and lowest pressure drop conditions. The plate representing the liner wall is modelled using a separate solid continuum which has the same physical properties as the material (Inconel 718) used to create the test plates for the Biot scale rig in terms of density, specific heat and thermal conductivity. This type of continuum uses a coupled solid energy model to solve the energy equation and simulate the transfer of heat within the region.

T_{0c}	$300K$	T_∞	$455K$
ΔP_{plate}	$2000, 9000 Pa$	U_∞	$37.5 m/s$
Tu_∞	0.20	ΛL_∞	$32.9 mm$

Table 8 –CFD inlet boundary conditions – Internal Conjugate Heat Transfer

As before, the main flow inlet velocity, turbulence properties and temperature boundary conditions are set to reflect the experimental conditions with the constant plenum inlet pressure drop previously used. For the conjugate case, instead of using adiabatic walls to represent the plate surfaces, a contact interface is used to represent the interfaces between the solid and the fluid to allow the transfer of heat between the two regions. The grid sequencing method is again employed to give the solution a suitable starting point relative to the initial conditions.

4.2.3.4   Stopping Criteria and Post Processing

As with previous cases, the simulations are run until the residuals asymptote to a minimum in each case. The average temperature at a number of cross section locations through the passage and both the total and surface integral heat transfer through the surface of the passage are also monitored for convergence. The heat transfer through the passage surface is used to determine a Stanton number for that geometry which in turn is used to rank each design in order to determine which transfers heat from the liner wall into the coolant air most efficiently and thus has the greatest potential for reducing the metal temperature whilst keeping the amount of cooling air required to a minimum.

4.3   Computational Resources

As these simulations are aimed at providing a relatively rapid assessment of a given cooling geometry, it is important to consider the computational resources required to run the models described here. All simulations carried out as part of this work are run on one of two workstation engineering machines operated by the Heat Transfer Group within the Rolls-Royce UTC at Loughborough University. While these machines are more powerful than a standard desktop PC, they are still single machines operating within a typical desktop workstation form factor. The more powerful of the machines utilises dual Intel® Xeon® E5-2630 Hex-Core CPUs running at 2.3GHz allowing a total of 12 parallel processes, though only 11 are utilised at any given time, and 96GB RAM. The second machine has a single Intel® Xeon® E5-1620 Quad-Core CPU running at 3.6GHZ and 64GB RAM, a maximum of three parallel processes are used on this machine. Run times vary depending on grid density and which machine is used but typically calculations such as those outlined above can be completed in a day or less. These represent relatively modest engineering workstation machines.

5   Experimental Results and Discussion

The results of the experimental tests are presented and discussed in this section. These are split up into the adiabatic film effectiveness measurements using the PSP technique and the overall effectiveness measurements using the IR thermography technique. Results are presented as both surface maps showing the effectiveness distribution over the plate surface and span-wise averaged results. Both experiments investigate the effect of varying freestream turbulence levels as well as momentum ratio. The six different plate designs are investigated with the objective of ranking the six designs in terms of both overall and adiabatic film effectiveness and sensitivity to both turbulence levels and momentum ratio as well as using the performance information to help identify particular strengths associated with each design.

5.1   Adiabatic Effectiveness Measurement – PSP Technique

The temperature of the gas immediately adjacent to the wall sets up the boundary condition for convective heat transfer into the wall, as such it is of great benefit to know the distribution of coolant on the surface. By looking at the effect of freestream turbulence, momentum ratio and hole geometry on the adiabatic film effectiveness it is possible to gain performance information required to optimise the cooling scheme utilised at various locations within the combustion chamber.

5.1.1   Effect of Freestream Turbulence

Surface maps of adiabatic film effectiveness are presented in even numbered Figures 63 to 71 which show the effect of freestream turbulence levels on the first five geometries at the highest and lowest momentum ratio conditions tested. Generally, it is difficult to pick out any major differences between turbulence conditions from this data, particularly at the higher momentum ratios. Even with the addition of a $10D$ cylinder 60mm ($\approx 30D$) upstream of the test plate (Figure 61) designed to simulate the highly turbulent conditions behind a combustor dilution port there is little impact caused by these increased freestream turbulence levels. A spanwise average is taken over a central strip of each test plate as indicated in Figure 62, representing a spanwise average between periodic boundaries, much like is modelled numerically. When comparing the spanwise averaged results small differences are easier to identify with some designs being more sensitive to freestream turbulence than others.
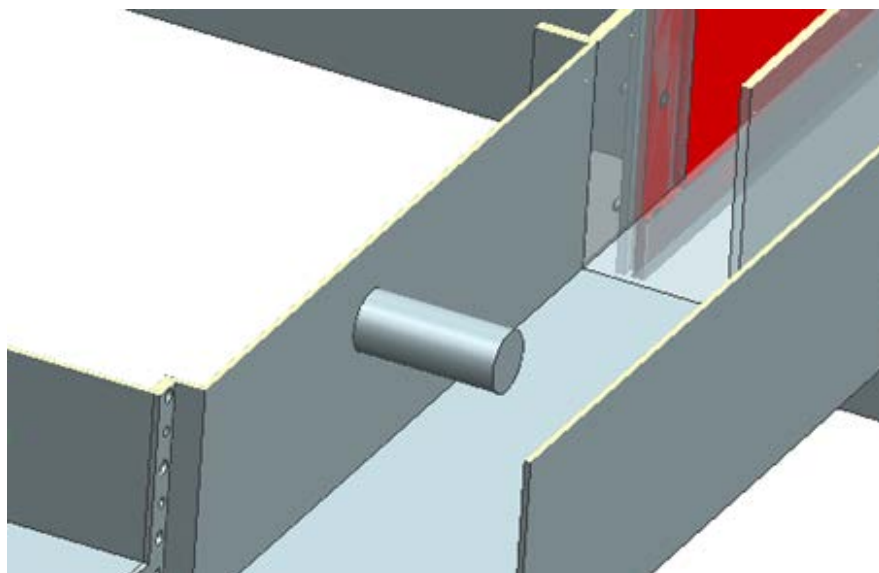
Figure 61 – View of cylinder used as port flow blockage simulant
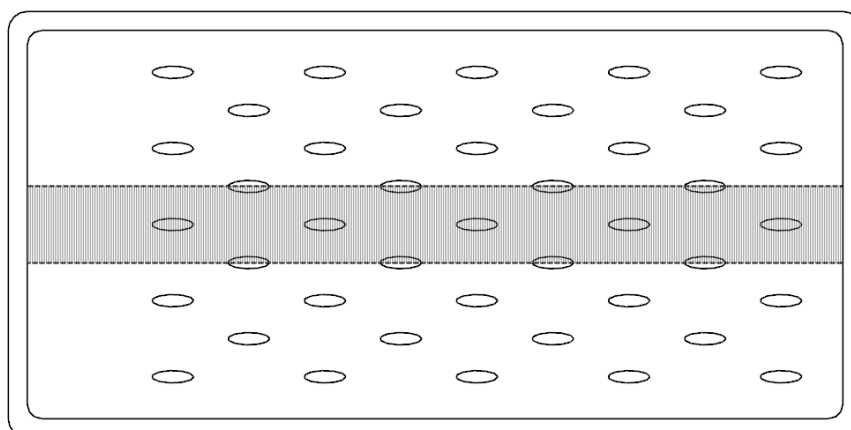
Figure 62 – Illustration of spanwise averaged area (shaded)

5.1.1.1 Cylindrical Effusion Geometry

Figures 63 and 64 show the 2D surface contours and spanwise averaged adiabatic effectiveness data for the plain cylindrical hole effusion test plate. From the surface contours it can be seen that increasing the freestream turbulence intensity causes the coolant jet to mix with the freestream flow much sooner in the streamwise direction as evidenced by the reduced length of the coolant trail downstream of the hole exits. This can be seen in both high and low coolant flow rate results, though the effect appears greatest at the lowest momentum ratio. While reducing the streamwise trace length, the increase in turbulence levels appears to increase the spanwise spreading, particularly as distance along the plate increases, this trend was also noted by Martin (57). However, the difference in absolute effectiveness is small and when plotted as a spanwise average this increased mixing appears to have very little effect even at the lowest

momentum ratio encountered here until after the fifth row. From this point the increased mixing caused by the enhanced turbulence has the general effect of reducing the effectiveness of the coolant attached to the surface.

At the higher momentum ratio the effect of turbulence on the spanwise averaged effectiveness is small up to the third row, after which the increased spanwise mixing caused by the higher turbulence intensity results in a slight increase of span-averaged effectiveness, again similar trends were identified by Martin (57). This trend continues up to the seventh row, after which there is once again little difference between turbulence conditions. The slight bias seen in the coolant traces is due to the build direction of the DLD manufacturing technique resulting in a slightly asymmetrical cross section. Slight bias is seen by all geometries tested as part of this study but does not favour either direction indicating it is not due to test section flow bias.

5.1.1.2 *Spey Fan Effusion Geometry*

Figures 65 and 66 show the results for the Spey fan design. From the 2D surface contours it can be seen that the fanned exit to the hole causes the coolant to spread out laterally resulting in a much wider area of coverage downstream of the holes. However, due to the large divergence angle of the fanned section the flow remains attached to one side rather than filling the entire fan. The diffusion to a lower exit velocity caused by the diverging section also results in the coolant jet remaining attached to the surface, greatly increasing the cooling effectiveness. Small peaks are visible in the spanwise averaged data upstream of the hole exits at the lower turbulence levels. These are thought to be due to shadows within the hole exit caused by the angle of the illumination source; the effect of which is to greatly reduce the signal to noise ratio in the shadowed region resulting in extremely erroneous data and as such these peaks are not physical and should be disregarded.

At the lower momentum ratio condition, increasing the freestream turbulence level improves the lateral spreading of the coolant as can be seen by a reduction in the adiabatic effectiveness gradient across the effusion surface. This increases the spanwise averaged film effectiveness by up to 0.03 towards the downstream end of the plate. Unlike in the cylindrical hole case, this increase in spanwise spreading is not accompanied by a notable decrease in the streamwise extent of the coolant film. This is a result of the majority of the coolant mass remaining close to the wall in the fanned case, whereas for the cylindrical case much of the coolant mass is ejected further into the freestream allowing the mainstream gas to remain in the near wall region.

At the higher momentum ratio, the difference caused by the increased lateral spreading is generally negated by the increased mass of coolant on the surface. With the exception of the area between the trailing edge of the first row and leading edge of the second, there is little difference in spanwise averaged film effectiveness, with all three sets of data collapsing together. Martin (57) saw a difference between turbulence conditions at this higher flow condition, however, through use of a large scale factor and the manufacturing techniques used the hole definitions are much more symmetric with the flow exiting the fans down the centreline. This contrasts with the results presented in this study, which show bias in the coolant trace with the coolant preferring one side of the fan, this is again due to the DLD manufacturing process. In the Spey fan case a flat spot is seen down one side of the metering section, with such a major asymmetry causing the flow to attach to one side in the exit fan. This appears to influence the interaction of the coolant and mainstream flows, increasing the resilience of the coolant to freestream turbulence.

5.1.1.3   Modified Fan Effusion Geometry

Figures 67 and 68 show the results for the Modified fan geometry. The exit of the hole is fanned as with the Spey fan geometry, but with the fan starting much earlier and at a reduced fan angle. This encourages the coolant to spread in the spanwise direction as well as reduce the exit velocity. Jet penetration into the freestream is decreased leaving more coolant on the plate surface. The shadowed area on the leading edge of some of the hole exits can be seen at the lowest turbulence condition but due to the narrower profile of the hole exit in this location, the number of erroneous data points is reduced compared to the Spey geometry and thus the small peaks in the spanwise averaged data are far less pronounced.

As in the cylindrical hole case, the effect of increased turbulence intensity on the lower flow condition is a reduction in the streamwise spreading of the coolant. However, due to the diffusing section causing the coolant to spread in the spanwise direction, the change in lateral mixing between turbulence cases is not as pronounced. The gradients between cooling holes however indicate that increasing turbulence level reduces the streamwise extent of the cooling film between holes. The spanwise averaged results show that for the first two rows the overall effect of increasing turbulence is to reduce the average effectiveness by up to 0.03 beyond the first row, reducing as the film develops. After the third row there is little difference between

turbulence cases, with the higher turbulence level resulting in increased average effectiveness for the final two rows as the film streaks between holes mix out.

Once again at the higher momentum ratios, though a difference in the qualitative distribution of coolant is evident in the surface maps, the spanwise averaged data shows a very slight reduction in coolant film effectiveness as increased turbulence intensity causes both a reduction in streamwise and increase in spanwise spreading to a similar degree. This is in agreement with the small reduction in spanwise averaged adiabatic effectiveness seen by Martin (57) at similar flow conditions.

5.1.1.4 Slotted Effusion Geometry

The 2D surface contours and spanwise averaged film effectiveness results for the Slotted geometry are shown in Figures 69 and 70 respectively. This design uses a different hole array pattern where roughly twice the number of holes are placed in the spanwise direction while almost doubling the spacing between coolant hole rows. Also, contrary to the other designs considered as part of this study, the design of the fanned hole passage does not diverge in the spanwise direction, instead fanning in the streamwise direction. As with the other fanned designs this reduces the exit velocity, decreasing the jet penetration and encouraging the coolant to stay attached to the surface. The lack of lateral divergence results in much narrower coolant trails downstream of each hole compared with the fanned geometries, but by fanning in a direction normal to the surface, the effectiveness in this region is greatly improved over the plain cylindrical hole design.

As with the other geometries tested, the effect of increasing the freestream turbulence level is to increase the lateral spreading of the coolant while reducing the length of the high effectiveness region downstream of the hole exit. This results in well-defined longitudinal streaks between holes at low turbulence conditions and which mix out at the higher turbulence condition. Once again, the addition of the simulated port flow blockage is negligible when compared to the high turbulence case.

Due to the spanwise spacing of the holes being of a similar magnitude to the hole exit width, full coverage is accomplished after the second row. However, the decreased streamwise spreading of the coolant combined with the increased distance between cooling rows is detrimental to the spanwise averaged film effectiveness. This is the cause of the crossover from the higher

spanwise averaged results for the high turbulence case between the first and second rows and lower average after the second row. The same trends are seen at both high and low momentum ratios, with a general offset of about 0.05 indicating the advantage of running at higher wall pressure drop.

5.1.1.5 Circular Helix Effusion Geometry

Figures 71 and 72 show the 2D surface contours and 1D spanwise averaged adiabatic film effectiveness distributions for the Circular Helical geometry. A reduced fan angle of 12° is defined for the diverging exit section compared with the Spey fan geometry. This, combined with the change in approach conditions generated by the helical passage results in the coolant filling this fanned portion of the hole, creating a wide area of high film effectiveness downstream of the hole exit at all tested flow conditions. This effect, combined with the reduced exit velocity caused by both enhanced diffusion in the fan section as well as the increased pressure drop within the upstream helical flow passage, results in the coolant remaining on or close to the surface. With so much coolant mass remaining very close to the wall, the effect of increasing the turbulence intensity appears to disperse the coolant flow laterally across the plate, increasing the average effectiveness particularly at the lower momentum ratio. At this condition, an increase in the spanwise average film effectiveness by as much as 0.04 is seen at the start of the cooled patch which slowly reduces along the length of the plate as the effectiveness reaches the maximum value. The surface contours also indicate that the flow is under-expanded as it exits onto the plate surface. In combination with the close proximity of the hole exits, this is likely to result in the coolant streams mixing and interacting with each other, further reducing jet momentum and helping to keep the coolant closer to the surface and distribute it laterally across the plate.

At the higher momentum ratio the increase in effectiveness with freestream turbulence level is less pronounced, with the difference in effectiveness with position along the plate length dropping much faster. This is a result of the generally high effectiveness as the mass of coolant on the surface reaches an asymptotic state reducing the potential for improvement.

As with the other designs tested, adding the port blockage simulation has little effect over the increase in bulk freestream turbulence intensity at all flow conditions.

Figure 63 - Cylindrical hole adiabatic film effectiveness at various turbulence and momentum ratio conditions
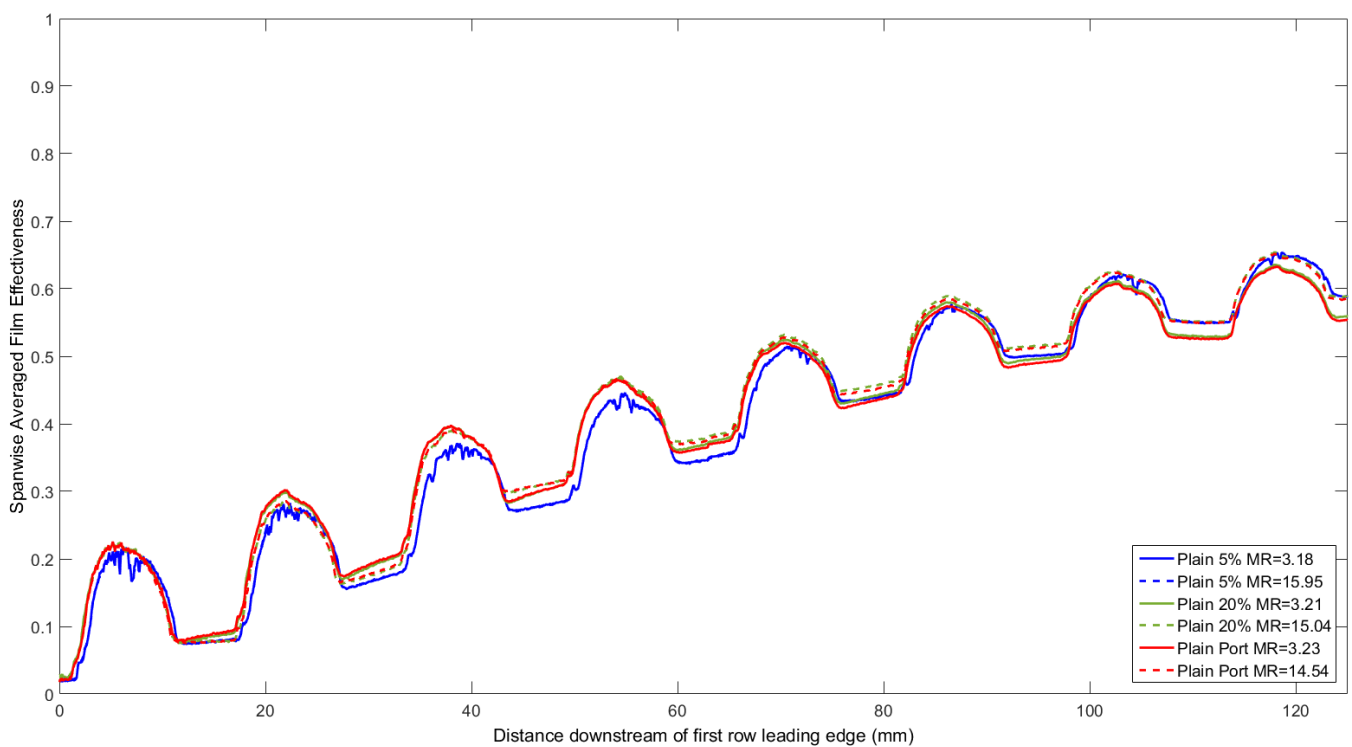
Figure 64 - Cylindrical hole spanwise averaged adiabatic film effectiveness at varying freestream turbulence levels
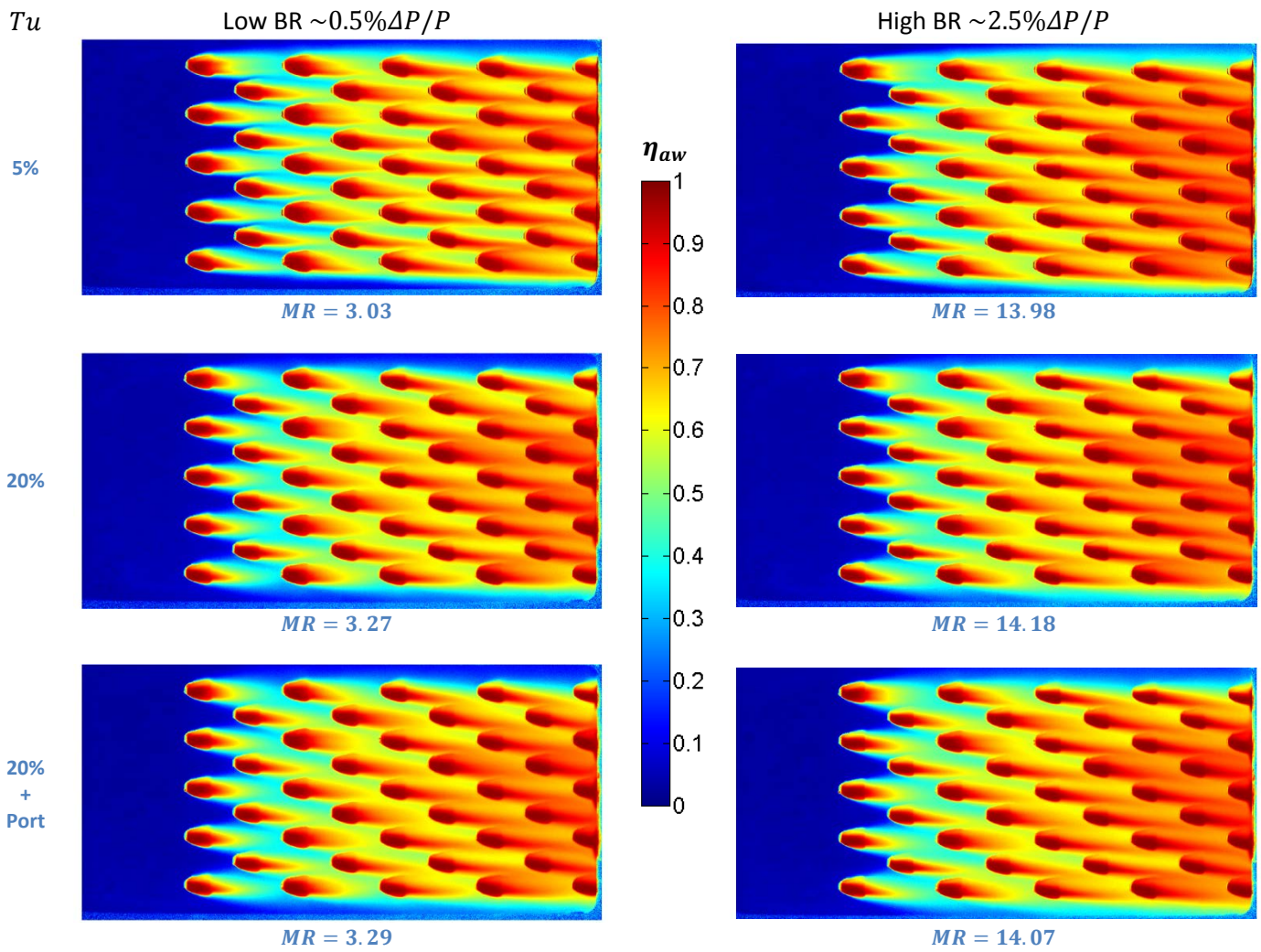
Figure 65 – Spey Fan adiabatic film effectiveness at various turbulence and momentum ratio conditions
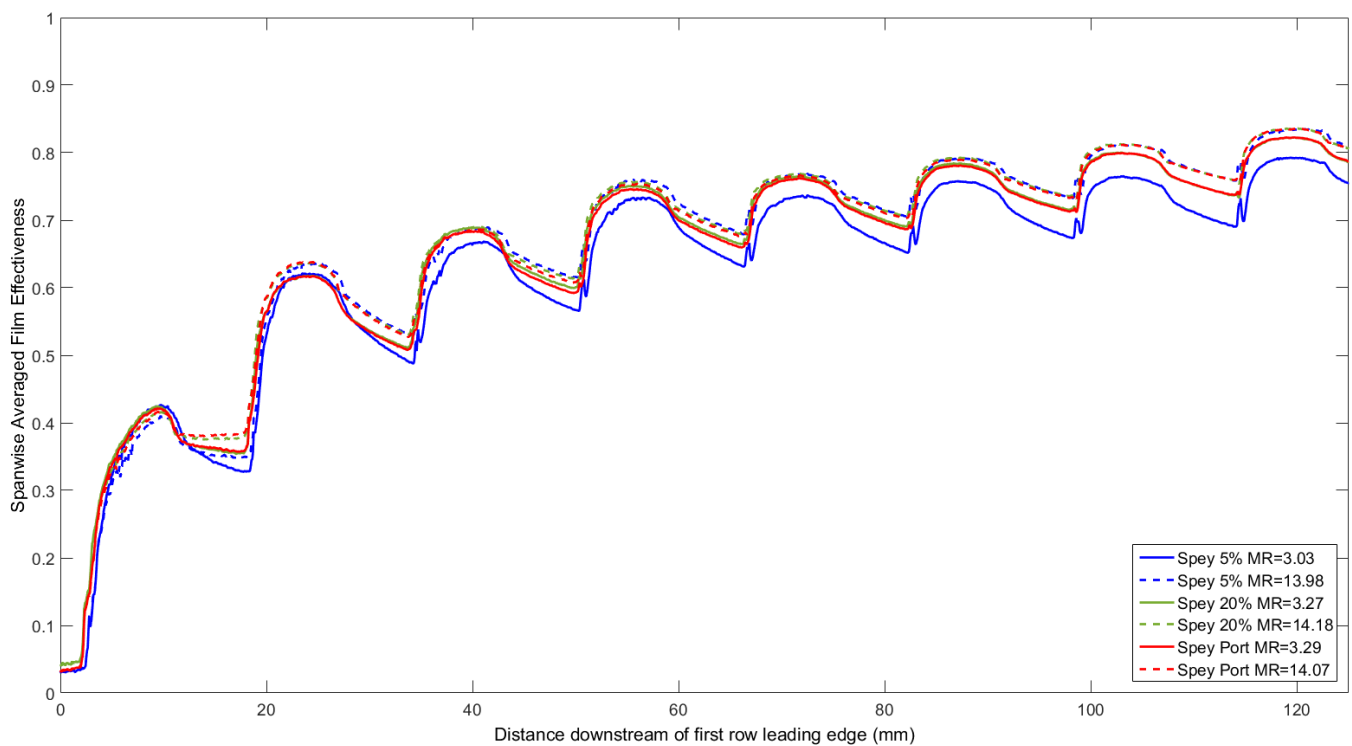
Figure 66 – Spey Fan spanwise averaged adiabatic film effectiveness at varying freestream turbulence levels
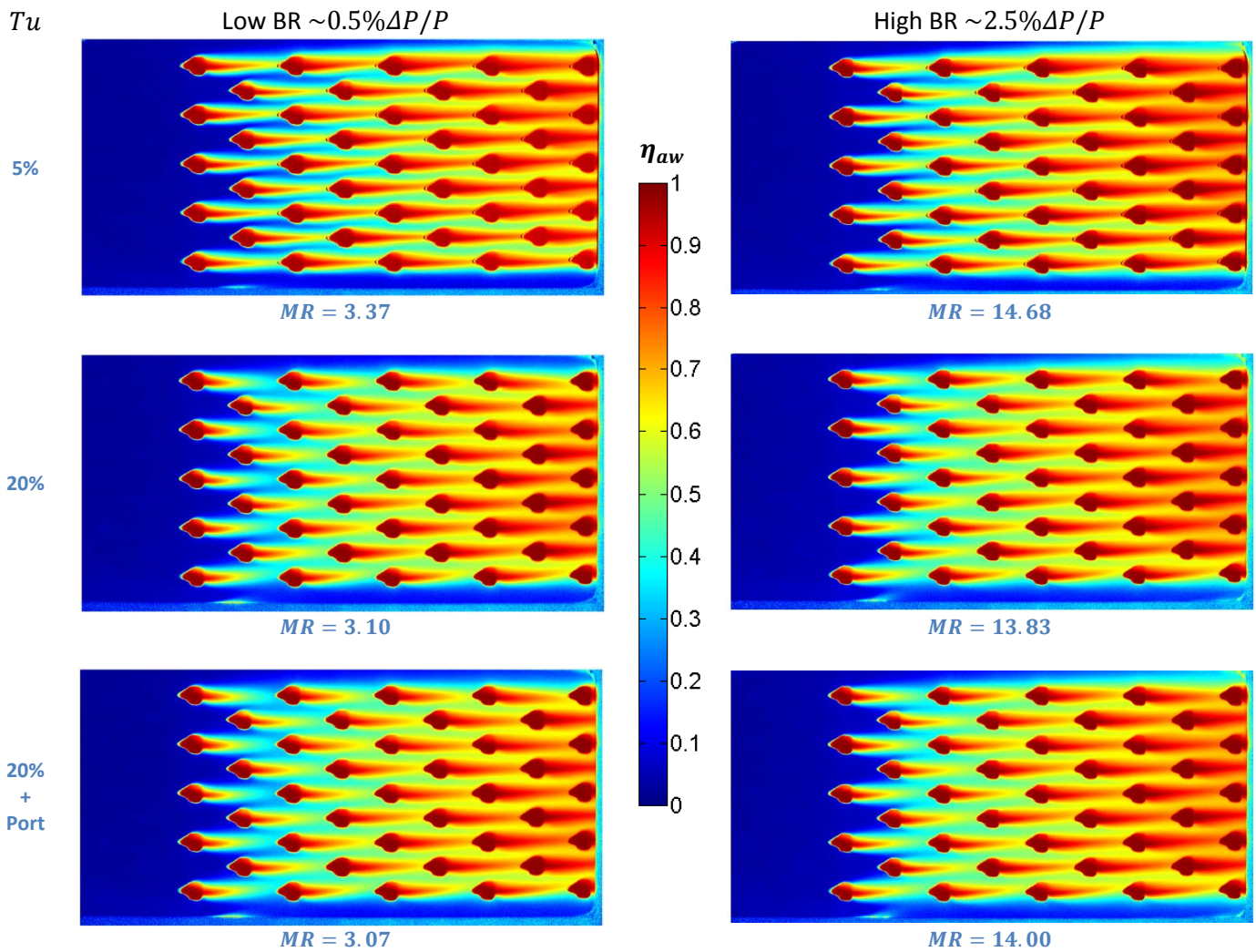
Figure 67 – Manufacturable Fan adiabatic film effectiveness at various turbulence and momentum ratio conditions
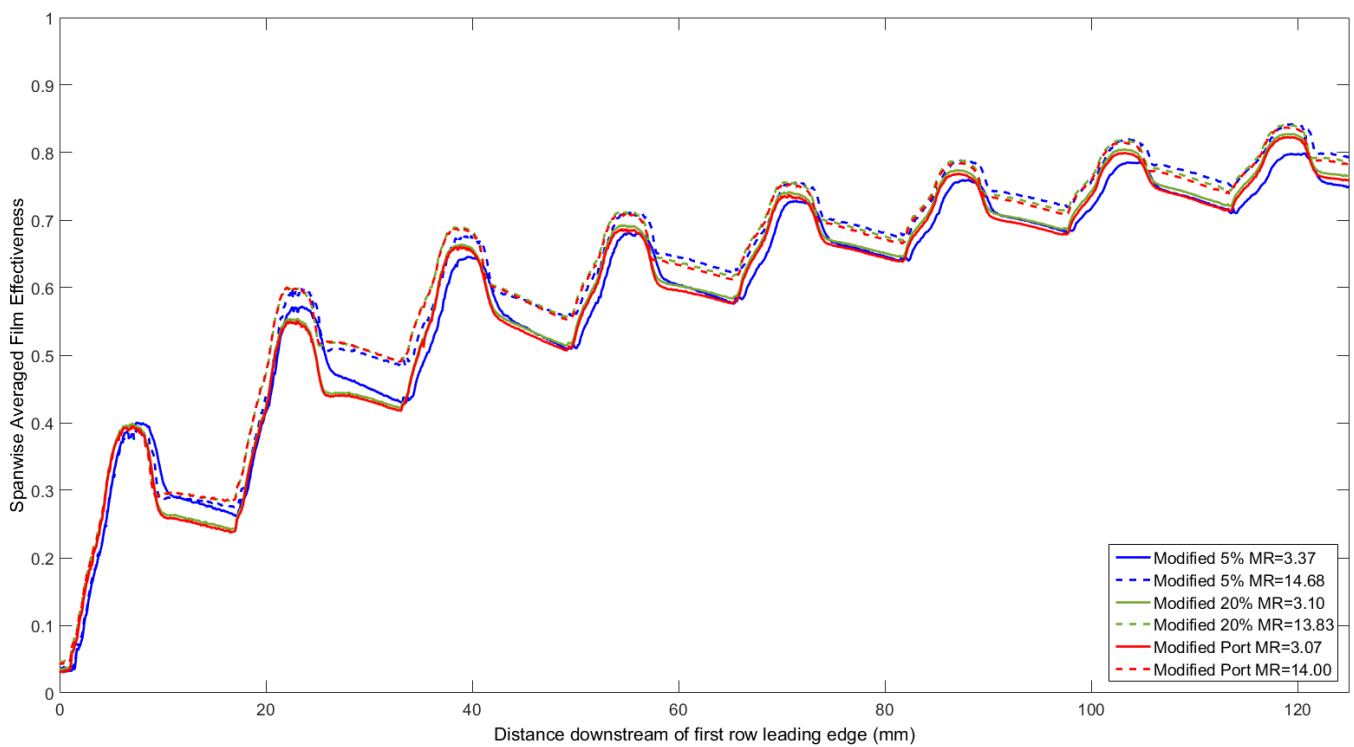
Figure 68 – Manufacturable Fan spanwise averaged adiabatic film effectiveness at varying freestream turbulence levels

Figure 69 – Slotted adiabatic film effectiveness at various turbulence and momentum ratio conditions
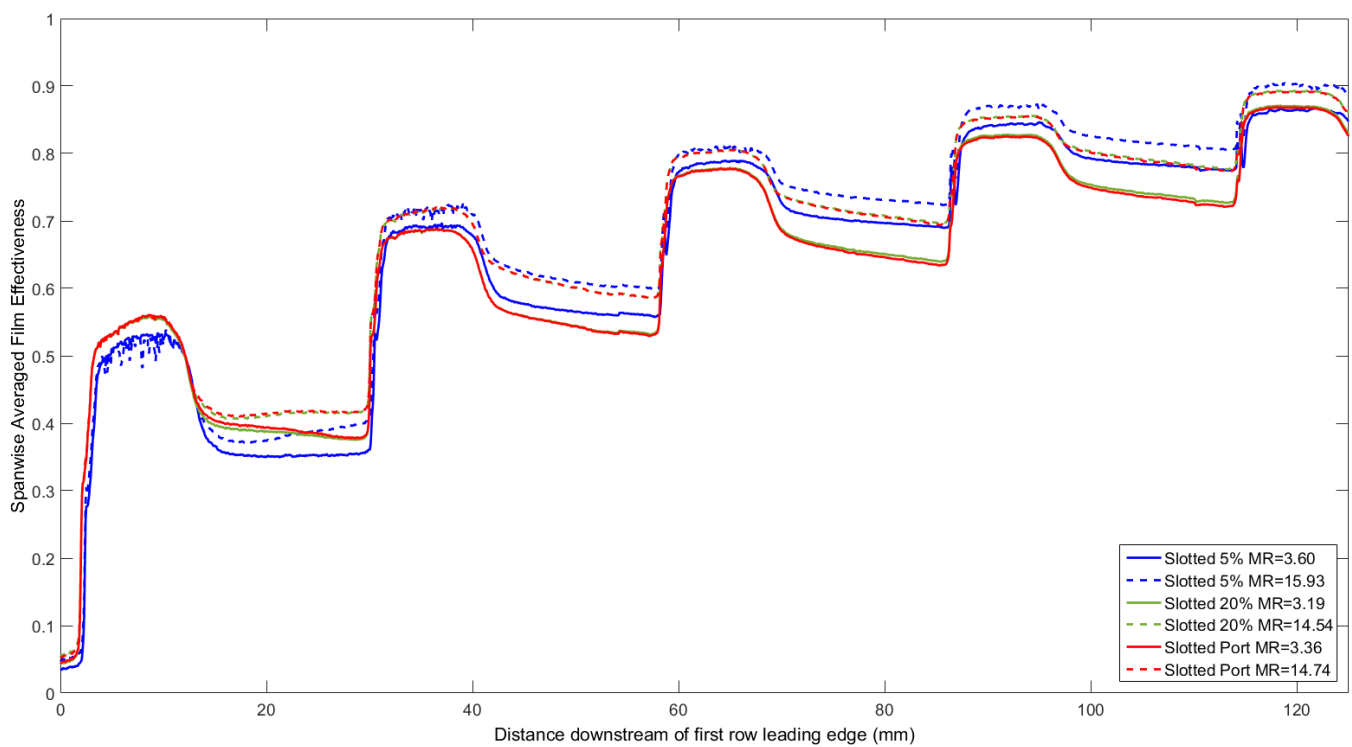
Figure 70 - Slotted spanwise averaged adiabatic film effectiveness at varying freestream turbulence levels
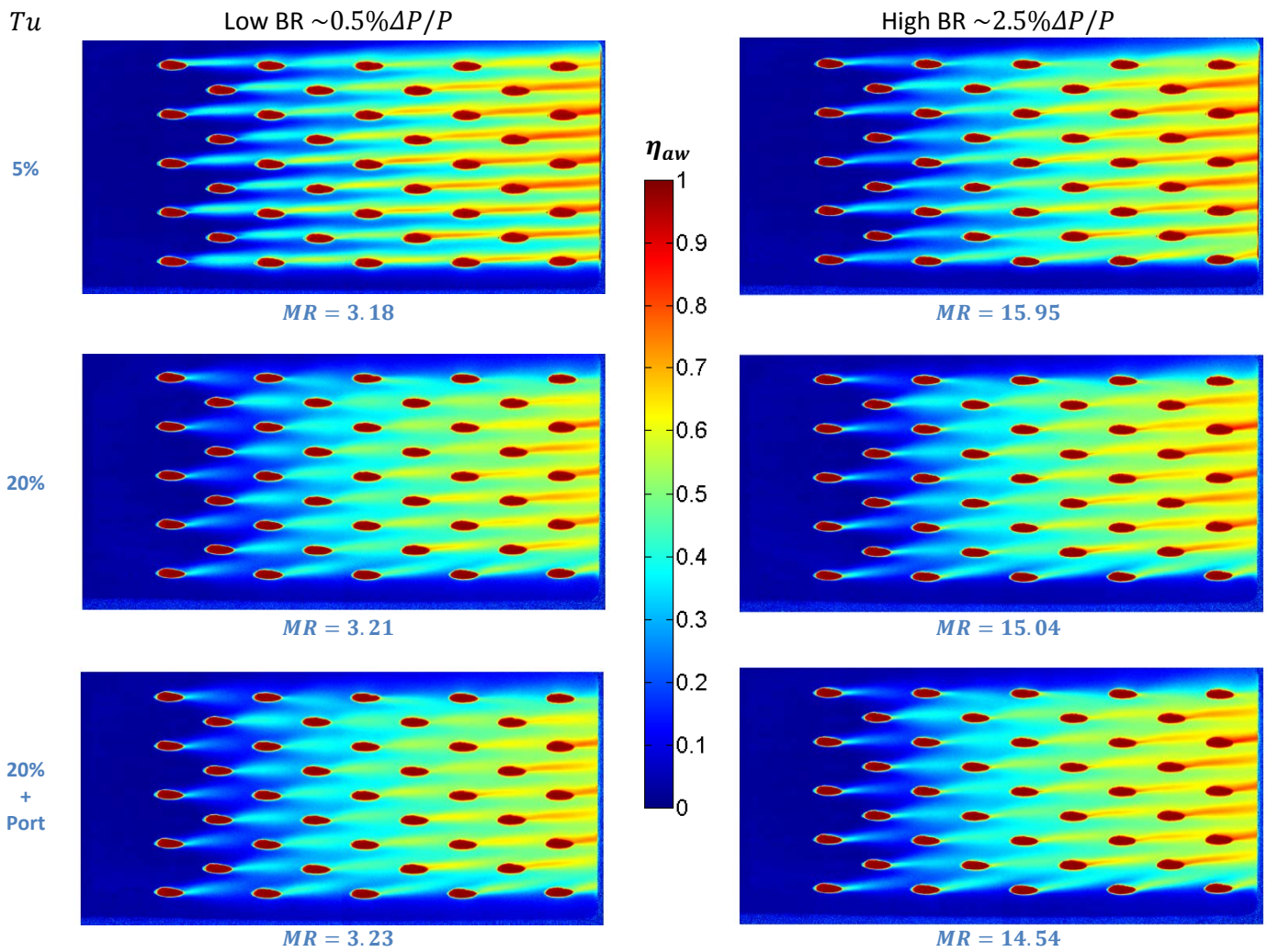
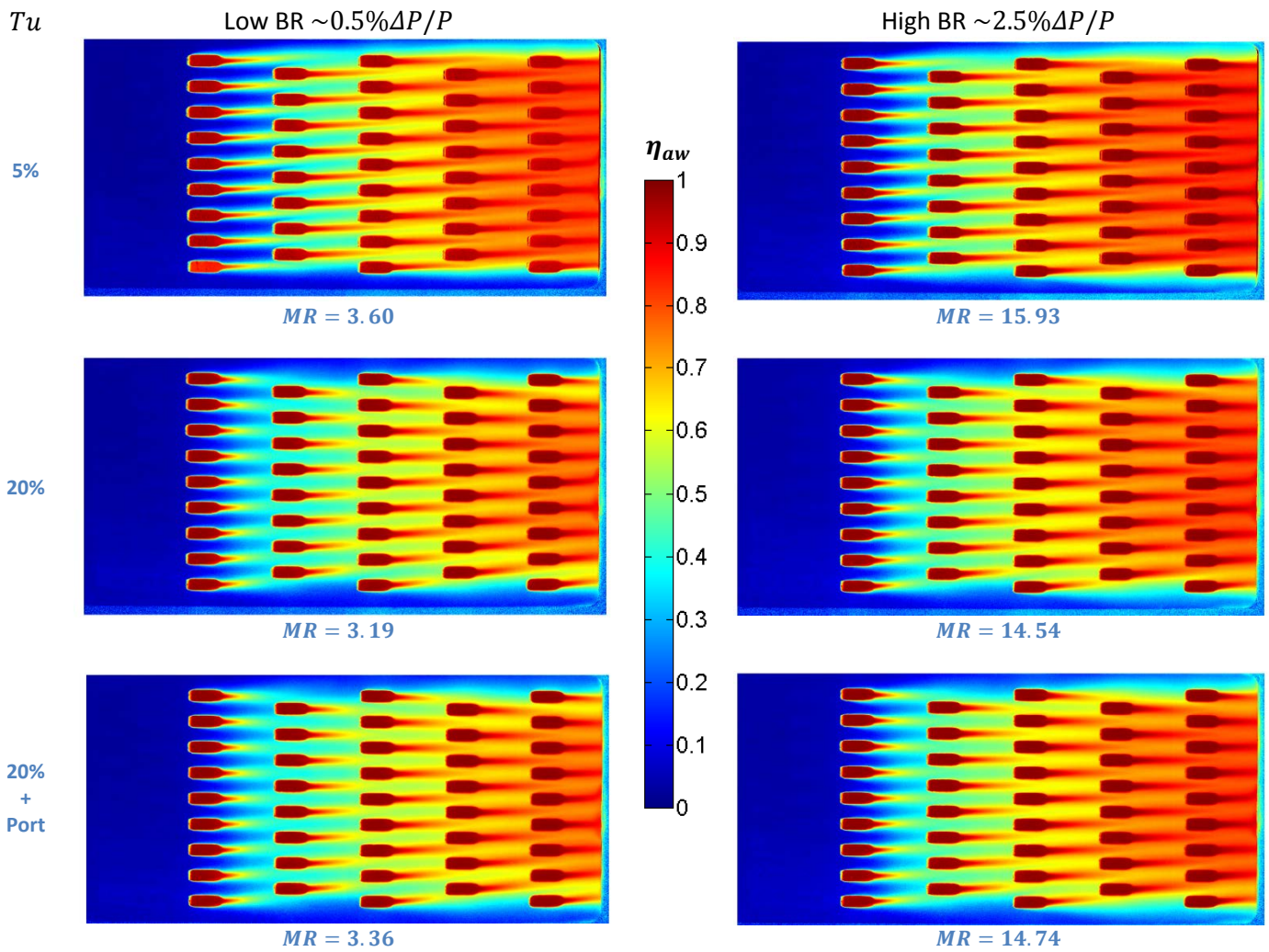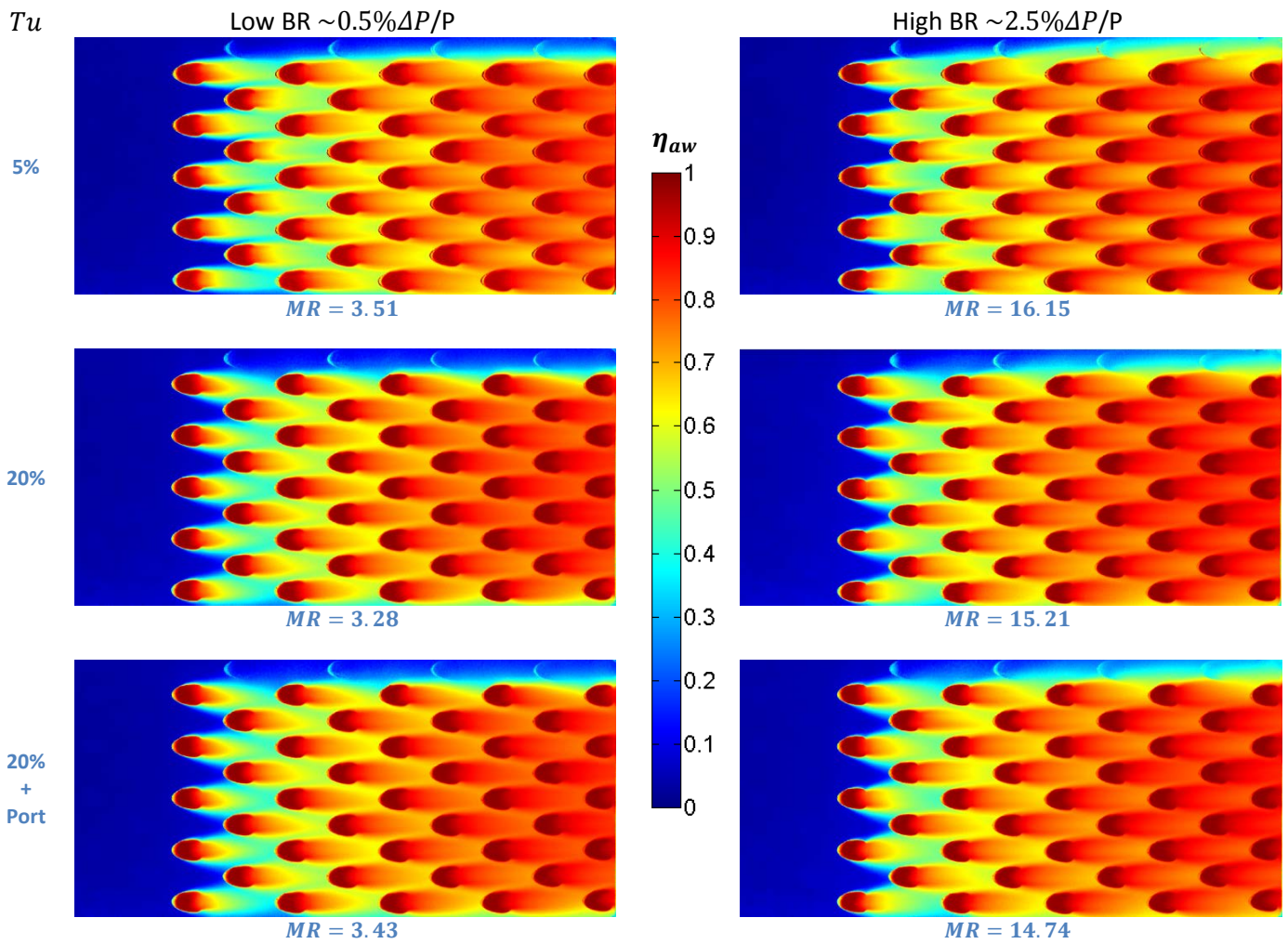**Figure 71 – Circular Helix adiabatic film effectiveness at various turbulence and momentum ratio conditions**
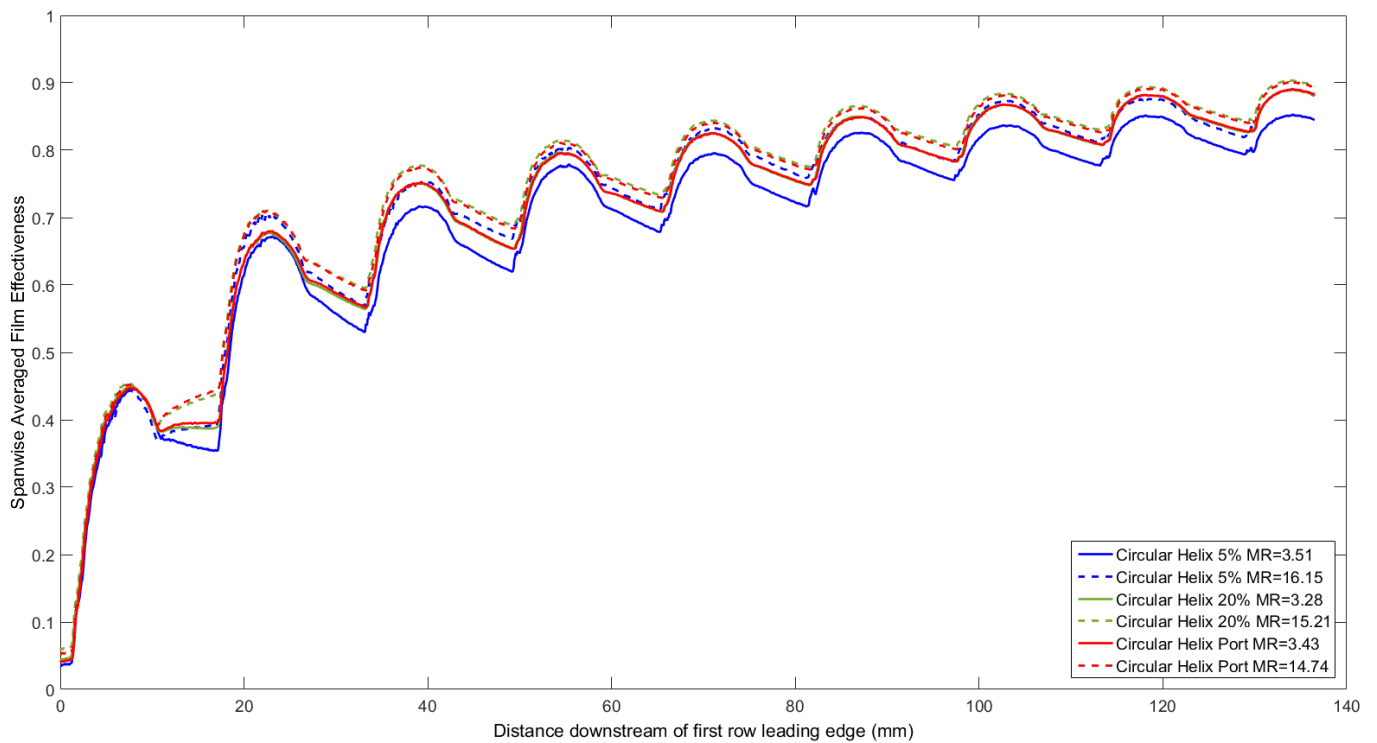
Figure 72 – Circular Helix spanwise averaged adiabatic film effectiveness at varying freestream turbulence levels

5.1.2 Effect of Coolant Momentum Ratio

Surface maps and spanwise averaged adiabatic effectiveness plots are presented for all test plates at the five momentum ratio conditions and for the highest freestream turbulence intensity level of 20%. Data for the remaining 5% turbulence condition is presented in Appendix A.1. In this section the sensitivity of the surface film to momentum ratio is investigated. As expected, increasing the momentum ratio across the plate generally increases the cooling effectiveness as more coolant is injected. Introducing more coolant however can result in diminishing returns in terms of adiabatic film effectiveness, with a larger difference between the two lowest blowing conditions than for the two highest. The differences between high and low momentum ratio are relatively small and difficult to identify when looking at the 2D surface film effectiveness contours but become more apparent when considering the spanwise averaged data.

5.1.2.1 *Cylindrical Effusion Geometry*

Figures 73 and 74 show the adiabatic film effectiveness results for the cylindrical hole case at the 20% turbulence intensity condition. The cylindrical hole design shows a slight increase in spanwise averaged effectiveness between the first and third rows at the lowest momentum ratio condition. By close inspection of the 2D surface contours it can be seen that this is due to the coolant spreading laterally over the surface downstream of the first two rows of coolant holes and is thought to be a result of the lower jet velocity. By the third row the jets begin to interact and the cooling patterns look similar between conditions, with the higher momentum ratio conditions showing slightly higher absolute effectiveness levels as a result of increased amounts of coolant being introduced. This results in the divergence of the spanwise averaged film effectiveness plots with distance along the plate. The maximum difference in spanwise averaged film effectiveness between highest and lowest momentum ratio conditions is 0.03 towards the trailing edge of the plate.

5.1.2.2 *Spey Fan Effusion Geometry*

The 2D adiabatic film effectiveness surface contours and spanwise averaged results for the Spey fan geometry at the 20% turbulence intensity condition are presented in Figures 75 and 76. From the surface contours it can be seen that there are no major differences in coolant distribution between conditions. It is also noted from the spanwise averaged plot that the four highest momentum ratio conditions show almost equal performance within the bounds of

uncertainty, indicating that the maximum performance of this geometry is reached at a relatively low blowing ratio. The maximum difference in spanwise averaged effectiveness between the lowest and highest flow conditions is 0.02 towards the end of the plate. The 2D surface contours indicate this small difference is a result of a slightly reduced extent of the coolant in the streamwise direction at the lowest momentum ratio condition. Subtle differences are visible between the four highest momentum ratio conditions and these are most pronounced at the edges of the plate, with a slightly wider spreading pattern visible as the blowing ratio increases.

5.1.2.3 Modified Fan Effusion Geometry

Figures 77 and 78 show data collected for the Modified fan geometry at the 20% turbulence intensity condition. This geometry shows more variation between momentum ratio conditions than the other designs, with a maximum difference in spanwise averaged effectiveness of 0.07 in the area between the second and third cooling hole rows. This large difference is a result of the greater streamwise extent of the coolant at increased coolant blowing ratio and where the coolant does not mix in with the mainstream air as rapidly. As distance along the plate increases, the fresh coolant air mixes with the air of previous rows and increasing momentum ratio simply increases the effectiveness of the already established cooling film. This results in a reduction in difference between flow conditions until a maximum performance level for this geometry is reached, whereby further increasing the coolant flow rate has no appreciable effect. This is indicated by the spanwise averaged effectiveness plots where the measured data collapse onto a single line. This maximum appears to be at a momentum ratio of around 12, with the 11.94 and 13.83 conditions showing very similar effectiveness distributions from the first row onwards. The difference between momentum ratio conditions reduces as distance along the plate and hence number of cooling rows increases, with similar performance seen from row 5 onwards at momentum ratio conditions of 6.22 and higher.

5.1.2.4 Slotted Effusion Geometry

The Slotted geometry adiabatic film effectiveness 2D surface contours and spanwise averaged results at the 20% turbulence intensity condition are shown in Figures 79 and 80. This is another design which shows noticeable variations in spanwise averaged film effectiveness between momentum ratios, with maximum difference between the $MR = 3.15$ and 14.54 conditions of 0.06 between rows 2 and 4. This is clearly seen in the surface contours where the

streamwise extent of the coolant increases with momentum ratio. Due to the increased longitudinal distance between successive cooling hole rows the coolant jet has more opportunity to mix by turbulent diffusion before being replenished by the next row. As a result, the difference in spanwise averaged film effectiveness between low and high momentum ratio conditions decreases much more slowly than for the other array patterns. Once again as the momentum ratio increases the improvement in cooling effectiveness reduces until a maximum is reached, in this case the spanwise averaged performance data collapses at a momentum ratio of ≈ 12.5, equivalent to a wall pressure drop at engine conditions of $\Delta P/P$ of 2%.

5.1.2.5 Circular Helix Effusion Geometry

Figures 81 and 82 show the 2D surface contours and spanwise averaged adiabatic film effectiveness for the Circular Helical geometry at the 20% turbulence intensity condition for various momentum ratio settings. From this data it can be seen that the performance of the Circular Helical geometry shows similar trends to the Spey fan geometry, with the spanwise averaged performance quickly reaching its maximum effectiveness value at a momentum ratio of 6.30, equivalent to $\Delta P/P$ of 1% at engine conditions, with only a small difference of around 0.03 between the highest and lowest momentum ratio conditions after the second row. This value reduces as distance along the plate increases. Results are more spread out between the first and second cooling hole rows with a maximum difference in spanwise averaged effectiveness of 0.05. Looking at the surface contours this change appears to be attributable to the greater mass of coolant exiting the hole and remaining attached to the surface resulting in a larger area of high effectiveness behind each cooling hole. Another feature of note is the positive gradient in spanwise averaged effectiveness between rows 1 and 2. From the surface contours, this appears to be an effect of the gradual divergence of the fanned section encouraging spanwise spreading of the coolant to the point where coolant has almost filled the space between holes by the point at which the second cooling hole row is reached. This combines with the lower exit velocity which maintains the coolant closer to the surface, reducing the fall in streamwise performance resulting in an overall increase in spanwise averaged performance. With the exception of the area downstream of the first row and at the lowest momentum ratio condition, performance at the other conditions is almost identical within the bounds of uncertainty, with the only noticeable change in surface distribution occurring at the edges of the array where the increasing mass of coolant shows greater lateral mixing.

5.1.2.6 Rectilinear Helix Effusion Geometry

Surface contours and spanwise averaged adiabatic effectiveness plots are given in Figures 83 and 84 for the Rectilinear Helical geometry at a turbulence intensity of 20% and over a similar range of coolant flow conditions. This geometry reaches a maximum performance level at a momentum ratio of 8.52, equivalent to an engine $\Delta P/P$ of 1.5%, with a maximum difference in performance between highest and lowest momentum ratio conditions of 0.03 after the second row. Again the performance between the first and second rows shows slightly more variation between conditions than downstream of the second row. Through interrogating the surface contours it can be seen that this is a result of increasing lateral spreading of the coolant at increased momentum ratio conditions resulting in a larger width of surface covered. As the second row of holes fills the voids remaining by the first row, this increased spreading is met by the newly emerging coolant.

The results obtained for this design show increased effectiveness in the region leading up to the first row of cooling holes, the effectiveness measured in this area should be at or very close to zero, however for this set of results this is not the case, with effectiveness indicated at just below 0.1. This is not a real effect as it is not possible for the adiabatic effectiveness in this region of the flow to be greater than zero, instead it is likely caused by some other error source, either illumination inconsistency between images or the test not quite running isothermal throughout as a result of the performance of the inline heater used when heating the coolant gas. In either case this increases the measured intensity of the paint emission and therefore the measured adiabatic effectiveness. However, this increased intensity has reducing effect at increasing adiabatic effectiveness levels due to the inverse relationship between intensity ratio and partial pressure ratio of the paint. Therefore, due to the high levels of adiabatic effectiveness measured for this geometry this small increase in intensity has little impact on the measured effectiveness downstream of the second row of cooling holes.

Figure 73 - Cylindrical hole adiabatic film effectiveness at various momentum ratio conditions and $Tu = 20\%$

Figure 74 - Cylindrical hole spanwise averaged adiabatic film effectiveness at various momentum ratio conditions and $Tu = 20\%$
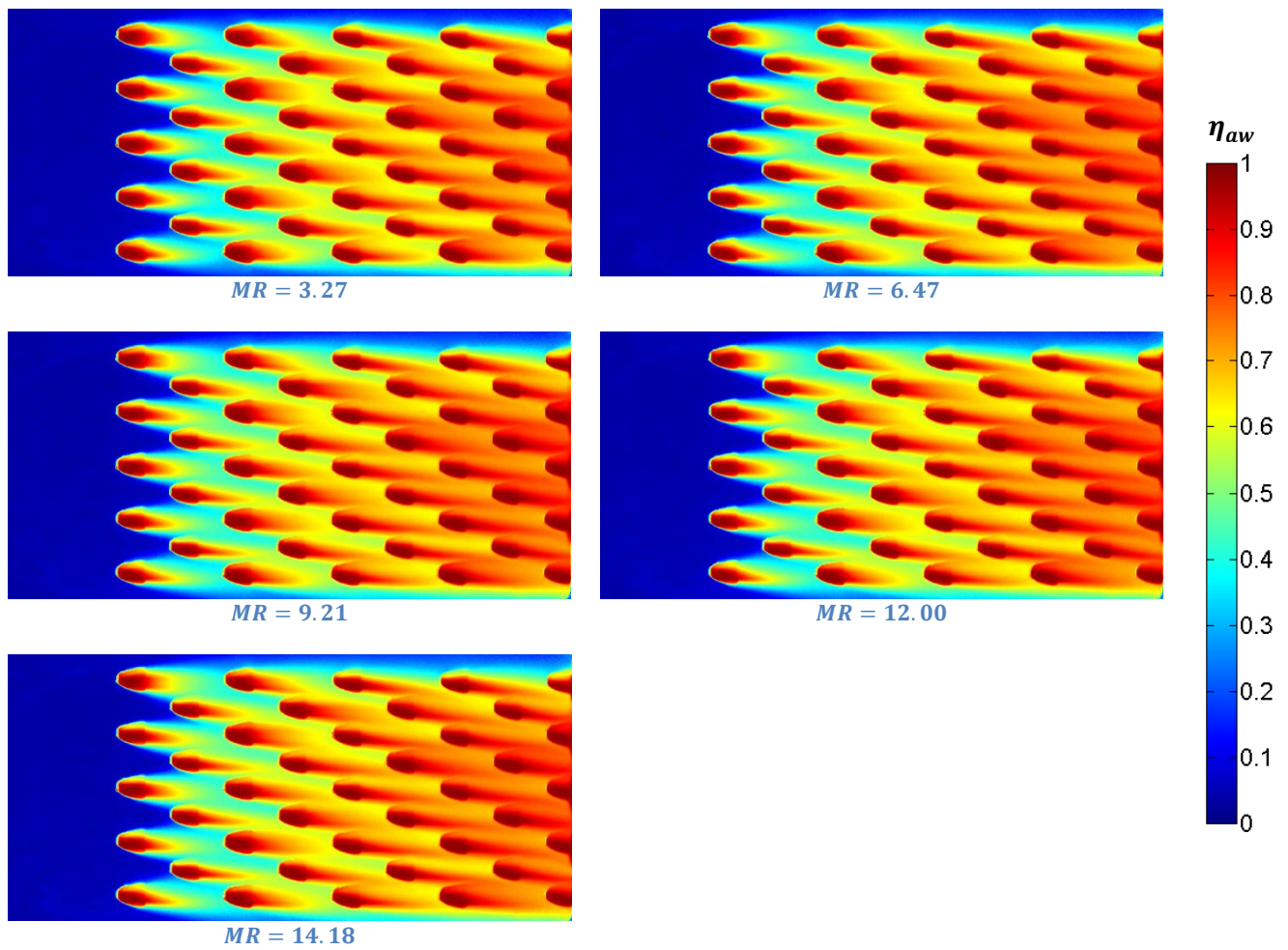
Figure 75 – Spey fan adiabatic film effectiveness at various momentum ratio conditions and $Tu = 20\%$
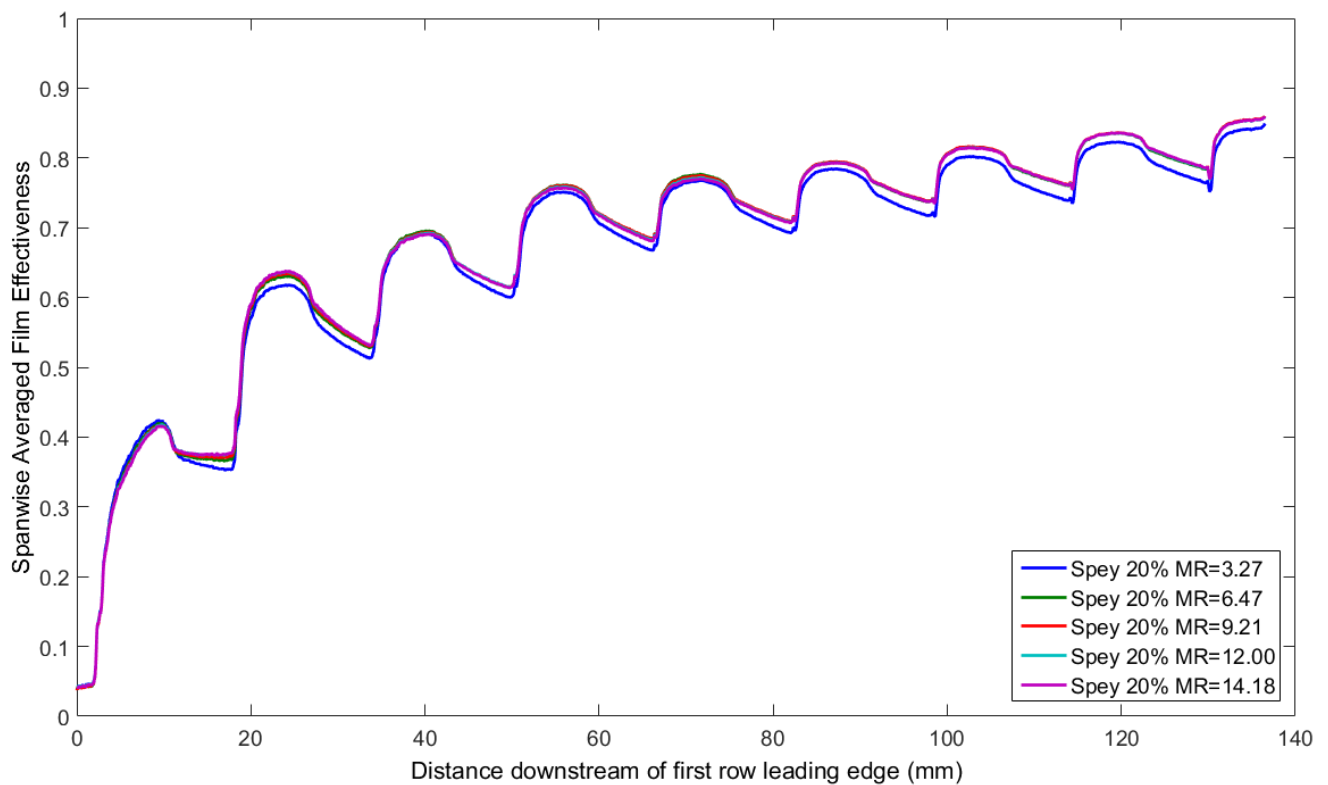
Figure 76 – Spey fan spanwise averaged adiabatic film effectiveness at various momentum ratio conditions and $Tu = 20\%$
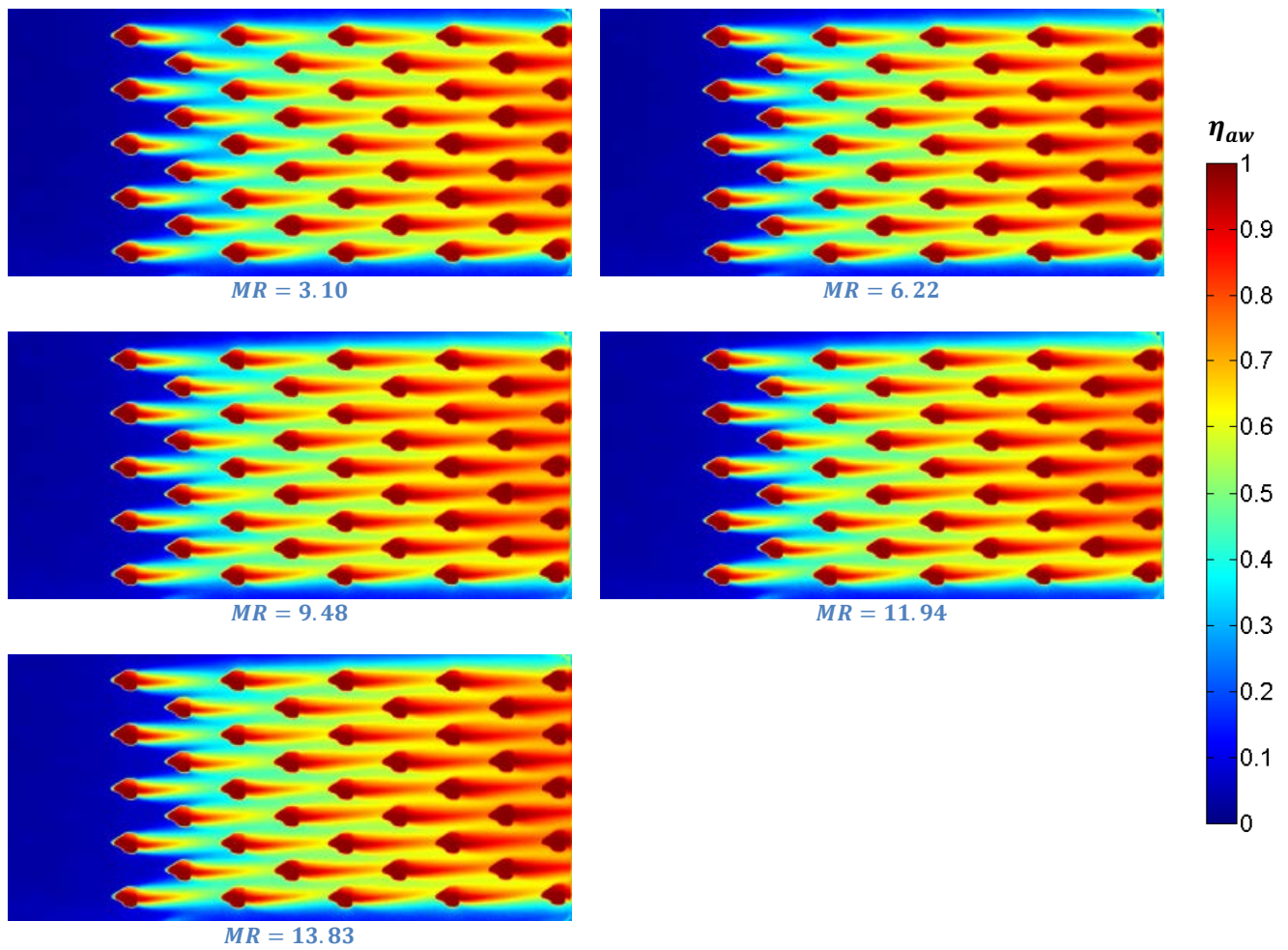
Figure 77 – Modified fan adiabatic film effectiveness at various momentum ratio conditions and $Tu = 20\%$
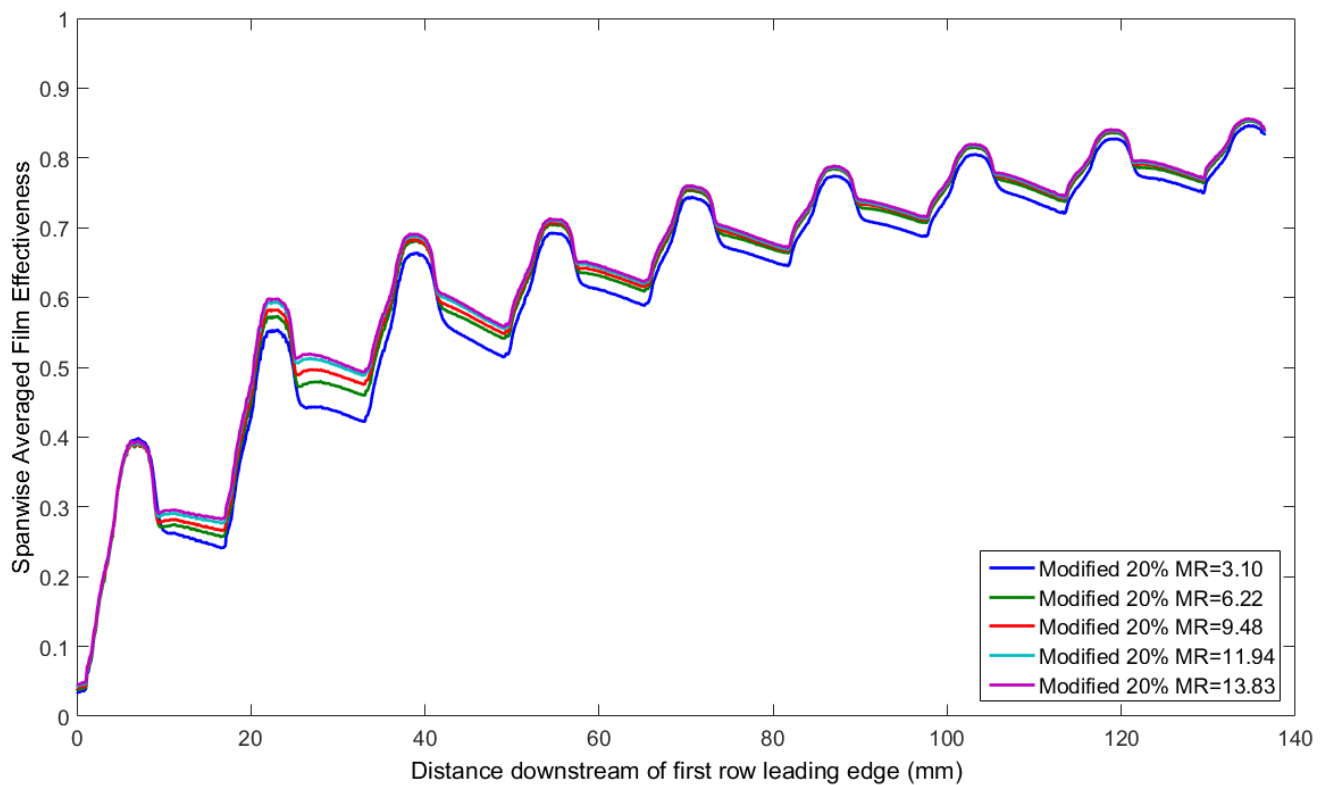
Figure 78 – Modified fan spanwise averaged adiabatic film effectiveness at various momentum ratio conditions and $Tu = 20\%$

Figure 79 - Slotted adiabatic film effectiveness at various momentum ratio conditions and $Tu = 20\%$
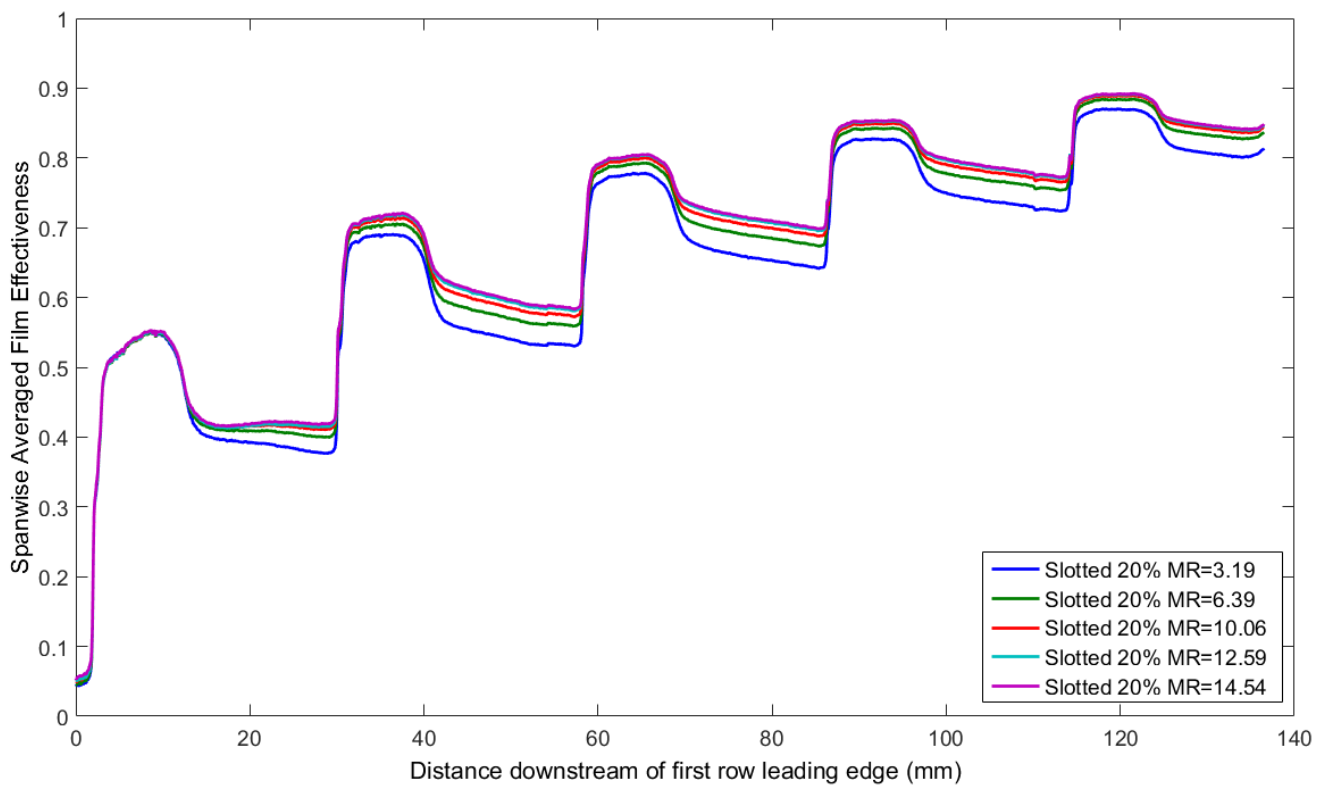
Figure 80 - Slotted spanwise averaged adiabatic film effectiveness at various momentum ratio conditions and $Tu = 20\%$

$MR = 3.28$

$MR = 6.30$

$MR = 9.65$

$MR = 11.95$

$MR = 15.21$
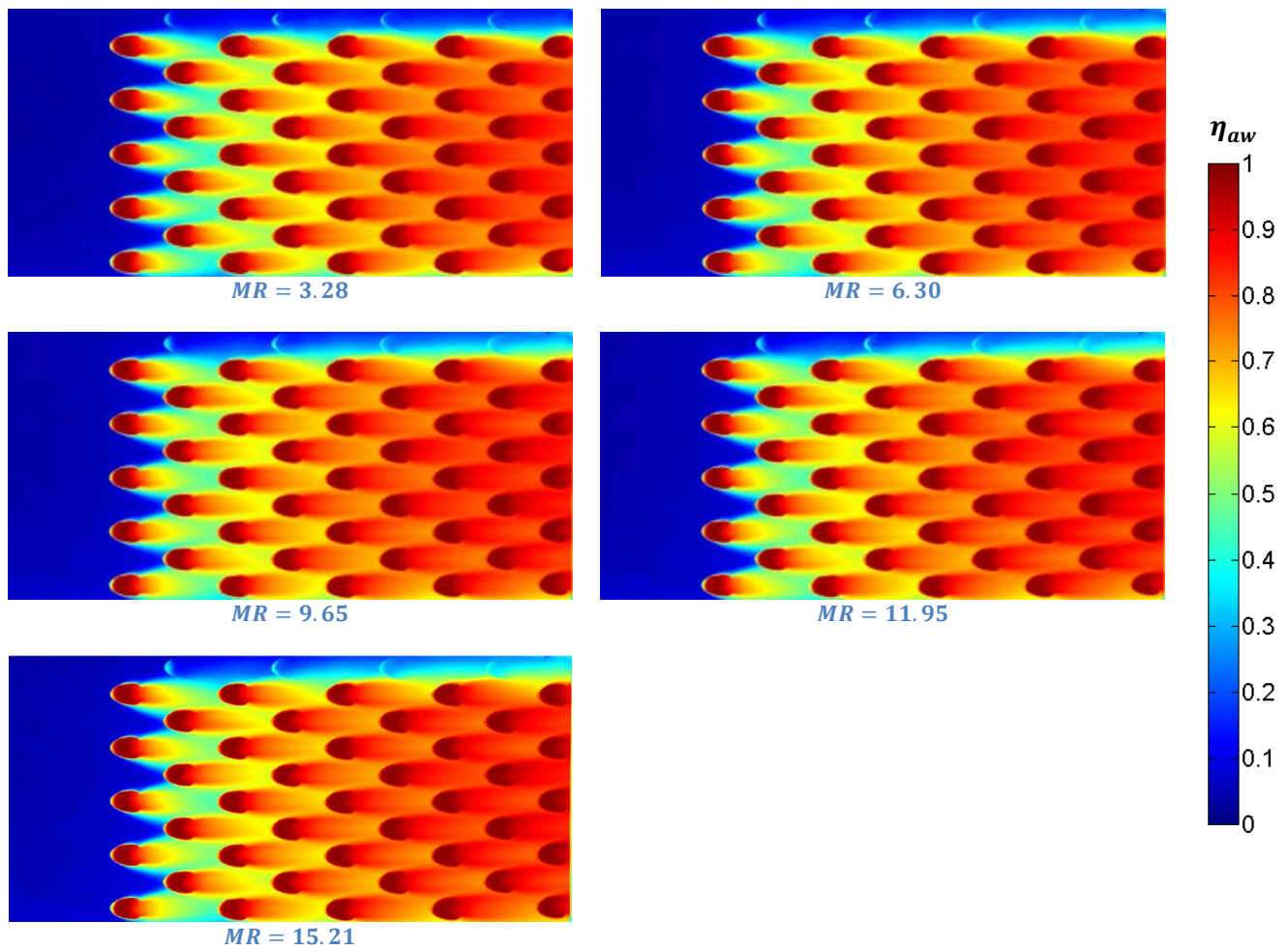
Figure 81 – Circular Helix adiabatic film effectiveness at various momentum ratio conditions and $Tu = 20\%$
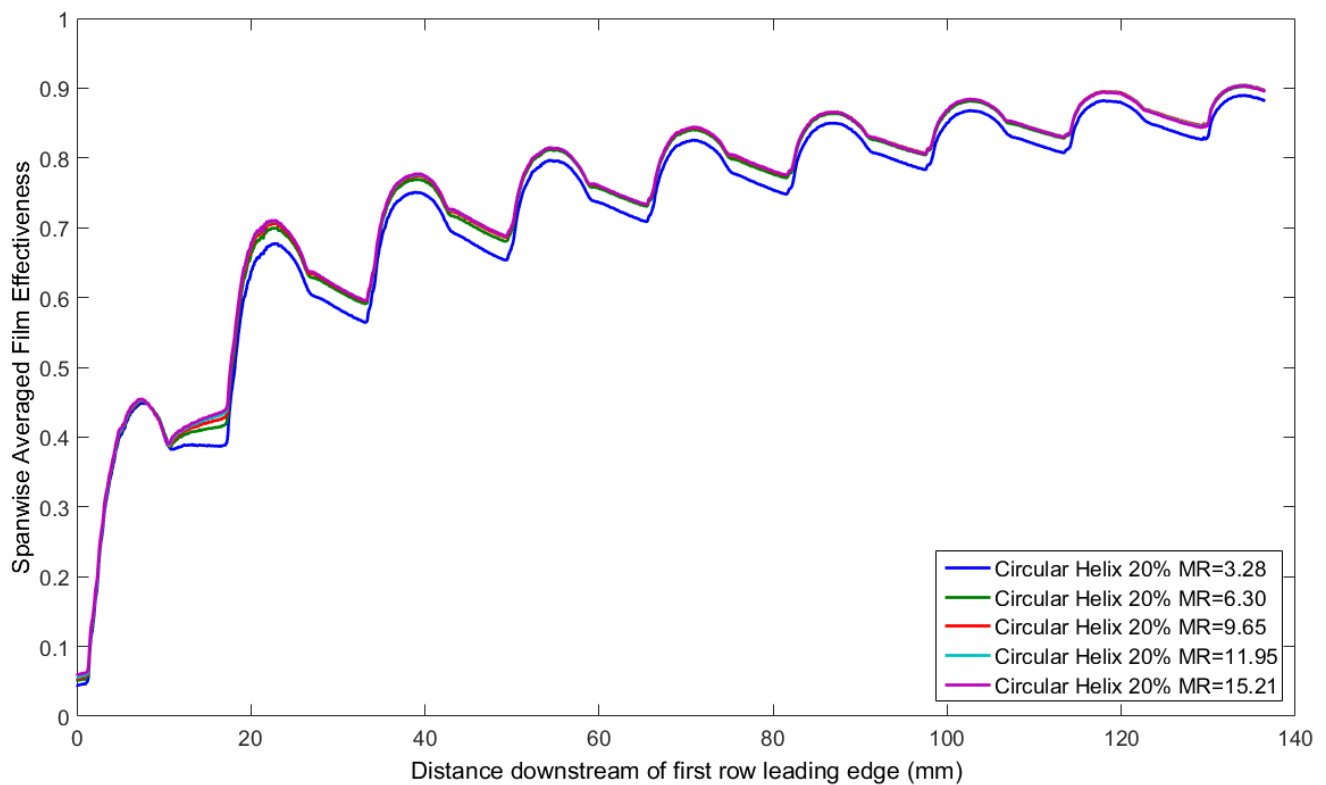
Figure 82 – Circular Helix spanwise averaged adiabatic film effectiveness at various momentum ratio conditions and $Tu = 20\%$
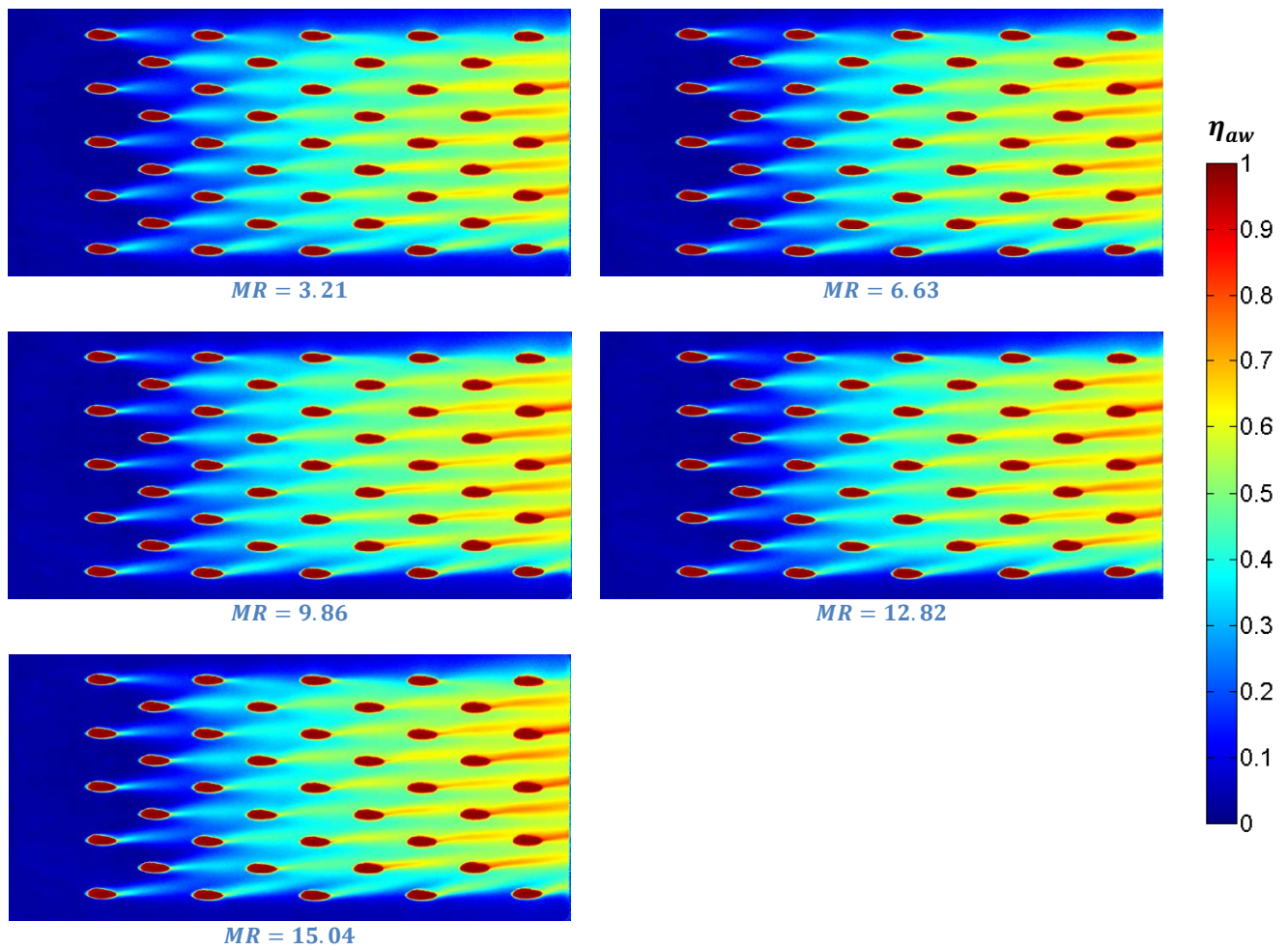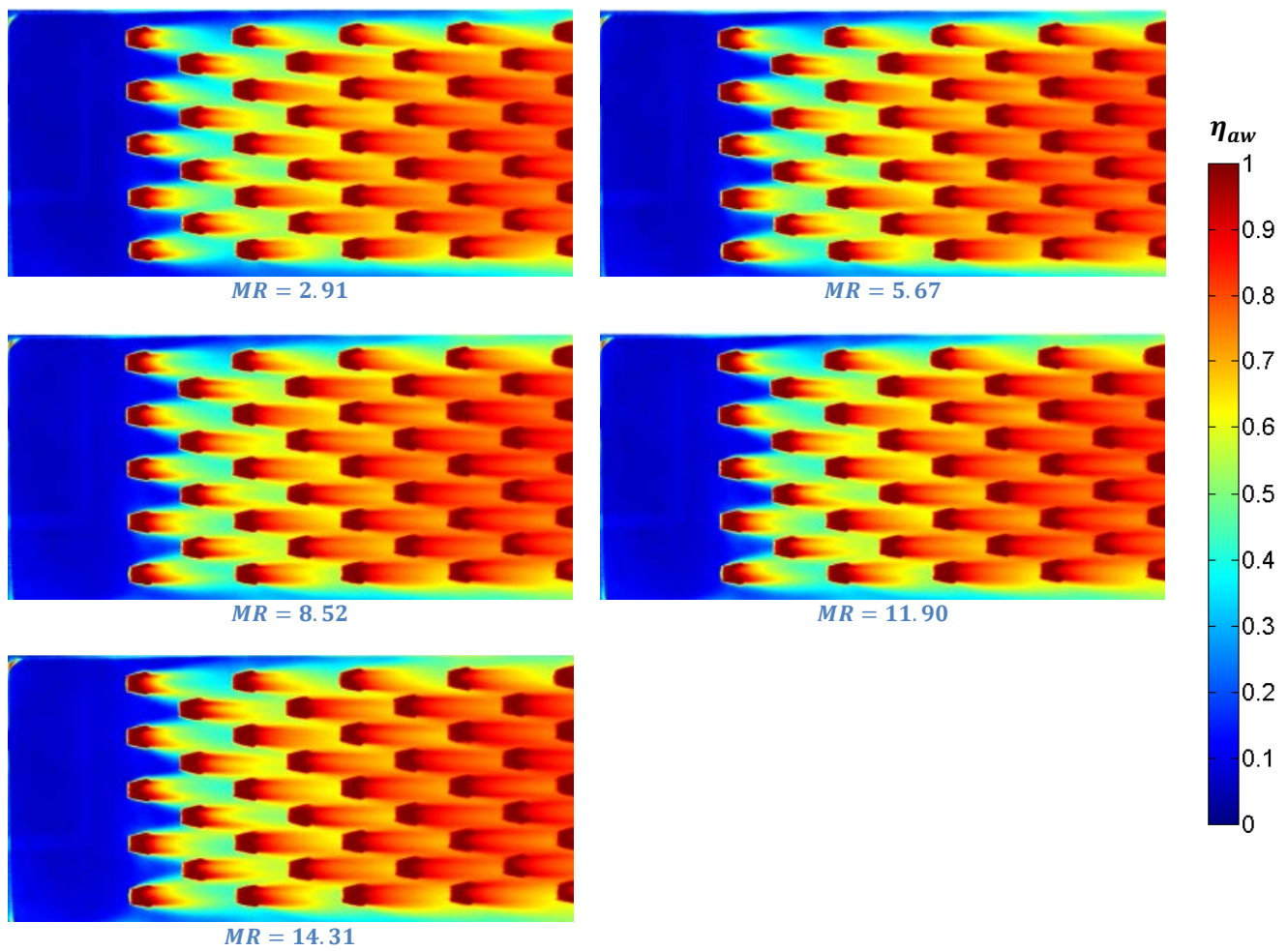
Figure 83 – Rectilinear Helix adiabatic film effectiveness at various momentum ratio conditions and $Tu = 20\%$
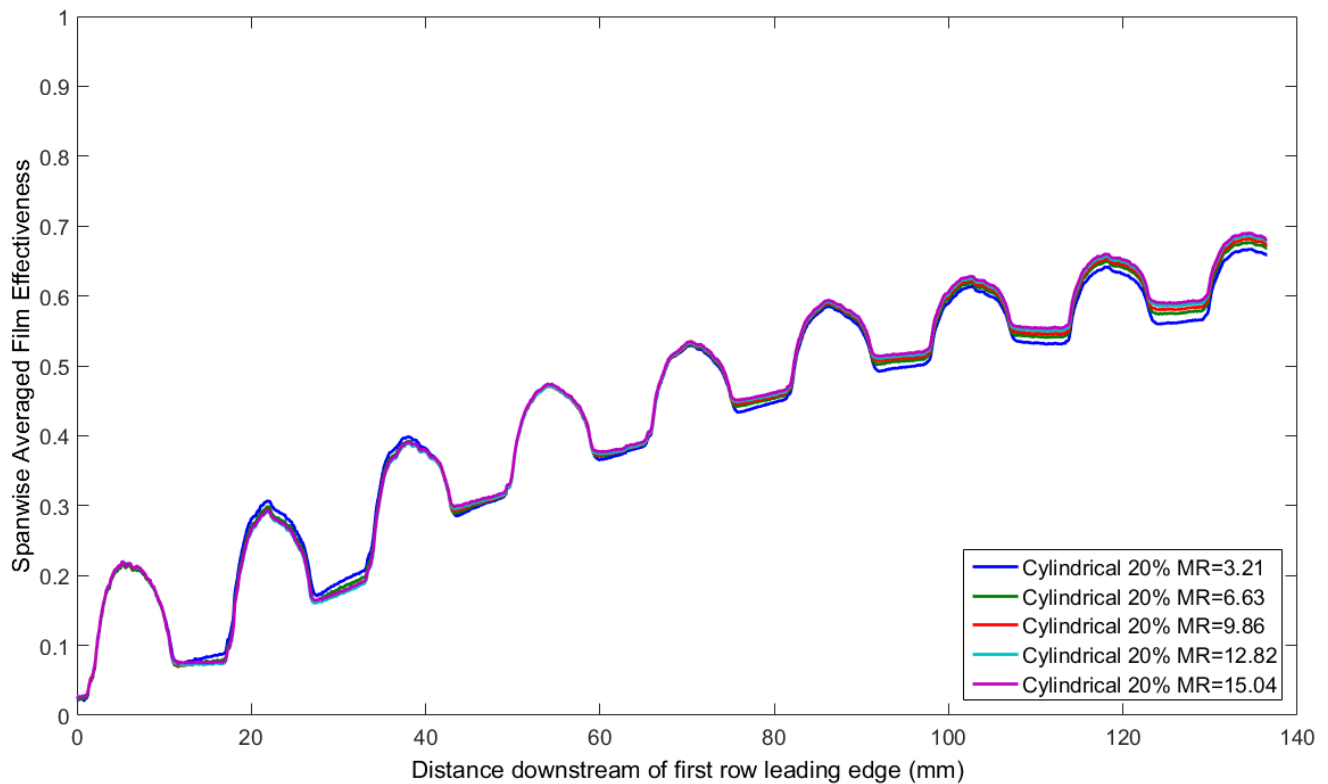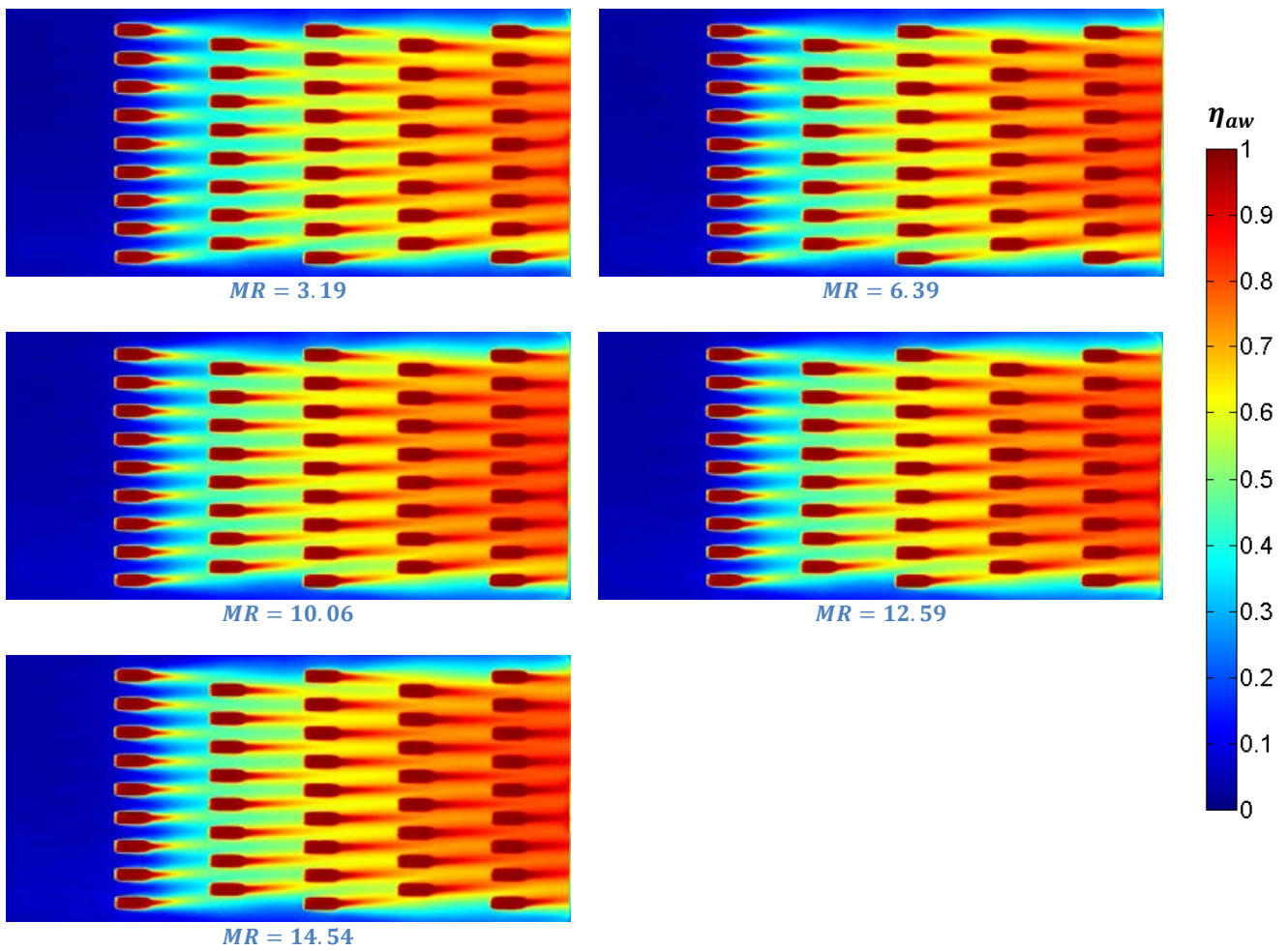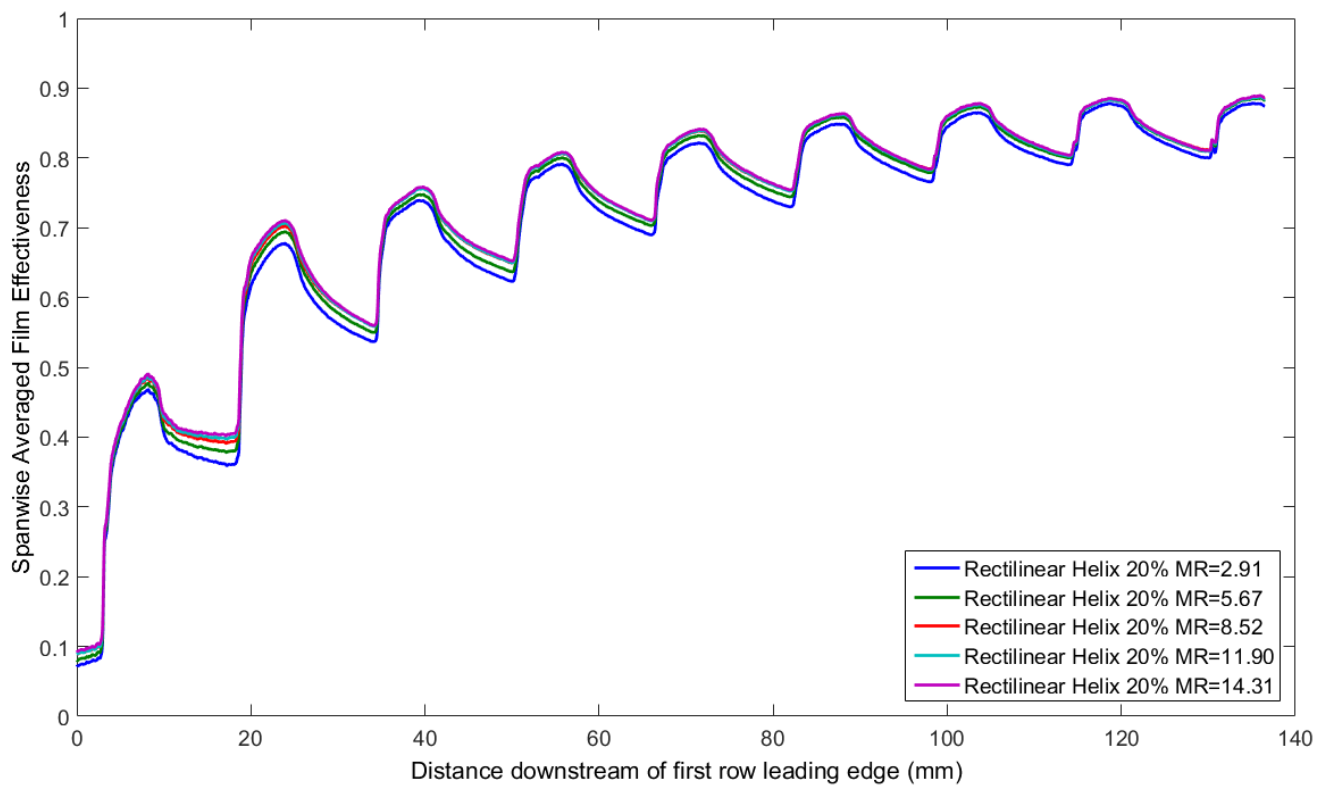

Figure 84 – Rectilinear Helix spanwise averaged adiabatic film effectiveness at various momentum ratio conditions and $Tu = 20\%$

5.1.3   Effusion Hole Geometry

In this section the adiabatic film effectiveness performance of the different hole geometries are compared directly. Due to differences in the design and manufacture of each test plate over time the first row of cooling holes are not located in the same place in all designs, with the cylindrical holes starting closer to the upstream edge of the test plate than the other designs. For direct comparison purposes therefore, the spanwise averaged data in each case are shifted so the leading edge of the first row of hole exits are always located at the same point. The geometries are compared at the high freestream turbulence intensity condition and at the highest and lowest momentum ratio conditions equivalent to wall pressure drops of 0.5% and 2.5% at engine cycle conditions. Surface contour data for the $\cong 15$ momentum ratio condition is given in Figure 85 and a spanwise averaged plot in Figure 86, similar data for the $\cong 3$ momentum ratio condition is given in Figures 87 and 88.

It is immediately apparent that all of the more complex geometries produce a superior film to the Cylindrical hole case at all observed conditions, with the Cylindrical design only reaching a spanwise averaged effectiveness of 0.5 by the last row of the cooling array. In comparison to the remaining geometries which reach this level by the second row of coolant holes. The major factor causing this superior performance is the tendency for the coolant to remain close to the surface through a reduction in jet velocity as a result of flow diffusion within a fan-like geometry located at the effusion hole exit. Through fanning the exit and reducing the jet velocity the actual blowing and momentum ratios are reduced, a factor which is critical to creating a good film. A second contributor to the increased performance comes as a result of ensuring the coolant covers a wider lateral area; the two methods of accomplishing this are lateral fanning of the hole exit, as employed by the Spey, Modified, Circular and Rectilinear Helical geometries, and decreased lateral pitch, as used by the Slotted geometry. Both methods give rise to much better coolant coverage from the first row onwards.

As the coolant delivery holes in the Slotted design are more tightly packed in the lateral direction, a smaller surface area is exposed to the mainstream flow. This gives rise to the much higher spanwise averaged adiabatic effectiveness of 0.5 in line with the first row as roughly half the area is taken up by the coolant holes. This then drops to around 0.4 as the coolant jet spreads over the surface before being replenished by the second row. In order to keep the plate porosity consistent with the other designs, the longitudinal spacing of the holes is

increased, resulting in the coolant having to cover a larger streamwise area before being augmented by the successive row. As a result, despite starting at a higher initial average adiabatic film effectiveness than the other designs, the Slotted geometry is out performed by all the laterally fanned designs as their second row of coolant is injected much sooner, allowing the film to be more incrementally enhanced. The lack of lateral fanning results in much less spanwise spreading of the coolant after exiting the hole resulting in a much less uniform effectiveness pattern.

From the 2D surface contours it can be seen that the Spey and Modified fanned geometries suffer from poor hole definitions caused by the DLD manufacturing technique. Due to the inherent build direction there is an obvious asymmetry within the holes of both these and the cylindrical hole test plates. The other test plates indicate no obvious signs of asymmetric manufacture on the surface contour data. The Slotted geometry is designed with an asymmetric inlet and flow passage which appears to minimise the effect of build direction. Any exit flow asymmetry for the Slotted or Helical designs is a result of the asymmetrical design of the flow passages. Insensitivity to build direction is an important feature of any DLD enabled design.

The two helical geometries show a slight bias towards one side of the fanned section; this is thought to be due to the direction of the internal helix presenting the fan with a biased flow at its entry. It can also be seen that despite similar span averaged results, the Rectilinear Helical design shows a less uniform surface effectiveness distribution than the Circular Helical geometry with the coolant favouring the corners of the fan. The performance of these two designs is similar with the Circular Helical design showing slightly better spanwise averaged performance over the majority of the plate. The spanwise averaged plot for the rectilinear design shows that the area upstream of the first coolant hole is at a higher effectiveness level of 0.1 compared to the other designs which are all in the region of 0.02-0.05. This is thought to be a result of either illumination inconsistency between images or slight temperature difference of the plate surface. This has the effect of increasing the spanwise average upstream of and in line with the first row of cooling holes and as a result, the data for the rectilinear design appears to be higher than the Circular Helical case. In the absence of this effect the performance of the two designs in this region is considered to be comparable.

The Spey, Slotted, Circular and Rectilinear Helical designs all show similar performance after the first row with spanwise averages of around 0.35-0.4 but with the Circular Helical design showing slightly better performance than the other geometries. The Modified fan design returns around 0.3 in this area. This design is hampered by the lack of lateral spreading of coolant as it emerges from the plate due to the very low divergence angle of the fanned portion of the hole. A similarly reduced spanwise averaged effectiveness would be expected of the Slotted design had the lateral spacing of the holes been in line with the other hole arrays.

As number of cooling rows increase the importance of the internal geometry and fan design become apparent as the Spey design diverges from the two helical geometries. This indicates that the exit velocity from the hole and hence jet penetration into the mainstream flow are an important factor in determining the maximum film effectiveness of a given array. Due to the increased pressure drop within the internal length of the helical geometries the flow has less momentum as it emerges from the hole and hence cannot penetrate as far into the mainstream flow. Thus increasing the proportion of coolant remaining close to the wall and hence film effectiveness. The fans of the helical designs have also been defined with reduced fan angle compared to the Spey geometry and as a result, the coolant fills the fan more successfully, avoiding coolant separation within the fanned section. Conversely the Modified fan does not diffuse aggressively enough to promote spanwise spreading of the coolant and as a result shows poorer distribution of coolant than the other laterally fanned geometries.

It is also worth noting that the porosity of the Spey fan is reduced compared with the other geometries as a result of the flat spot created during manufacture, resulting in a reduced amount of coolant emerging from the holes compared with the other designs. However, as seen in the previous section, this design is insensitive to coolant flow rate at the range of momentum, ratio conditions considered, therefore this decreased porosity is unlikely to have much effect on the ranking of this design in terms of adiabatic effectiveness.
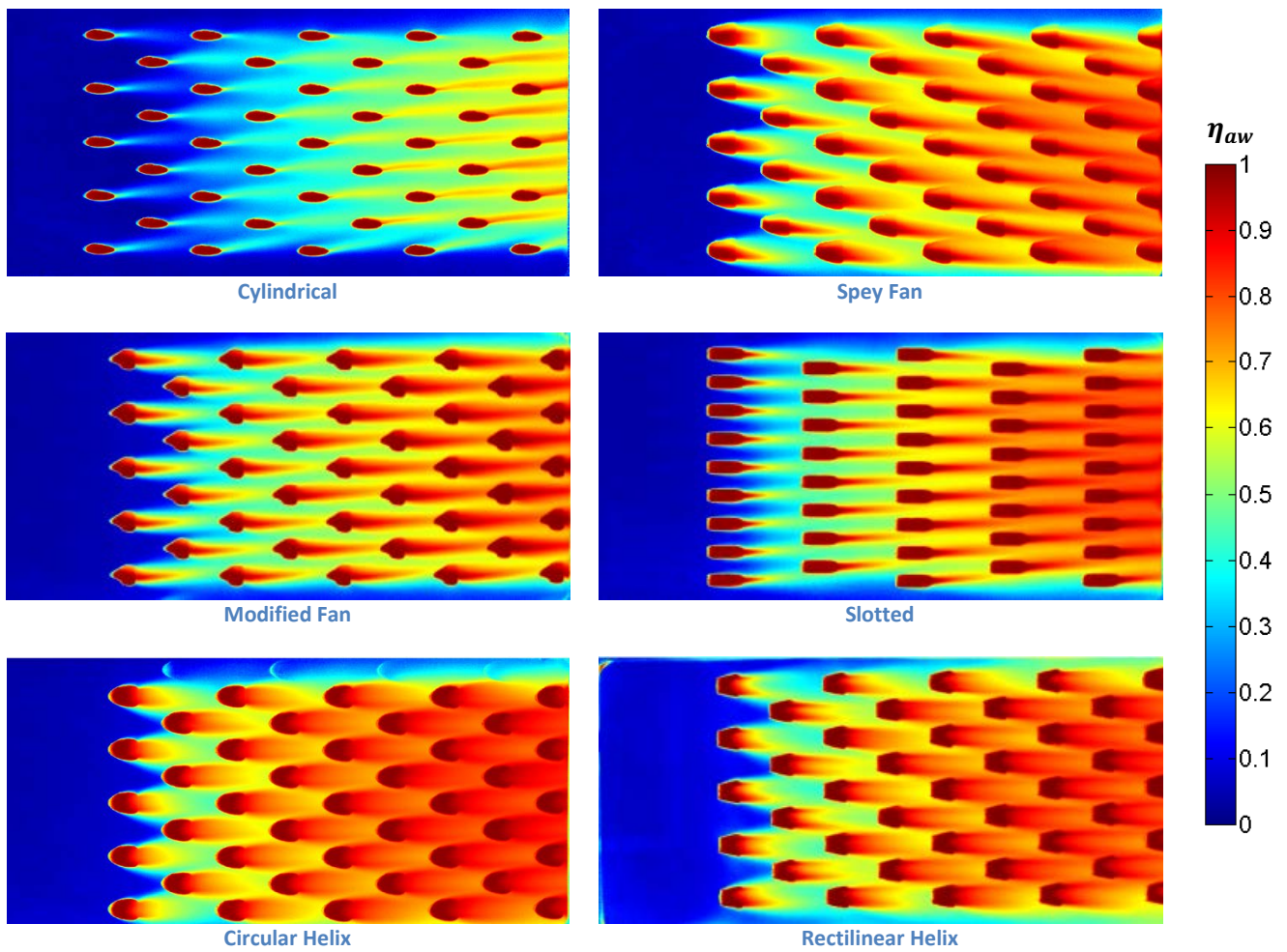
Figure 85 – Geometry comparison of adiabatic effectiveness surface map, $MR \cong 15$ and $Tu = 20\%$
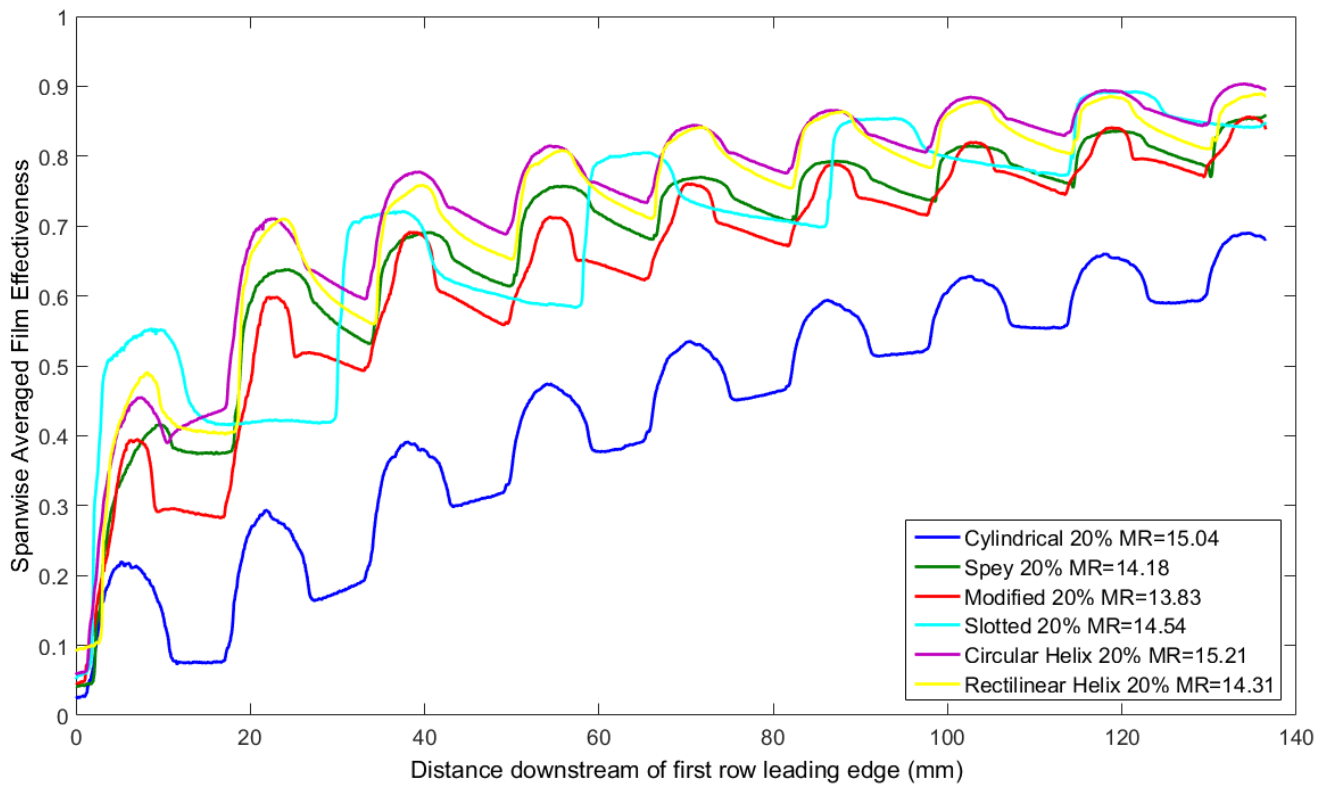
Figure 86 – Geometry comparison of span-wise averaged adiabatic effectiveness, $MR \cong 15$ and $Tu = 20\%$
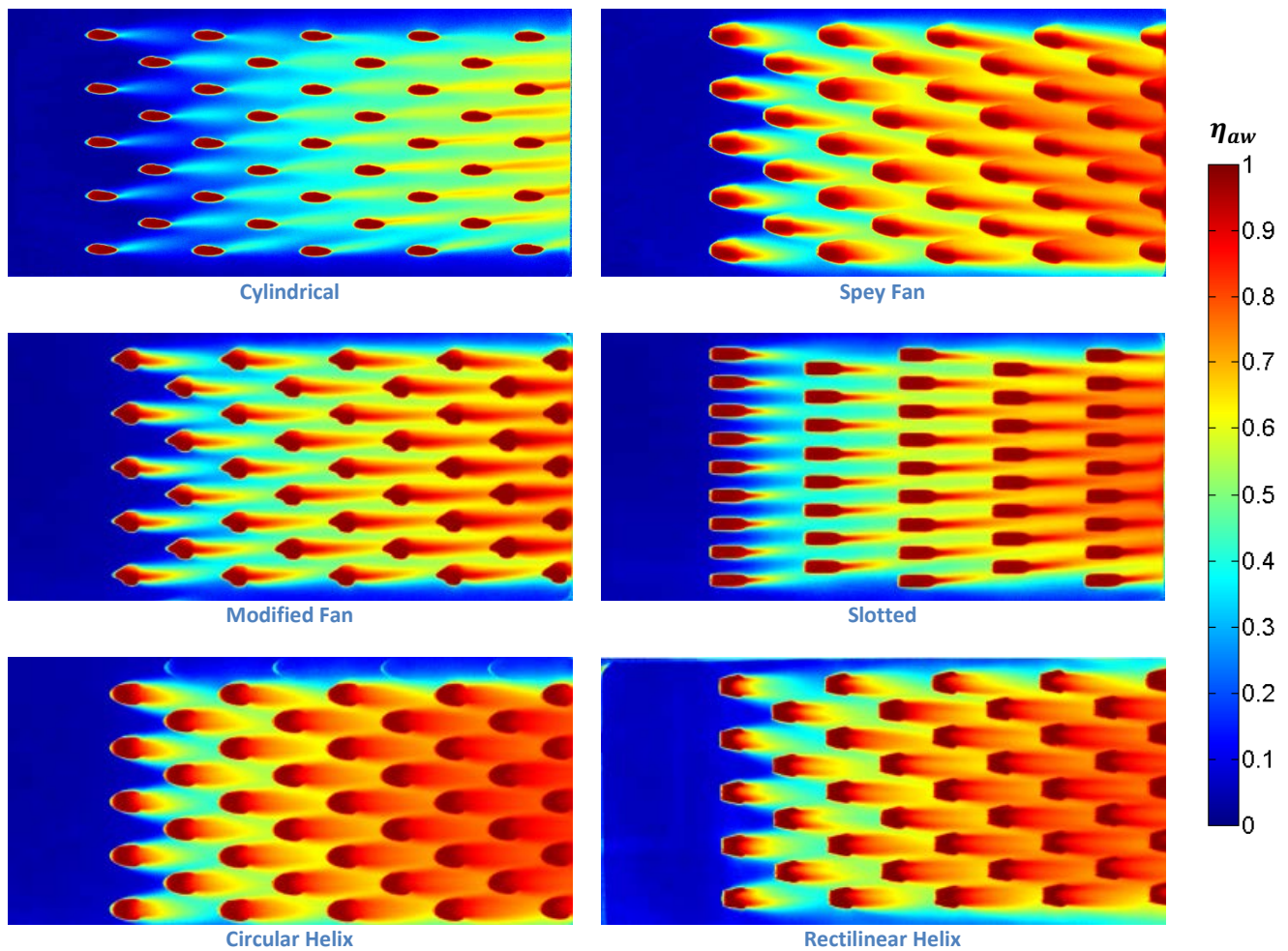
Figure 87 – Geometry comparison of adiabatic effectiveness surface map, $MR \cong 3$ and $Tu = 20\%$
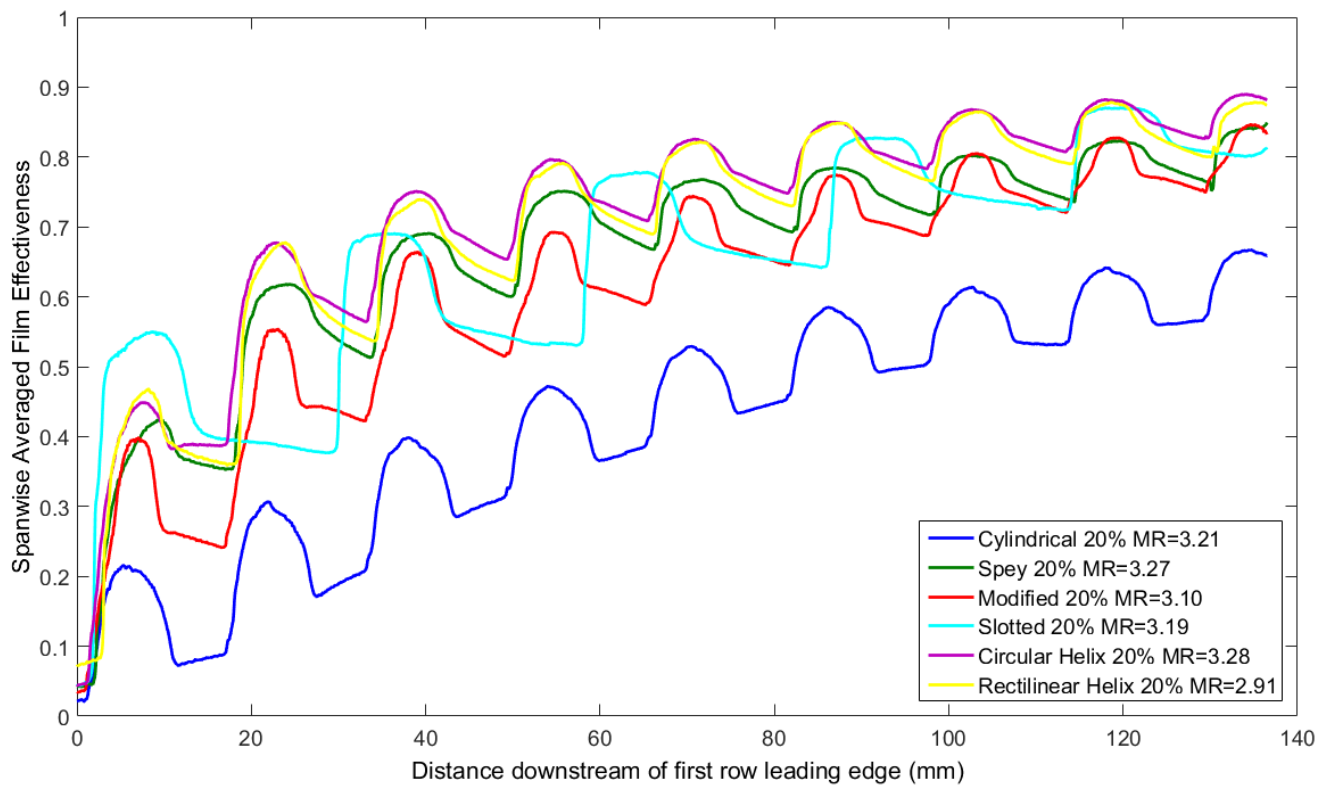
Figure 88 – Geometry comparison of span-wise averaged adiabatic effectiveness, $MR \cong 3$ and $Tu = 20\%$

5.2   Overall Effectiveness Measurement – IR Thermography

Overall effectiveness is a measure of the actual metal temperature of the wall and through careful scaling it is possible to conduct rig scale experiments to infer representative metal temperatures at engine cycle conditions. A number of the major heat transfer mechanisms present in the engine are included in these experiments, including the cooling film providing the hot side convective heat transfer driving temperature, conduction through the metal wall together with the internal effusion geometry providing a convective heat transfer path out of the wall and into the cooling flow passing through the passages. The radiative loads associated with the combustion flame are not accounted for in these experiments, nor is the convective heat transfer caused by cold side cross flow within the feed annuli surrounding the combustor.

In order to understand the influence a number of parameters have on the overall effectiveness and hence the metal temperature, experiments directed at the effect of freestream turbulence levels, momentum ratio and cooling passage geometry are conducted on the 6 test plates previously discussed.   As the adiabatic film effectiveness results show little discernible difference is caused by the blockage characteristics of a mixing port, this test condition is not repeated for the overall effectiveness measurements. Results are again presented as both 2D surface contours of the overall effectiveness and spanwise averaged over the same central strip as illustrated earlier in Figure 62. Surface contours for the highest and lowest momentum ratio conditions at the two freestream turbulence conditions are presented in every other numbered figure from Figure 89 to Figure 100 with spanwise averaged plots presented in the remaining figures in this number range.   The only exception to this is the Rectilinear Helical geometry which was only tested at the 20% freestream turbulence intensity condition. Surface contours for all tested conditions are also presented in Appendix A.2.

5.2.1   Freestream Turbulence

Spanwise averaged plots of overall effectiveness are presented below with solid lines representing the lower 5% turbulence case and the dashed lines representing the higher 20% turbulence intensity condition. Unlike with the adiabatic film effectiveness results, freestream turbulence intensity has a notable effect on overall effectiveness with all tested geometries showing a decrease in overall effectiveness at the higher turbulence condition. However, from the adiabatic film effectiveness study it can be seen that the driving temperature is not necessarily increased, with the Spey and Circular Helical geometries showing increased film

effectiveness and hence reduced gas temperature at high turbulence levels and low blowing ratios. Therefore the increase in metal temperature must be due to the increased heat transfer coefficient on the plate surface caused by the increased turbulent flow intensity. This indicates that while no difference was seen in the adiabatic effectiveness results when the port blockage simulant was used, the associated increase in freestream turbulence intensity level might have a strong influence on overall effectiveness. This also shows that adiabatic effectiveness alone is not enough to fully characterise the cooling of the wall under a convective heat load, with further information of HTC distribution required to give better understanding of actual wall temperatures.

5.2.1.1 *Cylindrical Effusion Geometry*

From the 2D surface contours of overall effectiveness presented in Figure 89 it can be seen that through increasing the freestream turbulence level the maximum effectiveness decreases. From interrogation of the spanwise averaged results, there is a maximum decrease in the overall effectiveness of around 0.03 and which is consistent for all coolant flow rates. The data from the two turbulence conditions remains roughly equal up until around the second row of cooling holes, at which point the data begin to diverge, with the effectiveness of the low turbulence conditions continuing to rise steadily along the plate length before reaching a maximum around the seventh row. Performance then falls as the end of the array is reached and no more coolant holes are present to remove heat from within the wall. A similar trend is found at low momentum ratios and high turbulence. However as the flow rate increases at high turbulence levels, a double peak is seen in the spanwise averaged data coinciding with a second patch of higher effectiveness between the first and second rows; this is believed to be caused by a local increase in HTC after the second row. As the film performance of the cylindrical hole is relatively poor, the local temperature in this region is still high but through introducing the coolant into the mainstream, the flow downstream of the injection site is more unsteady causing an increase in local HTC as seen by Martin. (57) The combination of increased local HTC with poor coolant coverage results in an area of increased heat transfer into the plate and hence higher local surface temperatures. As the coolant film builds up, the increase in local HTC is offset by the cooler driving temperature and the heat transfer is decreased again, reducing the plate temperature downstream of the 4th row.

5.2.1.2 Spey Fan Effusion Geometry

At the lowest momentum ratio the overall effectiveness of the Spey fan geometry is relatively unaffected by the freestream turbulence intensity, with both distributions of spanwise averaged overall effectiveness almost collapsing. However the adiabatic film effectiveness plots at the same conditions show a difference in driving temperature, particularly towards the end of the plate. From this it may be surmised that the contribution to heat transfer caused by turbulent mixing of the coolant and its reduction in the driving temperature is roughly equal to the increase in HTC caused by the same process. At higher momentum ratios the adiabatic film effectiveness is not affected by the increased turbulence levels, therefore the increased HTC causes the heat transferred into the wall to be increased and hence reduces overall effectiveness by up to 0.02.

5.2.1.3 Modified Fan Effusion Geometry

As the adiabatic film performance of the Modified fan shows little sensitivity to freestream turbulence intensity at all of the coolant flow conditions here, the overall effectiveness results indicate that once again the increased HTC on the surface caused by the local turbulent conditions has the effect of reducing the overall effectiveness and increasing the wall temperature. At the lowest momentum ratio the difference between low and high turbulence cases is around 0.02, rising to 0.03 at all other cooling flow conditions.

5.2.1.4 Slotted Effusion Geometry

As for the cases above, the effect of increasing the freestream turbulence intensity is to reduce the overall effectiveness. The Slotted design showed reduced adiabatic film effectiveness at increased turbulence levels, resulting in a difference in overall effectiveness of 0.031 at the lowest coolant flow condition reducing to 0.026 at the highest momentum ratio. This reduction in difference is a result of the reduced effect of freestream turbulence on the adiabatic film performance at higher coolant momentum ratios. A double peak similar to that found in the cylindrical case data is also seen in the spanwise averaged plot, indicating a similar increase in local HTC downstream of the first row of coolant holes in an area where cooling film performance is poor. This is supported by the 2D surface contours of the high turbulence, high flow condition where clear streamwise streaks are visible downstream of each of the cooling holes. Here film performance is locally good enough to compensate for the increased HTC caused by the introduction of coolant onto the surface. However in the area between coolant

holes where the film is poor, the localised temperature is higher and so the spanwise average is lower than the area upstream of the first row. In these regions the internal heat removal is high enough to reduce the temperature of the plate before the coolant has been introduced and the HTC augmented.

5.2.1.5 Circular Helix Effusion Geometry

The Circular Helical design also follows the same trend of reduced overall effectiveness at increased freestream turbulence levels. The only exception being at the lowest momentum ratio where the increased turbulence case shows slightly higher spanwise averaged overall effectiveness up to the seventh row of coolant holes. The adiabatic film effectiveness shows a similar trend at this same blowing condition, with the spanwise average increasing from the 5% to the 20% turbulence intensity condition. Therefore the difference in overall effectiveness is attributed to the difference in gas temperature at the wall driving the convective heat transfer. The performance difference between high and low turbulence conditions increases with increasing momentum ratio up to a maximum of 0.015.

5.2.2 Effect of Coolant Momentum Ratio

In addition to improvements in the film performance discussed in the previous section, increasing the wall momentum ratio and hence coolant flow rate through the cooling passages removes more heat from the wall internally. Since conventional effusion cooling designs rely on simple straight through holes, little of the cooling potential of the coolant air is utilised. The DLD process allows the internal passages to be designed in such a way as to increase the amount of heat removed by the coolant through more complex internal flow passages before being ejected onto the surface to form the protective film layer. This section identifies how altering the wall momentum ratio influences the overall effectiveness as measured on the hot-side surface. Referring to the adiabatic effectiveness plots discussed earlier, it can be seen that for the majority of designs tested a maximum film performance is reached at a momentum ratio of ≈ 6, equivalent to a liner pressure drop of $1.0\%\ \Delta P/P$ at the engine cycle conditions considered here. Therefore, any difference in overall effectiveness at the higher flow rates must be attributable to the internal heat removal mechanism. Overall effectiveness data will collapse onto a single line as the maximum cooling potential of a given solution is reached. Spanwise averaged results are shown in odd numbered figures from Figure 90 to 100 alongside the 2D surface contours at the highest and lowest momentum ratio conditions. All surface

contours are also presented in Appendix A.2. Values quoted in the following sections relate to the 20% freestream turbulence intensity case only.

5.2.2.1 Cylindrical Effusion Geometry

Adiabatic film effectiveness shows little sensitivity to momentum ratio at the conditions tested. However, there is a notable increase in overall effectiveness as momentum ratio increases. This increase is therefore a result of increased HTC over the surface of the cooling holes within the wall. By increasing the effusion wall blowing ratio, the velocity of the flow through the passages is increased which in turn increases the transfer of heat from the wall and into the coolant through forced convection. From Figure 90 it can be seen that the greatest increase occurs between the lowest two blowing conditions, with the difference in peak spanwise averaged effectiveness reducing from around 0.02 for the lowest to about 0.003 (within the margin of uncertainty) for the highest momentum ratio condition. This suggests a state of diminishing returns has been reached with further increases in coolant flow having little benefit. This optimum condition is the point at which relatively good film coverage is achieved. However, upstream of the first row of cooling holes there is a large difference between all coolant flow conditions. Since this is at the upstream edge of the array before any coolant has been introduced onto the surface, the major mechanism for heat removal is via the internal cooling passages and therefore the large difference between overall effectiveness indicates the performance benefits achievable through good internal cooling design.

5.2.2.2 Spey Fan Effusion Geometry

As indicated earlier, the adiabatic film effectiveness is largely insensitive to momentum ratio at the higher freestream turbulence levels and therefore the difference seen in overall effectiveness is caused by the removal of heat through the internal flow passages. The benefit of increasing blowing ratio is again subject to diminishing returns. The difference between peak spanwise averaged overall effectiveness values decreases from 0.018 for the lowest blowing ratio conditions to 0.002 (within the margin of uncertainty) for the highest. This difference is dependent on the adiabatic film effectiveness, with a larger difference notable in areas with relatively poor film coverage. In this particular case, upstream of the third row of cooling holes, where more heat is transferred into the wall and therefore can be removed by the internal flow passages.

5.2.2.3   Modified Fan Effusion Geometry

As for the Spey fan case, the same pattern is seen for the Modified fan geometry. With the relatively small sensitivity of film performance to momentum ratio, yet notable sensitivity of overall effectiveness, it may be concluded that the internal cooling performance is improved with increased momentum ratio.   Again this improvement in performance is subject to diminishing returns as the wall blowing ratio increases. The difference between peak spanwise averaged overall effectiveness at the lowest conditions is 0.03 and between the two highest conditions this improvement drops to 0.004 (within the margin of uncertainty).   Due to the increased lay angle from 17° to 21° of the holes in this design, the internal passage length is shorter than any of the other geometries tested.   As a result, the performance differences between blowing conditions are larger as the internal cooling mechanism is less efficient and therefore more sensitive to coolant flow rate.

5.2.2.4   Slotted Effusion Geometry

As seen in Figure 80, there is a noticeable difference in adiabatic film performance with momentum ratio for the Slotted design, particularly at the lower flow rates tested. However, due to the long passage lengths and wider Slotted cross section, the overall effectiveness difference between conditions is not as large as for the traditional cylindrical cross section geometries discussed previously. The differences in peak overall effectiveness are 0.016 and 0.002 (within the margin of uncertainty) between the two lowest and highest momentum ratio conditions respectively. This indicates that a good internal cooling geometry can compensate in part for a poorer cooling film coverage.

5.2.2.5   Circular Helix Effusion Geometry

The Circular Helical geometry is the first geometry to be designed to maximise the heat transfer through the internal flow passage. As a result, the overall effectiveness is high even at lower cooling flow rates, with a difference between the two lowest peak spanwise averaged values of 0.011 reducing to less than 0.001 (within the margin of uncertainty) for the two highest momentum ratio conditions. This very small difference suggests that the maximum potential of this geometry is reached at much lower momentum ratios than for the geometries discussed above. For example, the overall effectiveness data indicate the difference between the highest and second lowest conditions is less than 0.002, which is less than the margin of uncertainty. The performance difference up to the third row of cooling holes is much smaller than is

observed for those geometries discussed above, with no discernible difference between results at the two highest blowing rates.

5.2.2.6 *Rectilinear Helix Effusion Geometry*

The Rectilinear Helical geometry represents an attempt to further improve the contribution of internal heat transfer to the overall effectiveness performance through the use of a square cross section promoting stronger secondary flows. Examining the spanwise averaged plot of overall effectiveness it can be seen that this geometry shows similar performance to that of the Circular Helical design at all conditions. At the two lowest momentum ratio conditions, the difference between peak spanwise averaged overall effectiveness is 0.009, reducing to less than 0.002 (within the margin of uncertainty) between the two highest. As the adiabatic film effectiveness is more or less equal at all flow conditions, particularly the three higher blowing ratios, the data shows that this cooling system reaches its maximum potential at much lower flow rates than the more conventional straight through passages.
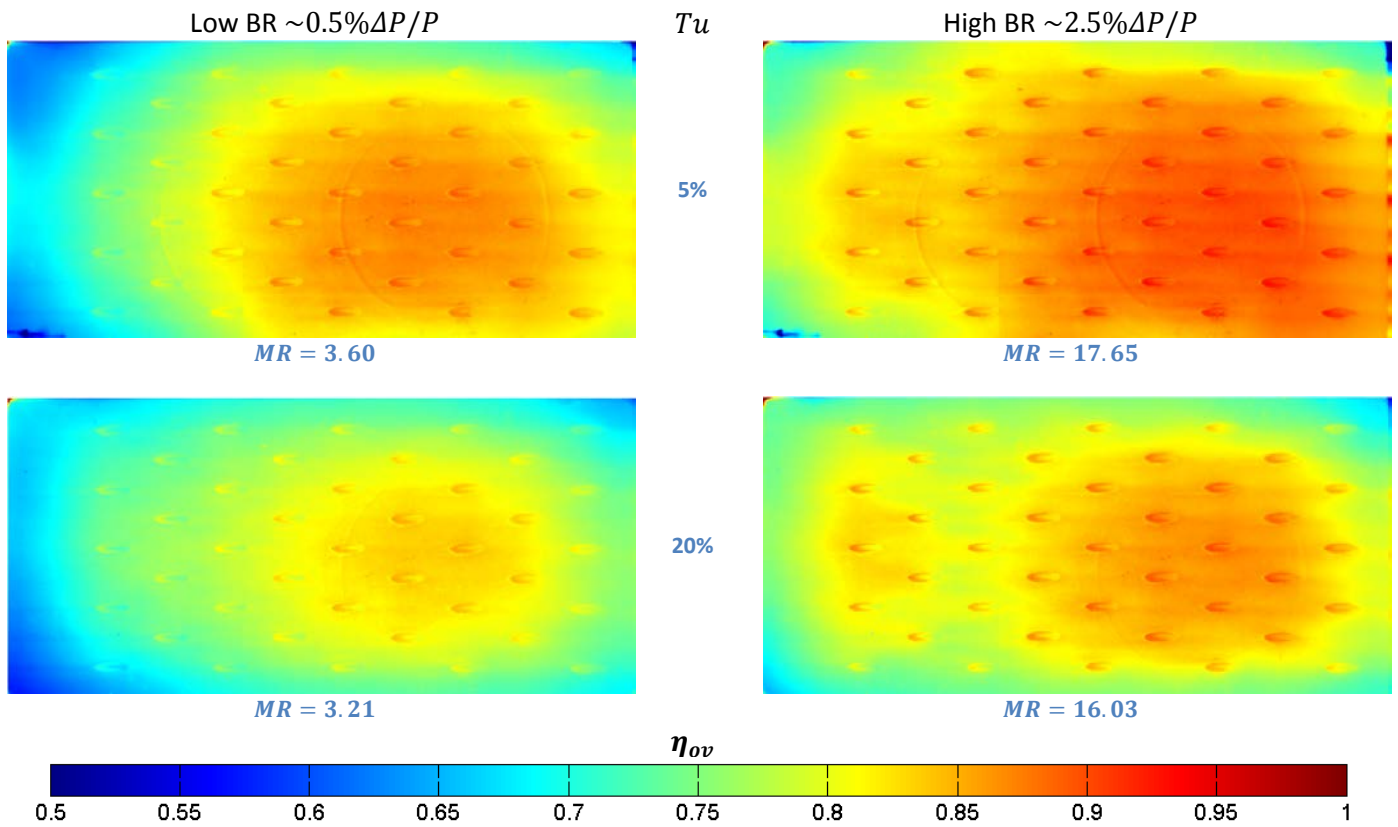
Figure 89 - Cylindrical hole overall effectiveness at various turbulence and blowing ratio conditions
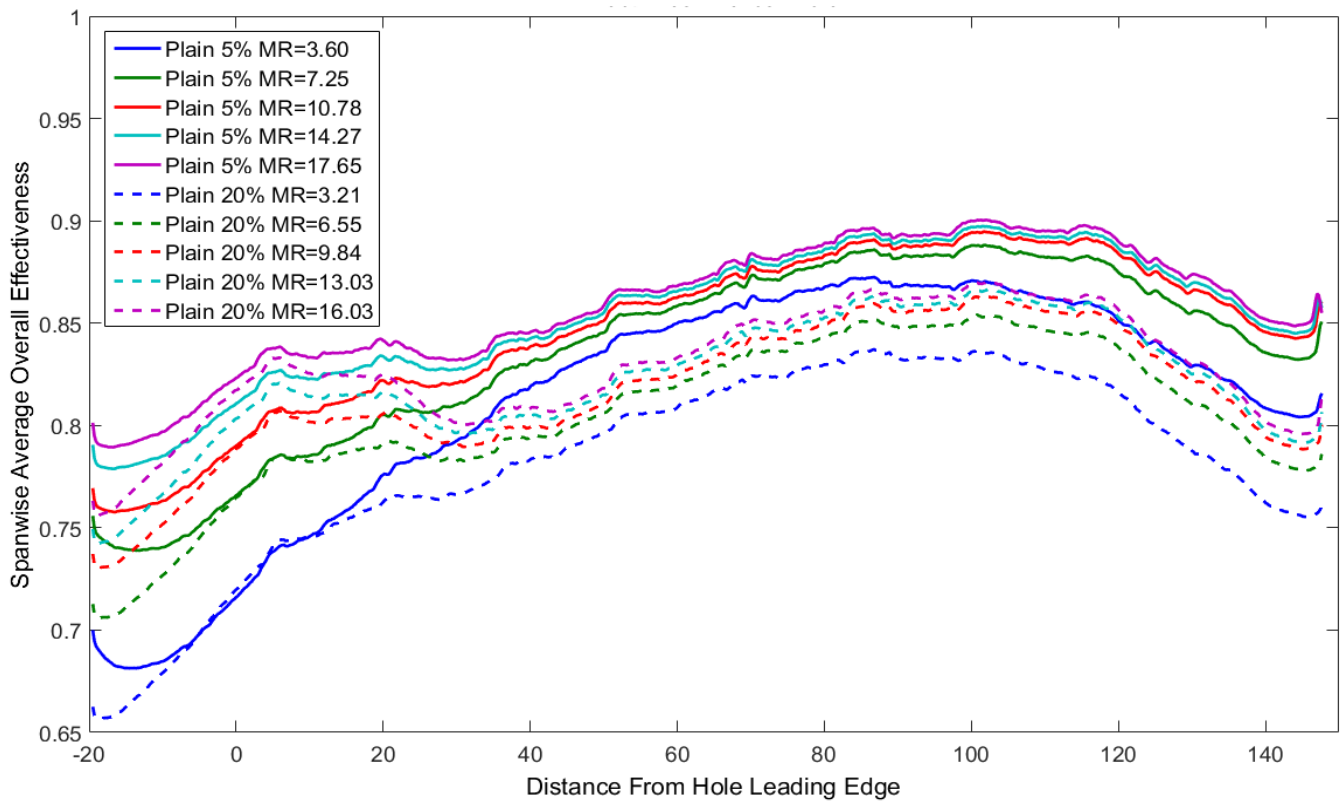
Figure 90 - Cylindrical hole spanwise averaged overall effectiveness at varying freestream turbulence levels
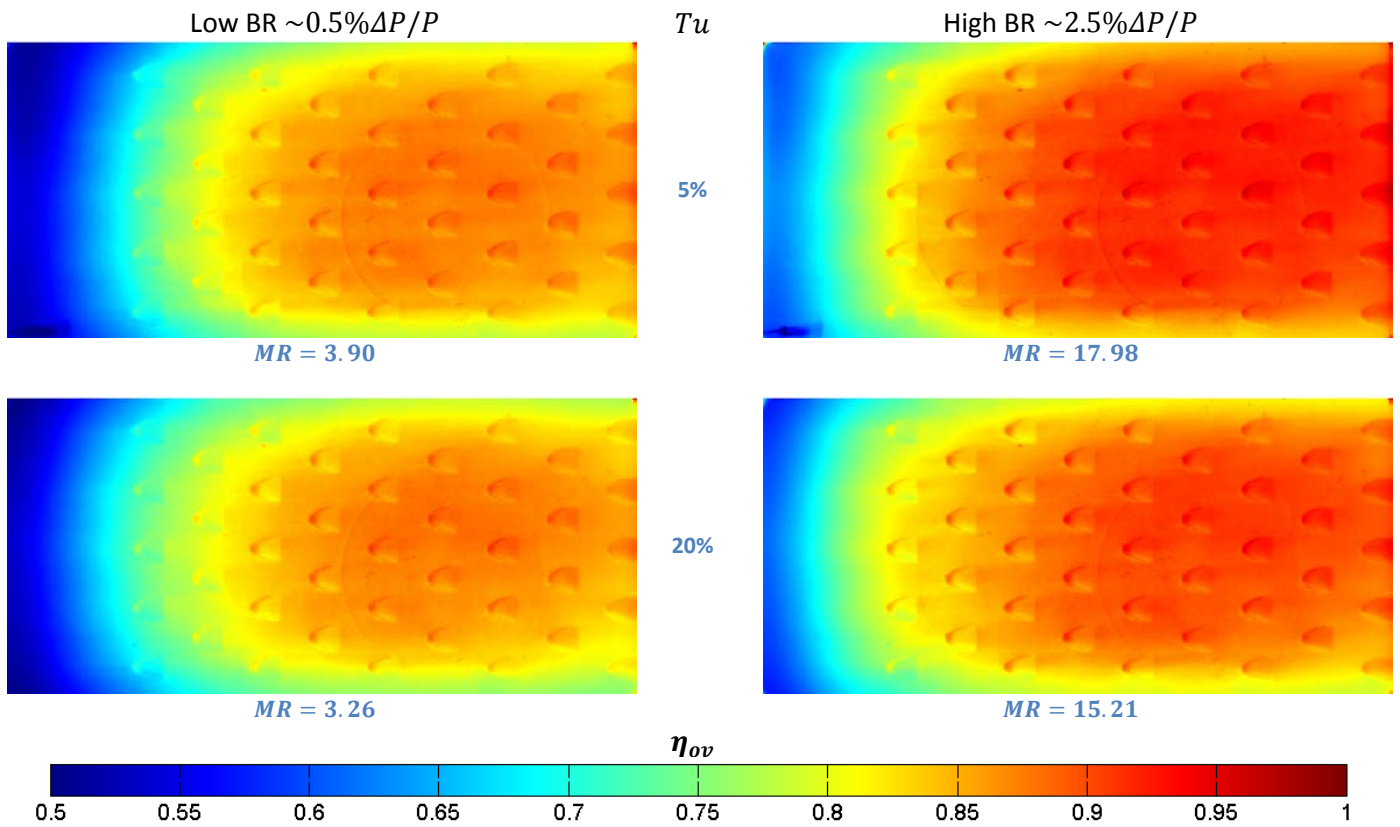
Figure 91 – Spey fan overall effectiveness at various turbulence and blowing ratio conditions
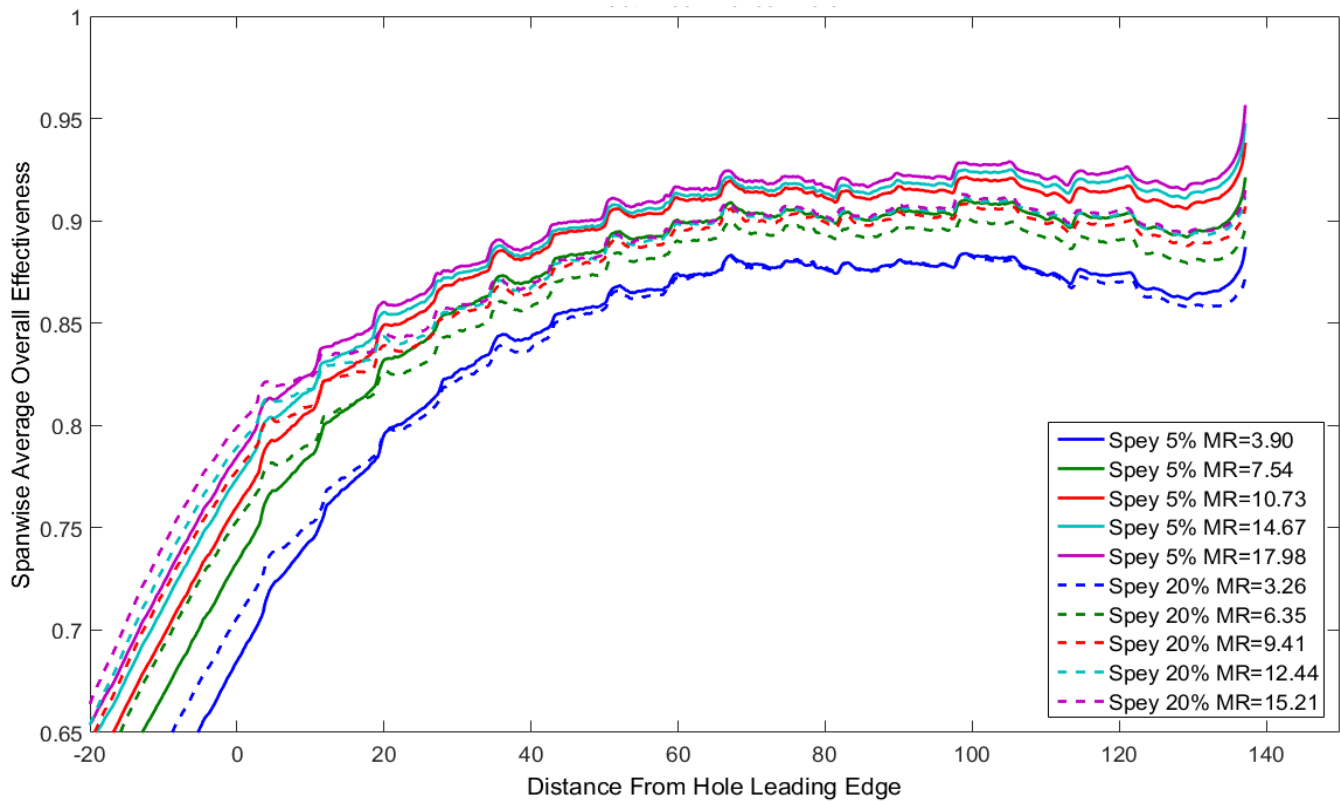
Figure 92 – Spey fan spanwise averaged overall effectiveness at varying freestream turbulence levels
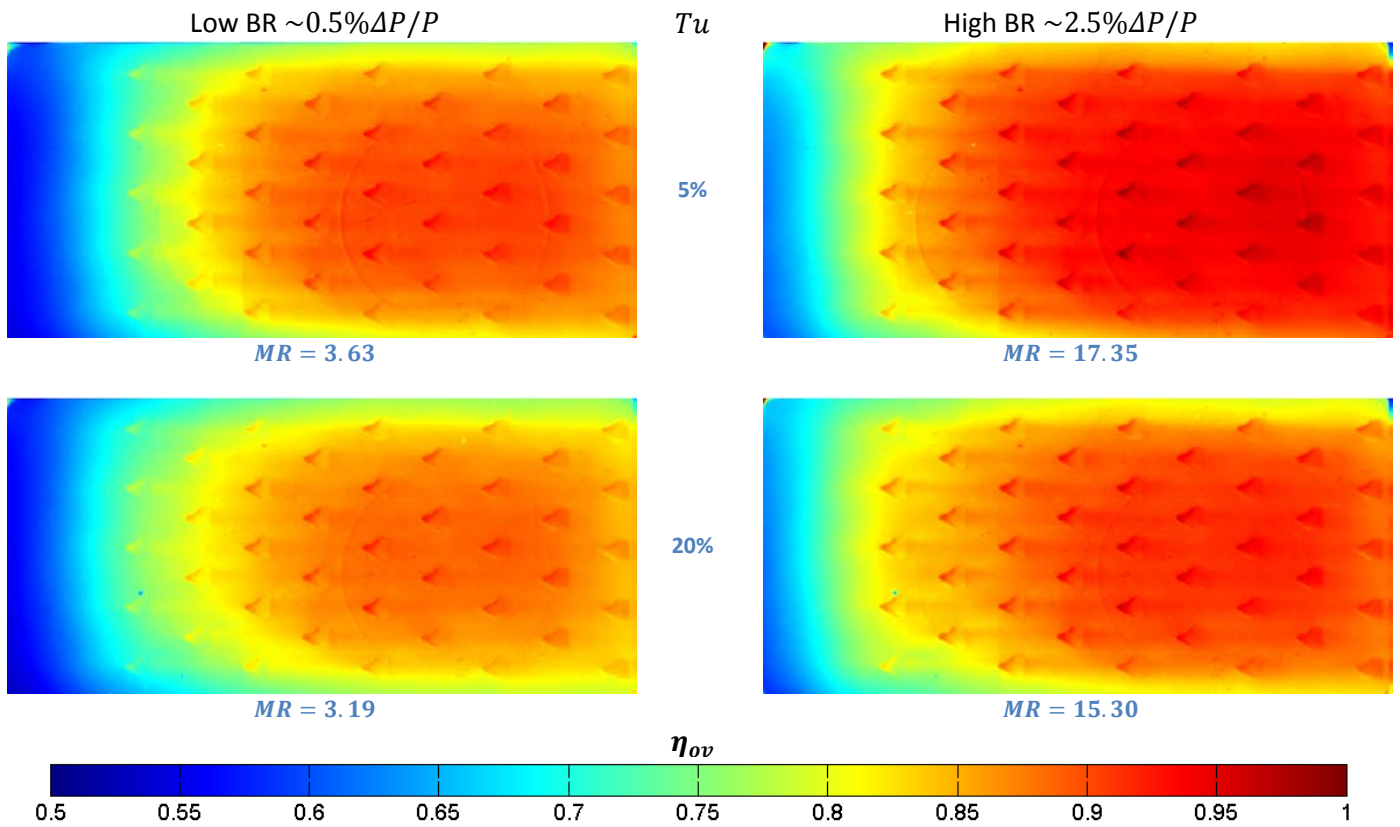
Figure 93 – Modified fan overall effectiveness at various turbulence and blowing ratio conditions
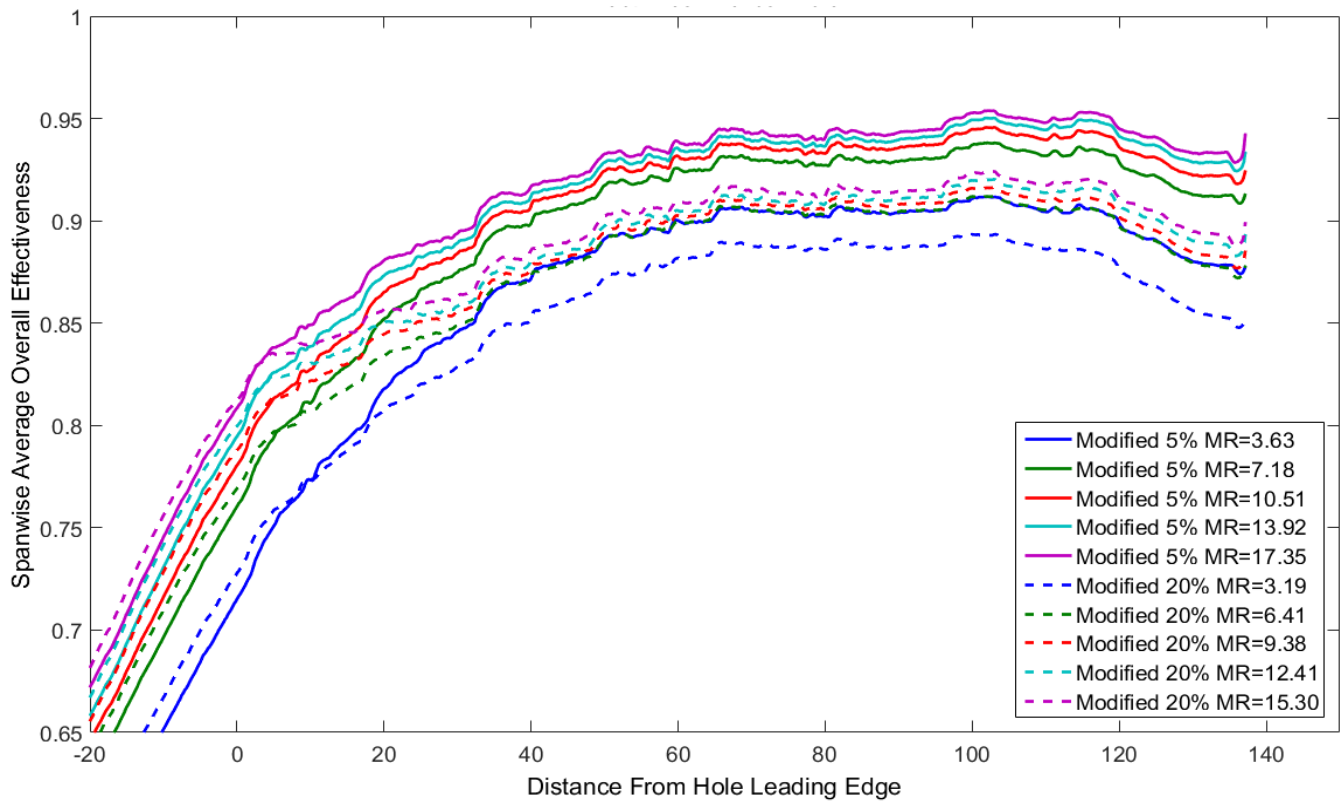
Figure 94 – Modified fan spanwise averaged overall effectiveness at varying freestream turbulence levels
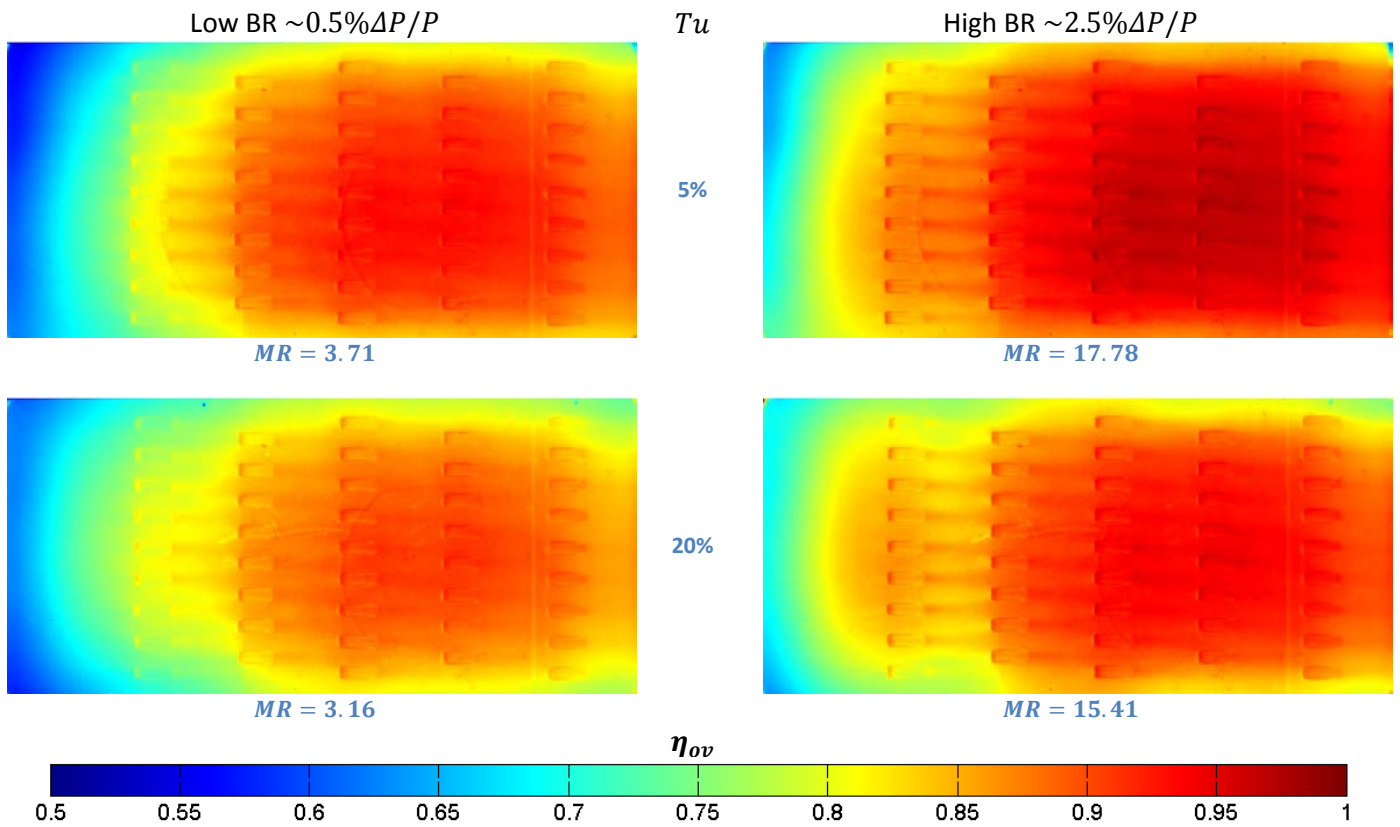
Figure 95 – Slotted overall effectiveness at various turbulence and blowing ratio conditions
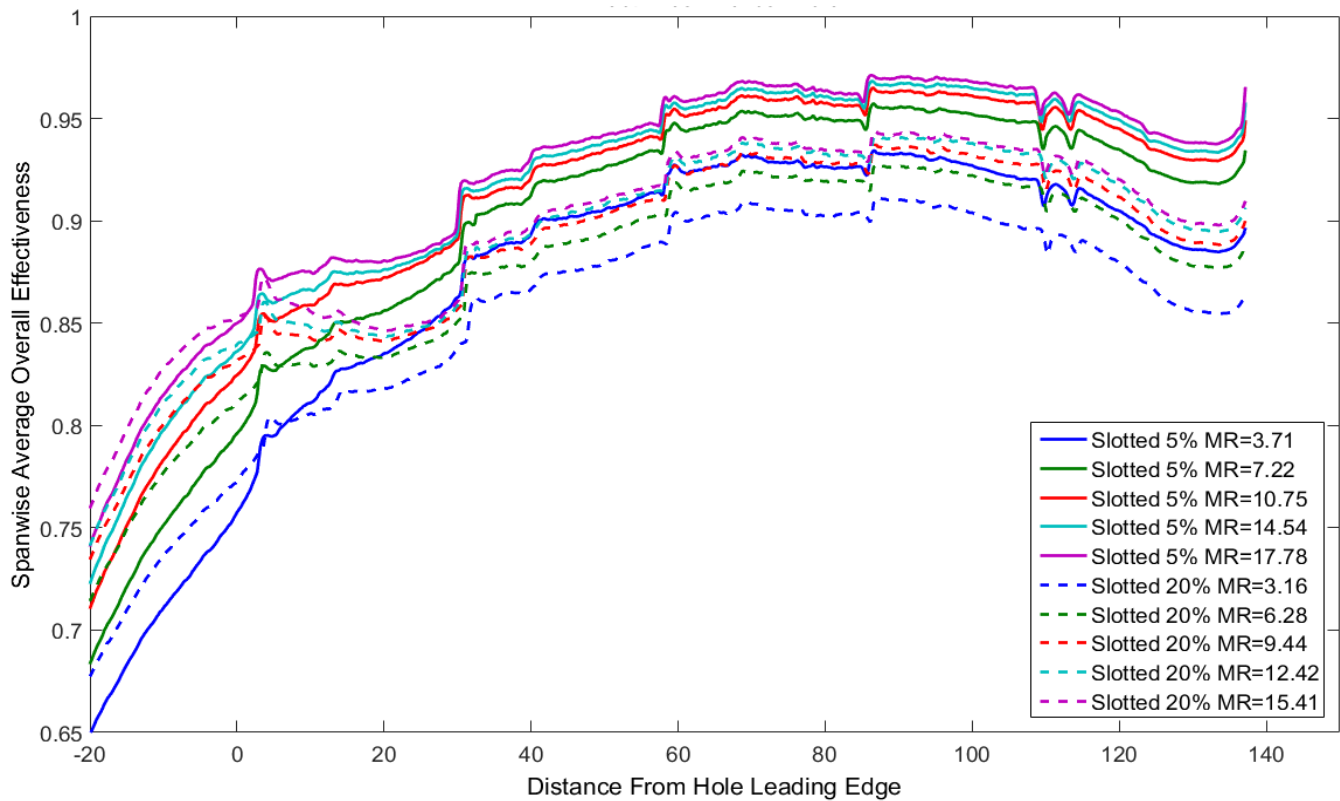
Figure 96 – Slotted spanwise averaged overall effectiveness at varying freestream turbulence levels

Figure 97 – Circular helix overall effectiveness at various turbulence and blowing ratio conditions

Figure 98 – Circular helix spanwise averaged overall effectiveness at varying freestream turbulence levels
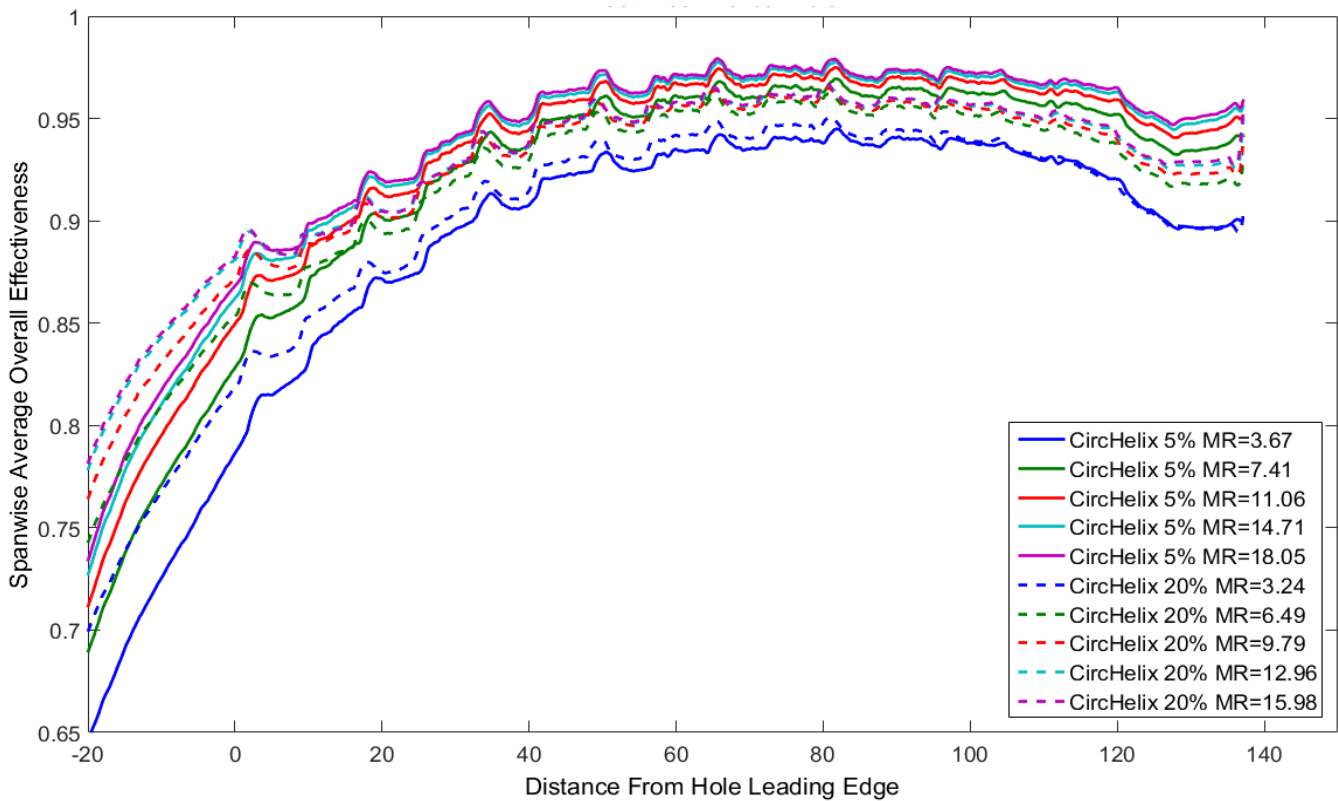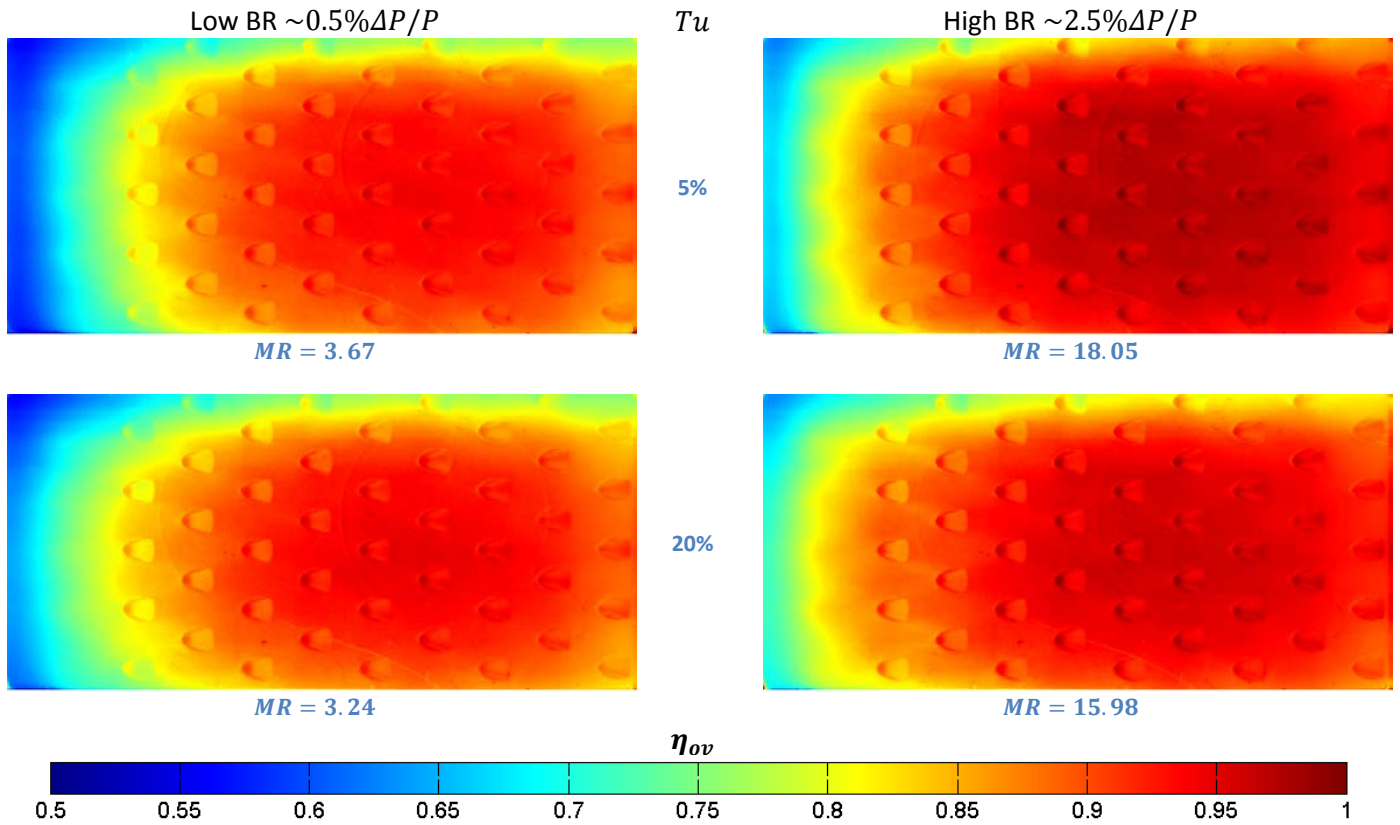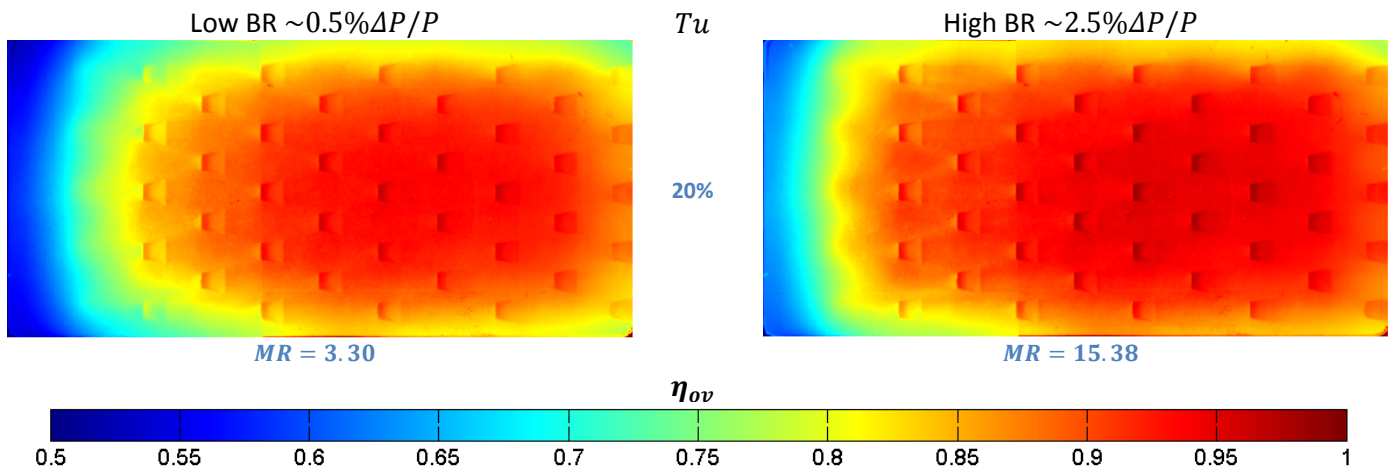
Figure 99 – Rectilinear helix overall effectiveness at various turbulence and blowing ratio conditions
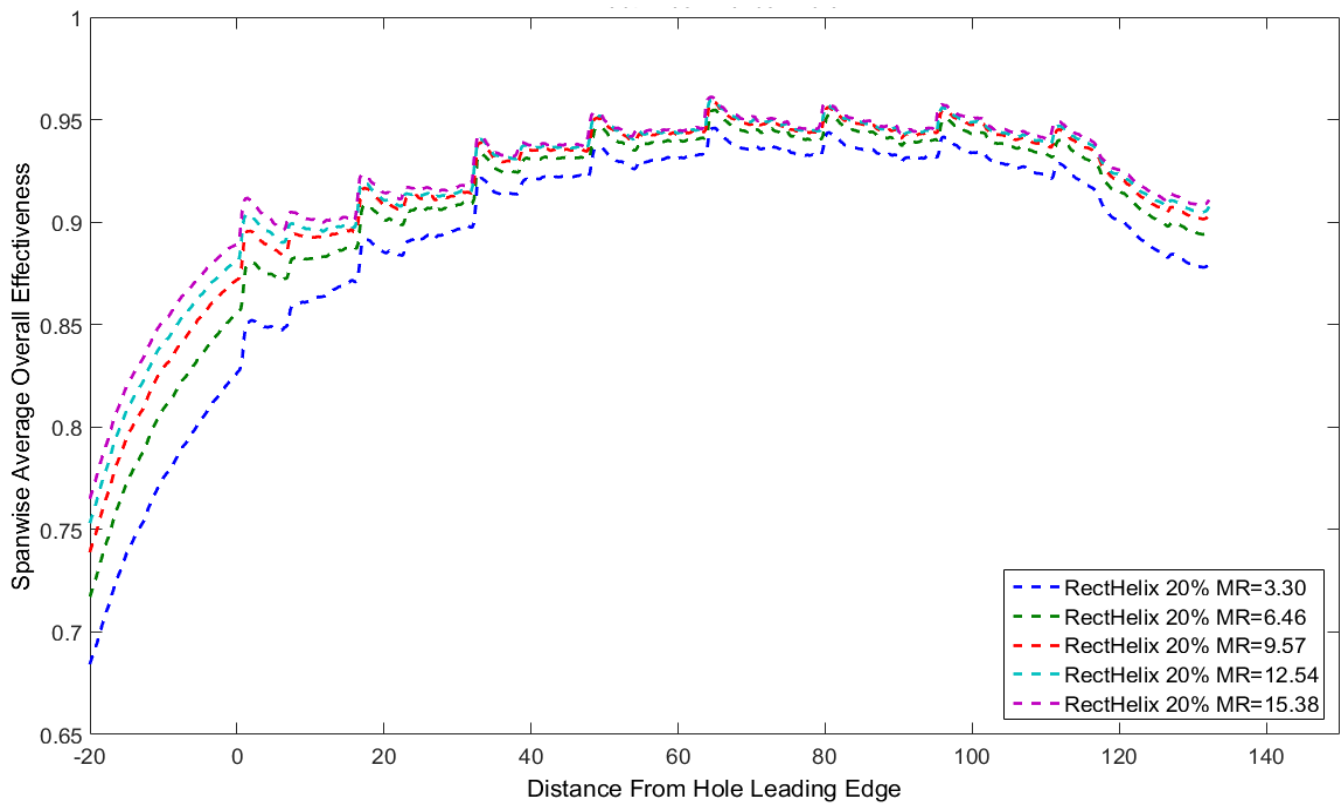
Figure 100 – Rectilinear helix spanwise averaged overall effectiveness at varying freestream turbulence levels

5.2.3   Effusion Hole Geometry

In this section the overall effectiveness performance measured for each effusion hole geometry are compared. As previously mentioned, the first row of cooling holes are not located in the same streamwise position along the plate in all designs, with the Cylindrical holes significantly closer to the leading edge of the plate than for the other cases. As these are conjugate heat transfer experiments, this difference in geometry is more significant than for the adiabatic film effectiveness tests because the boundary between the plate and the mounting frame is much closer to the internal cooling passages in the cylindrical design. This results in the shallower initial gradient in spanwise effectiveness with streamwise position and therefore it is difficult to draw conclusions about the relative performance of this geometry to the others in this upstream area. However, this boundary condition should have little to no effect on the results obtained mid-way along the plate, allowing comparisons to be made in this region. All other plates have the cooling holes located in roughly the same initial position and can be compared over the entire data set more easily. As with the adiabatic film effectiveness study, results are compared at the 20% freestream turbulence intensity conditions and at momentum ratios of around 3 and 15 equivalent to $\Delta P/P = 0.5\%$ and 2.5% at engine cycle conditions respectively.

Figure 101 presents 2D surface contour data at the highest momentum ratio condition with spanwise averaged data plotted in Figure 102.   From the spanwise averaged overall effectiveness data it can be seen that the geometries fall into three rough groupings. First, the cylindrical geometry acts as the baseline, with the lowest performance over the length of the plate and spanwise averaged effectiveness in the 0.80-0.85 band. Next, the geometries which promote good film performance improve on the base line with spanwise averaged performance levels in the region of 0.85-0.90.   Finally, the helical geometries which combine good film performance with strong internal heat removal return the best performance with spanwise averaged values of 0.90-0.95. Due to the different array pattern used by the Slotted geometry it does not fit neatly into any of the groups but instead bridges the gap between the film only and internally improved designs. This difference in overall effectiveness infers a reduction in minimum metal temperature of around 100K when scaled back up to engine cycle conditions.

By packing a large number of cooling passages in the same spanwise location, a significant amount of heat can be removed from within the wall by the first row. This gives rise to the high initial effectiveness of the Slotted design as seen in the patch of relatively high effectiveness

prior to the exit of the first row of cooling holes. This is followed by a region of decreased average effectiveness in the space between cooling passages. This reduction in performance is somewhat lessened by the coolant film ejected by the first row covering the surface, reducing the driving temperature of the convective heat transfer into the wall. This process repeats, with the tightly packed cooling passages removing heat from the wall, whilst the areas with no internal cooling are protected by an increasingly effective film resulting in the high overall performance of this design. Alternating hot and cold streaks are also present in the spanwise direction, particularly downstream of the first two rows. These occur as a result of the good film coverage immediately downstream of the hole exits and the poor spanwise spreading of the film. As a result, there is a difference in effectiveness of around 0.025 between the hot and cold streaks which approximates to an engine equivalent temperature difference of the order 25K.

The cylindrical and Spey fan geometries share the same internal cooling arrangement, with roughly the same passage length for both with only a slight reduction due to the fanned exit of the Spey geometry. However, due to the smaller hole diameter used for the Spey design, the surface area over which heat can be removed from the wall as the coolant passes through the internal passage is reduced compared to the cylindrical design.   However the overall effectiveness results for the Spey geometry show a general improvement over the cylindrical design. This is to be expected as the film produced by the fan at the effusion hole exit is significantly better than that produced by a simple cylindrical hole, resulting in less heat being transferred into the hot side of the wall in the first place. The reduced porosity of the Spey geometry will also reduce the internal area of the holes and therefore heat pickup, thus, if the porosity was matched correctly with the other geometries the overall effectiveness performance would be expected to increase slightly, though it would still lie in the same region as the Modified fan design.

While the Modified fan has increased lay angle and hence shorter passage length, the cross sectional area increases as the passage diverges resulting in a larger surface area over which heat transfer can take place. As a result, even though the film performance of the Modified fan geometry is slightly worse than the Spey fan, the overall effectiveness is slightly higher. This indicates that whilst more heat is entering the wall through the hot side surface, this is more than compensated for by the increased heat removal from within the cooling passages. The

average overall effectiveness for the Modified fan is 0.01 higher than for the Spey fan, equating to roughly 10K metal temperature for the engine cycle replicated here. The data provided by the 2D surface contours show that, while not as pronounced as in the Slotted design, some streamwise streaking is noticeable in the Modified design. Again, this is a result of the very high film effectiveness immediately downstream of the hole exit but poor spanwise spreading resulting in an alternating thermal gradient in the spanwise direction. This effect is reduced to the point where it is not noticeable in the surface contour data for the Spey design which benefits from a wider spreading of coolant over the surface.

The two helical geometries have much longer internal passage lengths providing a greater surface area over which the coolant passing through the wall can remove heat. This combined with careful design of the fanned exit results in very high levels of both adiabatic film and overall effectiveness. The influence of the internal cooling can be clearly seen in the area upstream of the first row of cooling holes where the overall effectiveness for both helical designs reach a level equal to the maximum performance of the cylindrical design well before the coolant has emerged onto the surface. The two helical designs show similar spanwise averaged adiabatic film effectiveness performance as well as similar spanwise averaged overall effectiveness with the circular cross section providing slightly better performance than the rectilinear cross section after the second row of cooling holes. This is likely due to the sharp corners in the square cross section promoting a more streaky cooling film pattern as identified in the adiabatic film effectiveness surface contours. The rectilinear design shows very slightly better spanwise averaged overall effectiveness levels up to the second row, indicating that the square cross section is promoting slightly better internal heat removal than the circular design.

Figures 103 and 104 respectively show the surface maps and spanwise averaged plots of overall effectiveness at the lower $M \approx 3$, equivalent to engine $\Delta P/P = 0.5\%$ and $Tu = 20\%$ condition. As before, three groups are distinguishable with the cylindrical design providing the lowest peak performance in the region of 0.82, the Spey and Modified fanned geometries showing similar peak performance of around 0.87 and the two helical geometries showing the highest peak performance of around 0.94. The Slotted geometry lies slightly above the middle category at this condition with peak performance in the 0.90 region. The difference between cylindrical and helical performance represents a reduction in minimum metal temperature of around 120K at the engine cycle conditions used to scale these experiments.

Comparing these values to those recovered at the higher momentum ratio, a constant decrease in overall effectiveness once the film is established of around 0.03 is seen in the designs with simple internal passages. This decrease is reduced to only 0.01 for the helical geometries. This peak cooling performance is most likely a result of the insensitivity to momentum ratio of the coolant film produced by these designs. Comparing the cooling performance leading up to the first row of hole exits, a larger difference is seen between the two momentum ratio conditions. The overall effectiveness difference $\sim 4D$ upstream of the hole leading edge for the cylindrical and Spey designs is of order 0.10, for the Modified fan and Slotted designs this reduces slightly to 0.09 and the helical designs show the lowest decrease in performance of 0.07. These differences between initial and established overall effectiveness values reduce once the film is introduced by the first row, with the difference halving by the second row of passage exits. This suggests that the helical geometries are more suited to being used effectively with lower air mass flow requirements than conventional designs, freeing that air up to be used in a more efficient application such as combustion emission management or cooling of life critical turbine components.
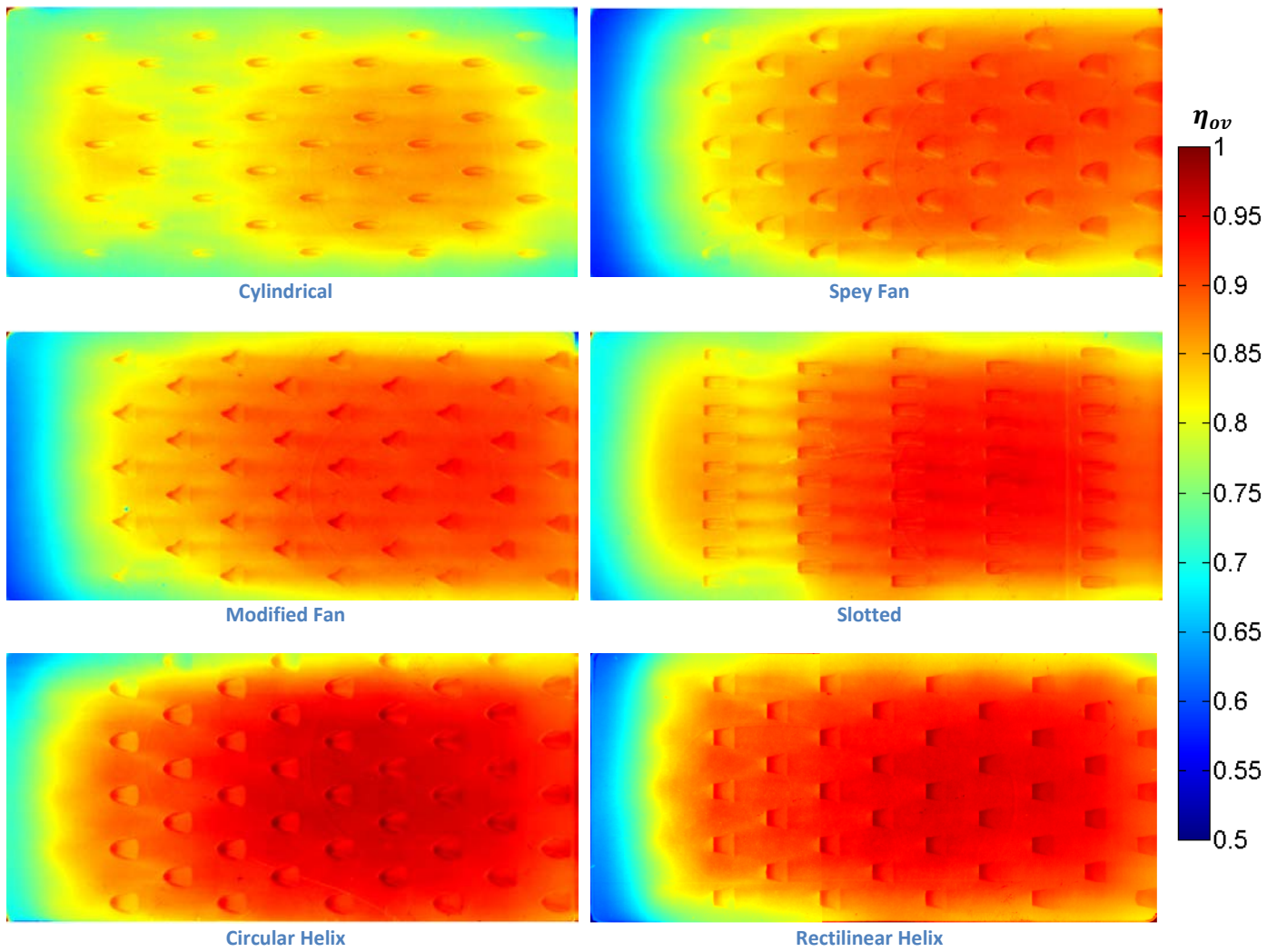
Figure 101 – Geometry comparison of overall effectiveness surface map, $MR \cong 15$ and $Tu = 20\%$
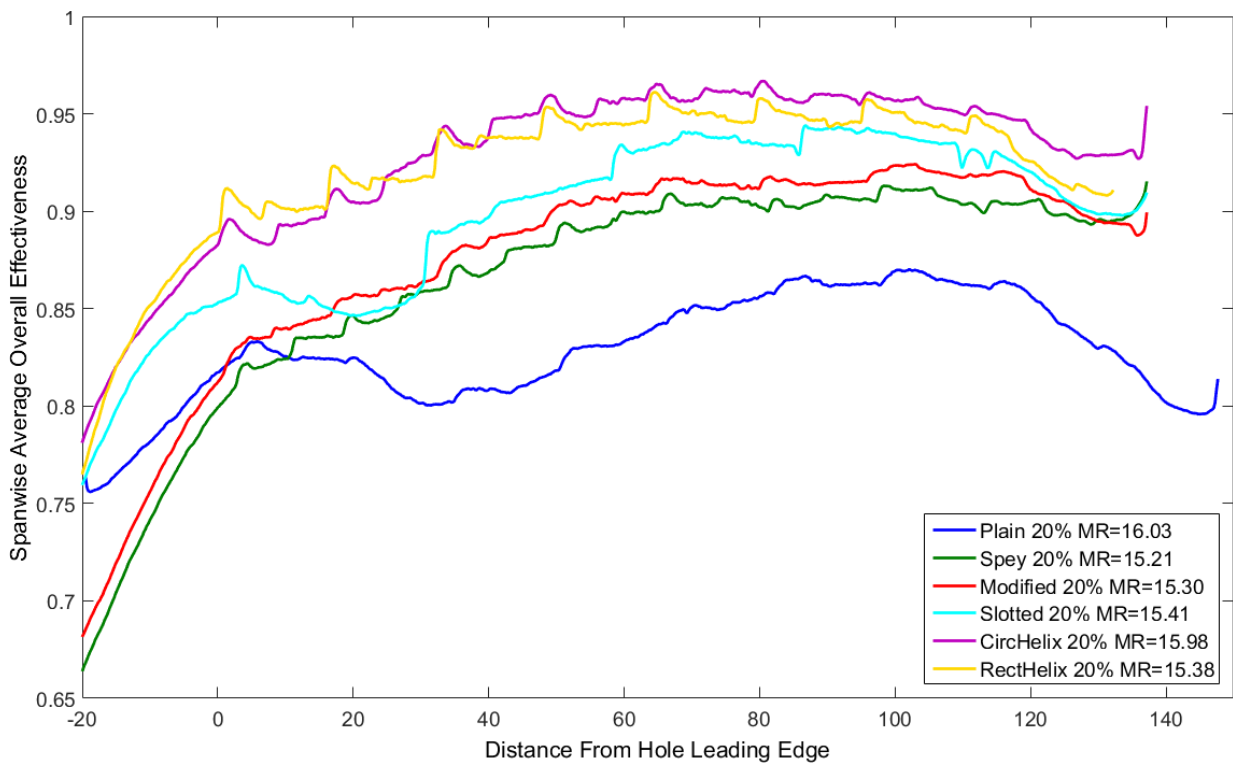
Figure 102 – Geometry comparison of span-wise averaged overall effectiveness, $MR \cong 15$ and $Tu = 20\%$

146
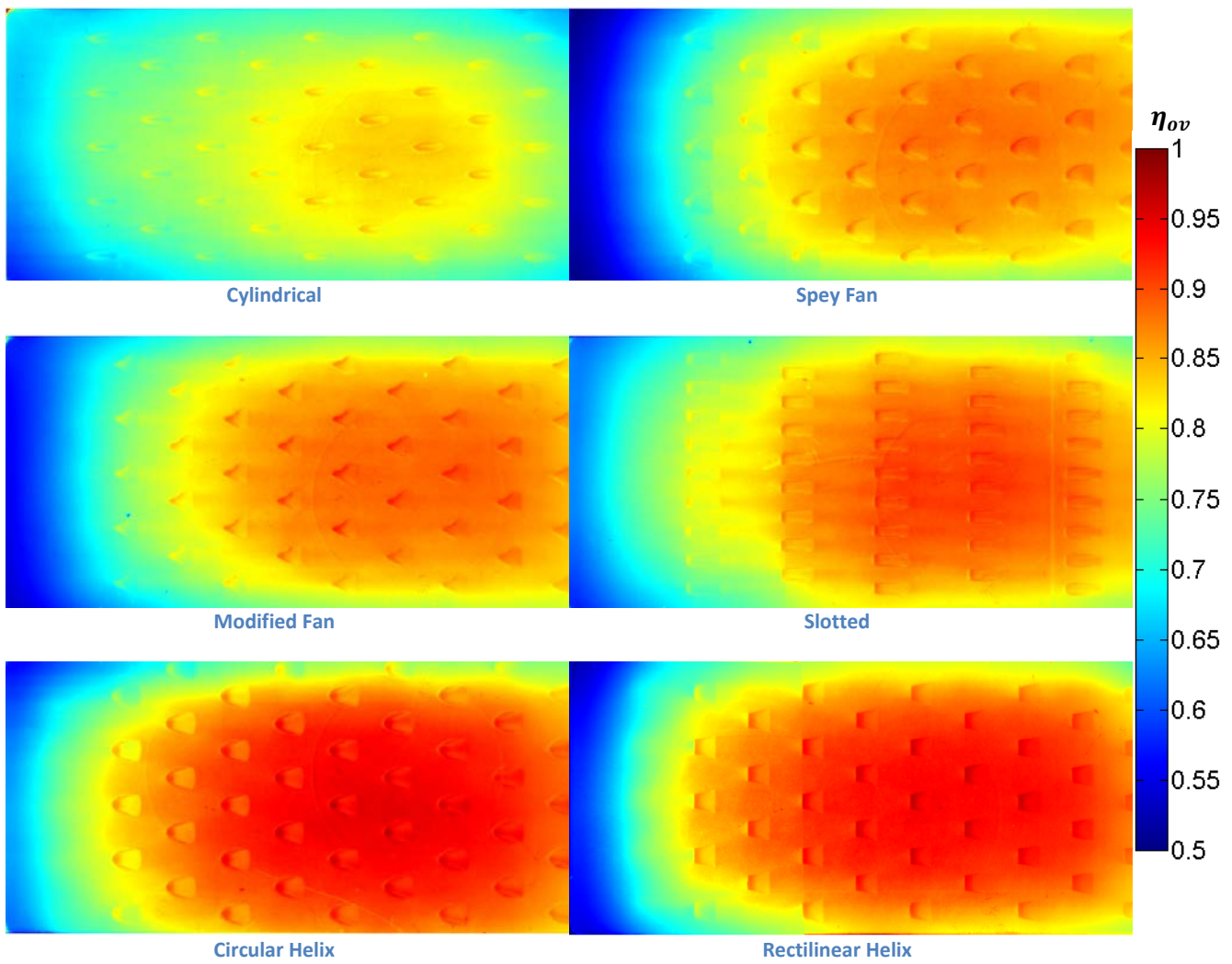
Figure 103 – Geometry comparison of overall effectiveness surface map, $MR \cong 3$ and $Tu = 20\%$
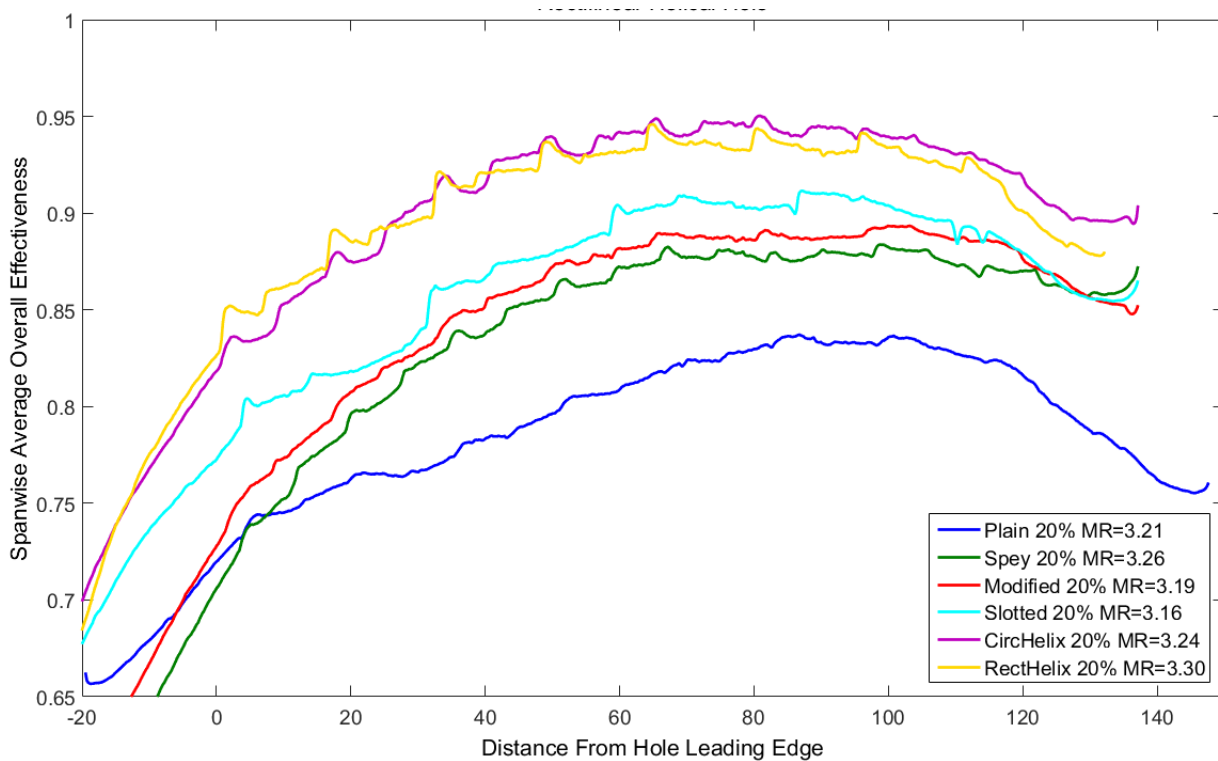
Figure 104 – Geometry comparison of span-wise averaged overall effectiveness, $MR \cong 3$ and $Tu = 20\%$

6   CFD Investigation

This section contains the results of the computational study and compares the simulated results to those obtained through experimental methods for adiabatic film effectiveness. Computational simulations are also used to compare the internal performance of the various geometries in order to better understand how alterations to the internal passages influences the amount of heat passed into the cooling air and how much of the cooling potential of that air is utilised.

6.1   Adiabatic Film Effectiveness

As with the experimental results, 2D surface contours and spanwise averaged data are extracted from the computational simulations. As the simulation makes use of a periodic boundary it represents the asymptotic case at the centre of an effusion array. Therefore, to compare directly with experimental data, edge effects are removed and periodicity preserved by trimming the spanwise extremities of the measured 2D surface contours.

Computational 2D surface contours are created using a smooth filled contour displayer within StarCCM+. This interpolates the cell vertex values in order to smooth the data between the mesh cells, resulting in a high resolution pixel image. A custom 256 band colour map is defined and used to display surface contour data based on the same colour scale used by Matlab when post-processing and displaying experimental data. By utilising the same colour mapping scheme for both experimental and computational results the 2D surface contours can be directly compared.

The other major comparison to experimental results considers the span-wise averaged surface effectiveness. In order to make this comparison the surface contour data from the simulation are extracted and imported into a Matlab script which calculates the area averaged surface effectiveness in each pixel row. The x-axis is then scaled to mm in order to match the experimental data.

6.1.1   2D Surface Contour Data

Figures 105 through 110 compare the 2D surface contour data obtained through both experimental and computational methods at the highest and lowest momentum ratio and turbulence intensity conditions. Qualitatively it can be seen that whilst the experimental results show only slight sensitivity to both momentum ratio and turbulence intensity, the CFD data is

much more variable, with large differences between conditions, particularly at the high turbulence-low momentum ratio condition. This trend is seen across all cooling hole geometries tested. This reduced coolant/mainstream momentum ratio, combined with the high freestream turbulence intensity level (which manifests as time averaged isotropic velocity fluctuations in steady state RANS based CFD simulations) results in the coolant flow mixing out into the freestream flow more readily.

Figure 105 contains the 2D surface contour data for the Cylindrical hole design. Comparing the high and low turbulence intensity computational results for the low momentum ratio cases, it can be seen that the coolant trace becomes wider in the spanwise direction as a result of the increase mixing due to freestream turbulence intensity. Data from the fanned geometries also show that the streamwise length of the coolant trail is reduced with increased turbulence intensity. This effect is less notable in the cylindrical data as a significant proportion of the coolant jet penetrates into the freestream, with only a small trail of coolant visible on the surface downstream of each cooling hole.

Through comparing the experimental and computational data given in Figure 105 it is apparent that the RANS based turbulence model is inadequate in correctly modelling the turbulent mixing processes present in a jets in crossflow-type problem. This is not unexpected as the turbulence effects in this problem are anisotropic and therefore poorly captured by the isotropic nature of the two-equation RANS model. Through treating the turbulence as isotropic the spanwise spreading of the coolant is under-predicted whilst the streamwise spreading is over-predicted. This results in the long-thin coolant trails downstream of the cooling holes seen in the computational data compared with the much wider spread of coolant seen in the equivalent experimental data. As a result the cylindrical hole simulations generally under-predict the adiabatic film effectiveness.

The high momentum ratio data presented in Figure 106 shows that the CFD captures the asymmetric flow pattern caused by the coolant flow 'sticking' to one side of the fan due to the large diverging angle of the Spey fan geometry. However, this phenomenon is not present in the low pressure drop CFD data, likely as a result of the low exit flow velocity resulting in the crossflow becoming the dominant factor influencing the flow within the fan. The experimental data shows the flow favouring one side at the low pressure drop condition due to the physically asymmetric flow passage and flat spot resultant from the manufacturing process. As before

however, the largest difference between experimental and computational data is as a result of the isotropic treatment of the turbulence effects, with the simulation showing narrower regions of high effectiveness extending further in the streamwise direction compared with the experimental data.

Figure 107 shows the data obtained for the Modified fan design. It must be noted that due to the immaturity of the DLD manufacturing method the experimental geometry is again asymmetric, with the left and right hand sides of the passage departing from the design intent to differing degrees. This is most easily seen in the exit definition, in particular on one side of the fanned hole exits showing deformity when compared to the 'perfect' geometry used for the simulations. This is most visible at the left-hand edge of the hole exits and is apparent in the measured surface contours looking downstream. The right-hand edge shows the s-shaped curve that would be created from the three-hole drilling operation used when conventionally manufacturing this hole type, whereas this s-shape is much less distinct on the left-hand edge. As a result the experimental data show the coolant again favouring attachment to one side of the fanned geometry, rather than filling the fan as the CFD data indicate. Once exiting the fan the coolant is expected to spread in the spanwise direction leaving a broader area of high effectiveness, similar to that shown in the low momentum ratio, high turbulence intensity computational data. However, the majority of simulated test cases show a long, narrow region of high effectiveness, with the width of the coolant trail narrowing with distance from the hole. This can again be attributed to the inability of the turbulence model to accurately account for the anisotropic nature of the turbulent flow both through the gently diverging section and the jet-crossflow interaction.

The Slotted geometry relies less on lateral diffusion within a fanned section close to its exit but instead upon a more gradual diffusion in a direction normal to the plate surface. As a result it can be seen from Figure 108 that the difference between experimental and simulated results lies mainly in the extended length of the cooling trails downstream of the hole exits. The major exception to this is the low momentum ratio, high turbulence condition, in which a much larger proportion of the coolant remains on the surface in the simulation, resulting in the relatively large areas of high adiabatic effectiveness around the hole exits. However this appears to be a local effect since the coolant does not build up as strongly along the plate length as shown by the lower adiabatic film effectiveness towards the downstream edge of the plate compared

with the other conditions. This is likely due to the increased mixing caused by increasing the turbulence intensity and the low momentum of coolant exiting the holes resulting in the coolant mixing more rapidly with the main stream flow.

Figure 109 shows data for the Circular Helical design. Both the CFD and experimental data indicate that increased freestream turbulence intensity has little effect on the surface distribution of coolant at high momentum ratio, with only a small difference in the spanwise width of the coolant trace between high and low turbulence cases. However the simulated results show generally higher levels of adiabatic effectiveness than measured through experimental methods. Another notable difference between CFD and experimental results lies within the diverging section. While the simulation shows the coolant filling the entire volume of the fan with a reduction in film effectiveness shown only after the coolant has broken out onto the surface of the plate, the measurements indicate a slight reduction of adiabatic effectiveness towards the trailing edge of the fanned section along its centreline. This is likely due to the low momentum carried by the fluid as it exits the helical section and is diffused by the fanned section. As this low momentum flow is ejected into the mainstream the coolant jet is deflected towards the surface, providing little in terms of jet thickness to hamper the oncoming mainstream flow. This mainstream flow is allowed to move closer to the wall whilst mixing with the coolant and reducing the effectiveness slightly at the end of the fan.

This reduction in effectiveness within the fanned section close to the centreline is also shown in the experimental results for the Rectilinear Helical geometry shown in Figure 110. Once again this is not visible in the simulated results, although the two forks of coolant that this effect causes can be seen in the high momentum ratio data. At the lower momentum ratio the simulation indicates the coolant mixes with the mainstream evenly and the forks do not form although they are visible in the experimental data. Experimental data is only available for the higher turbulence intensity case for the Rectilinear Helical geometry. In this case the simulation of the higher momentum ratio condition over-predicts the adiabatic effectiveness while under-predicting at the lower momentum ratio condition.

It is well established that conventional RANS based turbulence models are ill suited to jets in crossflow type problems due to the highly anisotropic nature of the turbulence field. Therefore is it not expected that the simulations would provide good accuracy when comparing the absolute effectiveness values and their distribution. By comparing the surface contours of

various solutions the simulations can however provide an indication as to how the different cooling solutions rank relative to one another. This comparison is made in Figure 111 at the highest momentum ratio and turbulence intensity conditions. From this data it is immediately apparent that the Cylindrical hole design performs worst, with the helical geometries providing significantly better cooling performance both in terms of magnitude and film coverage. The remaining effusion geometries are predicted to perform in between which is in agreement with the conclusion drawn from the experimental data presented in section 5.1.3.

Experiment

CFD

$MR = 3.32, \ Tu = 5\%$

Experiment

CFD

$MR = 14.94, \ Tu = 5\%$

Experiment

CFD

$MR = 3.32, \ Tu = 20\%$

Experiment

CFD

$MR = 14.94, \ Tu = 20\%$

η_{ad}

0.0   0.10   0.20   0.30   0.40   0.50   0.60   0.70   0.80   0.90   1.0
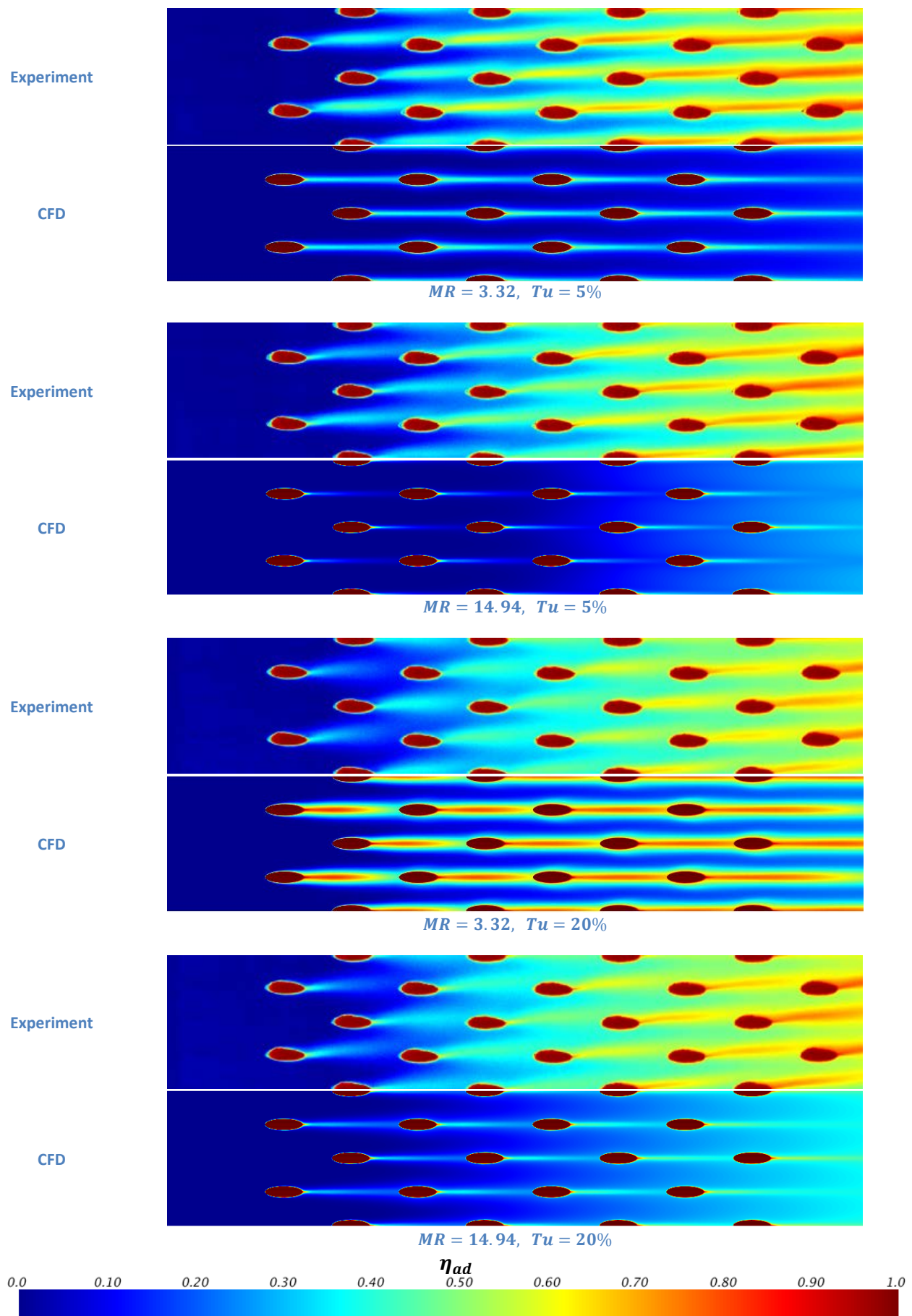
Figure 105 - Cylindrical hole adiabatic effectiveness comparison between experiment and CFD
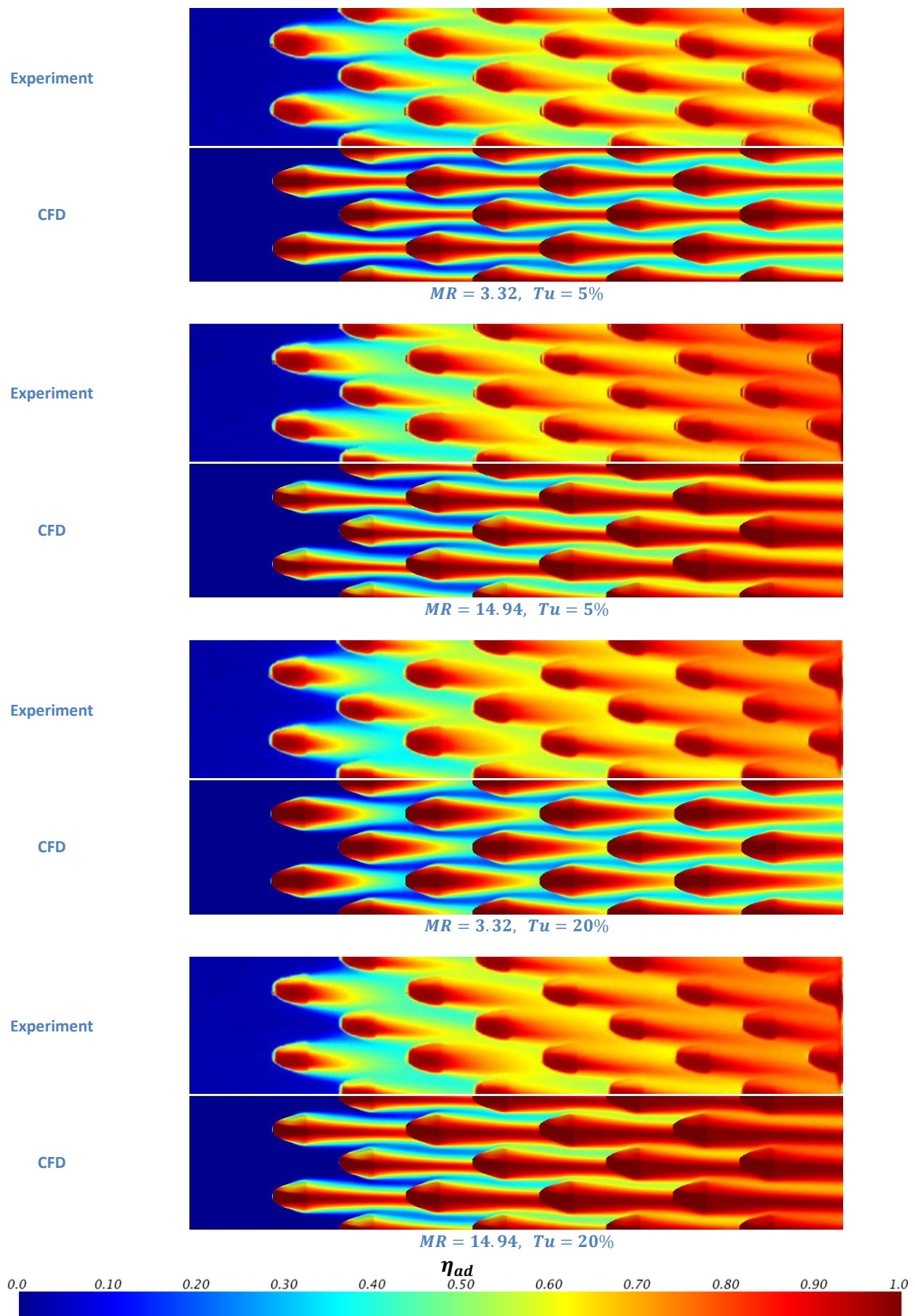
Figure 106 - Spey fan adiabatic effectiveness comparison between experiment and CFD
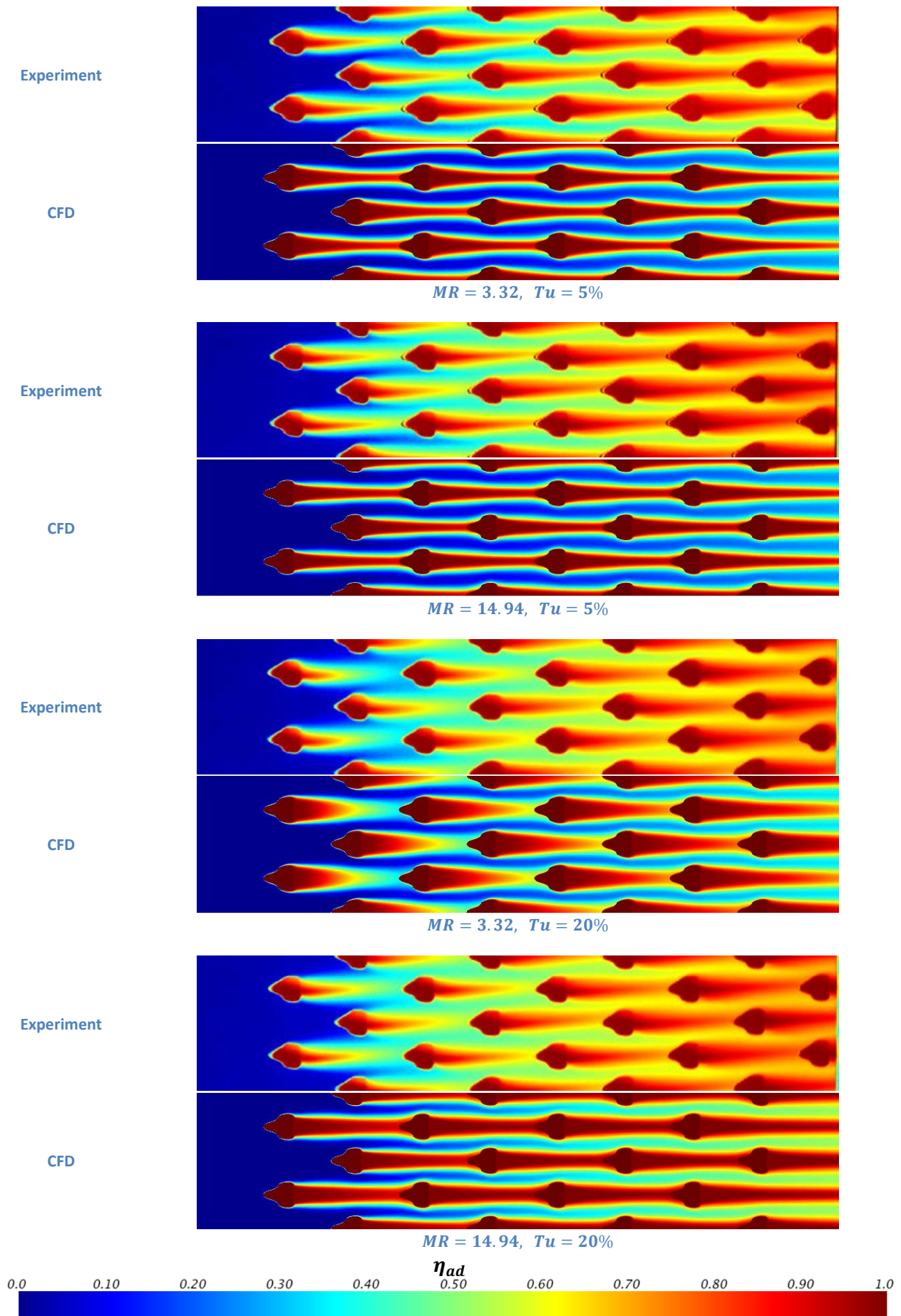
Figure 107 - Modified fan adiabatic effectiveness comparison between experiment and CFD
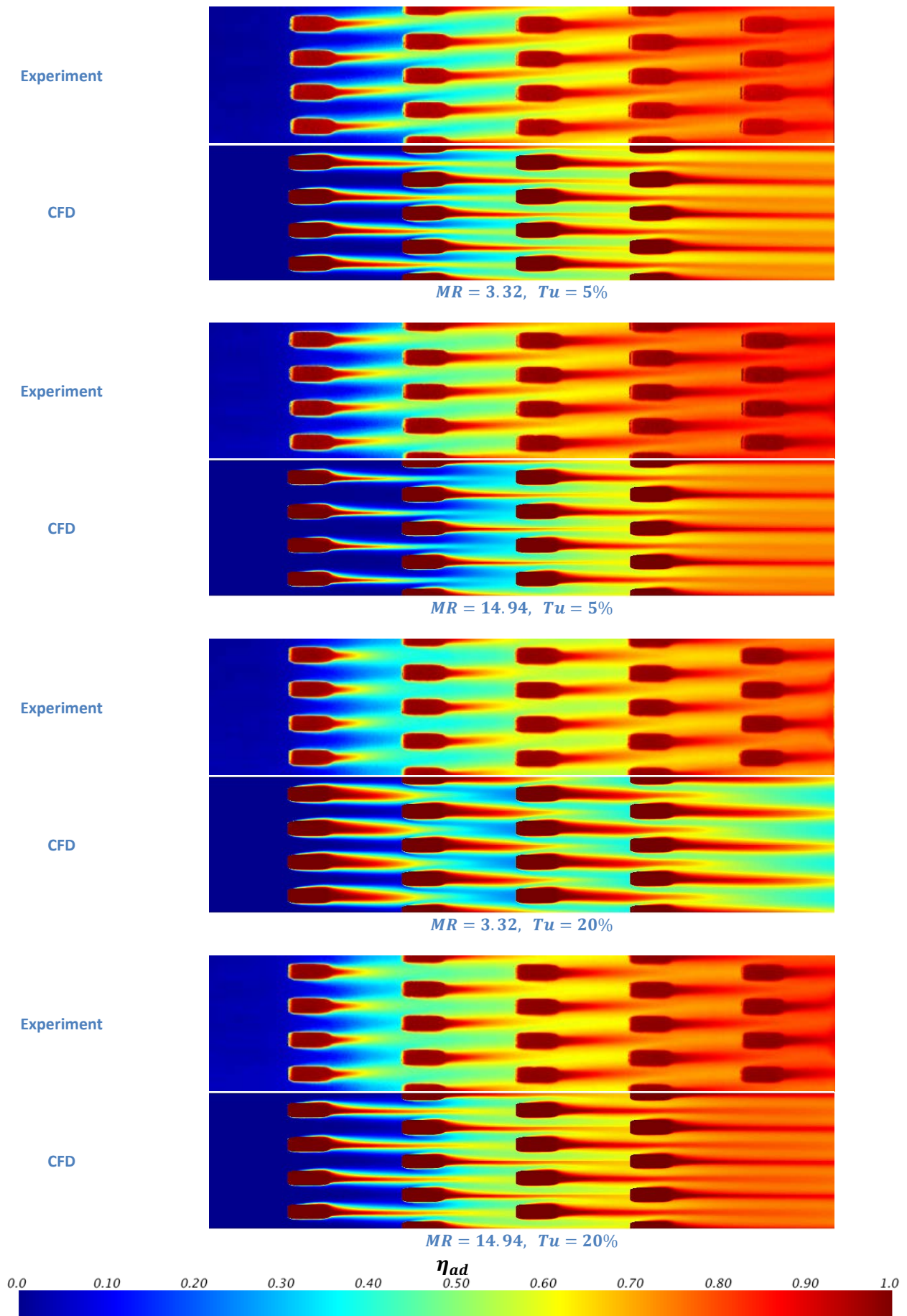
Figure 108 – Slotted adiabatic effectiveness comparison between experiment and CFD
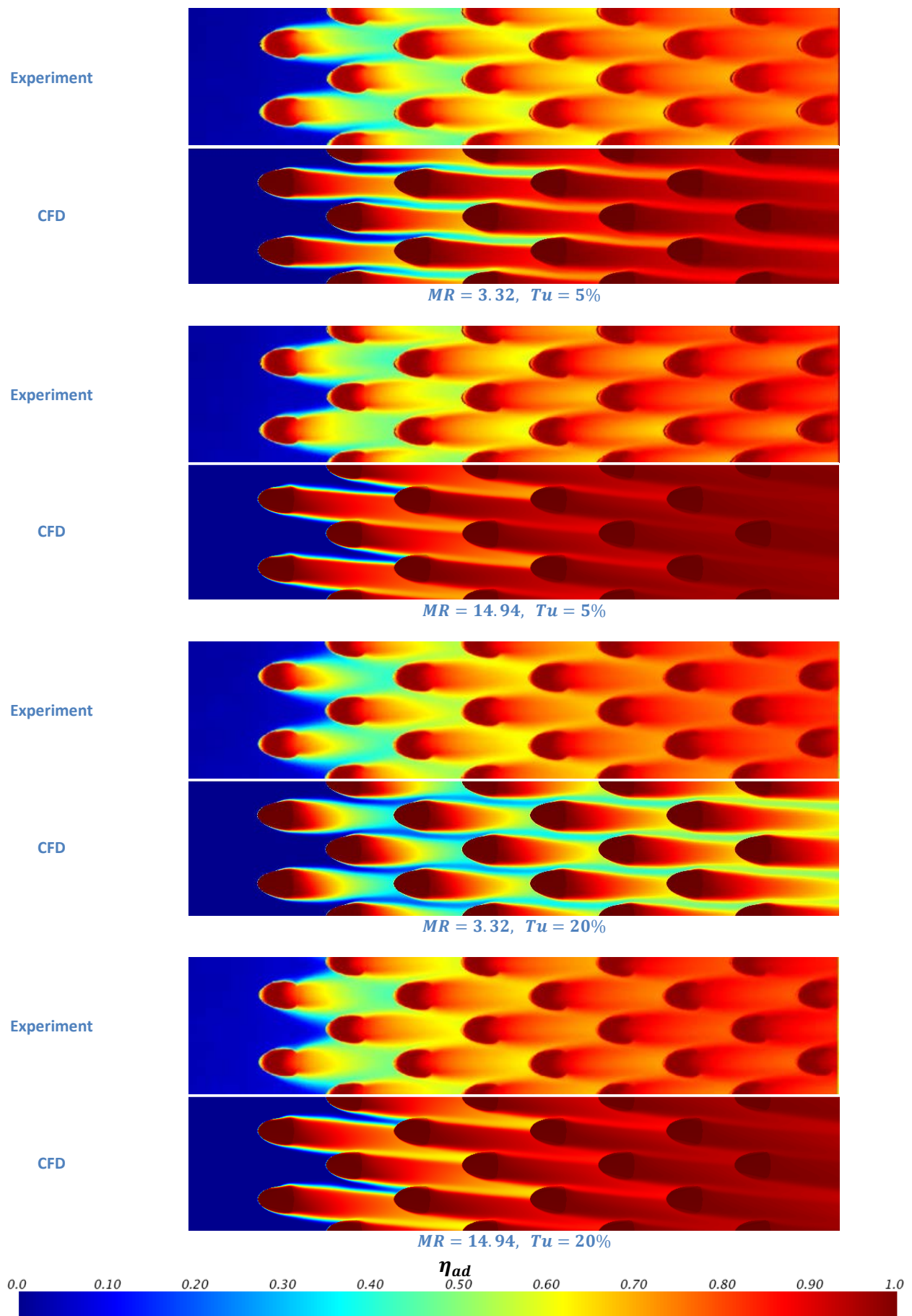
Figure 109 – Circular helix adiabatic effectiveness comparison between experiment and CFD

CFD

$MR = 3.32, \ Tu = 5\%$

CFD

$MR = 14.94, \ Tu = 5\%$

Experiment

CFD

$MR = 3.32, \ Tu = 20\%$

Experiment

CFD

$MR = 14.94, \ Tu = 20\%$

η_{ad}

0.0   0.10   0.20   0.30   0.40   0.50   0.60   0.70   0.80   0.90   1.0
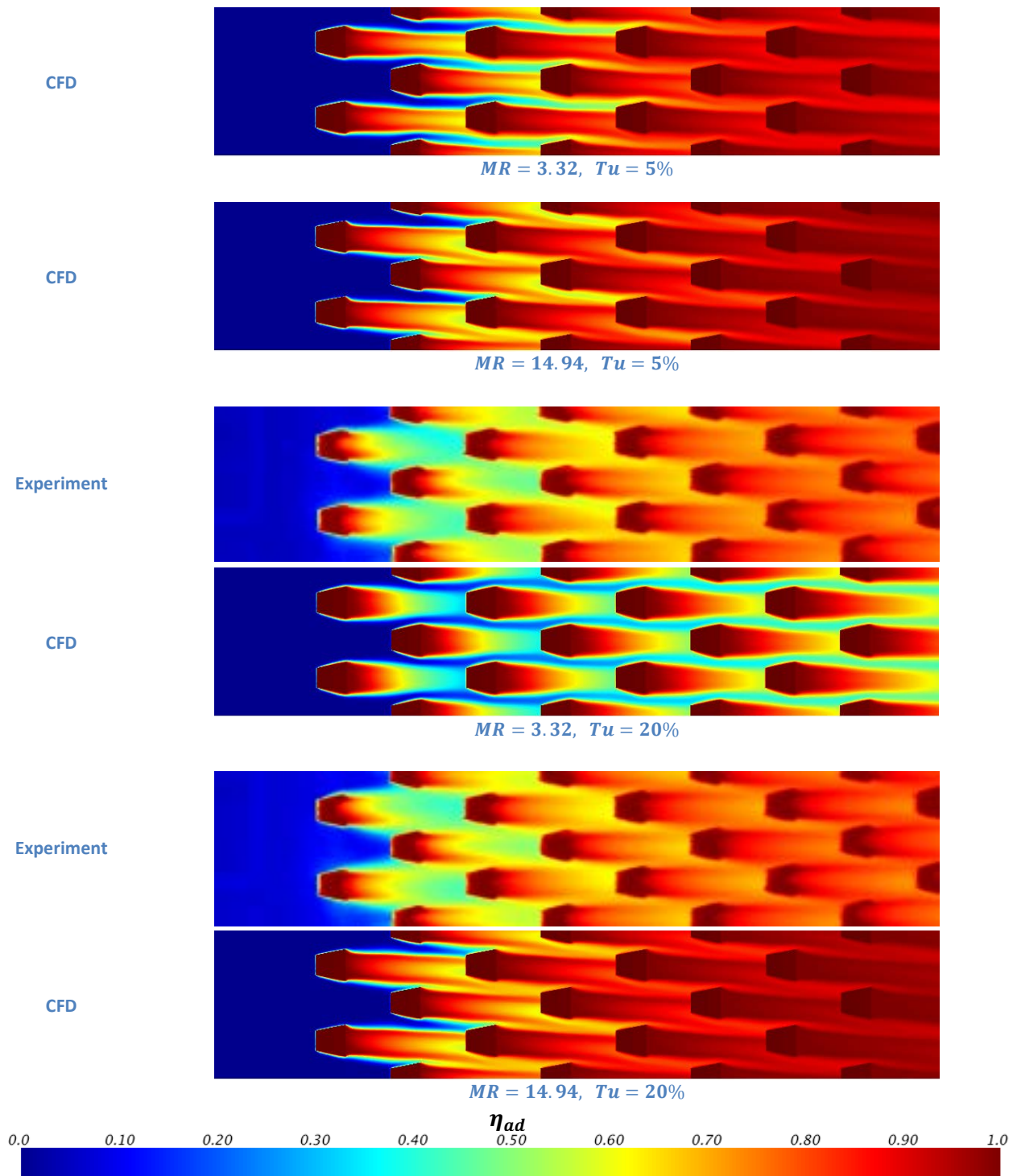
Figure 110 – Rectilinear helix adiabatic effectiveness comparison between experiment and CFD
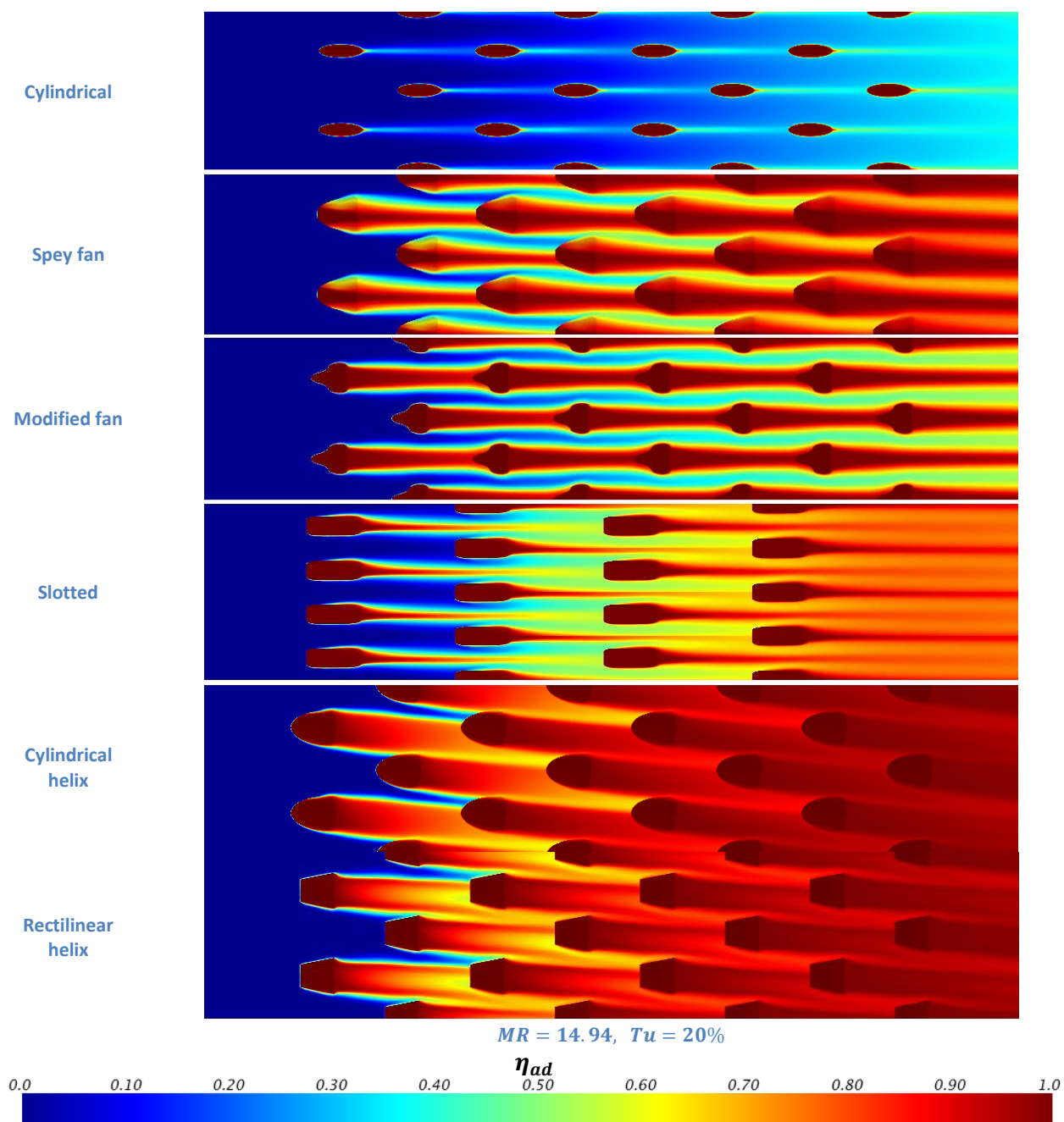
Figure 111 – Comparison of CFD results of various geometries at high momentum ratio and freestream turbulence intensity

6.1.2 Spanwise Averaged Data

Figures 112 to 117 show plots of spanwise averaged film effectiveness acquired through both experiment and simulation for each of the six geometries at the same conditions described in the previous section. Solid lines represent experimental data while dashed lines indicate data obtained through CFD simulations.

As suggested by the 2D surface contour data in Figure 105, the simulation does not match the experimental results for the Cylindrical hole case. Instead, as shown in Figure 112, the spanwise averaged film effectiveness is under-predicted by as much as 0.4. The only condition that could be considered to approximate the experimental data is at the $Tu = 20\%$ and $MR = 3.32$ condition but even this shows poor agreement after the 5$^{\text{th}}$ row of cooling holes. As these tests represent single skin type geometries, the pressure drop over the plate and hence blowing ratio is into the detached jet region for a cylindrical hole with flow generally remaining attached up to $BR = 0.7$ before becoming fully detached at $BR = 1$ as reported by Martin (57). While increasing freestream turbulence intensity increases the blowing ratios at which transition and detachment occur, the conditions considered in this study (the minimum blowing ratio considered is 1.75) are firmly in the detached jet regime. Therefore it is expected that the realisable $k - \varepsilon$ turbulence model used in this study is unable to capture the flow physics leading to the coolant pattern seen in the experimental data, however, the reasons behind this shortcoming in modelling detached jets is unexplained (66).

By fanning the exit region of the hole the exit velocity is reduced, resulting in a coolant flow that remains attached to the surface even at the highest blowing ratios applied here. The computational code is much better at modelling attached flows and hence the simulated spanwise averaged data for the remaining geometries provides a more favourable comparison to the experimental data. This is immediately apparent for the Spey fan case displayed in Figure 113. Here the data are generally similar with spanwise averaged adiabatic film effectiveness slightly over predicted at the higher momentum ratio conditions and slightly under-predicted at the lower momentum ratio condition. However, while the experimental data show little sensitivity to freestream turbulence level at the higher momentum ratios, the computational data indicate a mean difference of around 0.04. Conversely, the simulation indicates little sensitivity to freestream turbulence intensity at the lowest momentum ratio condition while the

spanwise averaged experimental data, and indeed the simulated 2D surface contours, both show a notable difference.

Figure 114 shows the spanwise averaged adiabatic film effectiveness plots for the Modified fan geometry. Here the simulations show an increased sensitivity to the freestream turbulence levels when compared with the experimental data. This is due to the increased turbulent mixing at higher turbulence intensity increasing the spread of the coolant. This brings the spanwise mixing of the coolant film more in line with that seen through the PSP experiment. However it is it should be noted again that the asymmetric nature of the physical plate caused by the DLD build direction, results in geometry which departs from that used for the computational domain. A rigorous and detailed comparison of the experiments and predictions performed for this geometry is therefore difficult.

With the exception of the $Tu = 20\%$ and $MR = 3.32$ case, Figure 115 shows that while initially under-predicting the film performance by a large margin (up to 67%), the Slotted simulation agrees more closely with the experimental data in the downstream direction as more rows of coolant are introduced. At the low turbulence, high momentum ratio condition the $k - \varepsilon$ turbulence model is unable to properly simulate the jet in crossflow interaction at the high momentum ratio resulting from the small area ratio of the fan. In this case the jet appears to be mostly detached similar to the cylindrical hole geometry.

Simulated data for the two helical designs is presented in Figures 116 and 117 for the circular and rectilinear cross sections respectively. Again the different flow conditions are largely similar with the exception of the high turbulence intensity, low momentum ratio condition. Both geometries show under-predicted film effectiveness performance compared to the experimental data at this condition of around 0.07-0.1. The film performance is over-predicted at the higher momentum ratio and lower turbulence intensity conditions. This over-prediction is large, with differences up to 0.14 seen in some areas due to the decreased lateral mixing caused in part by the isotropic turbulence model.

This inability to predict the absolute performance of the various geometries is expected when using a simple 2-equation RANS based turbulence model, partially because they treat turbulence as an isotropic property. One of the principal objectives of this study however is to determine if numerical modelling can be used to rank candidate cooling designs in order to

quickly down select geometries for further, more comprehensive investigation through either more complex simulations or experimental testing. In this case, the ability to capture the relative performance of many candidate designs becomes an important and desirable goal for the aerothermal engineer. This particular attribute is shown in Figure 118 which displays the relative ranking predicted for each of the geometries described here. This plot indicates that the best performance is given by the two helical geometries with the Circular cross section performing very slightly better than the Rectilinear case with a difference of around 0.02. The Spey fan geometry then falls 0.11 below with the Modified fan around 0.1 below that. The Slotted design lies around the same level as the Spey and Modified fanned designs due to the increased spacing between subsequent cooling rows and the Cylindrical design is then placed around 0.45 below the rest. While the differences between the performance levels are smaller in the experimental data, as can be seen in Figure 86, the ranking of the six geometries is the same. On this basis the computational method is useful as a tool to provide a first approximation of potential new effusion cooling designs.

Figure 112 - Cylindrical hole spanwise averaged overall effectiveness comparison between experiment and CFD

Figure 113 – Spey fan spanwise averaged overall effectiveness comparison between experiment and CFD
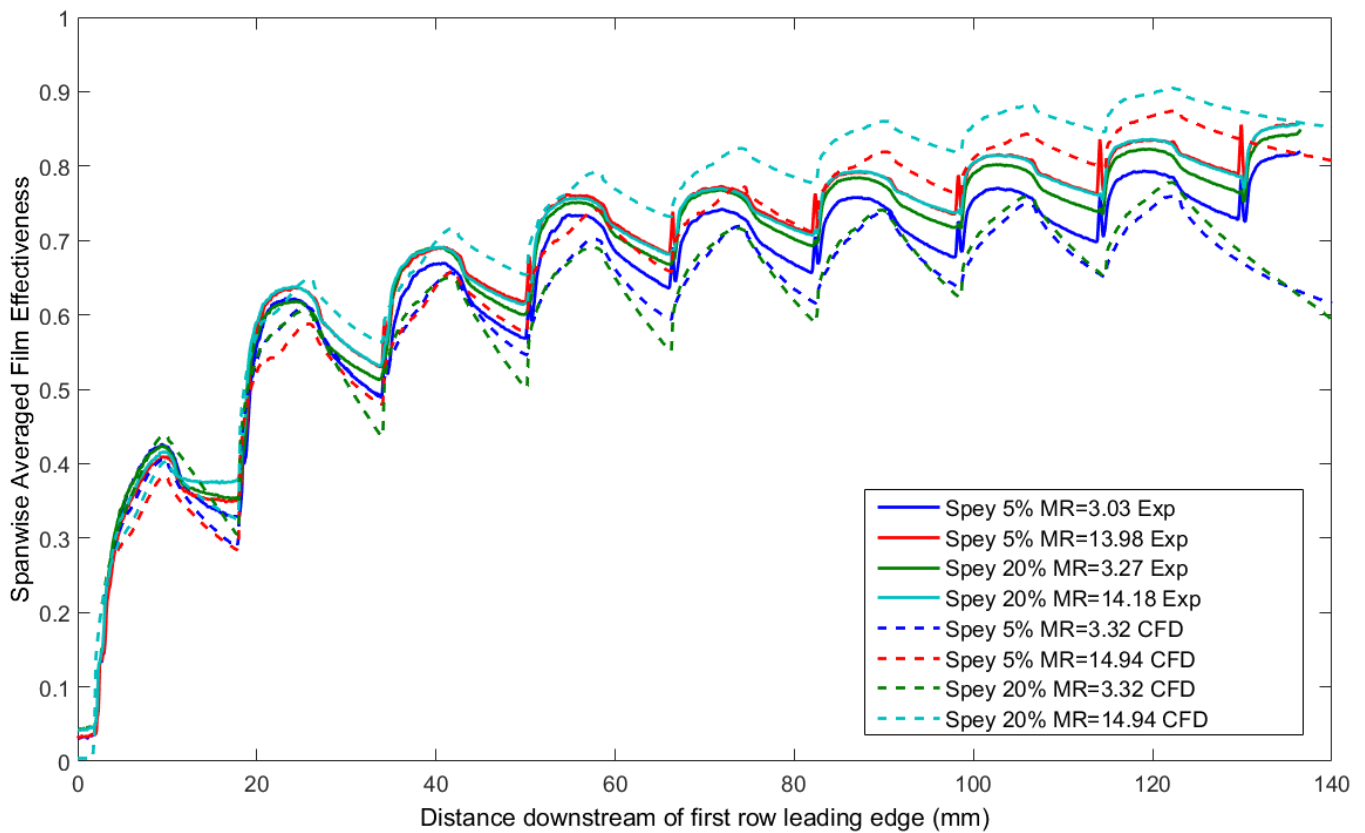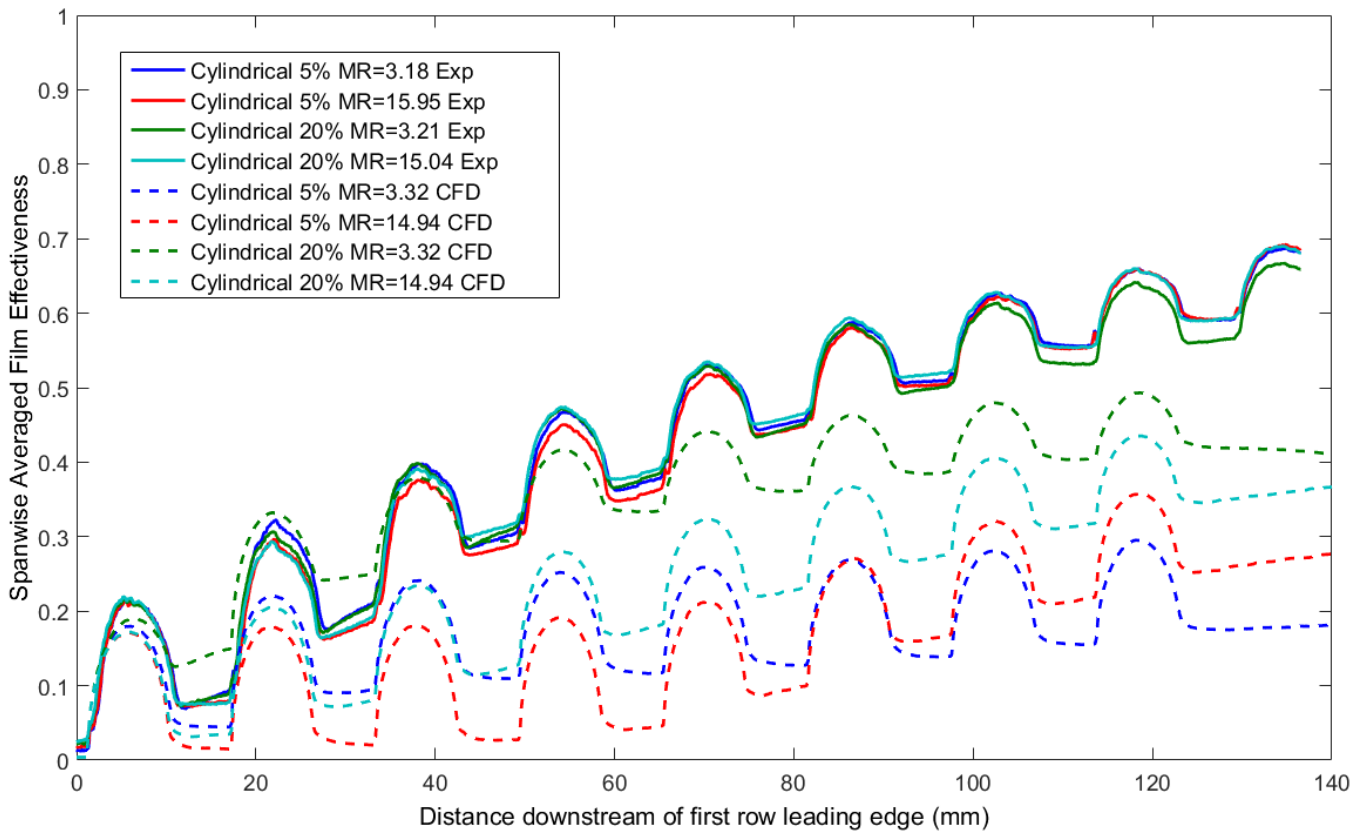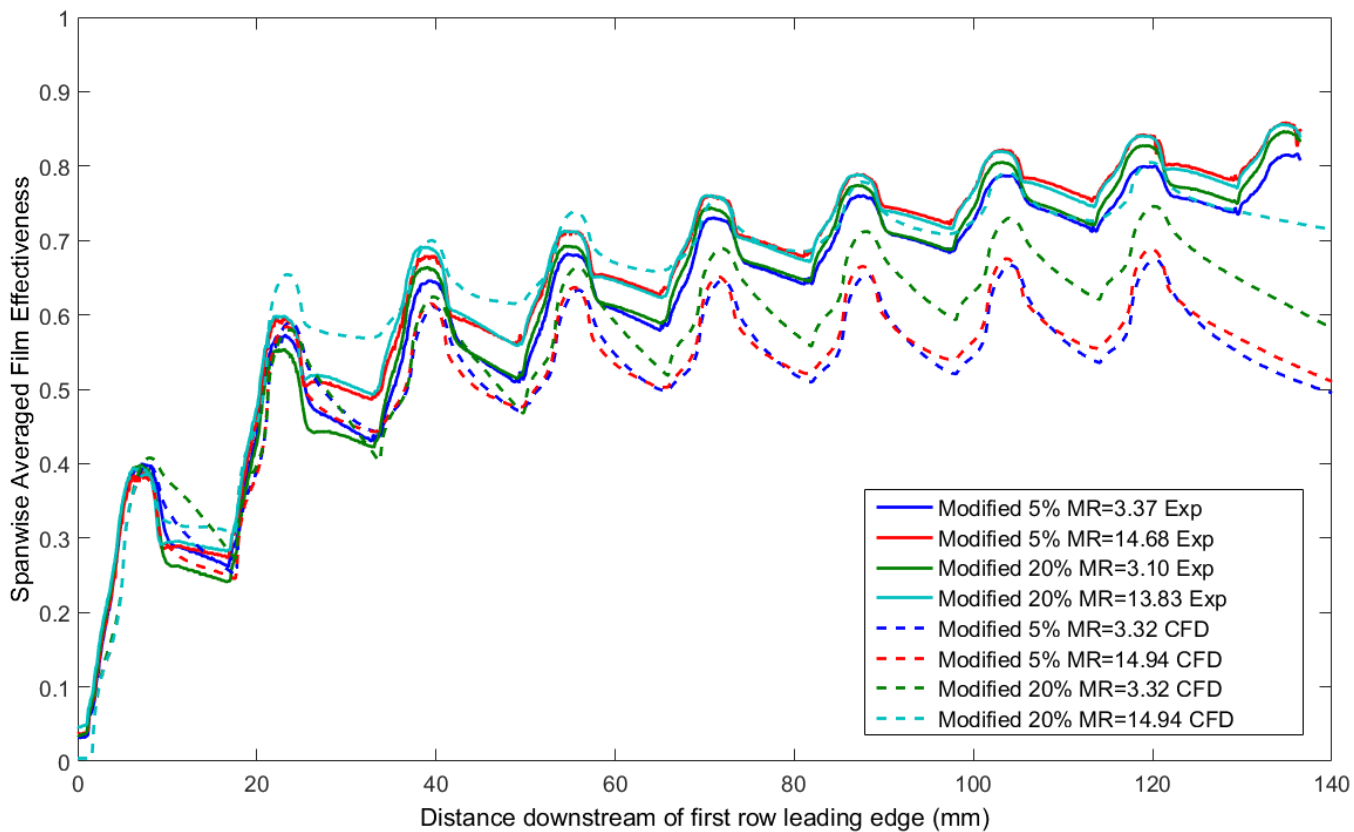
Figure 114 – Modified fan spanwise averaged overall effectiveness comparison between experiment and CFD
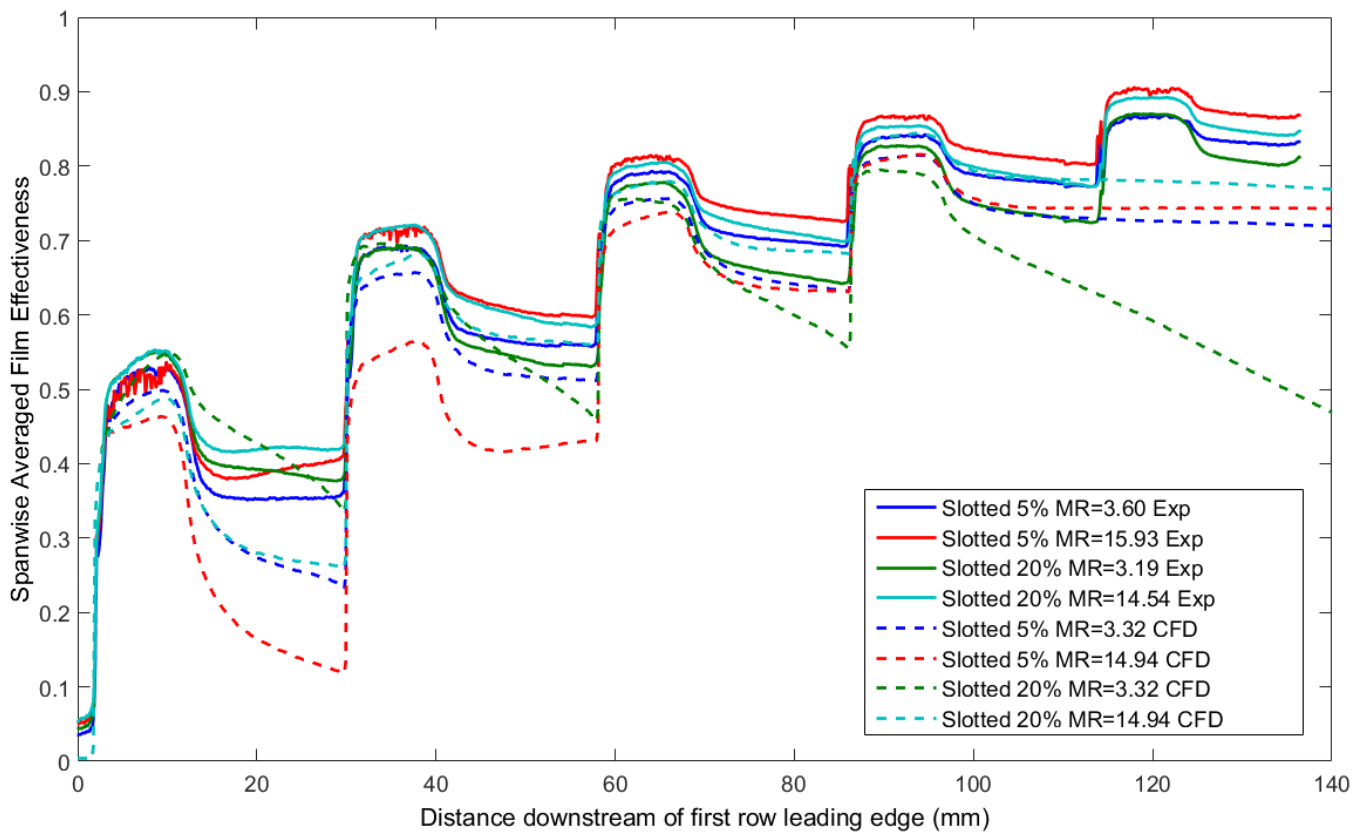
Figure 115 – Slotted spanwise averaged overall effectiveness comparison between experiment and CFD
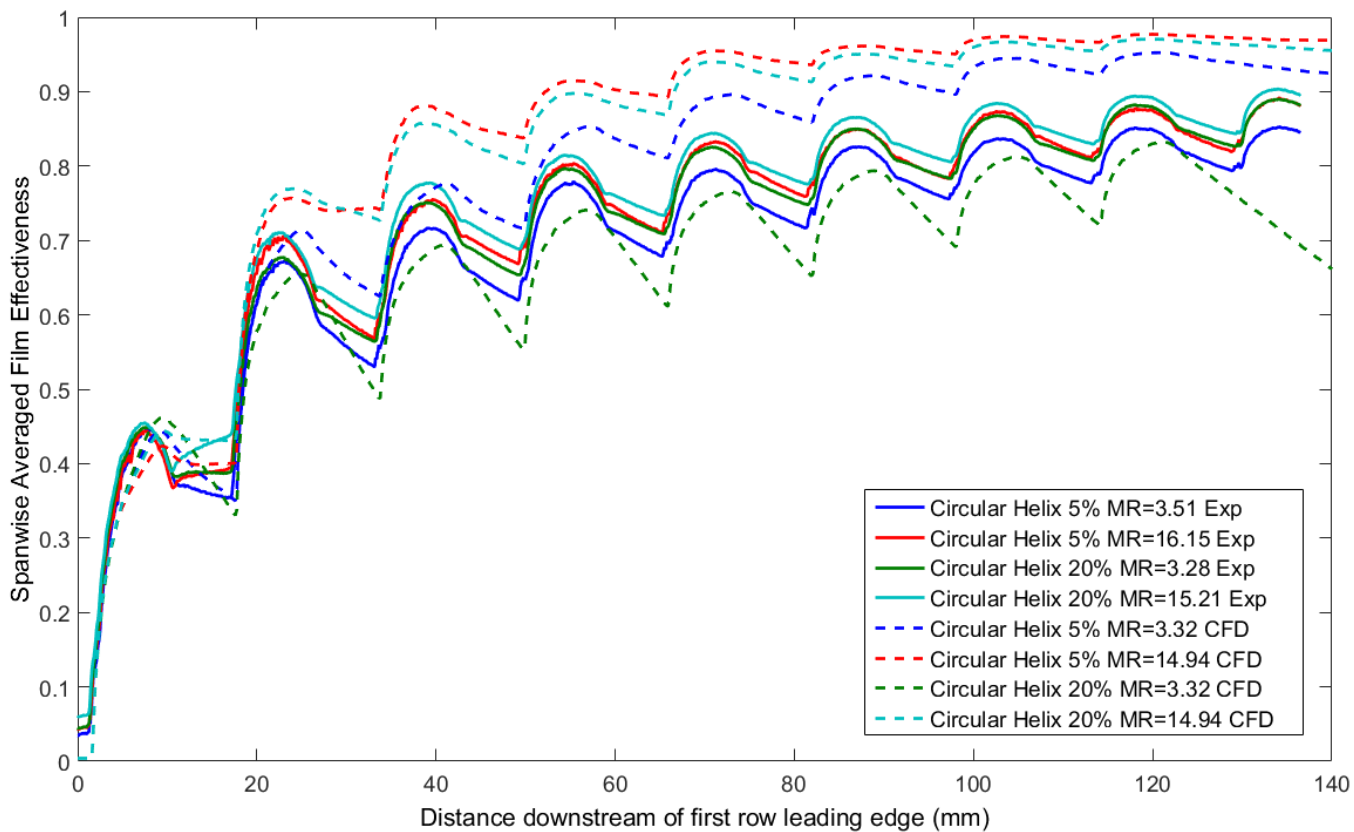
Figure 116 – Circular helix spanwise averaged overall effectiveness comparison between experiment and CFD
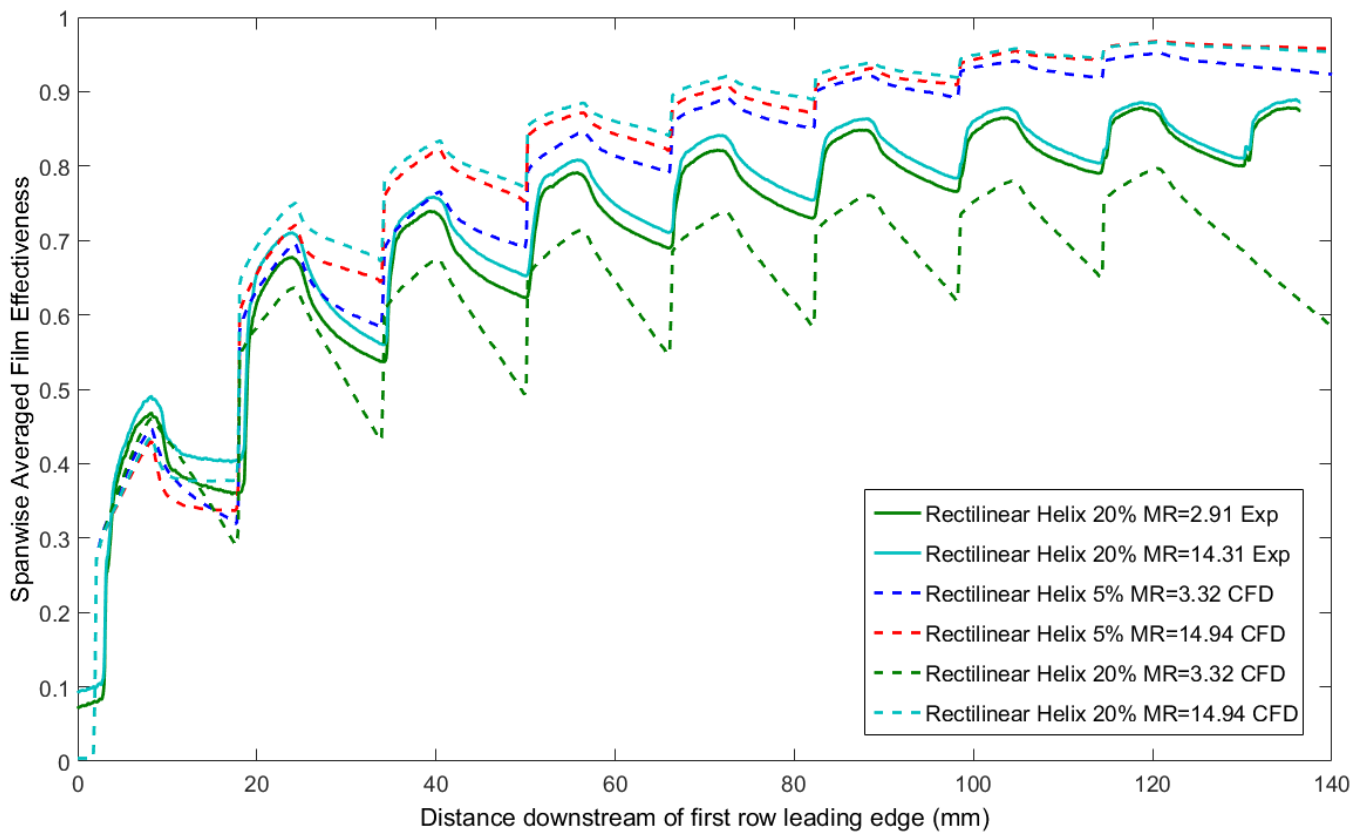
Figure 117 – Rectilinear helix spanwise averaged overall effectiveness comparison between experiment and CFD
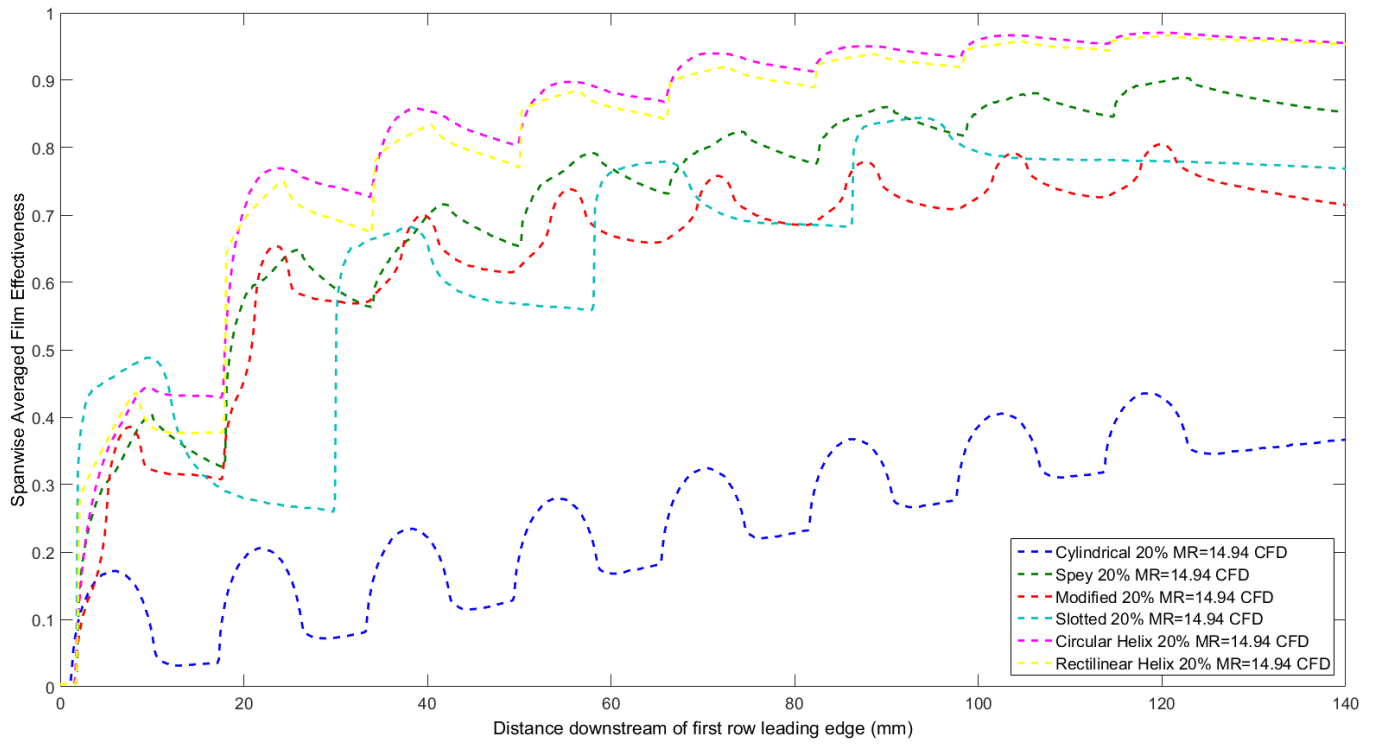
Figure 118 – Computational geometry comparison of span-wise averaged adiabatic effectiveness, $MR = 14.94, Tu = 20\%$

6.2   Conjugate Calculation

Measurement of the heat transfer due to internal heat removal within the cooling passages is the next step in understanding the performance of the combustor wall cooling geometries highlighted in this study. However, such measurements are not possible using the experimental techniques described and utilised as part of this study and are therefore beyond the scope of this piece of work. Therefore a brief computational approach is taken by looking at a single hole in a simulated infinite row with the same spacing as employed for the single hole adiabatic simulations and applying a conjugate heat transfer model to estimate the cooling performance of each design. Heat transfer through the internal surface of the hole is then extracted for each geometry and used to determine a normalised Stanton number.

6.2.1   Stanton number

Stanton number is dimensionless number which relates the heat transfer into a fluid to its thermal capacity. It can also be represented in terms of the Nusselt number, Reynolds number and Prandtl number of the fluid. This allows the use of the Reynold analogy to relate the momentum and thermal boundary layers, and in turn, express a relationship between the shear force at the wall due to viscous drag and the total heat transfer at the wall due to thermal diffusivity.

$$St = \frac{h}{\rho U c_p}, St = \frac{Nu}{Re\ Pr} \qquad \text{Equation 87a,b}$$

A high Stanton number indicates that more of the cooling capacity of the fluid is being utilised as more heat is being transferred into each unit of fluid flowing over the surface of the passage. This gives some indication of the efficiency of the heat transfer for a given cooling geometry as there is a finite pressure drop across the wall driving the viscous flow field. The helical geometries in particular are designed with this in mind and aim to increase the heat transfer at the wall by utilising the available pressure drop to enhance skin friction. A high Stanton number also indicates that the exit temperature of the fluid is increased, reducing the effectiveness of the film layer. However, this temperature increase is relatively small due to the high flow rate of coolant. Consideration here is only given to the heat transfer within the cooling passage. Consequently, a bulk average internal heat transfer coefficient h^* (Equation 88a) is determined by normalising the surface integral boundary heat flux through the internal passage wall by the aerodynamic effective area of the passage. All geometries are designed to have the same

effective area at a certain design condition and simulations are run with the same temperature and pressure boundary conditions. Therefore a caparison of overall performance between designs is possible. This heat transfer coefficient is then used to calculate the value St^* (Equation 88b). The value St^* provides a non-dimensional performance parameter which allows the comparison of the candidate designs.

$$h^* = \frac{\int q'' \, dA}{A_{eff} \, (T_\infty - T_c)}, St^* = \frac{h^*}{\rho_c U c_{p_c}}$$

<div align="right">**Equation 88a,b**</div>

Where;

$$U = \sqrt{\frac{2(P_c - P_\infty)}{\rho_c}}$$

<div align="right">**Equation 89**</div>

Small differences in the predicted effective area are observed when running the simulations at the conditions defined as part of this study compared to the conditions of the original design specifications used to define the experimental test plates. While this difference is relatively small and consistent for the majority of designs, the Rectilinear Helical design shows an appreciable difference, resulting in a larger effective area than the other geometries. These differences in effective area have little effect for the majority of the designs but it is worth noting that there is some influence on the Rectilinear Helical results. Consequently, the predicted effective area is used to normalise h^* in order to compare the six geometries.

Table 9 shows St^* predicted for the six designs as well as the normalised mean exit temperature at the two momentum ratio conditions simulated. It can be seen that in terms of St^* the helical designs both perform better than the straight hole designs investigated by more than 30%. This is to be expected as the design philosophy behind adding the helical section is to increase the amount of heat transferred out of the wall and into the cooling air. This is accomplished through two mechanisms. First, increasing the passage length leads to an increase surface area exposed to the coolant and second, by utilising the increased velocity gradients at the wall resultant from the curvature of the helix to increase skin friction. It can also be seen that through manipulating the cross section of the coolant passage the heat transferred can be influenced slightly, with the Rectilinear Helical showing a performance reduction relative to the Circular Helical of about 6%. While it would be expected that using a rectilinear cross section would increase both internal surface area and skin friction and therefore St^*, this reduction

could be attributed to the limitations of the turbulence modelling method. Interrogation of the flow field shows an inability to accurately capture the secondary flow structures created by the confluent boundary layers in the sharp corners of the Rectilinear cross section design as seen by Mahmud Alam et. al. (62). However, the results of the IR experiment detailed in section 5.2.3 also indicate that the Circular cross section helical design does slightly outperform the Rectilinear design in terms of overall effectiveness with similar adiabatic film effectiveness levels, indicating that the internal HTC through the passages is slightly higher for the Circular cross section design.

The results indicate that the Spey fanned design has lower internal heat removing capability than the Cylindrical design; this is due to the increased discharge coefficient resulting in smaller hole metering diameter and therefore decreased surface area within the solid. While the fanned section does increase surface area, the reduction in velocity as well as the separation within the fanned section of the hole results in a reduction in heat flux and hence Nusselt number in this area. As the Modified fan employs a steeper lay angle the passage length is reduced compared with the Cylindrical and Spey designs, however the internal surface area is only slightly reduced due to the long diverging section creating a steady increase in cross sectional area. This divergence causes a reduction in flow velocity, decreasing the heat transferred and resulting in similar overall performance to the Spey geometry.

The Slotted design shows the lowest Stanton number meaning the cooling potential of the fluid is not being utilised as effectively as with the other designs. This is a result of the widening of the cross section from a circle to a slot, reducing the ratio of surface area to flow volume and resulting in a smaller proportion of the cooling air being in contact with the wall to enable heat transfer. The Slotted design also incorporates a fairly long fanned section which fans in the longitudinal direction starting from around the centre of the passage length. This has the disadvantage of reducing flow velocity as well as further reducing the surface area to volume ratio, the overall effect of which is a reduced Nusselt number on the surface compared with the other straight passage designs.

At the low momentum ratio condition the flow is not moving as quickly through the passage, reducing the heat transferred from the metal as a result of the lower velocity gradient at the wall. However the reduced pressure drop also means the bulk velocity is reduced by about half resulting in a lower thermal capacity. As the flow travels through the cooling passage slower, it

is allowed more time to pick up heat and therefore more of the coolant thermal capacity is utilised and the flow exits the cooling passage at a higher temperature. The Cylindrical design has a difference in maximum normalised temperature at exit of 0.085. The overall result is a reduction in total heat flux out of the metal, supporting the observation of reduction in overall effectiveness at this lower flow rate condition. At this reduced flow condition the difference in St^* between the Cylindrical and helical geometries increases to over 60%. This indicates that the helical passages retain strong heat transfer performance at low momentum ratios.

6.2.2 Normalised Exit Temperature

A more common approach to assessing the bulk internal heat transfer performance of cooling hole geometries is to determine the fluid temperature difference between hole inlet and exit. This temperature difference is normalised by the temperature difference between the coolant and mainstream inlet boundaries. A plane section is defined at the hole exit in each of the geometries and an area average of the normalised temperature is calculated on this plane. As more heat is transferred into the fluid the temperature will increase, therefore the higher the normalised exit temperature, the better the performance of the cooling geometry at a given condition. As with the St^* measure, increasing momentum ratio results in an increase in through hole velocity. As the air is travelling through the passage quicker it has less time to remove heat from the wall and therefore the normalised exit temperature is lower than for the lower momentum ratio condition.

The normalised exit temperature data tabulated in Table 9 suggests that the Spey fan geometry transfers more heat into the fluid than the other geometries. However, this is not the case. The separation within the fanned section causes hot mainstream gas to be ingested at the edges of the fan as indicated by the areas of high normalised temperature as illustrated in Figure 119. The normalised exit temperature is calculated on a plane section across the exit, therefore this ingested flow is included in the average, resulting in a sizable increase in average exit temperature. Due to the low exit momentum of the flow from the Circular Helical design a small area of mainstream gas ingestion is again seen in a small patch towards the left hand side of the exit when looking downstream, although to a much lesser extent than for the Spey fan geometry.

With the exception of the Spey fan geometry, the relative performance of the six designs follows the same trends as noted previously, with the helical geometries showing a 30% larger

temperature increase than the straight designs. The Cylindrical and Modified Fan designs show similar performance and the Slotted design has the lowest temperature increase of around 20% less than the Cylindrical design, indicating lower heat transfer within the passage.

At the lower momentum ratio design the order remains the same but the relative differences change, with the Slotted design now showing only 8% reduction over the Cylindrical design. The benefit of coiling the internal passage again becomes more apparent at this lower flow rate condition, with the increased temperature difference of the Rectilinear design over the Cylindrical increasing to 45%.

Design	Stanton Number, $St*$		Normalised Exit Temperature	
	$MR = 14.94$	$MR = 3.32$	$MR = 14.94$	$MR = 3.32$
Cylindrical	0.124	0.179	0.169	0.282
Spey Fan	0.117	0.183	0.308	0.427
Modified Fan	0.116	0.176	0.172	0.292
Slotted	0.090	0.154	0.137	0.259
Circular Helix	0.172	0.303	0.256	0.431
Rectilinear Helix	0.161	0.286	0.217	0.408

Table 9 – Internal heat transfer performance

$MR = 14.94$ $MR = 3.32$

$MR = 14.94$ $MR = 3.32$
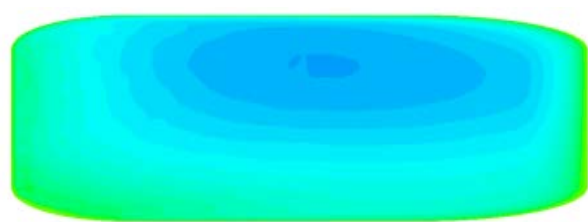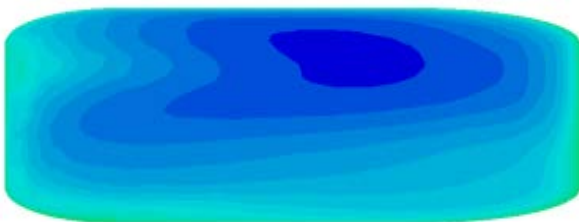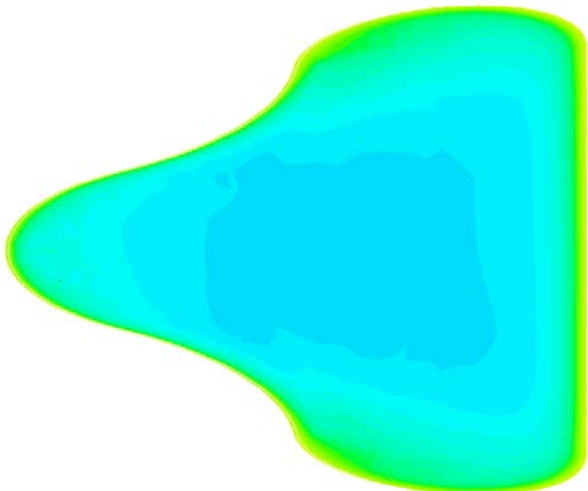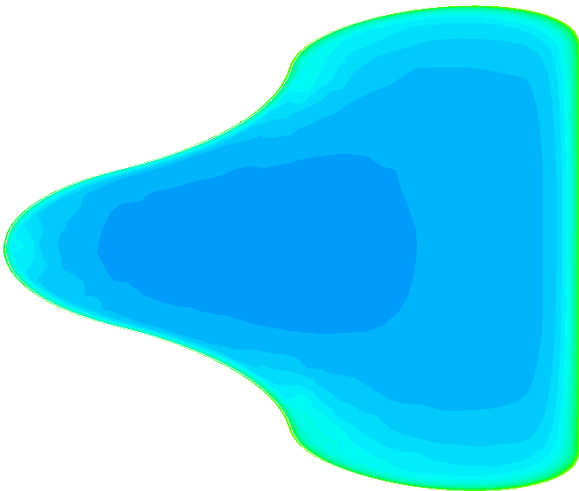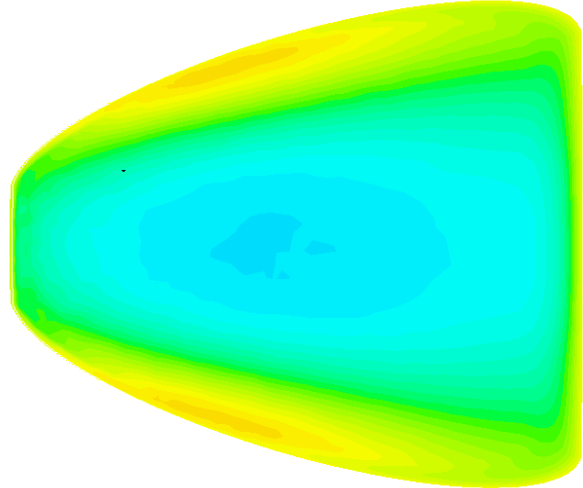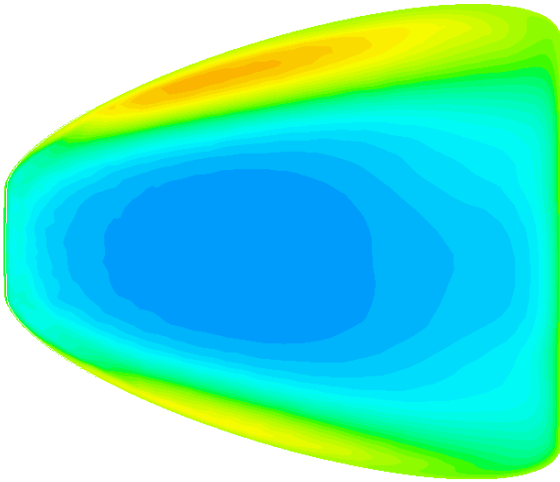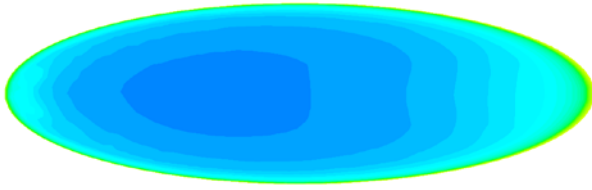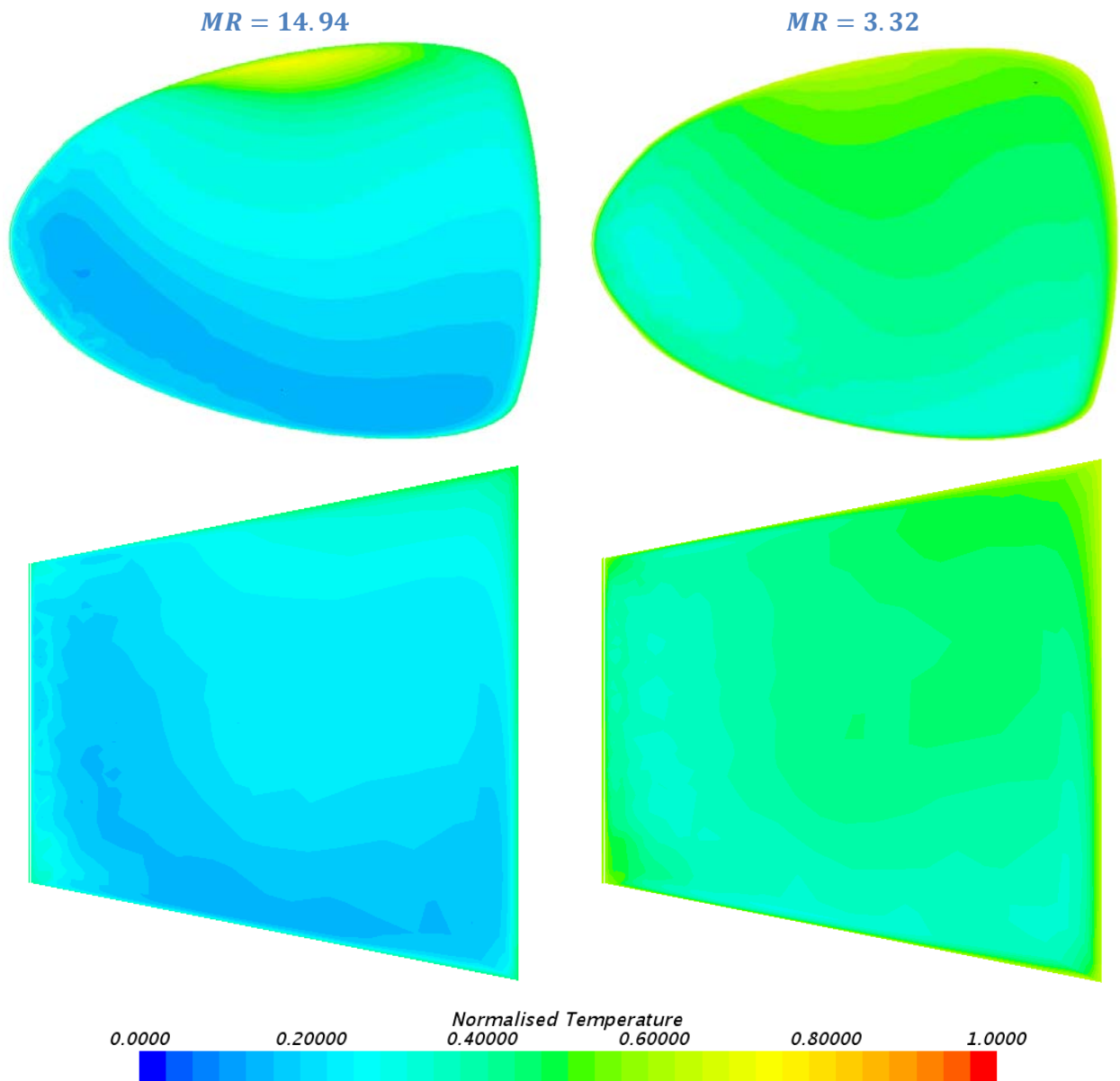
Figure 119 – Cross section of normalised temperature field at hole exit

7 Conclusions

This aim of this research is to develop and implement a number of tools to allow the assessment of different effusion cooling geometries using a number of performance measures. These tools are used to assess a range of sample cooling geometries and develop understanding of the effects of factors such as freestream turbulence intensity and pressure drop on both adiabatic and overall effectiveness performance measures. In order to achieve this both computational and experimental techniques have been developed and implemented with the use of a pre-existing test rig.

These methods are used to evaluate and rank the adiabatic film effectiveness, overall effectiveness and internal heat pickup performance of a number of representative combustor effusion cooling geometries at various freestream turbulence intensity conditions and momentum ratios. Six cooling geometries are considered ranging from simple angled cylindrical holes to more complex designs which can only be manufactured using additive manufacture methods such as DLD, including one design with a square cross section helically coiled passage and fanned exit region. The tools developed allow geometries to be assessed and ranked based on various parameters using quick and inexpensive methods.

The following sections summarise the results of the PSP based adiabatic film effectiveness measurements and overall effectiveness measurements made using the IR thermography technique as well as adiabatic film effectiveness and internal heat pickup simulations carried out using a RANS based computational method with modifications to reduce computational cost.

7.1 Adiabatic Film Effectiveness - Pressure Sensitive Paint

A technique which has not been previously used within the Aeronautical and Automotive engineering department at Loughborough University involving the use of pressure sensitive paint (PSP) is introduced and developed as part of this project. In this study PSP is used to measure the adiabatic film effectiveness of combustor representative cooling arrays. Through the use of this technique it is possible to measure the adiabatic effectiveness using a heat-mass transfer analogy, allowing the same metal test plates to be used for both adiabatic and overall effectiveness measurements. The six geometries are all tested at various pressure drop

conditions with momentum ratios in the range 3-16 and at both high (~20%) and low (~5%) turbulence intensity conditions.

The spanwise averaged data shows that the effect of freestream turbulence level can be to both improve and reduce the adiabatic film effectiveness depending on both the momentum ratio as well as the underlying design of both the cooling passage and their spatial distribution over the surface. It can also be seen that the sensitivity to freestream turbulence levels generally reduces at increased momentum ratio conditions.

The general effect of increasing freestream turbulence intensity on the distribution of injected coolant over the plate surface is to reduce the streamwise extent of the coolant and to promote its spreading in the spanwise direction.

There are no major differences between results obtained at different momentum ratio conditions, indicating that no mode changes occur within the range of conditions tested, equivalent to blowing ratios in the range 1.75-4.1. As expected at blowing ratio conditions above 1, the jet emerging from the cylindrical hole is detached from the surface. However due to the decreased velocity resultant from the fanned exit section, the jets emerging from all fanned geometries remain attached to the plate surface.

A maximum performance level is reached at $MR \cong 6.25$ for the majority of designs tested with all designs showing a small drop in performance at the $MR \cong 3$ condition. This indicates that increasing momentum ratio and hence coolant mass flow through the plate results in no performance benefit in terms of adiabatic film effectiveness past the $MR \cong 6.25$ mark. The main exception being the Slotted design which shows slight differences in spanwise averaged adiabatic film effectiveness at all but the highest momentum ratio condition as a result of the increased space between successive rows.

The Modified fan design shows a large performance difference of 0.04 between momentum ratio conditions after the first two rows of coolant injection. This difference reduces along the plate length with results collapsing towards the downstream end of the test plate.

Fanning the passage exit results in an immediate increase in film cooling performance, with all fanned designs showing significantly better film coverage than the Cylindrical hole design. Performance is improved in terms of developing a good film quickly, with fanned spanwise

averaged effectiveness increased by 0.2-0.3 downstream of the first row of cooling holes relative to the cylindrical design, as well as reaching a fully developed state after 3-5 rows compared to the Cylindrical design which does not reach a fully developed state after all 9 rows.

Fanning the exit also results in increased fully developed effectiveness level, with improvements in the 0.3-0.4 region over the non-fanned geometry.

Among the fanned geometries the designs employing aerodynamically efficient diverging sections produce the best film coverage with the helical geometries showing an improvement in spanwise averaged film effectiveness of around 0.1 over the Spey fan design.

Overall the PSP technique provides good results. It is able to capture expected physical effects such as separation within the fanned section of the Spey geometry. Accuracy and repeatability could be improved with modifications made to the lighting setup and use of a more sensitive camera as well as improvements to the experimental methodology such as banding the exposure in order to utilise more of the dynamic range of the camera in the low intensity, low effectiveness regions.

Application of the paint on metal test plates is relatively easy and is simple to remove allowing test plates to be used in multiple experiments utilising various measurement techniques. Calibration of the paint response is stable and easy to obtain with the equipment detailed in this report. Opportunities for improving the calibration process include the use of a PID controller to more consistently control the temperature of the calibration coupon as well as using a fixed lighting setup to provide consistent illumination to the entire surface in both calibration and test environments.

7.2   Overall Effectiveness - IR Thermography

IR thermography has previously been used within the research group to measure adiabatic film effectiveness using an ultra-low conductivity material test plate and correcting for conduction errors. Work done in parallel to this study expands this technique to measure overall effectiveness without requiring major modifications to the experimental procedures or methodology. In order to correctly scale the relative contributions of both convective and conductive heat transfer it is necessary to match both the Nusselt number and the Biot number respectively to the engine conditions. This is achieved through selection of the test plate material in order to provide the correct ratio of thermal conductivity between the air and metal

at experimental conditions. A representative engine metal temperature can then be calculated from scaled rig tests.

Experiments are carried out on the same test plates used in the PSP tests, requiring only that the PSP be removed from the plate surface and a flat black paint of known emissivity applied instead. A number of modifications to the rig are required when switching between IR and PSP experiments including switching between a closed and open loop configuration, switching between an IR transparent and plain glass optical access window and switching from a heated mainstream flow to running isothermally. Experiments are conducted over the same range of momentum ratio and freestream turbulence intensity conditions as for the adiabatic film effectiveness tests.

Unlike the adiabatic results, freestream turbulence intensity has a notable effect on overall effectiveness with all geometries showing a decrease in overall effectiveness at the higher turbulence intensity condition. However, the adiabatic test indicates that the driving temperature is not necessarily increased suggesting that the increased turbulence intensity results in an increased heat transfer coefficient. This indicates that to get a complete picture of effusion cooled wall performance, information about both adiabatic film effectiveness and HTC is required from the same experimental setup.

A double peak is seen in spanwise averaged overall effectiveness at high turbulence and momentum ratio conditions on the Cylindrical and Slotted designs due to the increased HTC downstream of the first row of cooling holes compounding with the poor film performance in this area increasing the heat load at the surface relative to the area upstream of the first row of holes.

The maximum difference between spanwise averaged overall effectiveness at low and high turbulence intensity conditions at the same momentum ratio is around 0.015 in the Circular helical design, 0.02 in the Spey fan design and up to 0.03 for the other designs tested.

Increasing momentum ratio increases the overall effectiveness for all designs. In addition to the small improvements seen in film effectiveness, the increase in momentum ratio also results in more heat removed through forced convection over the internal surface of the coolant passages.

Shorter passage lengths see a larger difference in peak spanwise averaged overall effectiveness between momentum ratio conditions at both the $MR \cong 16$ and $MR \cong 3$ ends of the range with larger differences seen between the lower conditions. The Cylindrical and Spey fan designs share the same passage length but due to the superior film created by the fanned exit section the Spey fan design shows much better overall effectiveness performance, overcoming the decreased internal heat removed as a result of the reduced diameter and hence internal surface area.

The increased internal surface area of the long diverging section of the Modified fan design contrasts with the reduced velocity resultant from the divergence to result in better overall effectiveness performance than the Spey fan even though the adiabatic film effectiveness performance is slightly worse.

By increasing the number of cooling passages in each row, the Slotted design shows high initial overall effectiveness. This indicates that tightly packing the holes into a single row increases the internal heat removal as well as providing good film coverage. However the increased longitudinal distance to the next row combined with the increased HTC between the first and second rows results in a dip in overall effectiveness performance, particularly at increased momentum ratio conditions. Downstream of the second row the film effectiveness is high enough to offset the increased HTC and therefore overall effectiveness increases.

The two helical geometries show higher overall effectiveness than the other designs tested in terms of both the entire plate as well as the area leading up to the first row of passage exits. The Rectilinear design has slightly higher performance over the first two rows indicating that the internal heat removal is slightly better than in the Circular design. The Circular design however shows higher overall effectiveness performance over the remainder of the plate due to the more uniform distribution of coolant produced by the rounded fan shape.

In summary, the designs tested fall into three loose categories with the Cylindrical design showing the lowest average performance of around 0.82-0.85 as a baseline. The Spey and Modified fan designs improve on this with performance in the 0.87-0.90 region and form the enhanced film category. The two helical designs show the best performance in the 0.94-0.95 region through a combination of both improved film and internal heat removal. The altered

array pattern used in the Slotted design results in performance levels which span the gap between the fanned and helical designs.

Potential improvements to this experiment include addition of a second loop allowing the coolant to be supplied in a more realistic combustor feed annulus arrangement rather than plenum fed and allowing optical access for IR measurements of the cold side to be made. This would allow the cold side flow to be delivered in a more representative cross-flow manner as well as better capturing the cold side cross flow and convective heat transfer. Another avenue for improvement would be the addition of a radiative heat load in order to completely capture the relative contributions of the heat transfer processes encountered in a real combustor environment and thus improve the accuracy of the representative metal temperature calculated through the overall effectiveness measure.

7.3   Adiabatic Film Effectiveness - CFD

The aim of the computational investigation is to develop a method of quickly assessing the adiabatic film effectiveness performance of a number of potential design solutions. As such a method of reducing the complexity of the computational mesh is developed whereby a single hole is simulated using a high definition mesh, the hole exit conditions are then extracted and used as an inlet boundary condition for a multi-hole array. This removes the need to simulate a large number of coolant holes and reduces the number of grid cells required by assuming the influence of the array pattern on the local flow through each hole is insignificant. As a first pass method of down selection this assumption was found to be acceptable.

RANS based turbulence models are known to be unable to properly capture the anisotropic nature of the turbulent flow developed in a jet in crossflow type regime. The 2D surface contours of adiabatic effectiveness show the spanwise spreading of coolant is under predicted while the streamwise extent is over predicted. Despite this shortcoming, this simplified approach has been shown to correctly rank each of the cooling geometries investigated here. Through comparing the surface contours it is possible to gain an understanding of the relative performance of the various cooling geometries as well as some indication as to the associated flow features. For example, the CFD captures the separation in the fanned section of the Spey geometry.

The simulations are run at both high (14.94) and low (3.32) momentum ratios as well as 20% and 5% turbulence intensity conditions and show significantly different coolant distribution for most designs at the high turbulence, low momentum ratio condition with the remaining conditions showing similar results as expected and suggested from the PSP experiments. This indicates that care must be taken when using this technique at low blowing rates.

Differences in spanwise averaged adiabatic film effectiveness between designs are greater in the CFD data, however they do follow the same trends as found in the PSP experiments, particularly at the most representative high turbulence and high momentum ratio conditions.

The Cylindrical hole shows the worst performance with spanwise averaged adiabatic film effectiveness levels in the 0.2-0.3 region, this is significantly improved upon by the Spey and Modified fanned designs which show similar effectiveness levels of around 0.7-0.8. The best performance is provided by the helical designs which both show very high effectiveness of >0.9. The CFD data shows the Slotted design performing similarly to the Spey fan geometry, however this is likely due to the RANS based turbulence model's inability to properly capture the film behaviour in the extended length between cooling rows in this geometry.

7.4 Internal Cooling – CFD

Investigation into the internal heat transfer characteristics of effusion cooling geometries is the next step in understanding the effusion cooling system. However, obtaining experimental data regarding the internal heat transfer performance is difficult and beyond the scope of this study. Therefore, a computational simulation is used to assess the internal heat transfer characteristics of a single hole in an infinite row with the same spacing as used in the test plate arrays. These simulations are carried out at $MR = 14.94$ and $MR = 3.32$ conditions and turbulence intensity of 20%.

To compare each of the designs, a modified Stanton number St^* is defined using a heat transfer coefficient h^* based on the heat transferred through the internal surface of the cooling passage and its effective area. The parameter St^* recognises the importance of the analogy between heat and momentum transfer and had been adopted here as a suitable non-dimensional parameter for comparing the internal convective cooling performance of each passage design. A non-dimensional temperature rise is also used as a more standard parameter for comparing heat transfer through a cooling passage.

The two helical geometries show similar performance and around a 30% increase in St^* relative to the Cylindrical design due to the extended internal surface area and increased wall shear stress created by coiling the passage.

The remaining three fanned geometries all show around a 5-25% decrease in St^* relative to the Cylindrical design. This is caused by a combination of the following factors;

- Reductions in hole diameter and hence surface area as a result of higher Cd values
- Reduction in flow velocity due to fanning
- Reduced passage length due to increased lay angle
- Poor surface area to volume ratio as a result of cross section shape

All designs show an increase in St^* at the lower momentum ratio condition relative to their individual results at the higher condition. At the lower flow condition the through hole velocity reduces. This lessens the convective heat transfer between the wall and the coolant but also the thermal capacity of the fluid. The result of which is an overall increase in the utilisation of the thermal capacity as more heat is removed per unit flow rate relative to the higher momentum ratio condition.

In terms of normalised temperature change across the passage similar trends are seen, with the Cylindrical and Modified geometries showing similar levels of temperature increase, the Slotted design about 20% less and the helical designs about 30% more at the $MR = 14.94$ condition. At the $MR = 3.32$ condition, changes in the relative differences to the Cylindrical baseline are observed for the Slotted design, which reduces to an 8% reduction, and the helical designs, which increase to a 45% relative performance gain.

Due to the separated flow region within the fan of the Spey design, mainstream air is drawn into the fanned region resulting in a much higher average temperature on the exit plane used to define the normalised temperature change, invalidating this result. Similarly, due to the low exit momentum in the cylindrical helix design, a small area of mainstream gas incursion into the fanned section is also visible, though in this case the hot air does not propagate to the metal surface.

7.5 Implications and Achievements

As part of this project a number of experimental and computational methods have introduced and developed, including the addition of pressure sensitive paint measurements of adiabatic film effectiveness, development of software enabling IR and PSP experiments to be run with minimal user input and introduction of a 2-part computational model to predict the adiabatic cooling performance of effusion cooling arrays. Using these tools a number of cooling geometries are assessed and their sensitivity to parameters including freestream turbulence levels and wall pressure drop explored. Baseline cooling hole designs are also compared with increasingly complex geometries enabled by the DLD manufacturing technique with large improvements in terms of wall temperature achieved. This implies that major increases in the potential cooling performance of combustor wall liners are possible and the techniques described as part of this work will allow designers to explore and optimise the expanded design space offered by new ALM based manufacture.

7.6 Outlook and Future Work

This study introduces a number of tools allowing the evaluation of combustor wall cooling geometries in terms of both adiabatic and overall effectiveness as well as briefly touching on assessing the contribution of the internal geometry. Six geometries are tested and simulated at a range of test conditions involving changes in both freestream turbulence intensity and momentum ratio. The next step in development of these techniques would be to utilise them for an optimisation study whereby other factors affecting film cooling performance are evaluated including both array based changes such as hole size, spacing and number as well as passage geometrical changes such as shape, injection and compound angle. This would allow sensitivity to these factors to be assessed and identification of the most important factors to forming a good cooling solution. This is particularly important with the introduction and development of manufacturing techniques such as DLD which opens up the available design space through reductions in restrictions due to both manufacture capability as well as cost.

Results obtained through use of the PSP technique could be utilised to develop a more representative turbulence model for a jets in crossflow situation as well as driving analytical models of the cooling system. Further development of the PSP technique itself to allow time dependent results to be taken would be possible through use of a fast response porous PSP formulation and CCD camera with high speed capture capabilities. A number of methods of

error reduction could also be implemented including the use of a more sensitive CCD camera or a High Dynamic Range type technique involving different exposure times allowing the dynamic range of the camera to be better utilised in the lower effectiveness regions where the intensity response of the paint is very low compared with the high effectiveness regions.

Future development opportunities for the test rig include addition of cold side crossflow capabilities to better capture the cold side flow field of the combustor liner as well as addition of a radiative heat load allowing the relative contribution of all three heat transfer mechanisms (i.e. conduction convection and radiation) to be captured and a more representative equivalent engine temperature to be backed out of the overall effectiveness measurements.

Improvements to the computational methodology include identification and implementation of a more representative turbulence model such as that used by Bacci and Fachinni (55) which attempts to account for the anisotropic nature of the turbulent flow. This would allow more confidence in the relative performance results of different cooling schemes.

As the internal heat transfer model only looks at a single hole in isolation, the technique could be improved to simulate a hole in the centre of an array and assess the asymptotic performance of each design. This model would also be a good candidate for a more in depth turbulence approach such as LES or DES, particularly for more complex geometries such as the Rectilinear design where secondary flow structures are predicted to influence the through hole heat transfer but are not captured by a RANS based approach. An experimental campaign looking at the internal heat transfer performance would also be useful in order to validate the computational results.

The preceding tools demonstrate the capability to optimise the design of combustor cooling geometries and it is hoped they will be continually used and developed in order to increase accuracy and enhance confidence in results allowing both more innovative and efficient cooling designs to be implemented in future generations of gas turbine engines.

8 References

1. **Rolls-Royce.** *The Jet Engine.* 5th Revised Edition. s.l. : John Wiley & Sons Inc, 2015. 9781119065999.

2. **Spittle, Peter.** Gas Turbine Technology. *IOPscience.* [Online] November 2003. [Cited: 19 May 2012.] http://iopscience.iop.org/0031-9120/38/6/002.

3. **Cerri, G., et al.** *Advances in effusive cooling techniques of gas turbines.* s.l. : Applied Thermal Engineering 27, 2007. 692-698.

4. **Bogard, D.G. and Thole, K.A.** *Gas Turbine Film Cooling.* s.l. : AIAA Journal of Propulsion and Power, 2006. AIAA-18034-904.

5. **Greffrath, F.** *Measurement of the temperature-dependent spectral emissivities of ceramic coatings.* Bochum : Rolls-Royce Deutchland Ltd & Co KG, Blankenfelde-Mahlow, 2012.

6. **Han, Je-Chin, Dutta, Sandip and Ekkad, Srinath.** *Gas Turbine Heat Transfer and Cooling Technology.* s.l. : CRC Press, 2012.

7. **Hartnett, J P.** Mass Transfer Cooling. [book auth.] W M Rohsenow, J P Hartnett and E N Ganic. *Handbook of Heat Transfer Applications.* New York, London : McGraw-Hill, 1998.

8. **Mahesh, Krishnan.** *The Interaction of Jets with Crossflow.* s.l. : Annual Reviews, 2013, Annual Review of Fluid Mechanics, Vol. 45, pp. 379-407.

9. **Thole, K, et al.** *Flowfield Measurement for Film-Cooling Holes With Expanded Exits.* s.l. : ASME, 1998, Journal of Turbomachinery, Vol. 120, pp. 327-336.

10. **Smith, S H and Mungal, M G.** *Mixing, structure and scaling of the jet in crossflow.* s.l. : Cambridge University Press, 1998, J. Fluid Mechanics, Vol. 357, pp. 83-122.

11. **Wurm, B, et al.** *Impact of Swirl Flow on the Cooling Performance of an Effusion Cooled Combustor Liner.* 12, s.l. : ASME, 11 Oct 2012, Journal of Engineering for Gas Turbines and Power, Vol. 134. 121503.

12. **Baldauf, S, et al.** *Correlation of Film-Cooling Effectiveness From Thermographic Measurements at Enginelike Conditions.* 4, s.l. : ASME, 07 Nov 2002, Journal of Turbomachinery, Vol. 124, pp. 686-698.

13. **Pedersen, D R, Eckert, E R. G and Goldstein, R J.** *Film Cooling With Large Denstiy Differences Between the Mainstream and Secondary Fluid Measured by the Heat-Mass Transfer Analogy.* 4, s.l. : ASME, Nov 1977, Journal of Heat Transfer, Vol. 99, pp. 620-627.

14. **Baldauf, S, Schulz, A and Wittig, S.** *High Resolution Measurements of Local Effectiveness by Discreet Hole Film Cooling.* 4, s.l. : ASME, Feb 1999, Journal of Turbomachinery, Vol. 123, pp. 758-765.

15. **Sinha, A K, Bogard, D G and Crawford, M E.** *Film-Cooling Effectiveness Downstream of a Single Row of Holes With Variable Density Ratio.* 3, s.l. : ASME, Jul 1991, Journal of Turbomachinery, Vol. 113, pp. 442-449.

16. **Launder, B E and York, J.** *Discrete-hole Cooling in the Presence of Free Stream Turbulence and Strong Favourable Pressure Gradent.* 11, s.l. : Elsevier, Nov 1974, International Journal of Heat and Mass Transfer, Vol. 17, pp. 1403-1409. ISSN 0017-9310.

17. **Kadotani, K and Goldstein, R J.** *Effect of Mainstream Variables on Jets Issuing from a Row of Inclined Round Holes.* 2, s.l. : ASME, Apr 1979, Journal of Engineering for Gas Turbines and Power, Vol. 101, pp. 298-304.

18. **Kadotani, K and Goldstein, R J.** *On the Nature of Jets Entering a Turbulent Flow: Part A - Jet-Mainstream Interaction.* 3, s.l. : ASME, Jul 1979, Journal of Engineering for Gas Turbines and Power, Vol. 101, pp. 459-465.

19. **Kadotani, K and Goldstein, R J.** *On the Nature of Jets Entering a Turbulent Flow: Part B - Film Cooling Performance.* 3, s.l. : ASME, Jul 1979, Journal of Engineering for Gas Turbines and Power, Vol. 101, pp. 466-470.

20. **Kohli, A and Bogard, D G.** *Effects of Very High Free-Stream Turbulence on the Jet-Mainstream Interaction in a Film Cooling Flow.* 4, s.l. : ASME, Oct 1998, Journal of Turbomachinery, Vol. 120, pp. 785-790.

21. **Kohli, A and Bogard, D G.** *Adiabatic Effectiveness, Thermal Fields,and Velocity Fields for Film Cooling With Large Angle Injection.* 2, s.l. : ASME, Apr 1997, Journal of Turbomachinery, Vol. 119, pp. 352-358.

22. **Schmidt, D L, Sen, B and Bogard, D G.** *Film Cooling with Compound Angle Holes: Adiabatic Effectiveness.* 4, s.l. : ASME, Oct 1996, Journal of Turbomachinery, Vol. 118, pp. 807-813.

23. **Sen, B, Schmidt, D L and Bogard, D G.** *Film Cooling With Compound Angle Holes: Heat Transfer.* 4, s.l. : ASME, Oct 1996, Journal of Turbomachinery, Vol. 118, pp. 800-806.

24. **Schmidt, D L and Bogard, D G.** *Effects of Free-Stream Turbulence and Surface Roughness on Laterally Injected Film Cooling.* New York : ASME, 1997. Proceedings of the 32nd National Heat Transfer Conference. Vol. 12, pp. 233-244. HTD-Vol. 350.

25. **Saumweber, Christian, Schulz, Achmed and Wittig, Sigmar.** *Free-Stream Turbulence Effects on Film Cooling With Shaped Holes.* 1, s.l. : ASME, Jan 2003, Journal of Turbomachinery, Vol. 125, pp. 65-73.

26. **Schulz, A.** *Infrared Thermography as Applied to Film Cooling of Gas Turbine Components.* 7, s.l. : IOP, 2000, Measurement Science and Technology, Vol. 11, pp. 948-956.

27. **Martin, Damian and Thorpe, Steven J.** *Experiments on combustor effusion cooling under conditions of very high free-stream turbulence.* Loughborough : ASME, 2012. GT2012-68863.

28. **Zhang, Luzeng, et al.** *Turbine Nozzle Film Cooling Study Using the Pressure Sensitive Paint (PSP) Technique.* Indianapolis : ASME, 1999. ASME 1999 International Gas Turbine and Aeroengine Congress and Exhibition. Vol. 3. 99-GT-196.

29. **Zhang, Luzeng J and Jaiswal, Ruchira Sharma.** *Turbine Nozzle Endwall Film Cooling Using Pressure-Sensitive Paint.* 4, s.l. : ASME, Feb 2001, Journal of Turbomachinery, Vol. 123, pp. 730-738.

30. **Ahn, Jaeyong, et al.** *Rotating Turbine Blade with Two Rows of Film Cooling Holes Using Pressure Sensitive Paint.* 4, s.l. : ASME, Oct 2005, Journal of Heat Transfer, Vol. 128, pp. 879-888.

31. **Jonsson, Magnus.** *Application of Photoluminescent Measurement Techniques for Quantitative Assessment of Turbine Film Cooling.* Lausanne : Swiss Federal Institue of Technology (EPFL), 2010. 4650.

32. **Jones, T V.** *Theory for the use of Foreign Gas in Simulating Film Cooling.* 3, s.l. : Elsevier, June 1999, International Journal of Heat and Fluid Flow, Vol. 20, pp. 349-354. ISSN 0142-424X.

33. **Dhall, Tarun, Humber, William G and Camci, Cengiz.** *Pressure Sensitive Paint for Analysis of Film-Cooling Effects on a Gas Turbine Blade Tip.* s.l. : Pennsylvania State University.

34. **Facchini, B, et al.** *Film-Cooling Adiabatic Effectiveness Measurement on a Real High Pressure Turbine Blade.* Firenze : University of Florence, 2013.

35. **Navarra, Kelly R.** *Development of the Pressure-Sensitive-Paint Technique for Advanced Turbomachinery Applications.* s.l. : Virginia Polytechnic Institute and State University, 1997.

36. **Liu, T and Sullivan, J P.** *Pressure and Temperature Sensitive Paints.* s.l. : Springer, 2005. 3-540-22241-3.

37. **Gebbie, David A, et al.** *PSP-Based Experimental Investigation of a Blanded Wing Body Aircraft.* Toronto : American Institute of Aeronautics and Astronautics, 2005. 23rd AIAA Applied Aerodynamics Conference. 2005-4719.

38. UniFIB Pressure Sensitive Paint Datasheet. [Online] www.psp-tsp.com.

39. **Anderson, John D.** *Computational Fluid Dynamics: The Basics with Applications.* s.l. : McGraw-Hill Education, 1995. ISBN 0070016852.

40. **Blazek, J.** *Computational Fluid Dynamics: Principles and Applications.* s.l. : Elsevier, 2001. ISBN 0080430090.

41. **Versteeg, H K and Malalasekera, W.** *An Introduction to Computational Fluid Dynamics: The Finite Volume Method.* s.l. : Pearson Education Ltd, 2007. ISBN 978-0-13-127498-3.

42. *Star CCM+ User Manual.*

43. **Nichols, R.H.** *Turbulence Models and Their Appliocation to Complex Flows rev 4.01.*

44. **CFD Online.** Mesh Calssification. *cfd-online.* [Online] 15 May 2007. [Cited: 21 May 2012.] http://www.cfd-online.com/Wiki/Mesh_classification.

45. **Page, G.** *CFD Grid Generation Lecture Slides.* s.l. : Loughborough University, 2011.

46. **ONERA.** Computation Fluid Dynamics and Aeroacoustics. *ONERA.* [Online] 25 November 2010. [Cited: 18 January 2012.] http://www.onera.fr/dsna-en/cassiopee/grid-generation-module.php.

47. **www.itk.org.** ParaView UG Curvilinear.png. *Insight Toolkit.* [Online] 10 December 2010. [Cited: 18 January 2012.] http://www.itk.org/Wiki/File:ParaView_UG_Curvilinear.png.

48. **CGNS.** Example Files. *CFD General Notation System.* [Online] [Cited: 18 January 2012.] http://cgns.sourceforge.net/CGNSFiles/Bruce/yf17.gif.

49. **CentaurSoft.** Prism Layers. *Centaur Software.* [Online] [Cited: 18 January 2012.] http://www.centaursoft.com/prism-layers.

50. **Mendez, S. and Nicoud, F.** *Large-eddy simulation of a bi-periodic turbulent flow with effusion.* s.l. : J. Fluid Mech., 2007.

51. **P. Miron, C.Beray, V. Sabelnikov.** *Effect of blowing rate on the film cooling coverage on a multi-holed plate: application on combustor walls.* s.l. : WIT press, 2004. ISBN 1-85312-705-1.

52. **Ceccerini, A., et al.** *Combined Effect of Slot Injection, Effusion Array and Dilution Hole on the Cooling Performance of a Real Combustor Liner Part 2: Numerical Analysis.* s.l. : ASME Turbo Expo, 2010. GT2010-22937.

53. **Ceccerini, A., et al.** *Combined Effect of Slot Injection, Effusion Array and Dilution Hole on the Cooling Performance of a Real Combustor Liner.* s.l. : ASME Turbo Expo, 2009. GT2009-60047.

54. **Harrison, K.L. and Bogard, D.G.** *Comparison of RANS Turbulance Models for Prediction of Film Cooling Performance.* Berlin : ASME Turbo Expo 2008, 2008. Vol. 4. GT2008-51423.

55. **Bacci, A. and Facchini, B.** *Turbulence modelling for the numerical simulation of film and effusion cooling flows.* s.l. : ASME Turbo Expo, 2007. GT2007-27182.

56. **Roy, S, Kapadia, S and Heidmann, J.** *Film Cooling Analysis Using DES Turbulence Model.* s.l. : ASME, 2003. GT2003-38140.

57. **Martin, Damian.** *Effects of High Intensity, Large-Scale Free-Stream Turbulence on Combustor Effusion Cooling.* s.l. : Loughborough University, 2013.

58. **Martiny, M, Schulz, A and Wittig, S.** *Mathematical Model Describing the Coupled Heat Transfer in Effucion Cooled Combustor Walls.* Orlando : ASME, 1997, Vol. 3. 97-GT-329.

59. **Kays, William M and Crawford, Michael E.** *Convective Heat and Mass Transfer.* s.l. : McGraw-Hill Science/Engineering/Math, 1993. ISBN 10:0070337217 / ISBN 13:9780070337213.

60. **Kline, S J and McClintock, F A.** *Describing Uncertainties in Single Sample Experiments.* s.l. : Mechanical Engineering, 1953, Mechanical Engineering, Vol. 75, pp. 3-8.

61. **Jayakumar, J.S.** *Helically Coiled Heat Exchangers.* s.l. : InTech, 2012. ISBN: 978-953-51-0278-6.

62. **Alam, MD, Begum, Delowara and Yamamoto, K.** *Flow Through a Helical Pipe with Rectangular Cross-Section.* s.l. : ANAME, December 2007, Journal of Naval Architecture and Marine Engineering, Vol. 4, pp. 99-110. 1813-8535.

63. **Shih, T. -H., et al.** *A New k-ε Eddy Viscosity Model for High Reynolds Number Turbulent Flows – Model Development and Validation.* Lewis Research Center, NASA. Cleveland : United States, 1994. Technical Report. NASA TM 106721.

64. **Peric, M. and Ferguson, S.** The advantages of polyhedral meshes. *plmmarketplace.* [Online] [Cited: 18th January 2012.] http://www.plmmarketplace.com/upload/Temp/The_Advantage _of_polyhedral.pdf.

65. **L. Guo, Y.Y. Yan, J.D. Maltson.** *Numerical study on discharge coefficients of a jet in crossflow.* s.l. : Elsevier, 2011. 323-332.

66. **Harrison, K.L. and Bogard, D.G.** *Comparison of RANS Turbulance Models for Prediction of Film Cooling Performance.* s.l. : ASME Turbo Expo 2008, 2008. GT2008-51423.

67. **Facchini, Bruno, et al.** *Adiabatic and Overall Effectiveness Measurements of an Effusion Cooling Array for Turbine Endwall Application.* s.l. : ASME, 2010, Journal of Turbomachinery, Vol. 132(4). 041008.

68. **Ceccerini, A., et al.** *Combined Effect of Slot Injection, Effusion Array and Dilution Hole on the Cooling Performance of a Real Combustor Liner.* Florida : ASME Turbo Expo, 2009. ASME Turbo Expo. GT2009-60047.

69. **Dittmar, J, Schulz, A and Wittig, S.** *Assessment of Various Film-Cooling Configurations Including Shaped and Compund Angle Holes Based on Large-Scale Experiments.* s.l. : ASME, 2003, Journal of Turbomachinery, Vol. 125(1), pp. 57-64. 2002-GT-30176.

70. **Thrift, A, Thole, K and Hada, S.** *Effects of an axisymmetric contoured end wall on a nozzle guide vane: Adiabatic effectiveness measurements.* 041007, 2011, Journal of Turbomachinery, Vol. 133(4).

71. **Varvel, Trent Alan.** *Shaped Hole Effects of Film Cooling Effectiveness and a Comparison of Multible Effectiveness Measurement Techniques.* s.l. : Texas A&M University, 2004.

72. **Jones, T V.** *Theory for the use of foreign gas in simulating film cooling.* 1999, International Journal of Heat and Fluid Flow, Vol. 20(3), pp. 349-354.

73. **Gebbie, David A, et al.** *PSP-Based Experimental Investigation of a Blended Wing Body Aircraft.* s.l. : AIAA, 2005. 23rd AIAA Applied Aerodynamics Conferece. AIAA2005-4719.

74. **Steiner, Patrick.** *Application of the Pressure Sensitive Paint Technique to the Turbomachinery Environment.* Lausanne : Swiss Federal Institute of Technology, 2001. 2297.

75. **Dhall, Tarun, Humber, William G and Camci, Cengiz.** *Pressure Sensitive Paint for Analysis of Film-Cooling Effects on a Gas Turbine Blade Tip.* s.l. : Pennsylvania State University, 2004.

76. **Andreini, Antonio, et al.** *Combined Effect of Slot Injection, Effusion Array and Dilution Hole on the Cooling Performance of a Real Combustor Liner Part 2: Numerical Analysis.* Glasgow : ASME Turbo Expo, 2010. ASME Turbo Expo. GT2010-22937.

77. **Acharya, Sumanta, Tyagi, Mayank and Hoda, Asif.** *Flow and Heat Transfer Predictions for Film Cooling.* May 2001, Annals of the New York Academy of Sciences, Vol. 934, pp. 110-125.

78. **Sasaki, M, et al.** *Film Cooling Effectiveness for Multirow Holes.* 1979, J. Eng. Gas Turbines Power, Vol. 101(1), pp. 101-108.

79. **Martin, Damian and Thorpe, Steven J.** *Experiments on Combustor Effusion Cooling Under Conditions of Very High Free-Stream Turbulence.* Copenhagen : s.n., 2012. ASME Turbo Expo. GT2012-68863.

80. **Walters, D K and Leylek, J H.** *A detailed analysis of film-cooling physics: Part I Streamwise injection with cylindrical holes.* 1997, Journal of Turbomachinery, Vol. 122(1), pp. 102-112.

81. **Li, Xueying, et al.** *Algebraic Anisotrpic Turbulence Modeling of Compound Angled Film Cooling Validated by Particle Image Velocimetry and Pressure Sensitive Paint Measurements.* 2014, Journal of Heat Transfer, Vols. 136(3), 032201.

82. **CFD Online.** Direct numerical simulation (DNS). *CFD Online.* [Online] [Cited: 17th January 2012.] http://www.cfd-online.com/Wiki/Direct_numerical_simulation_(DNS).

83. **CFD Online.** Y+ Wall distance estimation. *CFD Online.* [Online] [Cited: 18th January 2012.] http://www.cfd-online.com/Tools/yplus.php.

84. **Gordon, R. and Levy, Y.** *Optomization of Wall Cooling in Gas Turbine Combustor Through Three-Dimensional Numerical Simulation.* s.l. : Journal of Engineering for Gas Turbines and Power, 2005.

85. **Innovative Scientific Solutions Inc.** Pressure Sensitive Paints. *ISSI.* [Online] [Cited: 3 July 2014.] http://psp-tsp.com/index.php?id=115.

Appendix A Experimental Results

A.1 Adiabatic Film Effectiveness Results

A.1 Adiabatic Film Effectiveness Results

$MR = 3.18$

$MR = 6.60$

$MR = 9.94$

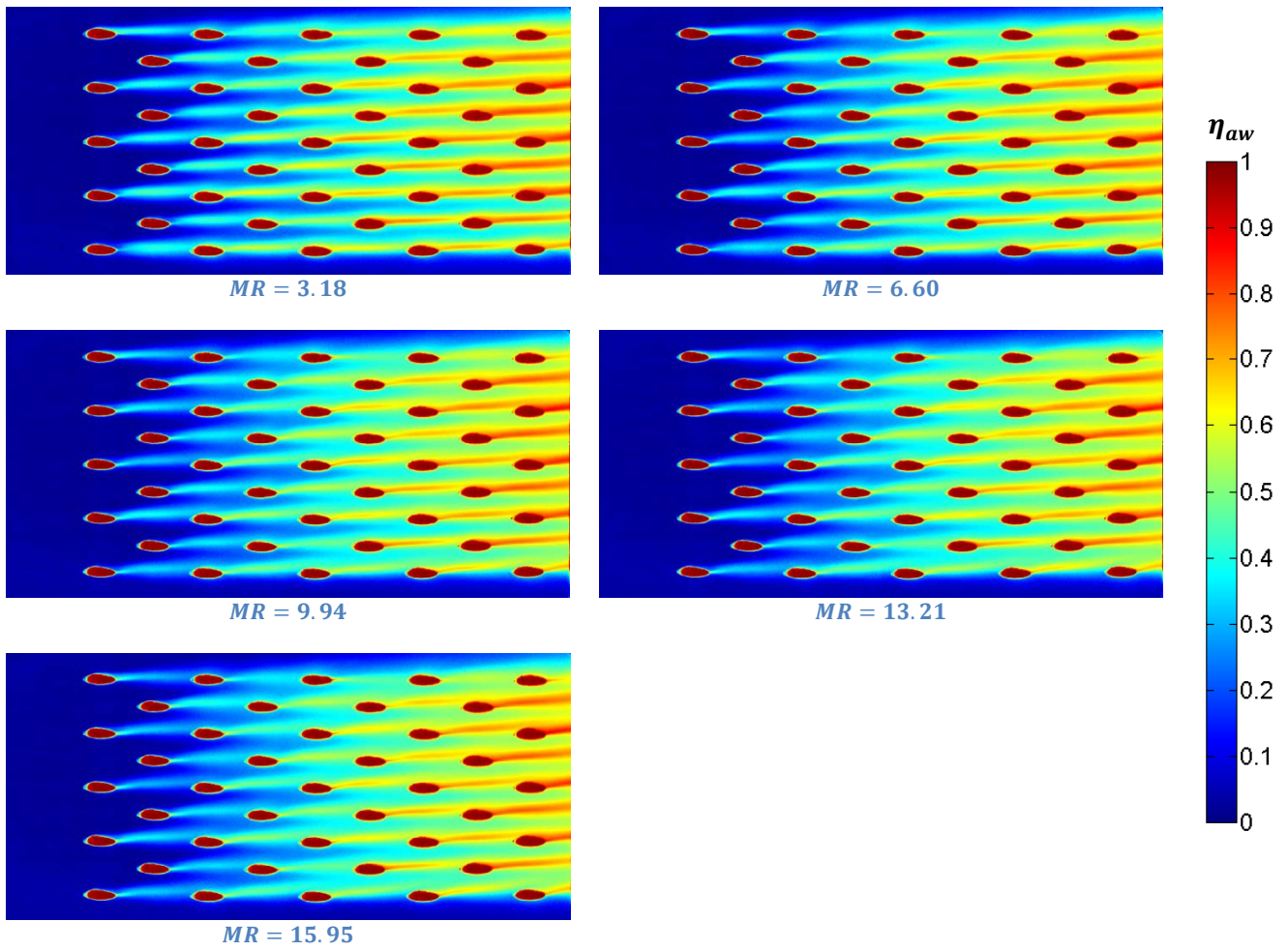$MR = 13.21$

$MR = 15.95$

Figure A-1 – Cylindrical hole adiabatic film effectiveness at various momentum ratio conditions and $Tu = 5\%$

Figure A-2 – Cylindrical hole spanwise averaged adiabatic film effectiveness at various momentum ratio conditions and $Tu = 5\%$

$MR = 3.03$ $MR = 6.14$

$MR = 8.91$ $MR = 11.67$

$MR = 13.98$

Figure A-3 – Spey fan adiabatic film effectiveness at various momentum ratio conditions and $Tu = 5\%$

Figure A-4 – Spey fan spanwise averaged adiabatic film effectiveness at various momentum ratio conditions and $Tu = 5\%$

A.1 Adiabatic Film Effectiveness Results

$$MR = 3.37$$
$$MR = 6.62$$
$$MR = 9.89$$
$$MR = 12.46$$
$$MR = 14.68$$

Figure A-5 – Modified fan adiabatic film effectiveness at various momentum ratio conditions and $Tu = 5\%$
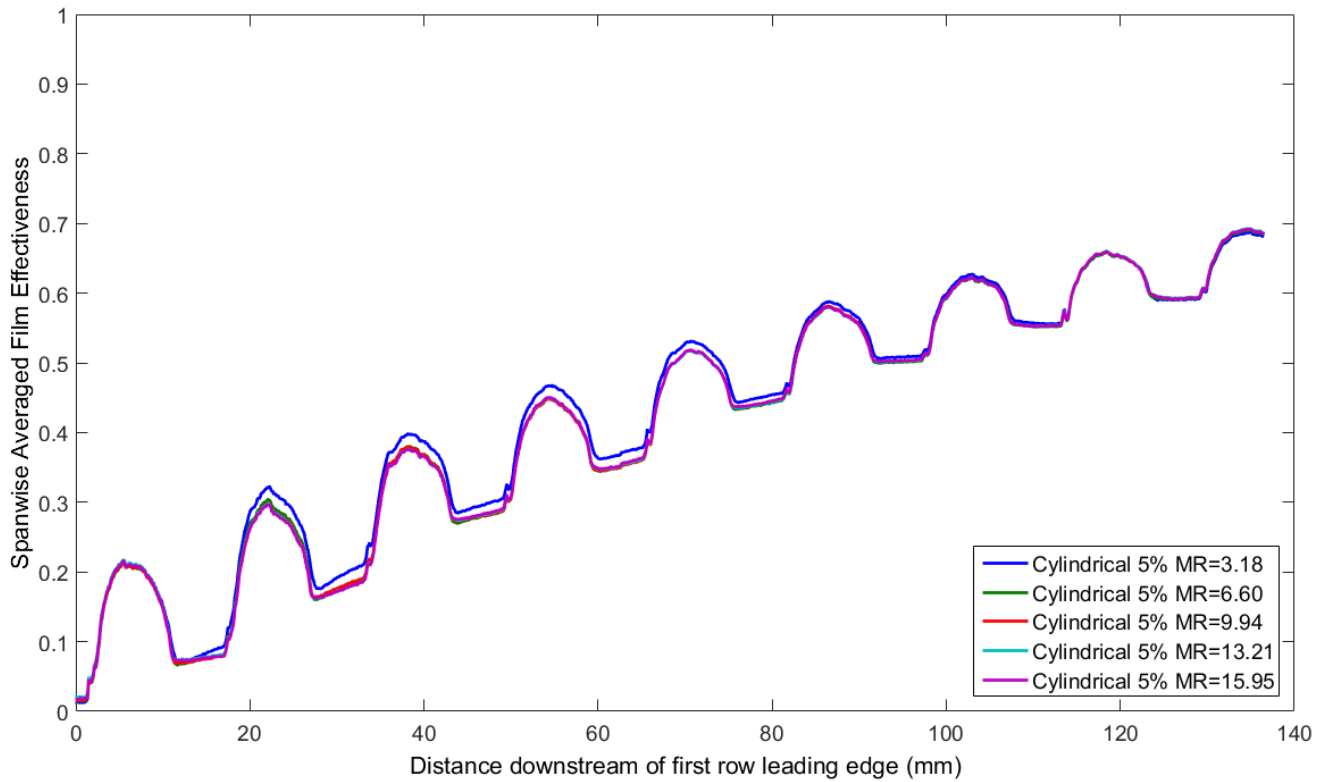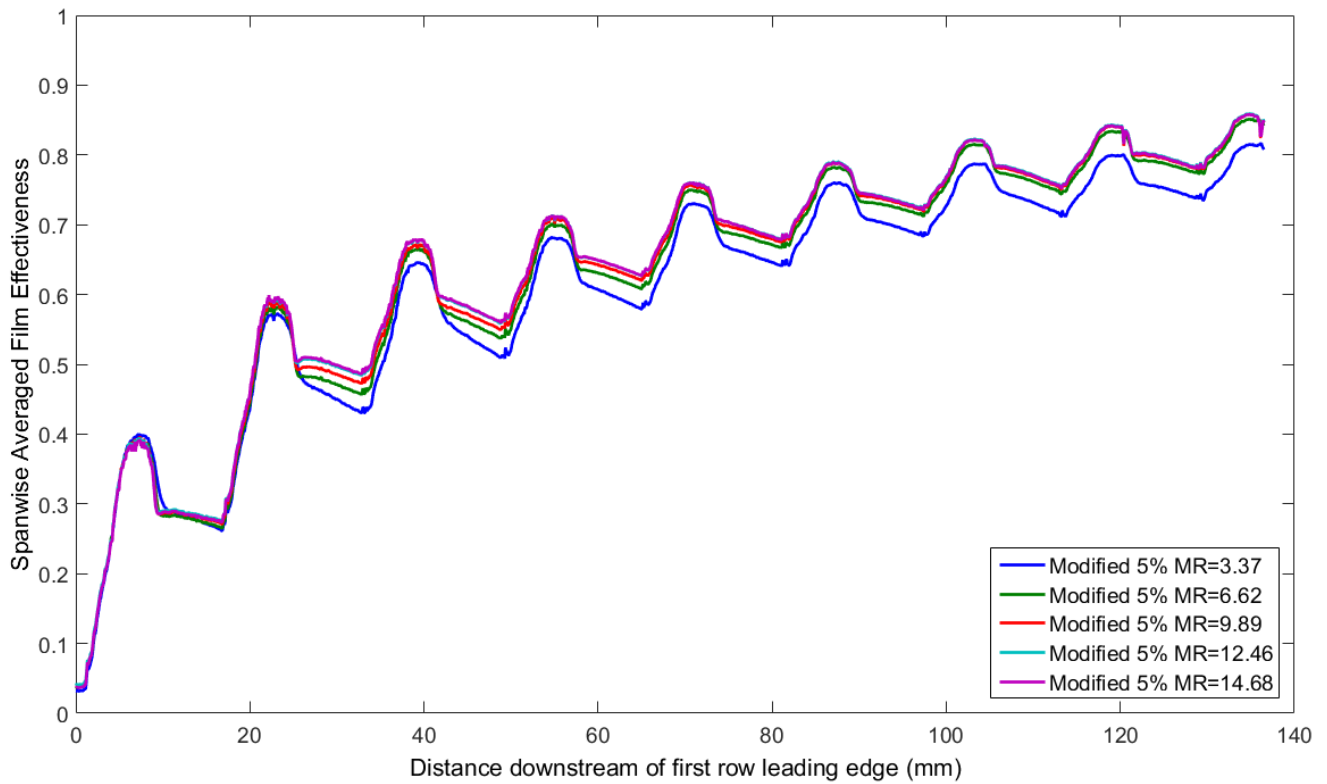

Figure A-6 – Modified fan spanwise averaged adiabatic film effectiveness at various momentum ratio conditions and $Tu = 5\%$

A.1 Adiabatic Film Effectiveness Results

$MR = 3.60$ $MR = 7.07$

$MR = 10.80$ $MR = 13.67$

$MR = 15.93$
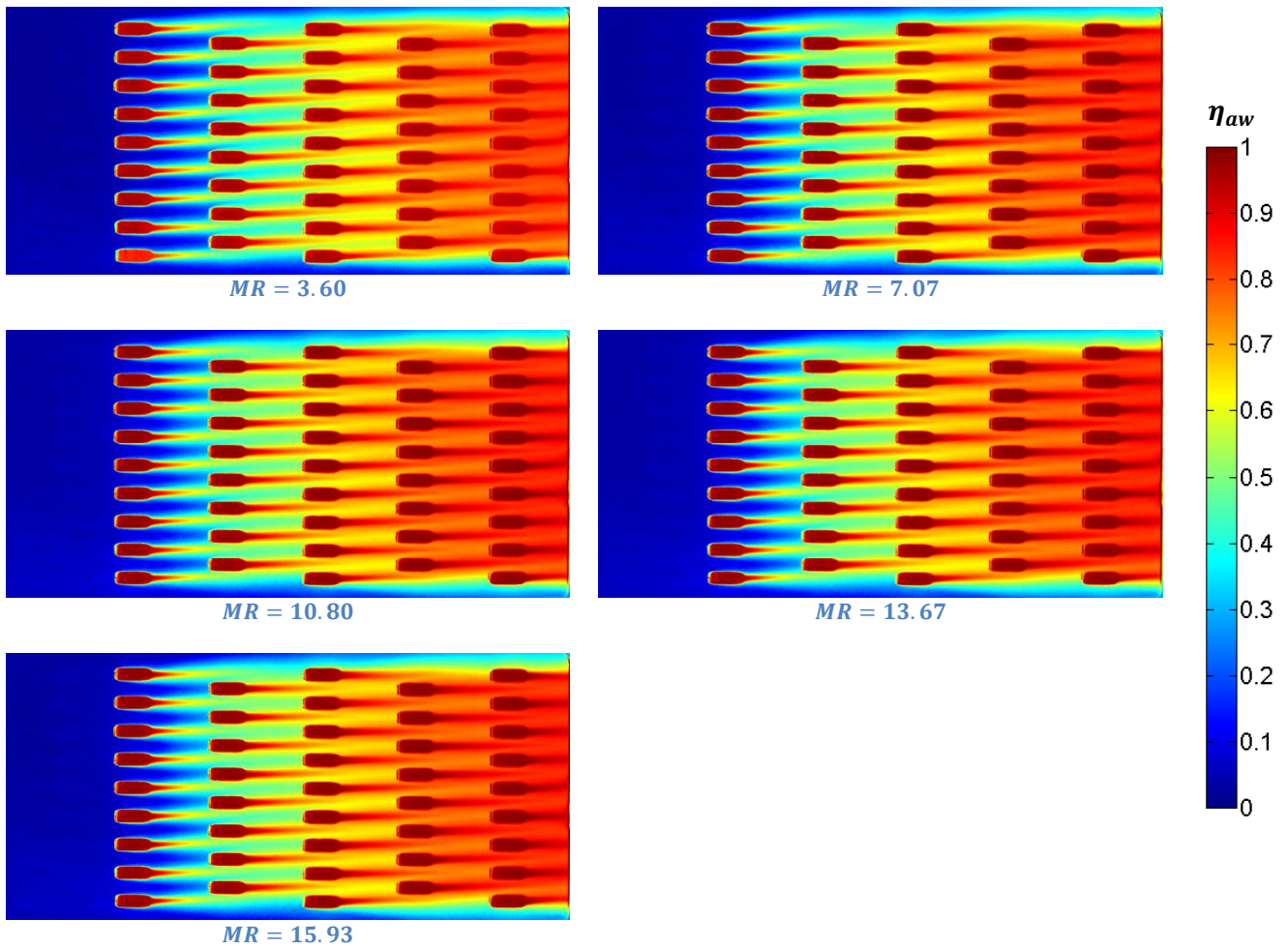
Figure A-7 – Slotted adiabatic film effectiveness at various momentum ratio conditions and $Tu = 5\%$
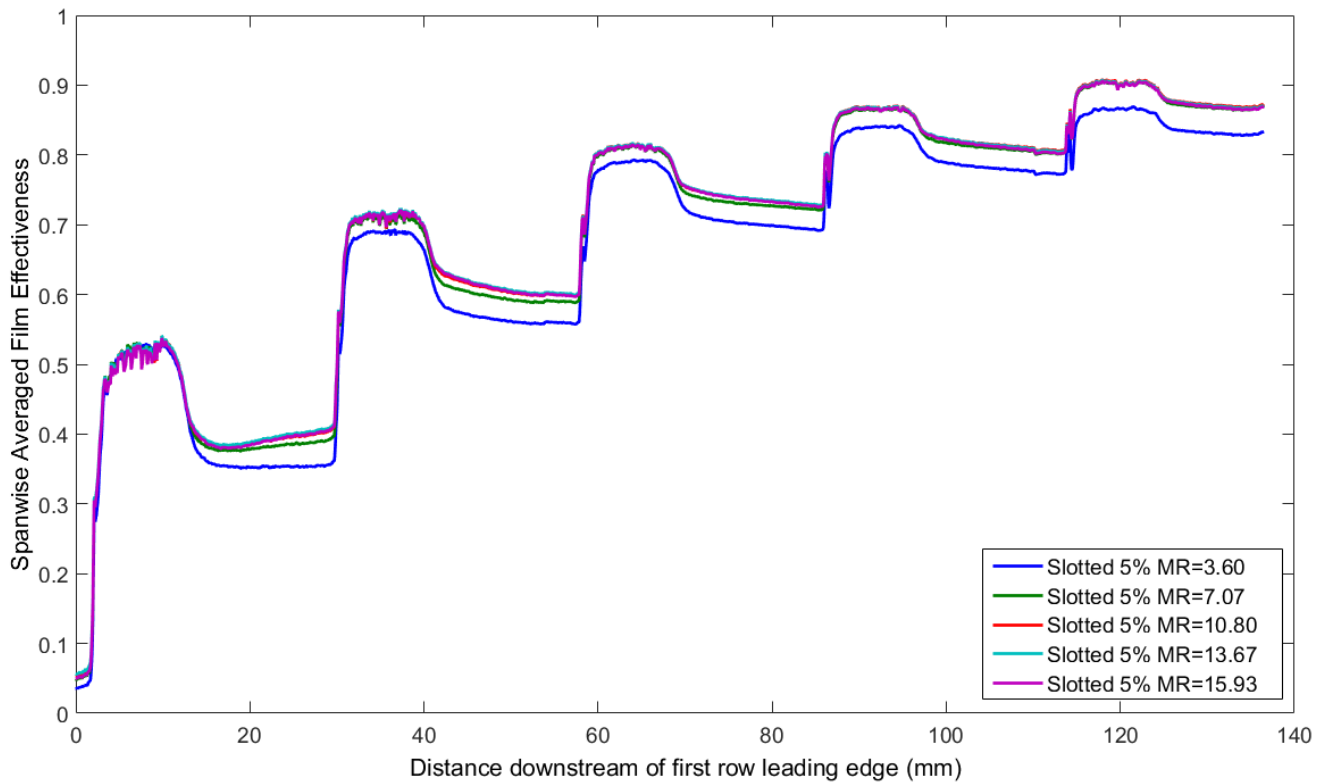
Figure A-8 – Slotted spanwise averaged adiabatic film effectiveness at various momentum ratio conditions and $Tu = 5\%$
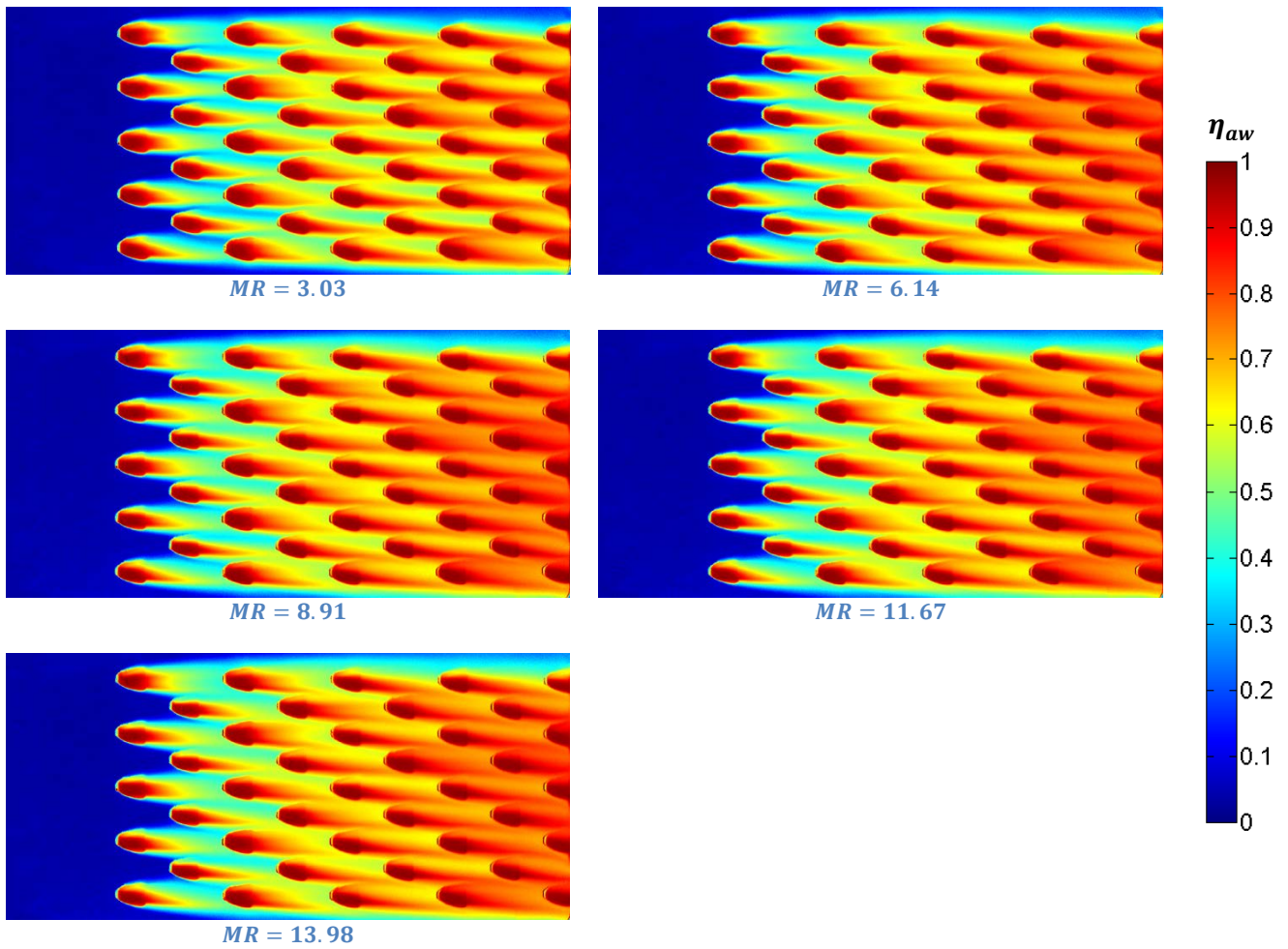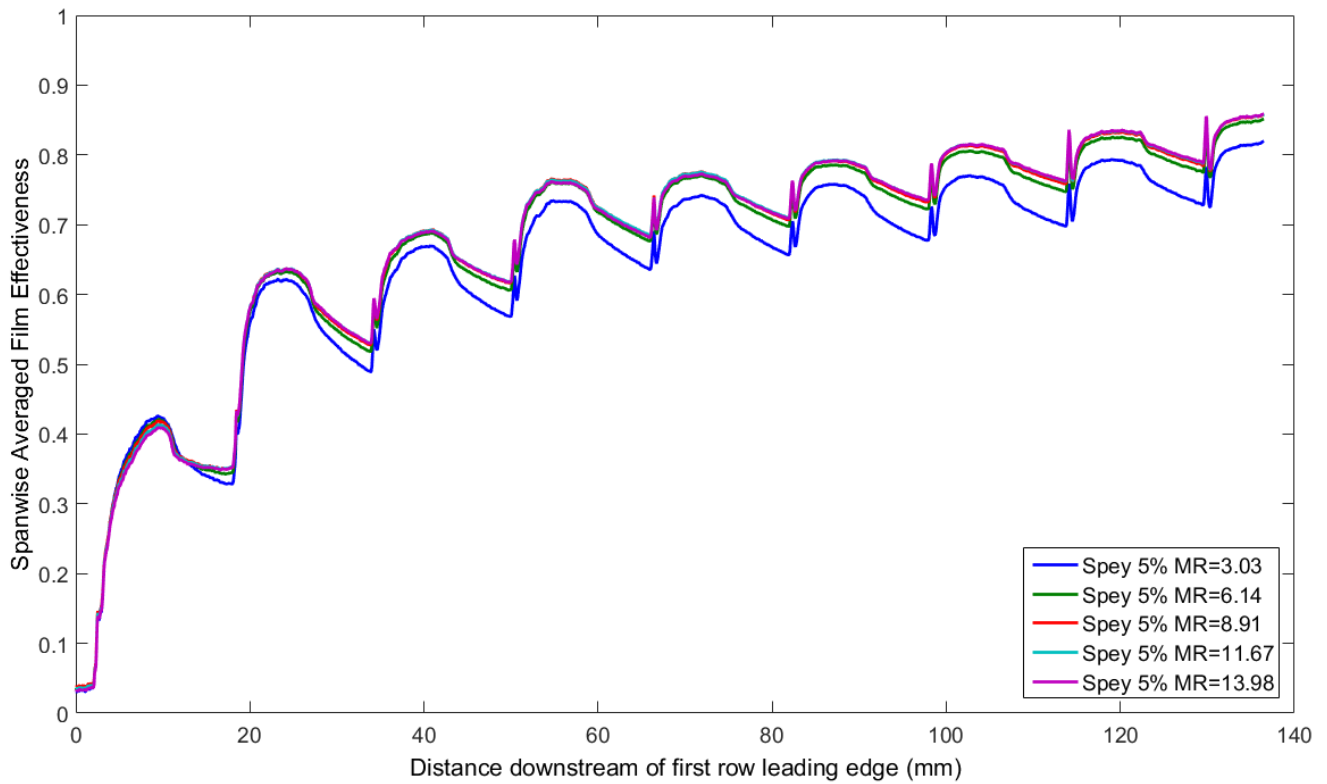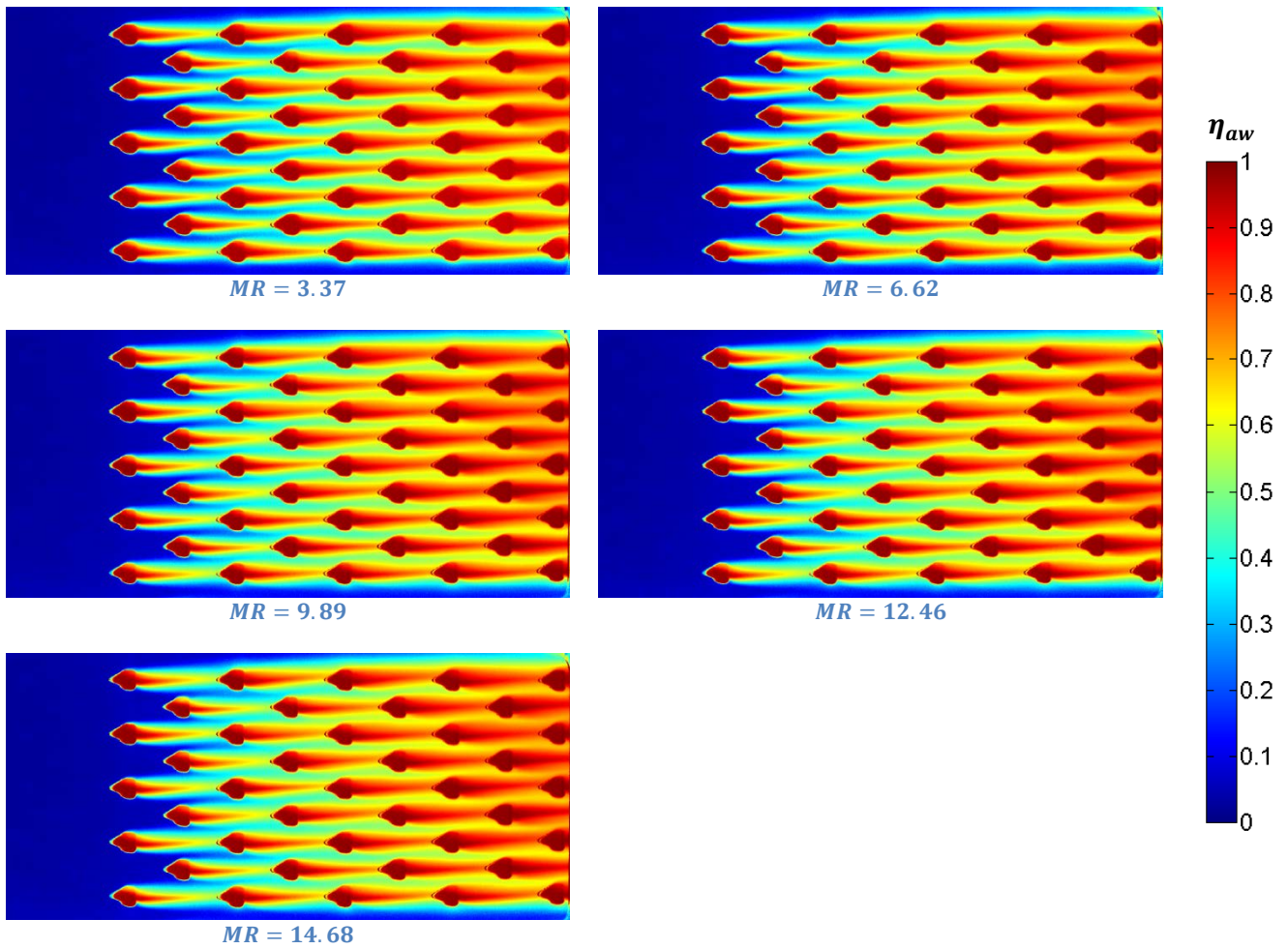
A.1 Adiabatic Film Effectiveness Results

$MR = 3.51$

$MR = 6.72$

$MR = 10.00$

$MR = 12.76$

$MR = 16.15$

η_{aw}
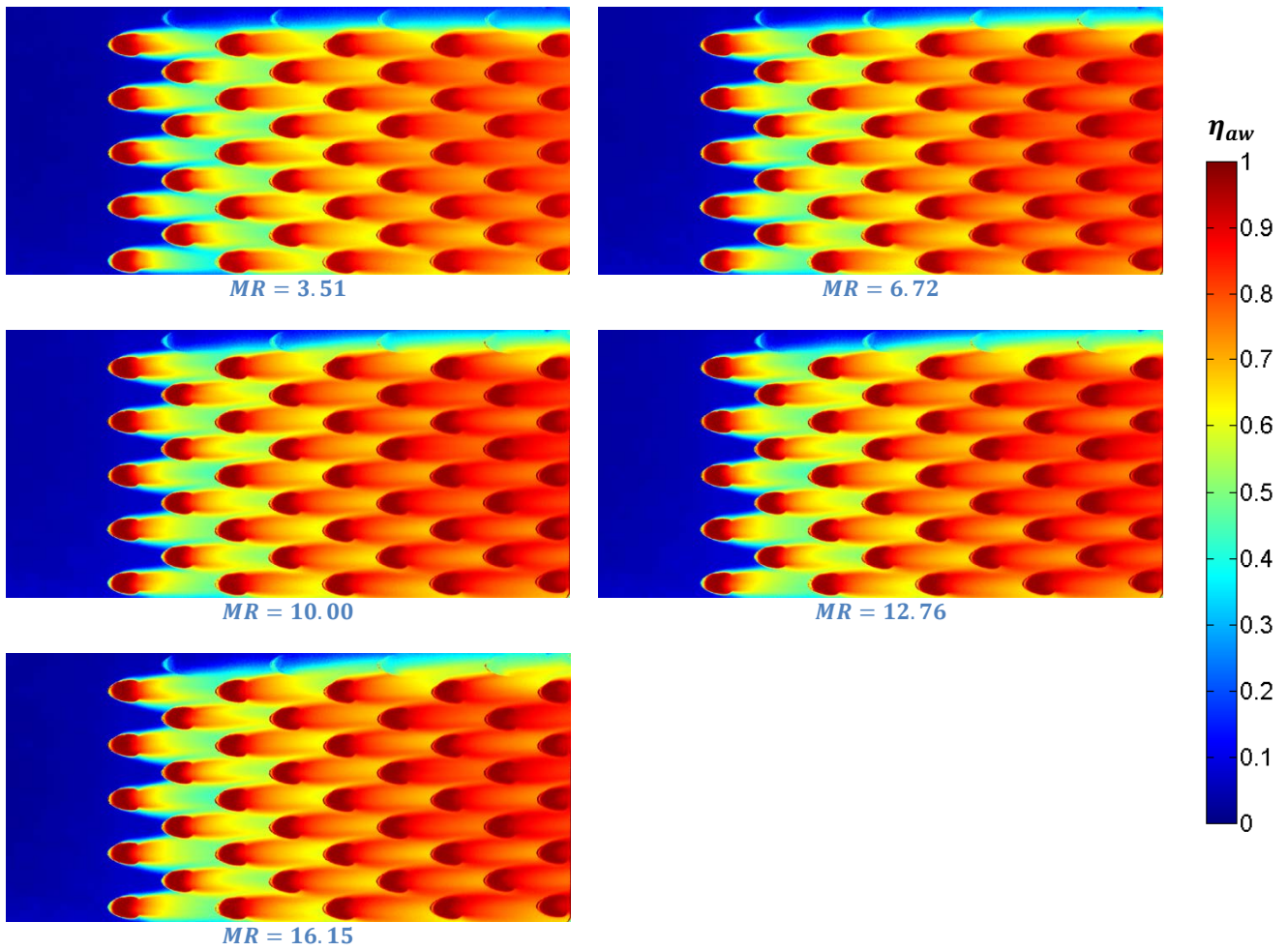
Figure A-9 – Circular Helix adiabatic film effectiveness at various momentum ratio conditions and $Tu = 5\%$
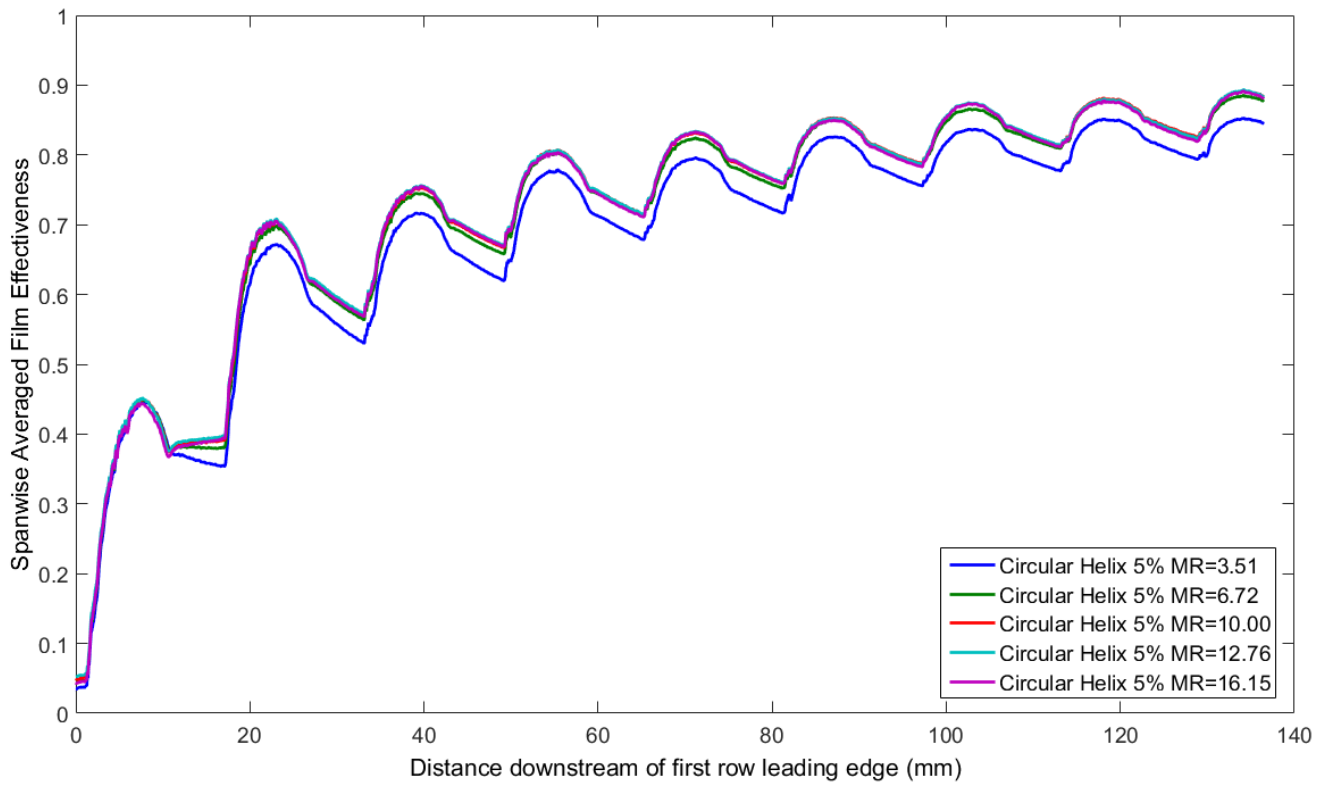
Figure A-10 – Circular Helix spanwise averaged adiabatic film effectiveness at various momentum ratio conditions and $Tu = 5\%$

A.2 Overall Effectiveness Results
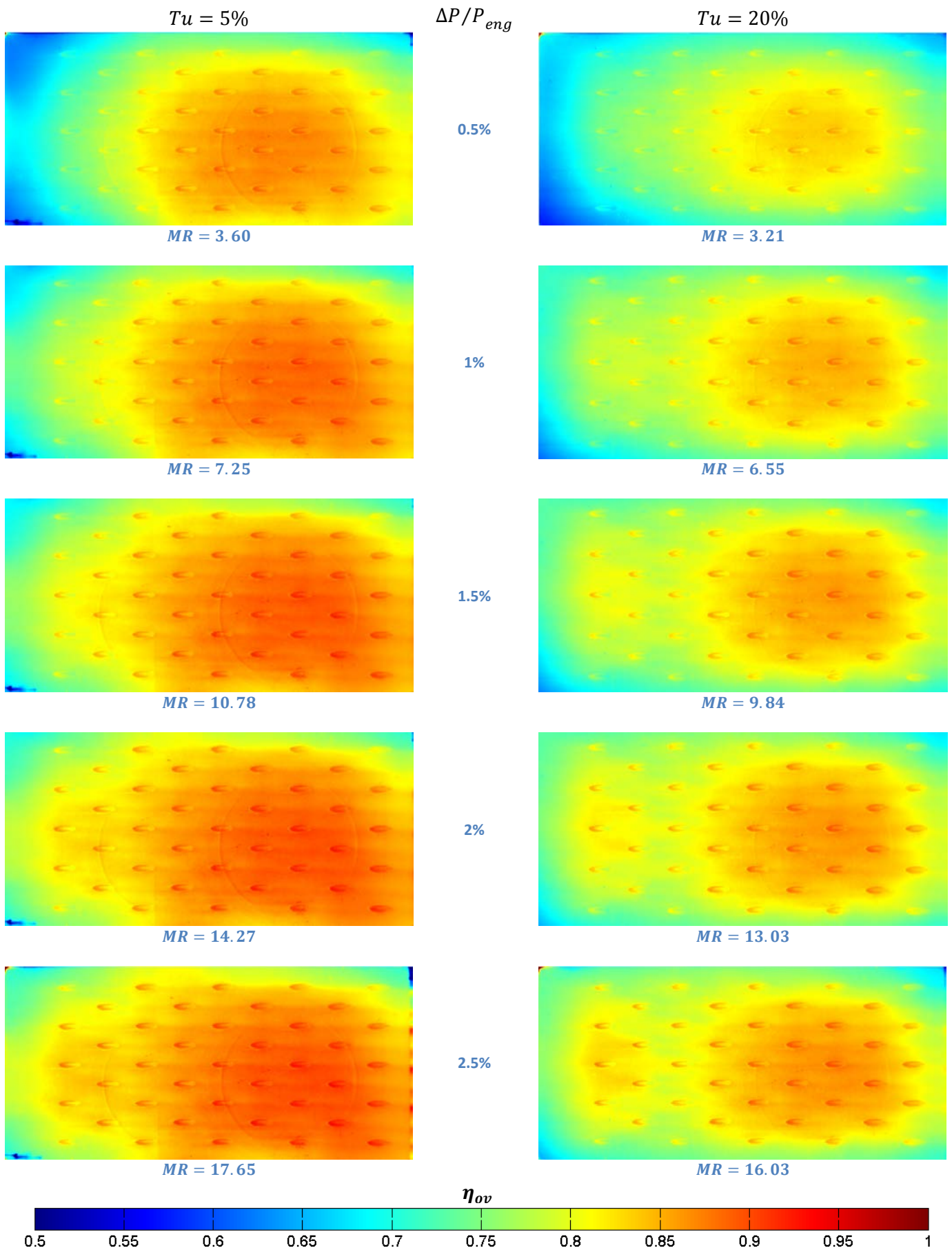
Figure A-11 – Cylindrical overall effectiveness at various turbulence and blowing ratio conditions
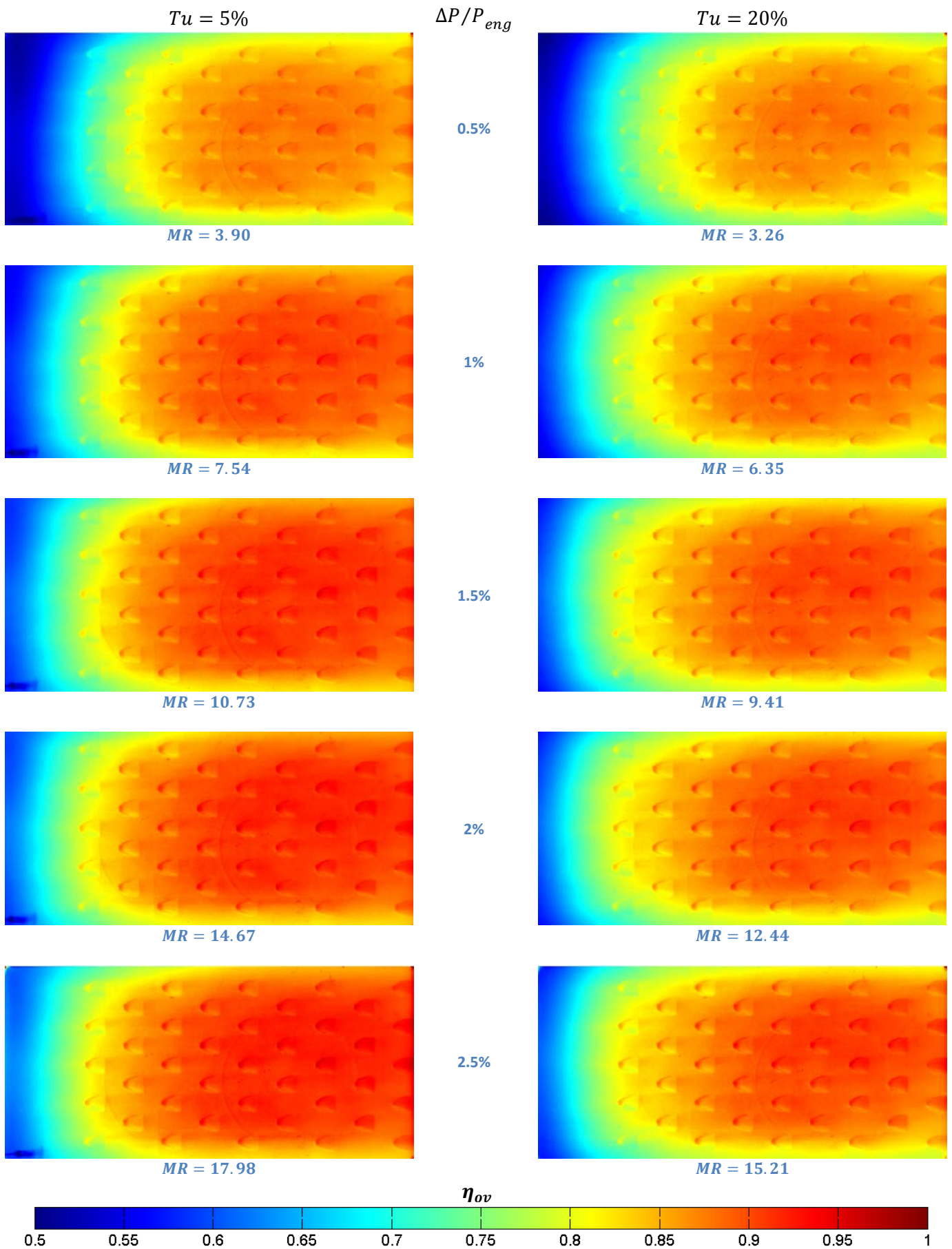
Figure A-12 – Spey fan overall effectiveness at various turbulence and blowing ratio conditions
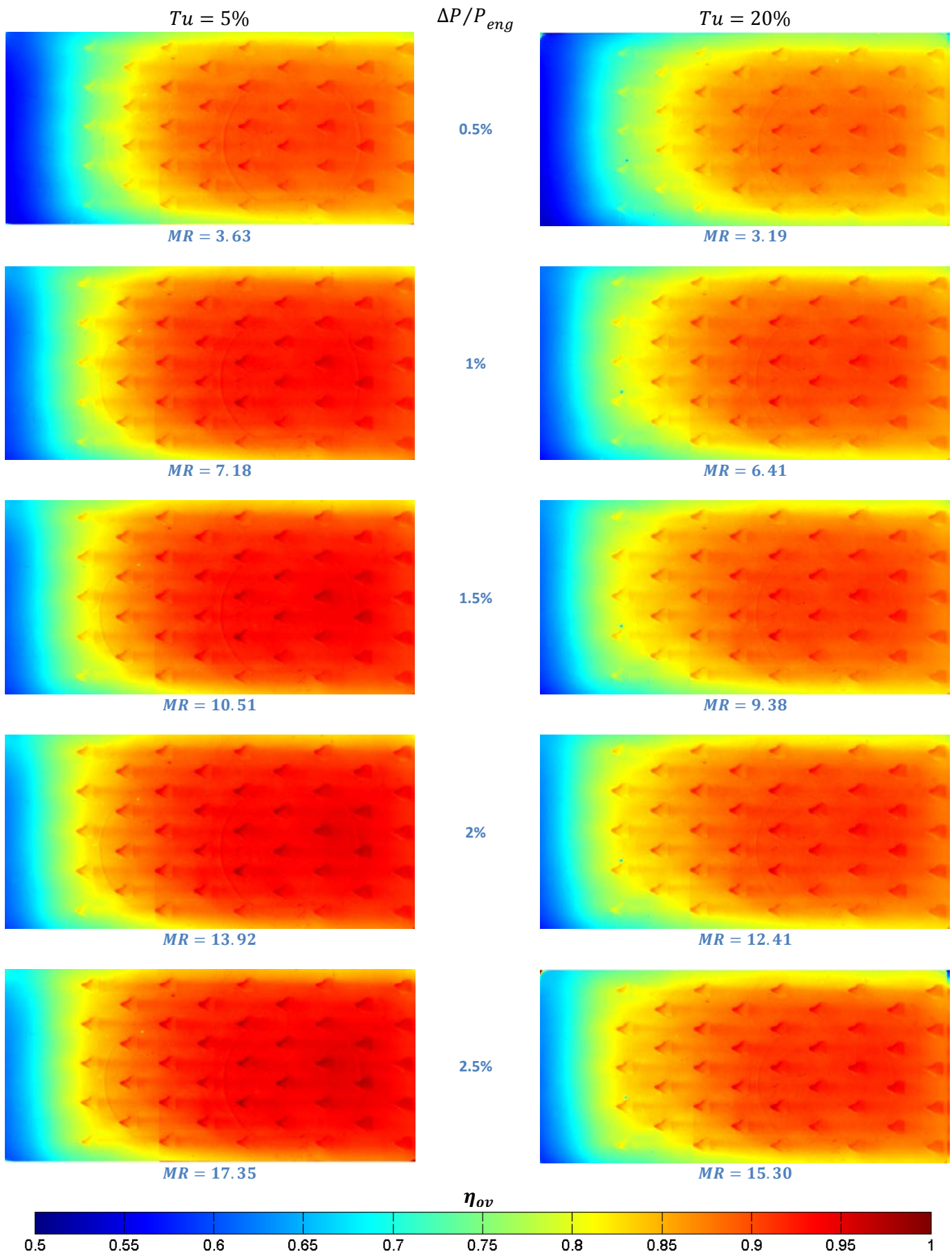
Figure A-13 – Modified fan overall effectiveness at various turbulence and blowing ratio conditions
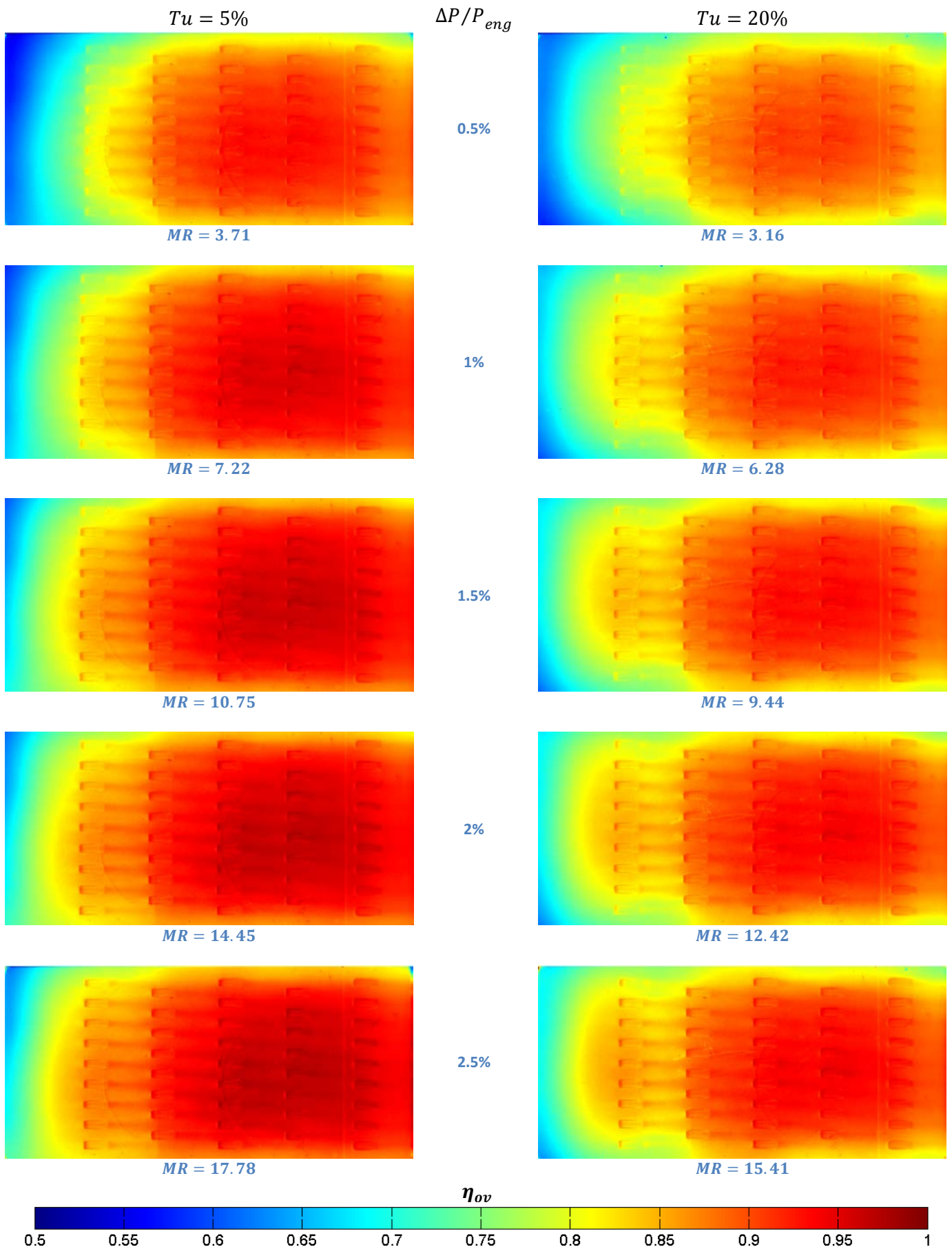
Figure A-14 – Slotted overall effectiveness at various turbulence and blowing ratio conditions

A.2 Overall Effectiveness Results
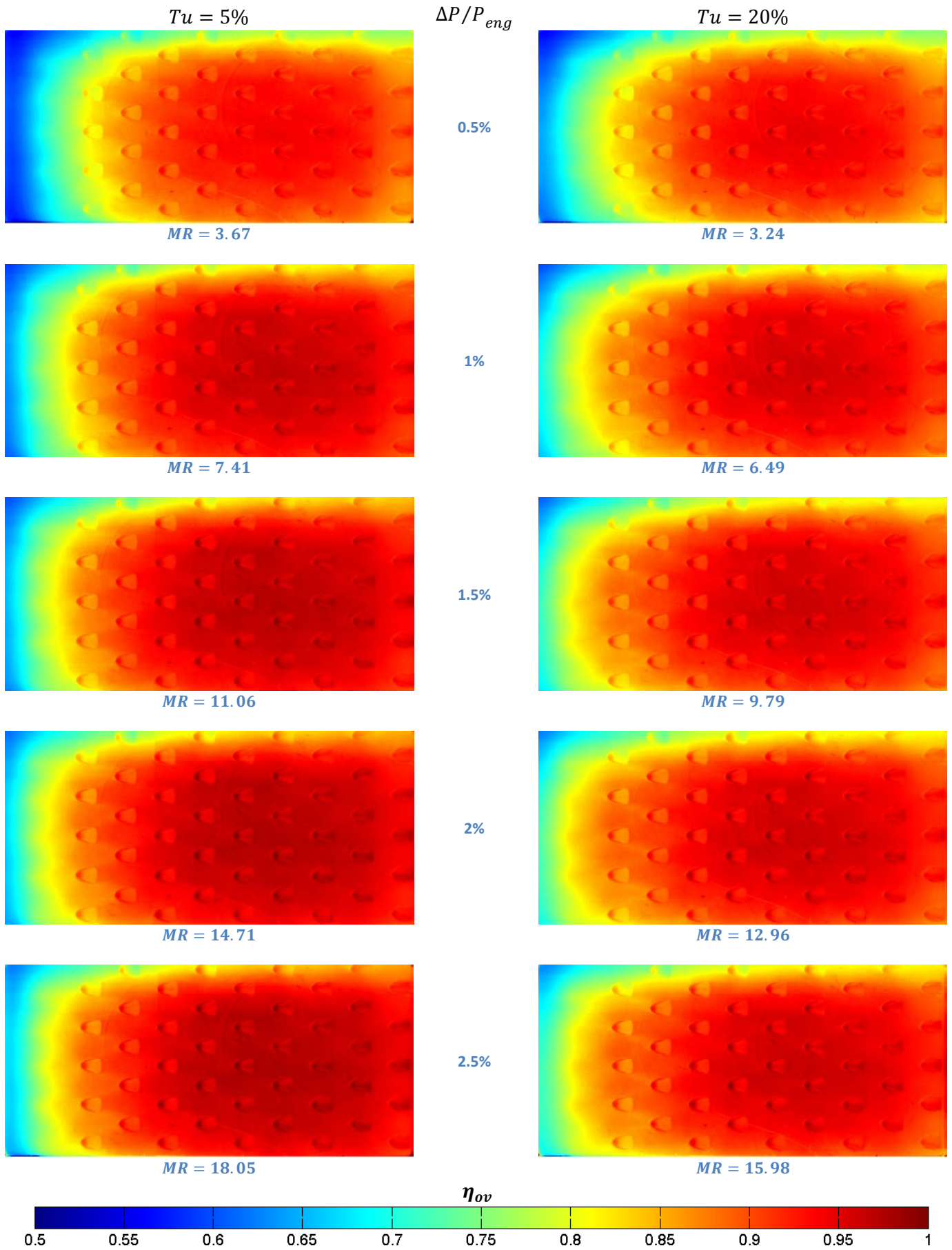
Figure A-15 – Circular Helix overall effectiveness at various turbulence and blowing ratio conditions

A.2 Overall Effectiveness Results

$$\Delta P/P_{eng}$$

$$Tu = 20\%$$

0.5%

$$MR = 3.30$$

1%

$$MR = 6.46$$

1.5%

$$MR = 9.57$$

2%

$$MR = 12.54$$

2.5%

$$MR = 15.38$$

$$\eta_{ov}$$

| 0.5 | 0.55 | 0.6 | 0.65 | 0.7 | 0.75 | 0.8 | 0.85 | 0.9 | 0.95 | 1 |

Figure A-16 – Rectilinear Helix overall effectiveness at various turbulence and blowing ratio conditions

Appendix B ASME GT2015-43210

GT2015-43210

MEASUREMENT AND PREDICTION OF ADIABATIC FILM EFFECTIVENESS OF COMBUSTOR REPRESENTATIVE EFFUSION ARRAYS

Jason Krawciw, Damian Martin, Paul Denman
Department of Aeronautical and Automotive Engineering
Loughborough University
Loughborough
Leicestershire, LE11 3TU, UK
Email: j.krawciw@lboro.ac.uk
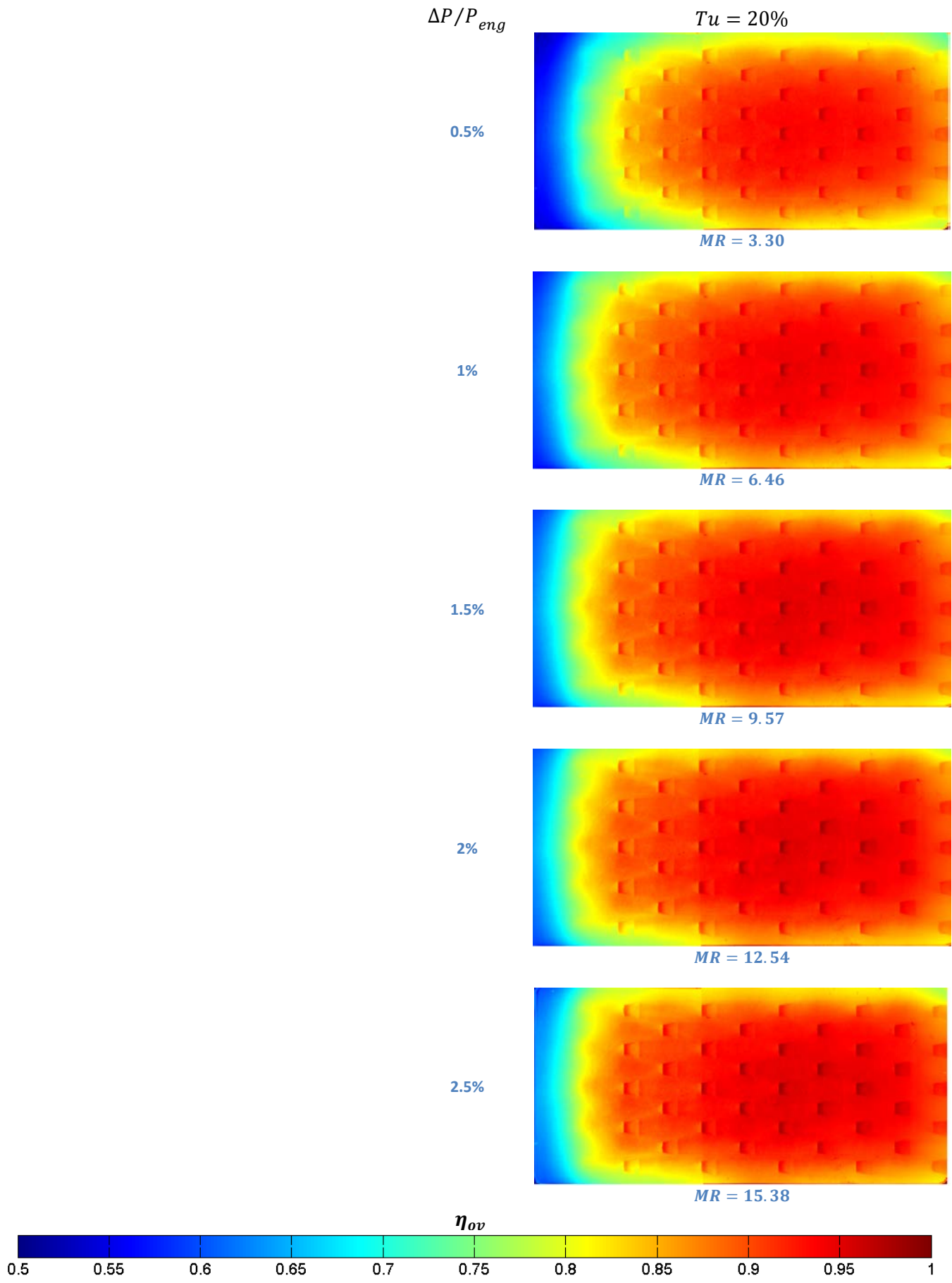
ABSTRACT

Thermal protection of gas turbine combustors relies heavily upon the delivery of a carefully managed film of coolant air to the hot-side of the combustor liner. Furthermore, improvements in engine sfc and the trend to ever more aggressive engine cycles means greater emphasis is being placed upon more efficient use of the proportion of combustion system air made available for cooling. As a result, there is a requirement to better understand the development of cooling films deposited onto the hot-side of the liner through complex effusion arrays. This study, therefore, is concerned with the prediction and measurement of adiabatic film effectiveness of a number of engine-representative designs. A RANS based CFD approach is used to predict film effectiveness in which computational cost is minimised by solving first for a single coolant passage to provide high fidelity, near-exit boundary conditions to the effusion arrays. Equivalent measurements are made for each test case using a Pressure Sensitive Paint (PSP) technique in which the oxygen-quenched fluorescence properties of the paint are employed together with a Nitrogen gas cooling simulant to determine adiabatic film effectiveness. This study demonstrates that whist the model under-predicts the mixing of the coolant with the main-stream flow, and hence the film development over the surface, the approach works well at quantifying the relative performance of each design.

NOMENCLATURE

C_d	Discharge Coefficient	[-]
$\dot{m}$	Mass Flow Rate	[kg/s]
y^+	Non-dimensional wall distance	[-]
ΛL	Turbulent Length Scale	[m]
A	Area	[m^2]
C	Concentration	[%]
DR	Density Ratio	[-]
I	Intensity	[counts]
L	Length	[m]
M	Blowing Ratio	[-]
P	Pressure	[Pa]
R	Gas Constant	[J/kg.K]
Re	Reynolds Number	[-]
T	Temperature	[K]
Tu	Turbulence Intensity	[%]
U	Velocity	[m/s]
d, D	Diameter	[m]
p	Hole Pitch	[m]
s	Hole Spacing	[m]
α	Lay Angle	[°]
γ	Ratio of Specific Heats	[-]
η	Adiabatic Effectiveness	[-]
ρ	Density	[kg/m^3]

Subscripts

air	Air condition
$c, cool$	Coolant
fg	Tracer gas condition
$m, main, \infty$	Mainstream
ref	Reference condition
w	Wall

INTRODUCTION

The combustion chamber of a modern gas turbine engine is a hostile environment; the combustor wall is exposed to high temperature loads as well as unsteady flow conditions. As such the requirement to cool the wall is made more complicated as high turbulence and unsteadiness of the flow drive up near wall velocities and therefore heat transfer (6). A large area of study, therefore involves generating a film of

relatively cool air over the combustor wall surface in order to protect it from the high temperature gas stream. A number of approaches to assessing the performance of this film have been studied involving both computational and experimental methods.

Adiabatic wall effectiveness measurements are generally obtained by manufacturing the test geometry from materials with extremely low thermal conductivity and using a range of methods to extract surface temperature such as Thermochromatic Liquid Crystal (67; 68) and IR Thermography (69; 70). These materials will always have some thermal conductivity, therefore post processing of measured data is required utilising either FEM modelling or implementation of the linear superposition principle. A comparison of a number of adiabatic film effectiveness measurement techniques for a single row of film cooling holes has been studied by Varvel (71).

The approach detailed in this study makes use of a Pressure Sensitive Paint (PSP) technique, in which fluorescence is quenched by oxygen in the air. By using Nitrogen as a tracer gas it is possible to determine the film effectiveness over a number of cooling array designs, derived from a heat-mass transfer analogy (72). PSP has been in use for a number of years for various applications including measuring static pressure distribution over surfaces such as aircraft bodies (73) and turbomachinery (35; 74). More recently the PSP technique has been developed in order to measure the film effectiveness of turbine blade cooling configurations (75; 34; 31).

Computational modelling of cooling arrays can also be used to determine adiabatic effectiveness, but due to the large number of coolant passages present, a number of simplifications and associated assumptions must be employed.

A symmetry boundary is often used on the hole centreline to approximate an infinite width domain whilst limiting the actual computational domain (76). This approach works well for simple geometry such as plain holes, but for asymmetrical geometries or flow conditions, a pair of periodic boundaries is required instead, where fluid properties are extracted from one boundary and used as the boundary condition of the other and vice-versa.

Coolant hole exit boundary conditions play an important part in predicting the film and setting up this boundary condition involves either a companion experiment to provide the necessary data, or inclusion of the entire coolant passage and feed geometry within the calculation (77). As the number of cooling holes increases, the inclusion of each cooling passage significantly increases the number of grid cells required. Traditionally techniques such as super position are utilised to extend the effectiveness results from a single row computation to a multi-row array (78), however this technique is limited as it does not capture the physical effects as the coolant hole exit flows interact.

In order to address this issue, a technique is introduced whereby the film effectiveness of a coolant array is predicted by first solving for a single coolant passage at high computational fidelity, then extracting the exit flow field and
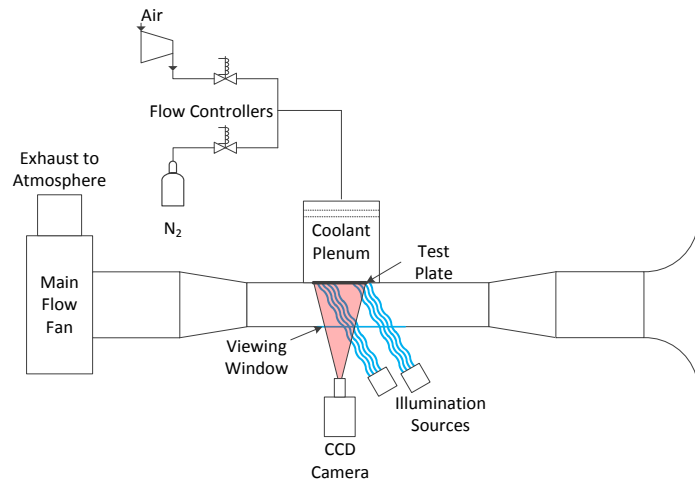

Figure 120 – Wind Tunnel Schematic

applying it as an inlet boundary for a full cooling array. This approach significantly reduces the overall cell count and computational cost.

EXPERIMENTAL ARRANGEMENT

The present study is carried out in a continuous flow wind tunnel at near-ambient conditions as indicated in Figure 43.

The test section of this facility is equipped with instrumentation that permits the measurement of adiabatic film cooling effectiveness, overall cooling effectiveness and flow velocity/turbulence parameters. Currently the facility is configured for the measurement of adiabatic film effectiveness of effusion cooled combustor type geometries. Essentially the facility is an open loop atmospheric wind tunnel driven by a 37kW centrifugal fan. The mainstream air is conditioned through a series of flow straightening grids and screens before entering the 150x150mm cross section test section. The working section contains a wall mounted Vernier[TM] Oxygen gas sensor which monitors the concentration of Oxygen in the mainstream cross flow. The effusion plates are mounted in a support frame which can accommodate test plates of length 170mm. Coolant flow is delivered by a plenum arrangement which is fed by two Alicat[TM] flow controllers, one controlling the flow of air and the other Nitrogen gas. The coolant temperature is maintained at the same temperature as the mainstream flow by an inline electrical heater (not shown). This ensures the tests are performed under isothermal coolant conditions. Optical access for imaging and illumination is provided by a plain float glass window. This is sufficiently large to enable illumination and imaging of the entire test plate.

Adiabatic film effectiveness measurements are determined by a steady state technique, measuring film concentration using pressure sensitive paint (PSP). A bright, single-luminophore PSP, UniFIB, with a response time of ~300ms and supplied by Innovative Scientific Solutions Inc. is utilised. The paint is airbrushed directly onto the test samples in multiple layers until a uniform coat is achieved. All test
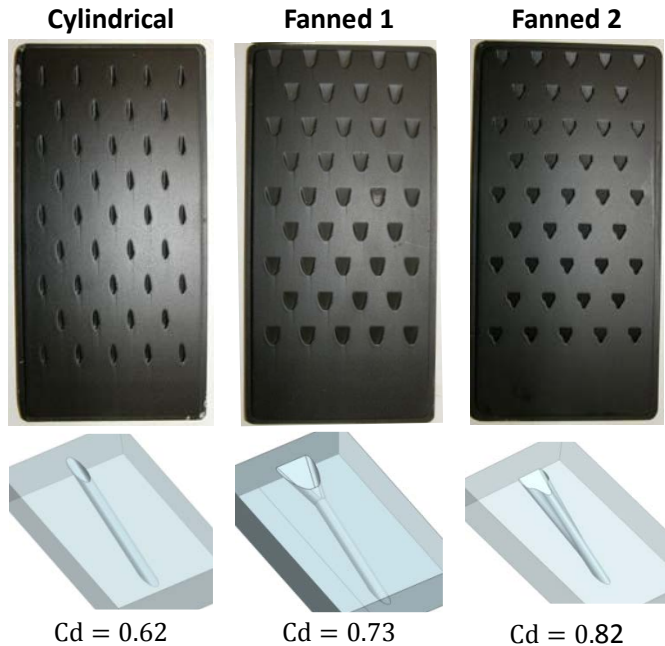
Cylindrical	Fanned 1	Fanned 2

$Cd = 0.62$	$Cd = 0.73$	$Cd = 0.82$

Figure 121 – Example Effusion Geomerty

plates and a calibration coupon are painted at the same time, allowing that particular batch to be calibrated with the paint having been applied in a consistent manner to each sample geometry.

Geometry

A total of three effusion arrays were manufactured for the present study and these are identified as Cylindrical, Fanned 1 and Fanned 2 in **Figure 121**. All three test plates were produced using a direct metal laser sintering process (DMLS). Hole diameters are scaled based on simulated Cd values in order to ensure the mass flow rate and pressure drop is consistent for the three designs. Simulations were carried out using a similar process to the single hole CFD calculations presented later in this paper.

Hole pitch and spacing is consistent through all three designs. Once manufactured the test plates are flow checked to validate the Cd values simulated with good agreement shown between the measured plate average and the simulated single hole Cd values.

Computational geometry is defined to mimic the experimental test plates, as such the models used to define the plate boundaries in the computational meshes are adapted from those used to manufacture the DLMS test plates. However, due to the immaturity of the manufacturing process used, the Fanned 1 test plate has a flat spot running the length of the metering section, reducing the effective diameter and hence plate porosity, a feature which was not reproduced in the computational model, resulting in lower mass flow for the experimental test plate at a given pressure drop in comparison to both the computational model and the other test plates considered. Additionally, due to the layered build direction, all three plates show slight asymmetry from left to right, another

feature which is not captured by the CFD model, though this difference is very slight and is not through to have much impact on the results as measured porosity is similar for the Cylindrical and Fanned 2 plates.

ADIABATIC EFFECTIVENESS MEASUREMENT

Pressure sensitive paint is used to determine the film cooling effectiveness on the effusion surface. This is a mixture containing photo luminescent molecules held in a permeable binder, which emits light with intensity proportional to the surrounding partial pressure of Oxygen. Employing the PSP as a sensor of Oxygen at the surface, the technique can deliver adiabatic film-cooling effectiveness using the analogy between heat and mass transfer (72). Any pressure variation on the PSP-coated surface creates a local variation in Oxygen partial pressure. This causes the emitted light intensity to change as a result of an Oxygen quenching process (35) and a digital camera is employed to detect this change in intensity. A calibration of intensity ratio to partial pressure enables the concentration to be calculated in the experiment by first running an experiment at constant gas concentration to determine the local pressure field, then running a subsequent experiment with an Oxygen free tracer gas to obtain a full partial pressure field. By taking the ratio of these conditions the surface local Oxygen concentration can be calculated and the heat-mass transfer analogy, Eq. **(90)**, applied to infer the local adiabatic effectiveness.

For both calibration and experiments, the camera used to measure the emitted intensity is a PointGrey Grasshopper 2 GigE containing a Sony ICX625 CCD sensor providing up to 5 Megapixels resolution at 2448x2048 at 15 frames per second and a 14-bit A/D converter with a dark red band pass filter (660nm±30nm). A 16mm f/1.4 lens is used for the test, with a 25mm f/1.4 lens used during calibration. Exposure time and gain are kept constant throughout calibration and testing. Illumination is provided by two Luxeonstar tri-star royal-blue LED clusters providing excitation light to the entire plate surface at a wavelength of 447.5nm.

$$\eta = \frac{T_{main} - T_{ad}}{T_{main} - T_{cool}} \equiv \frac{C_{O_{2\,main}} - C_{O_{2\,w}}}{C_{O_{2\,main}}} \qquad (90)$$

$$\therefore \eta = 1 - \frac{P_{O_{2\,fg}}/P_{O_{2\,ref}}}{P_{O_{2\,air}}/P_{O_{2\,ref}}} \qquad (91)$$

Calibration

The PSP is calibrated a priori using a separate test section which is sealed at both ends as illustrated in Figure 41. This chamber is vented to atmosphere ensuring that the paint is only responding to change in oxygen concentration and not pressure. The chamber is flooded with a range of concentrations by volume of air and Nitrogen gas from 0% to 20.9% Oxygen.
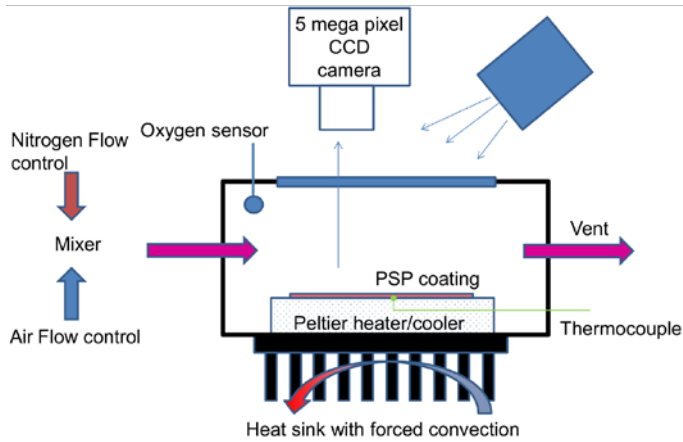
Figure 122 – Calibration Chamber

The concentration within the chamber is monitored using a Vernier[TM] Oxygen gas sensor. The same viewing window is employed for both calibration and experiment.

The flow mixture entering the chamber is controlled by a pair of Alicat[TM] flow controllers piped into a mixing chamber before entering the calibration chamber. The mixture is introduced slowly into the chamber and the O_2 concentration within the calibration chamber is monitored for convergence. At set points during this process, the flow is turned off and allowed to settle before images are captured.

The fluorescence of PSP is also dependent on temperature; and therefore the calibration coupon is also thermally bonded to a Peltier heater/cooler to allow calibration data to be obtained over a range of plate temperatures from 10-50°C. A K-type thermocouple embedded into the centre of the plate is used to monitor temperature.

Data then passes through a Matlab script to determine the calibration coefficients for the modified Stern-Volmer relationship:

$$\frac{P_{O_2}}{P_{O_2 \, ref}} \equiv \frac{C_{O_2}}{C_{O_2 \, ref}} = A(T)\left(\frac{I_{ref}}{I}\right)^2 + B(T)\frac{I_{ref}}{I} + C(T) \tag{92}$$
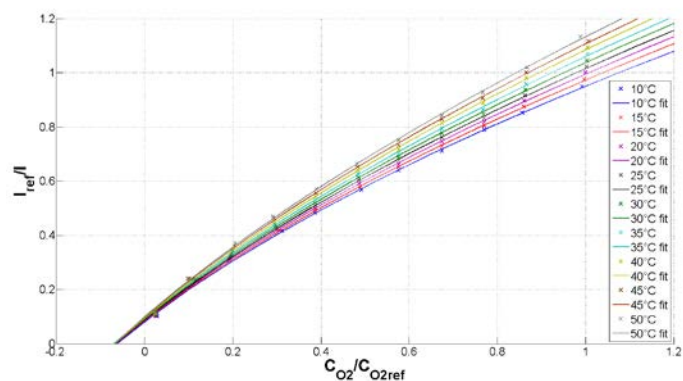

Figure 123 – PSP Calibration Curve

M	0.8-3.8	U_∞	36m/s
Re	$5.0\text{-}23.5 \times 10^3$	$T_{\infty,c}$	298K
ΛL	10D	Tu	5%

Table 10 – PSP Test Conditions

$$A = a_1 T^3 + a_2 T^2 + a_3 T + a_4$$
$$B = b_1 T^3 + b_2 T^2 + b_3 T + b_4 \tag{93}$$
$$C = c_1 T^3 + c_2 T^2 + c_3 T + c_4$$

By calibrating in a constant pressure environment, the pressure term in determining partial pressure can be ignored when taking a ratio to the reference condition, resulting in a calibration of intensity ratio against concentration ratio which is equivalent to partial pressure ratio. The reference condition is 20°C and 100% air (~20.9% O_2).

Typically 200 images are captured at each temperature and concentration combination with a further 200 captured with the lens cap on to act as a dark field correction. A mean for each set of images is then calculated. Images are corrected for stray light and dark current by subtracting the dark image from each illuminated image, known as flat-field correction.

$$I = I_{illuminated} - I_{dark} \tag{94}$$

The image is then cropped to ensure data points are only processed from the painted surface and a mean of this region calculated.

The intensity and concentration ratios relative to the reference condition are calculated for each concentration at a given temperature and a second order polynomial is fitted to obtain the coefficients A, B and C in Eq. **(92)** for that temperature. Once all temperature conditions are processed, a second order polynomial is fitted to each coefficient to determine their temperature response as in Eq. **(93)**. The resultant calibration curves are shown in Figure 42.

Test Procedure

In order to determine the effectiveness of the film, images must be captured at four test conditions: Test 1 involves capturing an image with no illumination to determine the background noise of the camera (I_{dark}). For test 2, the plate is illuminated with no air flowing to capture a known reference condition (I_{ref}). Test 3 is run using air as coolant at the appropriate main and coolant flow condition (I_{air}). Here any change in intensity will be due to the variation in static pressure on the surface of the plate. Finally, test 4 is conducted using Nitrogen gas as the coolant, the resultant images shows intensity variations as a result of changes in both local static pressure and concentration (I_{fg}).

Data Reduction

200 images are collected and averaged at each condition and used to calculate the time averaged intensity field. The dark field is then subtracted for each of the other

three images before the reference image is divided by each wind-on image to give the ratio I_{ref}/I used in Eq. **(92)**. The calibration is then applied to these images allowing the effectiveness to be calculated using Eq. **(91)**.

Test Conditions

The test conditions at which the present investigation is conducted are listed in **Table 10**. All measurements are carried out using the same optical components, LED cluster and camera employed during the PSP calibration procedure. Constant Temperature Anemometry measurements made in the freestream above the test plate indicate a turbulence intensity of 5% and an integral length scale close to 10 effusion hole diameters. Although the experiments described here are isothermal, the effect of density ratio on film behaviour and development is relatively small. Indeed previous testing indicates that density ratio has a second order effect on film effectiveness (79).

The flow field is aerodynamically scaled to representative engine conditions and is characterised by the Reynolds number, based on the hole diameter and pressure drop, and the blowing ratio of the emerging air.

$$Re_D = \frac{\sqrt{\frac{2\Delta P}{\rho}}\, D}{\upsilon} \qquad \textbf{(95)}$$

$$M = \frac{\rho_c U_c}{\rho_\infty U_\infty} \qquad \textbf{(96)}$$

By taking this approach and exploiting the fact that matter cannot be transferred through the wall, the thermal conductivity of the test plate material has no influence on the measured adiabatic effectiveness.

Uncertainty Analysis

Uncertainty is calculated according to the method outlined by Kline and McClintock (60) with a 95% confidence interval to be ±15% at η≈0.8 and ±22% at η≈0.2 based on calibration error of 8% obtained through repeat calibration tests, and camera intensity measurement error of 13-21% for the film effectiveness measured by the PSP and ±3% for the setting of blowing ratio. The Vernier O_2 sensor has an accuracy of ±1% volume O_2 and the K-type thermocouple of ±1.5K. The major contributor to error is the CCD camera used to record the luminescent intensity of the paint; this is a relatively basic CCD with a relatively low full well depth of 7300e⁻. Due to the inverse relationship between intensity and partial pressure, around 65% of the dynamic range of the sensor relates to effectiveness values >0.8, therefore any noise contributes to a strong error source, particularly in regions of low effectiveness. Other potential error sources for PSP measurements as detailed by Liu (36) include illumination stability, photodegradation and spectral leakage. However these are thought to be small in comparison to the uncertainty associated with the camera noise.
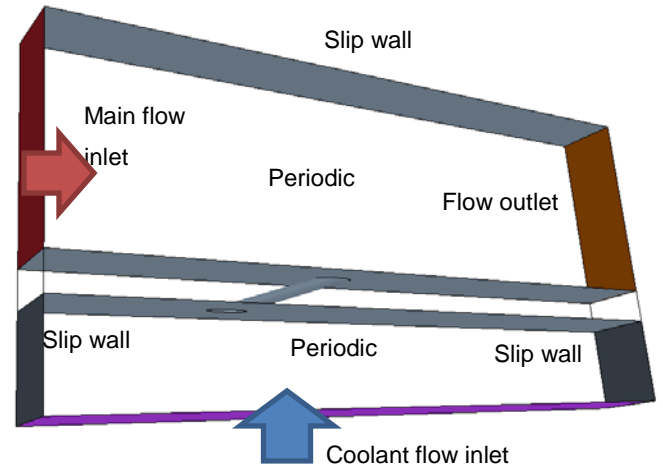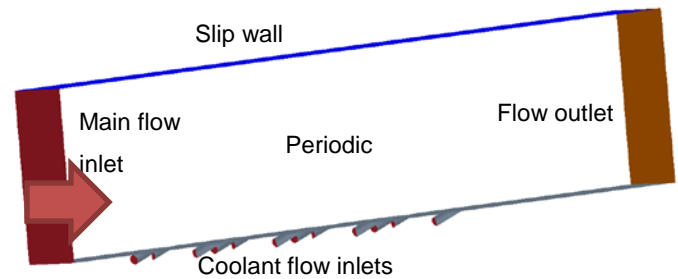

Figure 124 – Single Hole Boundary Conditions

Figure 125 – Multi Hole Boundary Conditions

NUMERICAL ANALYSIS

Geometry and Boundary Conditions

Two definitions are required for each design. The first models a single coolant passage fed by a plenum with a depth of 8D and exiting into a cross flow, **Figure 124**. This is used to simulate a single row of cooling holes. The second definition consists of an array of cooling holes which are cut off 2.7D upstream of the exit, **Figure 125**. This is used to simulate the effusion cooling plate and the distance chosen coincides with the start of the divergent section in the Fanned 1 geometry. This represents the biggest geometrical discontinuity of the three designs considered.

By solving the single hole case and establishing the internal flow field within the coolant passage of each effusion hole geometry, then extracting data from a plane just upstream of the exit and pasting that onto the full array case, as shown in Figure 57, the computational requirements of solving over the full array can be reduced. This approach provides high fidelity, near-exit boundary conditions which exert considerable influence on jet behaviour (80) without performing a full simulation of the entire effusion array. This enables modest computational resources to simulate the performance of multi-hole effusion arrays. While the effects of hole-to-hole interaction are not completely captured, this technique

simulates the flow in the exit region of the coolant holes, capturing the local interaction on the plate surface, such as how the exit flow influences the coolant distribution of previous rows, but not the global effects throughout the coolant passage, such as changes in velocity profile within the hole. As a result this methodology provides a useful technique to use as a first approximation, allowing down selection of different geometries.

In both definitions the domain is periodic between holes, effectively making the width infinitely repeating whilst solving on a domain of the same width as the hole spacing. A periodic boundary is chosen over a symmetry plane due to the non-aerodynamic fan used on the Fanned 1 design which results in a separation within the diverging section. This has been seen to cause the coolant to 'stick' to one side of the fan, a flow feature which is suppressed by the inclusion of a symmetry plane.

The main flow domain is extended so that the outlet is 35D downstream of the last row of cooling holes, with the inlet 15D upstream of the inlet of the first row of cooling holes. A slip wall defines the top wall of the main flow domain and is placed 12D above the hole exit.

Simulations are conducted using StarCCM+[TM], both to define the computational mesh and solve for the flow field. A triangular surface grid is generated on the geometry, with the mesh size reducing close to any curved features, this in turn is used to generate a polyhedral volume mesh to fill the domain, illustrated in **Figure 127**. An 18 layer prism mesh grows from the surfaces of the solid walls. The minimum cell thickness in the near wall area is chosen to give $y^+<1$. The volume mesh for the single hole domain cases contain around 600,000-800,000 cells rising to 2-5 million for the full array domain, dependent upon the complexity of the hole exit geometry. The grid size is chosen to ensure the solution is grid independent.

Simulations are run with main and coolant inlet temperatures of 298K, main inlet velocity of 36m/s air aligned with the hole direction to ensure a 0° compound angle and plenum inlet pressure of 11,500Pa Nitrogen to match the M~3.8 experimental condition, and 500Pa Nitrogen to match the M~0.8 condition. Main flow bulk turbulence conditions are set
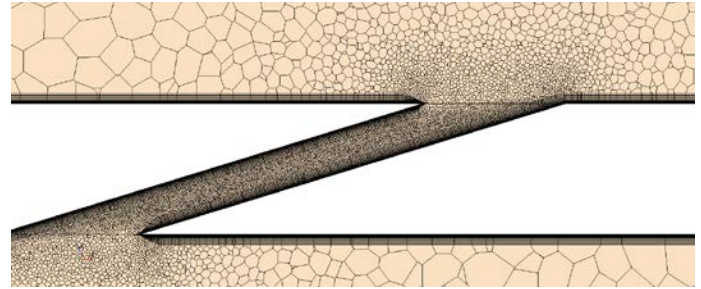

Figure 127 – Volume Mesh

to match the experimental conditions of 5% intensity and ~10D length scale.

Numerical Models

This study uses a RANS based approach utilising the Realizable Two-Layer k-Epsilon model available in StarCCM+[TM]. It is well known that the assumption of isotropic turbulence made by standard two-equation turbulence models leads to an under-prediction of the lateral spreading of the coolant whilst over-predicting the coolant mass on the centreline (76). However, this generally leads to a good prediction of spanwise averaged effectiveness. For ranking of the three wall effusion geometries described here however, these limitations are considered acceptable.

The flow solver treats the fluid as an incompressible ideal gas and a coupled flow/energy/species approach is used with a second order implicit scheme. Molecular diffusivity is computed based on a Schmidt number of 1.0. A multi-component gas model is also used to simulate a Nitrogen gas coolant simulant and air as the mainstream gas as in the experiments. Thermal and transport properties such as specific heat, conductivity and dynamic viscosity are kept constant for each gas species.

Computations generally take half a day to complete running 3 parallel processes on a desktop workstation containing an Intel[TM] Xeon E5-1620 quad core CPU at 3.6GHz with 64GB RAM.

Computations are monitored for convergence using residuals, mass flow balance between inlets and outlet, surface
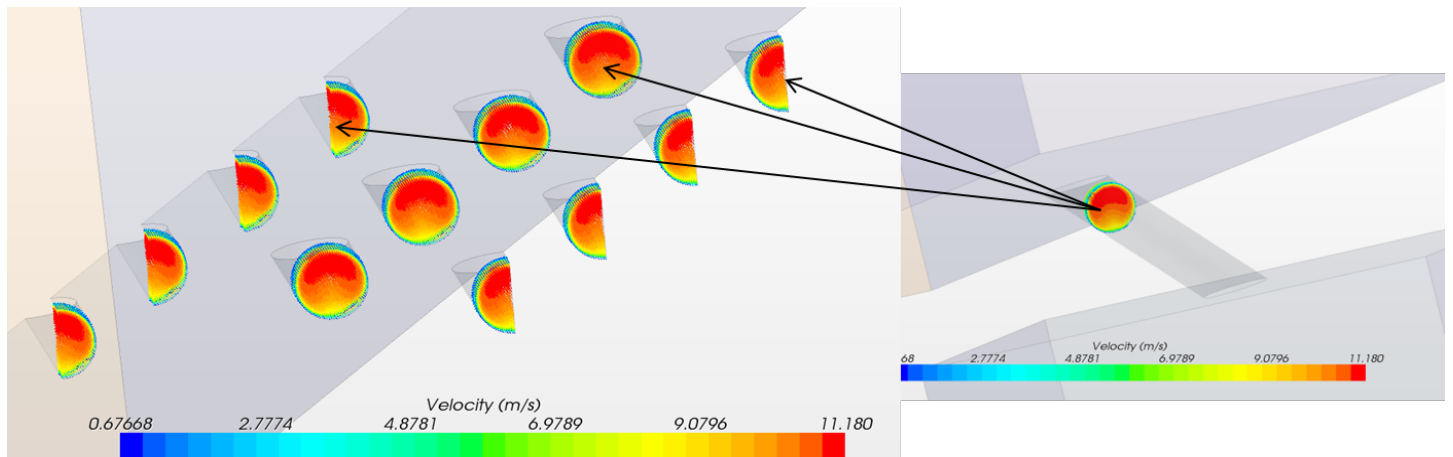

Figure 126 – Inlet Condition Mapping

averaged film effectiveness and, in the single hole cases, discharge coefficient of the flow through the coolant passage.

$$C_d = \frac{\dot{m}}{P_{0_c}\left(\frac{P_m}{P_{0_c}}\right)^{\frac{\gamma+1}{2\gamma}}\sqrt{\frac{2\gamma}{(\gamma-1)RT_{0_c}}\left(\left(\frac{P_{0_c}}{P_m}\right)^{\frac{\gamma-1}{\gamma}}-1\right)A}} \quad \textbf{(97)}$$

RESULTS AND DISCUSSION

Experimental Results

Spanwise averaged film effectiveness for the highest blowing ratio condition is plotted in Figure 130 with surface map data presented in **Figure 128**, with the lowest blowing ratio results presented in **Figure 131** and **Figure 133**. It can be seen that the PSP measurement technique effectively shows the distribution of coolant on the surface, with a marked difference visible between high and low blowing ratios. The area upstream of the first row of holes shows effectiveness values in the region 0-0.08 and hole exit values of >0.95, both of which are within expected calibration error. A clear trend is distinguishable, allowing the effectiveness of a given geometry to be effectively compared to others. The technique is able to capture the separation within the hole exit caused by the large diffusion angle (16°) of the Fanned 1 geometry, indicating particular areas where designs can be iterated in order to improve cooling film performance. This separation is not present in the Fanned 2 geometry due to the lower diffusion angle of the fan (11°). Figure 134 shows the spanwise averaged experimental data for the range of blowing ratio tested, it can be seen that the average effectiveness of all three designs reach a maximum whereby an increase in blowing ratio no longer results in an increase in effectiveness. This appears to be at a blowing ratio of about 1.5 for the cylindrical holes and 2.6 for the two fanned geometries. As expected, the cylindrical hole shows the poorest film effectiveness performance, while the two fanned geometries show similar performance levels at all blowing ratio conditions.

By using this method, benefits in terms of experimental flexibility and cost can be realised. The same test plates and major equipment can be used to determine both adiabatic film effectiveness as well as bulk effectiveness accounting for conduction through the solid wall, requiring only that the test plates be cleaned and repainted for the different testing schemes and a few minor modifications made to the test equipment.

CFD Results

Figure 130and **Figure 134Error! Reference source not found.** show the spanwise average film effectiveness calculated for each of the 3 geometries considered at the two blowing ratio conditions. It can be seen that with the exception of the Fanned

2 design at the higher blowing ratio condition, this CFD technique closely approximates the results given in the experiment. Surface temperature maps are presented in **Figure 129** and **Figure 132**, when compared to the results obtained through the PSP technique it can be seen that aside from the expected under prediction of lateral spreading and over prediction of centreline spreading, the predictions are reasonably accurate. This limitation of the turbulence model appears to have the greatest impact on the Fanned 2 geometry; this is thought to be as a result of the relatively clean exit flow in comparison with the Fanned 1 design, where separation is evident in the divergent section. As a result, reduced turbulent mixing is evident in the Fanned 2 design limiting the spanwise spreading of the coolant and causing the streaks. The combination of the isotropic turbulent mixing model with the higher lay angle of the Fanned 2 geometry results in the coolant being ejected farther into the main stream, meaning less of the coolant is on the surface combined with less spreading in the stream normal direction.

The reduced coolant flow resulting from the flat spot present in the Fanned 1 geometry is the most likely cause of the crossover between experimental and computational spanwise averaged results at the higher blowing ratio condition. For the first two rows the inability of the turbulence model to correctly simulate the turbulent mixing results in a lower spanwise averaged effectiveness, but once the film is more developed the increase in coolant mass flow becomes more apparent, resulting in a higher simulated effectiveness on the latter half of the plate.

These results are achieved with an average reduction in cell count of 50% relative to a full simulation of 8 rows of coolant passages including inlet plenum. As cooling hole geometries develop in complexity this saving becomes greater.

CONCLUSION

Two techniques for qualitatively assessing relative adiabatic film cooling performance of different combustor wall cooling concepts have been presented; one experimental and one computational. Utilizing the oxygen quenched luminescent properties of Pressure Sensitive Paint; a technique involving the use of Nitrogen as a tracer gas has been employed allowing the measurement of adiabatic film effectiveness without having to manufacture non-conducting test plates whilst giving high levels of special resolution. The results show expected trends, with the cylindrical hole having lower film effectiveness than the fanned geometries, which in turn show similar performance levels. However, improvements to this technique could be addressed with the use of more sensitive imaging equipment, with the CCD contributing a large part of the determined measurement uncertainty as any errors will propagate through both calibration and testing. Another area for improvement is ensuring that the illumination intensity is consistent across the entire test plate through a redesigned lighting setup.

A computational methodology for simulating the adiabatic film effectiveness of hole array geometries with reduced computational demand has also been developed

whereby in hole flow properties are extracted from a single high-fidelity simulation and used as an inlet boundary condition in a multi-row array. Both methods produce results which can be used to quickly rank designs. The computational method allows multiple designs to be simulated and assessed quickly before more expensive methods are employed. However, the results produced by CFD are limited by the simplifications imposed by RANS based turbulence models and therefore should not be used in assessing absolute performance. Designs which rely on spanwise spreading of coolant will be affected the most as indicated by the results for the Fanned 2 geometry. The use of an anisotropic adaptation to the turbulence model, such as presented by Li (81), could improve upon this limitation. The effects of hole-to-hole interaction on the through hole velocity profile will not be captured by this methodology; as a result care should be taken when using this methodology on an array where this effect is likely to have a profound impact on the cooling film. However the influence of hole-to-hole interaction on the coolant at hole exit and on the plate surface is simulated, providing some information on how moving from a single row to an array will change the coolant distribution on the surface.

Further work aimed at determining the effects of main stream turbulence is currently under way with the addition of a jets-in-crossflow turbulence generator, though the influence of turbulence intensity is likely to be minimal on a time averaged experiment with numerous rows of cooling holes such as this. Another avenue for further study is to assess the effects of crossflow and/or swirl component of the mainstream flow, a dominant feature of a real combustor flow field which is not captured in the current study. It is expected that such a flow field would have a noticeable effect on the cylindrical type hole design due to the separated nature of the jet at representative pressure drop conditions, while both the fanned designs show the jet remains attached and consequently should be less sensitive. Also as the spacing between rows is small the film can be quickly re-established. However, RANS based numerical turbulence models are known to struggle with high turbulence intensity conditions.

ACKNOWLEDGMENTS

REFERENCES1. **Rolls-Royce.** *The Jet Engine.* 5th Revised Edition. s.l. : John Wiley & Sons Inc, 2015. 9781119065999.

2. **Spittle, Peter.** Gas Turbine Technology. *IOPscience.* [Online] November 2003. [Cited: 19 May 2012.] http://iopscience.iop.org/0031-9120/38/6/002.

3. **Cerri, G., et al., et al.** *Advances in effusive cooling techniques of gas turbines.* s.l. : Applied Thermal Engineering 27, 2007. 692-698.

4. **Bogard, D.G. and Thole, K.A.** *Gas Turbine Film Cooling.* s.l. : AIAA Journal of Propulsion and Power, 2006. AIAA-18034-904.

5. **Greffrath, F.** *Measurement of the temperature-dependent spectral emissivities of ceramic coatings.* Bochum : Rolls-Royce Deutchland Ltd & Co KG, Blankenfelde-Mahlow, 2012.

6. **Han, Je-Chin, Dutta, Sandip and Ekkad, Srinath.** *Gas Turbine Heat Transfer and Cooling Technology.* s.l. : CRC Press, 2012.

7. **Hartnett, J P.** Mass Transfer Cooling. [book auth.] W M Rohsenow, J P Hartnett and E N Ganic. *Handbook of Heat Transfer Applications.* New York, London : McGraw-Hill, 1998.

8. *The Interaction of Jets with Crossflow.* **Mahesh, Krishnan.** s.l. : Annual Reviews, 2013, Annual Review of Fluid Mechanics, Vol. 45, pp. 379-407.

9. *Flowfield MEasurement for Film-Cooling Holes With Expanded Exits.* **Thole, K, et al., et al.** s.l. : ASME, 1998, Journal of Turbomachinery, Vol. 120, pp. 327-336.

10. *Mixing, structure and scaling of the jet in crossflow.* **Smith, S H and Mungal, M G.** s.l. : Cambridge University Press, 1998, J. Fluid Mechanics, Vol. 357, pp. 83-122.

11. *Impact of Swirl Flow on the Cooling Performance of an Effusion Cooled Combustor Liner.* **Wurm, B, et al., et al.** 12, s.l. : ASME, 11 Oct 2012, Journal of Engineering for Gas Turbines and Power, Vol. 134. 121503.

12. *Correlation of Film-Cooling Effectiveness From Thermographic Measurements at Enginelike Conditions.* **Baldauf, S, et al., et al.** 4, s.l. : ASME, 07 Nov 2002, Journal of Turbomachinery, Vol. 124, pp. 686-698.

13. *Film Cooling With Large Denstiy Differences Between the Mainstream and Secondary Fluid Measured by the Heat-Mass Transfer Analogy.* **Pedersen, D R, Eckert, E R. G and Goldstein, R J.** 4, s.l. : ASME, Nov 1977, Journal of Heat Transfer, Vol. 99, pp. 620-627.

14. *High Resolution Measurements of Local Effectiveness by Discreet Hole Film Cooling.* **Baldauf, S, Schulz, A and Wittig, S.** 4, s.l. : ASME, Feb 1999, Journal of Turbomachinery, Vol. 123, pp. 758-765.

15. *Film-Cooling Effectiveness Downstream of a Single Row of Holes With Variable Density Ratio.* **Sinha, A K, Bogard, D G and Crawford, M E.** 3, s.l. :
ASME, Jul 1991, Journal of Turbomachinery, Vol. 113, pp. 442-449.

16. *Discrete-hole Cooling in the Presence of Free Stream Turbulence and Strong Favourable Pressure Gradent.* **Launder, B E and York, J.** 11, s.l. : Elsevier, Nov 1974, International Journal of Heat and Mass Transfer, Vol. 17, pp. 1403-1409. ISSN 0017-9310.

17. *Effect of Mainstream Variables on Jets Issuing from a Row of Inclined Round Holes.* **Kadotani, K and Goldstein, R J.** 2, s.l. : ASME, Apr 1979, Journal of Engineering for Gas Turbines and Power, Vol. 101, pp. 298-304.

18. *On the Nature of Jets Entering a Turbulent Flow: Part A - Jet-Mainstream Interaction.* **Kadotani, K and Goldstein, R J.** 3, s.l. : ASME, Jul 1979, Journal of Engineering for Gas Turbines and Power, Vol. 101, pp. 459-465.

19. *On the Nature of Jets Entering a Turbulent Flow: Part B - Film Cooling Performance.* **Kadotani, K and Goldstein, R J.** 3, s.l. : ASME, Jul 1979, Journal of Engineering for Gas Turbines and Power, Vol. 101, pp. 466-470.

20. *Effects of Very High Free-Stream Turbulence on the Jet-Mainstream Interaction in a Film Cooling Flow.* **Kohli, A and Bogard, D G.** 4, s.l. : ASME, Oct 1998, Journal of Turbomachinery, Vol. 120, pp. 785-790.

21. *Adiabatic Effectiveness, Thermal Fields,and Velocity Fields for Film Cooling With Large Angle Injection.* **Kohli, A and Bogard, D G.** 2, s.l. : ASME, Apr 1997, Journal of Turbomachinery, Vol. 119, pp. 352-358.

22. *Film Cooling with Compound Angle Holes: Adiabatic Effectiveness.* **Schmidt, D L, Sen, B and Bogard, D G.** 4, s.l. : ASME, Oct 1996, Journal of Turbomachinery, Vol. 118, pp. 807-813.

23. *Film Cooling With Compound Angle Holes: Heat Transfer.* **Sen, B, Schmidt, D L and Bogard, D G.** 4, s.l. : ASME, Oct 1996, Journal of Turbomachinery, Vol. 118, pp. 800-806.

24. *Effects of Free-Stream Turbulence and Surface Roughness on Laterally Injected Film Cooling.* **Schmidt, D L and Bogard, D G.** New York : ASME, 1997. Proceedings of the 32nd National Heat Transfer Conference. Vol. 12, pp. 233-244. HTD-Vol. 350.

25. *Free-Stream Turbulence Effects on Film Cooling With Shaped Holes.* **Saumweber, Christian, Schulz, Achmed and Wittig, Sigmar.** 1, s.l. : ASME, Jan 2003, Journal of Turbomachinery, Vol. 125, pp. 65-73.

26. *Infrared Thermography as Applied to Film Cooling of Gas Turbine Components.* **Schulz, A.** 7, s.l. : IOP, 2000, Measurement Science and Technology, Vol. 11, pp. 948-956.

27. **Martin, Damian and Thorpe, Steven J.** *Experiments on combustor effusion cooling under conditions of very high free-stream turbulence.* Loughborough : ASME, 2012. GT2012-68863.

28. *Turbine Nozzle Film Cooling Study Using the Pressure Sensitive Paint (PSP) Technique.* **Zhang, Luzeng, et al., et al.** Indianapolis : ASME, 1999. ASME 1999 International Gas Turbine and Aeroengine Congress and Exhibition. Vol. 3. 99-GT-196.

29. *Turbine Nozzle Endwall Film Cooling Using Pressure-Sensitive Paint.* **Zhang, Luzeng J and Jaiswal, Ruchira Sharma.** 4, s.l. : ASME, Feb 2001, Journal of Turbomachinery, Vol. 123, pp. 730-738.

30. *Rotating Turbine Blade with Two Rows of Film Cooling Holes Using Pressure Sensitive Paint.* **Ahn, Jaeyong, et al., et al.** 4, s.l. : ASME, Oct 2005, Journal of Heat Transfer, Vol. 128, pp. 879-888.

31. **Jonsson, Magnus.** *Application of Photoluminescent Measurement Techniques for Quantitative Assessment of Turbine Film Cooling.* Lausanne : Swiss Federal Institue of Technology (EPFL), 2010. 4650.

32. *Theory for the use of Foreign Gas in Simulating Film Cooling.* **Jones, T V.** 3, s.l. : Elsevier, June 1999, International Journal of Heat and Fluid Flow, Vol. 20, pp. 349-354. ISSN 0142-424X.

33. **Dhall, Tarun, Humber, William G and Camci, Cengiz.** *Pressure Sensitive Paint for Analysis of Film-Cooling Effects on a Gas Turbine Blade Tip.* s.l. : Pennsylvania State University.

34. **Facchini, B, et al., et al.** *Film-Cooling Adiabatic Effectiveness Measurement on a Real High Pressure Turbine Blade.* Firenze : University of Florence, 2013.

35. **Navarra, Kelly R.** *Development of the Pressure-Sensitive-Paint Technique for Advanced Turbomachinery Applications.* s.l. : Virginia Polytechnic Institute and State University, 1997.

36. **Liu, T and Sullivan, J P.** *Pressure and Temperature Sensitive Paints.* s.l. : Springer, 2005. 3-540-22241-3.

37. *PSP-Based Experimental Investigation of a Blanded Wing Body Aircraft.* **Gebbie, David A, et al., et al.** Toronto : American Institute of Aeronautics and Astronautics, 2005. 23rd AIAA Applied Aerodynamics Conference. 2005-4719.

38. UniFIB Pressure Sensitive Paint Datasheet. [Online] www.psp-tsp.com.

39. **Anderson, John D.** *Computational Fluid Dynamics: The Basics with Applications.* s.l. : McGraw-Hill Education, 1995. ISBN 0070016852.

40. **Blazek, J.** *Computational Fluid Dynamics: Principles and Applications.* s.l. : Elsevier, 2001. ISBN 0080430090.

41. **Versteeg, H K and Malalasekera, W.** *An Introduction to Computational Fluid Dynamics: The Finite Volume Method.* s.l. : Pearson Education Ltd, 2007. ISBN 978-0-13-127498-3.

42. *Star CCM+ User Manual.*

43. **Nichols, R.H.** *Turbulence Models and Their Appliocation to Complex Flows rev 4.01.*

44. **CFD Online.** Mesh Calssification. *cfd-online.* [Online] 15 May 2007. [Cited: 21 May 2012.] http://www.cfd-online.com/Wiki/Mesh_classification.

45. **Page, G.** *CFD Grid Generation Lecture Slides.* s.l. : Loughborough University, 2011.

46. **ONERA.** Computation Fluid Dynamics and Aeroacoustics. *ONERA.* [Online] 25 November 2010. [Cited: 18 January 2012.] http://www.onera.fr/dsna-en/cassiopee/grid-generation-module.php.

47. **www.itk.org.** ParaView UG Curvilinear.png. *Insight Toolkit.* [Online] 10 December 2010. [Cited: 18 January 2012.] http://www.itk.org/Wiki/File:ParaView_UG_Curvilinear.png.

48. **CGNS.** Example Files. *CFD General Notation System.* [Online] [Cited: 18 January 2012.] http://cgns.sourceforge.net/CGNSFiles/Bruce/yf17.gif.

49. **CentaurSoft.** Prism Layers. *Centaur Software.* [Online] [Cited: 18 January 2012.] http://www.centaursoft.com/prism-layers.

50. **Mendez, S. and Nicoud, F.** *Large-eddy simulation of a bi-periodic turbulent flow with effusion.* s.l. : J. Fluid Mech., 2007.

51. **P. Miron, C.Beray, V. Sabelnikov.** *Effect of blowing rate on the film cooling coverage on a multi-holed plate: application on combustor walls.* s.l. : WIT press, 2004. ISBN 1-85312-705-1.

52. **Ceccerini, A., et al., et al.** *Combined Effect of Slot Injection, Effusion Array and Dilution Hole on the Cooling Performance of a Real Combustor Liner Part 2: Numerical Analysis.* s.l. : ASME Turbo Expo, 2010. GT2010-22937.

53. —. *Combined Effect of Slot Injection, Effusion Array and Dilution Hole on the Cooling Performance of a Real Combustor Liner.* s.l. : ASME Turbo Expo, 2009. GT2009-60047.

54. *Comparison of RANS Turbulance Models for Prediction of Film Cooling Performance.* **Harrison, K.L. and Bogard, D.G.** Berlin : ASME Turbo Expo 2008, 2008. Vol. 4. GT2008-51423.

55. **Bacci, A. and Facchini, B.** *Turbulence modelling for the numerical simulation of film and effusion cooling flows.* s.l. : ASME Turbo Expo, 2007. GT2007-27182.

56. **Roy, S, Kapadia, S and Heidmann, J.** *Film Cooling Analysis Using DES Turbulence Model.* s.l. : ASME, 2003. GT2003-38140.

57. **Martin, Damian.** *Effects of High Intensity, Large-Scale Free-Stream Turbulence on Combustor Effusion Cooling.* s.l. : Loughborough University, 2013.

58. *Mathematical Model Describing the Coupled Heat Transfer in Effucion Cooled Combustor Walls.* **Martiny, M, Schulz, A and Wittig, S.** Orlando : ASME, 1997, Vol. 3. 97-GT-329.

59. **Kays, William M and Crawford, Michael E.** *Convective Heat and Mass Transfer.* s.l. : McGraw-Hill Science/Engineering/Math, 1993. ISBN 10:0070337217 / ISBN 13:9780070337213.

60. *Describing Uncertainties in Single Sample Experiments.* **Kline, S J and McClintock, F A.** s.l. : Mechanical Engineering, 1953, Mechanical Engineering, Vol. 75, pp. 3-8.

61. **Jayakumar, J.S.** *Helically Coiled Heat Exchangers.* s.l. : InTech, 2012. ISBN: 978-953-51-0278-6.

62. *Flow Through a Helical Pipe with Rectangular Cross-Section.* **Alam, MD, Begum, Delowara and Yamamoto, K.** s.l. : ANAME, December 2007, Journal of Naval Architecture and Marine Engineering, Vol. 4, pp. 99-110. 1813-8535.

63. **Shih, T. -H., et al., et al.** *A New k-ε Eddy Viscosity Model for High Reynolds Number Turbulent Flows – Model Development and Validation.* Lewis Research Center, NASA. Cleveland : United States, 1994. Technical Report. NASA TM 106721.

64. **Peric, M. and Ferguson, S.** The advantages of polyhedral meshes. *plmmarketplace.* [Online] [Cited: 18th January 2012.] http://www.plmmarketplace.com/upload/Temp/The_Advantage_of_polyhedral.pdf.

65. **L. Guo, Y.Y. Yan, J.D. Maltson.** *Numerical study on discharge coefficients of a jet in crossflow.* s.l. : Elsevier, 2011. 323-332.

66. **Harrison, K.L. and Bogard, D.G.** *Comparison of RANS Turbulance Models for Prediction of Film Cooling Performance.* s.l. : ASME Turbo Expo 2008, 2008. GT2008-51423.

67. *Adiabatic and Overall Effectiveness Measurements of an Effusion Cooling Array for Turbine Endwall Application.* **Facchini, Bruno, et al., et al.** s.l. : ASME, 041008, 2010, Journal of Turbomachinery, Vol. 132(4). 041008.

68. *Combined Effect of Slot Injection, Effusion Array and Dilution Hole on the Cooling Performance of a Real Combustor Liner.* **Ceccerini, A., et al., et al.** Florida : ASME Turbo Expo, 2009. ASME Turbo Expo (GT2009-60047). GT2009-60047.

69. *Assessment of Various Film-Cooling Configurations Including Shaped and Compund Angle Holes Based on Large-Scale Experiments.* **Dittmar, J, Schulz, A and Wittig, S.** s.l. : ASME, 2003, Journal of Turbomachinery, Vol. 125(1), pp. 57-64. 2002-GT-30176.

70. *Effects of an axisymmetric contoured end wall on a nozzle guide vane: Adiabatic effectiveness measurements.* **Thrift, A, Thole, K and Hada, S.** 041007, 2011, Journal of Turbomachinery, Vol. 133(4).

71. **Varvel, Trent Alan.** *Shaped Hole Effects of Film Cooling Effectiveness and a Comparison of Multible Effectiveness Measurement Techniques.* s.l. : Texas A&M University, 2004.

72. *Theory for the use of foreign gas in simulating film cooling.* **Jones, T V.** 1999, International Journal of Heat and Fluid Flow, Vol. 20(3), pp. 349-354.

73. *PSP-Based Experimental Investigation of a Blended Wing Body Aircraft.* **Gebbie, David A, et al., et al.** s.l. : AIAA, 2005. 23rd AIAA Applied

Aerodynamics Conferece (AIAA2005-4719). 2005-4719.

74. **Steiner, Patrick.** *Application of the Pressure Sensitive Paint Technique to the Turbomachinery Environment.* Lausanne : Swiss Federal Institute of Technology, 2001. 2297.

75. **Dhall, Tarun, Humber, William G and Camci, Cengiz.** *Pressure Sensitive Paint for Analysis of Film-Cooling Effects on a Gas Turbine Blade Tip.* s.l. : Pennsylvania State University, 2004.

76. *Combined Effect of Slot Injection, Effusion Array and Dilution Hole on the Cooling Performance of a Real Combustor Liner Part 2: Numerical Analysis.* **Andreini, Antonio, et al., et al.** Glasgow : ASME Turbo Expo, 2010. ASME Turbo Expo (GT2010-22937). GT2010-22937.

77. *Flow and Heat Transfer Predictions for Film Cooling.* **Acharya, Sumanta, Tyagi, Mayank and Hoda, Asif.** May 2001, Annals of the New York Academy of Sciences, Vol. 934, pp. 110-125.

78. *Film Cooling Effectiveness for Multirow Holes.* **Sasaki, M, et al., et al.** 1979, J. Eng. Gas Turbines Power, Vol. 101(1), pp. 101-108.

79. *Experiments on Combustor Effusion Cooling Under Conditions of Very High Free-Stream Turbulence.* **Martin, Damian and Thorpe, Steven J.**

Copenhagen : s.n., 2012. ASME Turbo Expo (GT2012-68863). GT2012-68863.

80. *A detailed analysis of film-cooling physics: Part I Streamwise injection with cylindrical holes.* **Walters, D K and Leylek, J H.** 1997, Journal of Turbomachinery, Vol. 122(1), pp. 102-112.

81. *Algebraic Anisotrpic Turbulence Modeling of Compound Angled Film Cooling Validated by Particle Image Velocimetry and Pressure Sensitive Paint Measurements.* **Li, Xueying, et al., et al.** 2014, Journal of Heat Transfer, Vols. 136(3), 032201.

82. **CFD Online.** Direct numerical simulation (DNS). *CFD Online.* [Online] [Cited: 17th January 2012.] http://www.cfd-online.com/Wiki/Direct_numerical_simulation_(DNS).

83. —. Y+ Wall distance estimation. *CFD Online.* [Online] [Cited: 18th January 2012.] http://www.cfd-online.com/Tools/yplus.php.

84. **Gordon, R. and Levy, Y.** *Optomization of Wall Cooling in Gas Turbine Combustor Through Three-Dimensional Numerical Simulation.* s.l. : Journal of Engineering for Gas Turbines and Power, 2005.

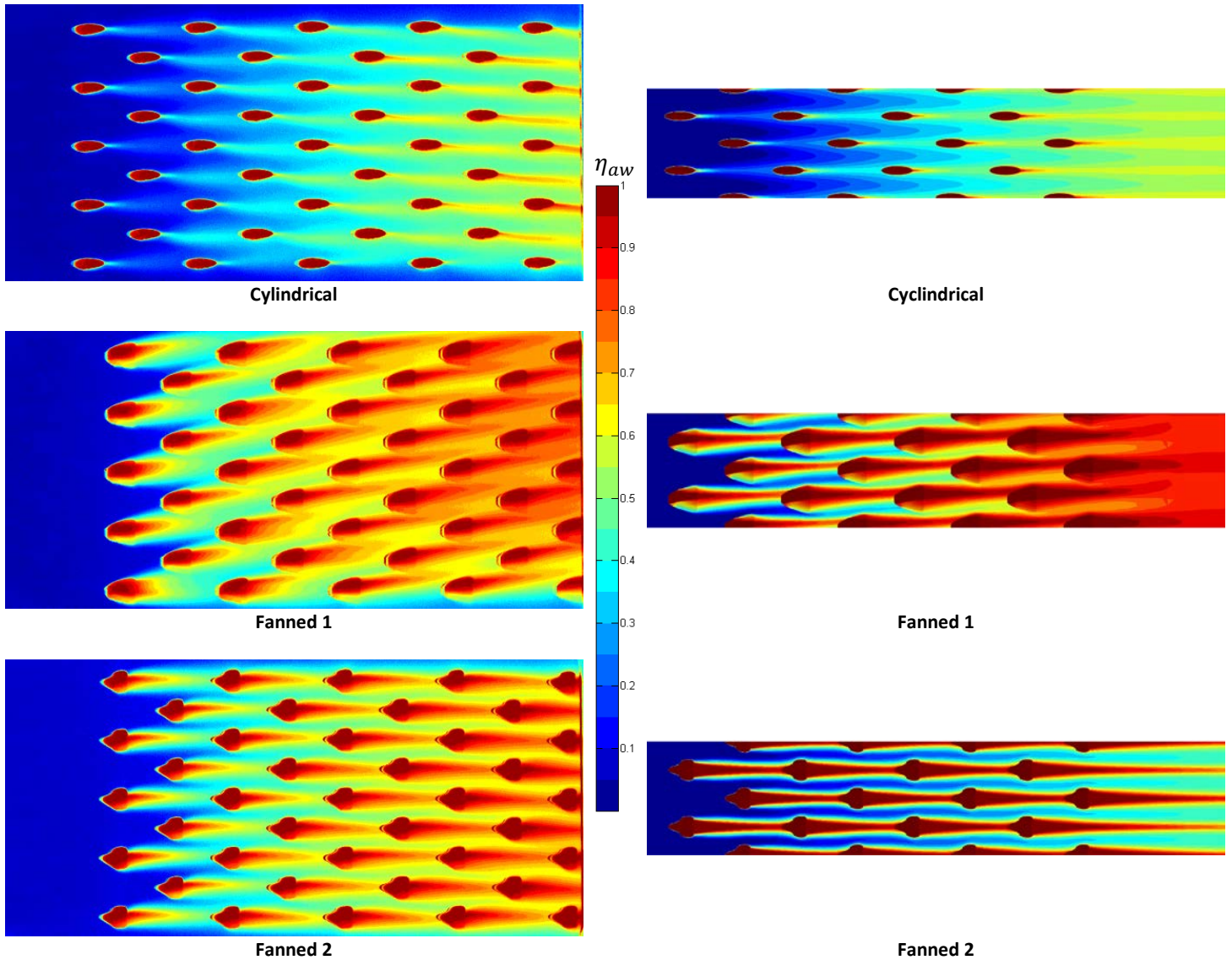85. **Innovative Scientific Solutions Inc.** Pressure Sensitive Paints. *ISSI.* [Online] [Cited: 3 July 2014.] http://psp-tsp.com/index.php?id=115.

Cylindrical

Fanned 1

Fanned 2

Figure 128 - PSP Measurements Film Effectiveness Surface Maps for M~3.8

η_{aw}

Cyclindrical

Fanned 1

Fanned 2

Figure 129 - Computational Film Effectiveness Surface Maps for M~3.8
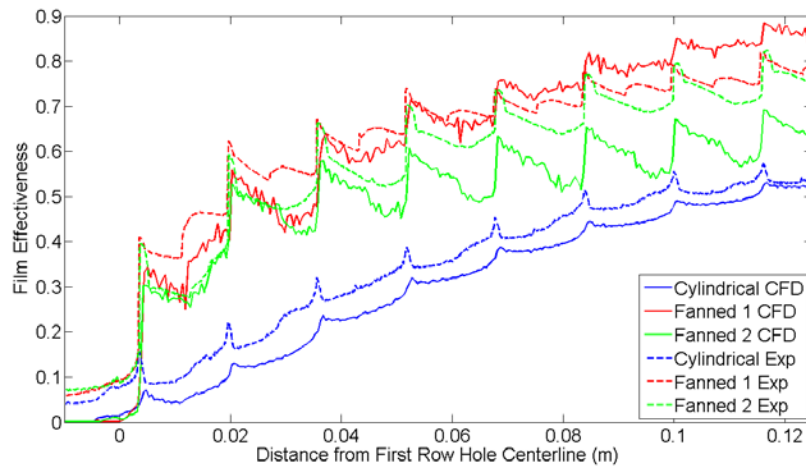
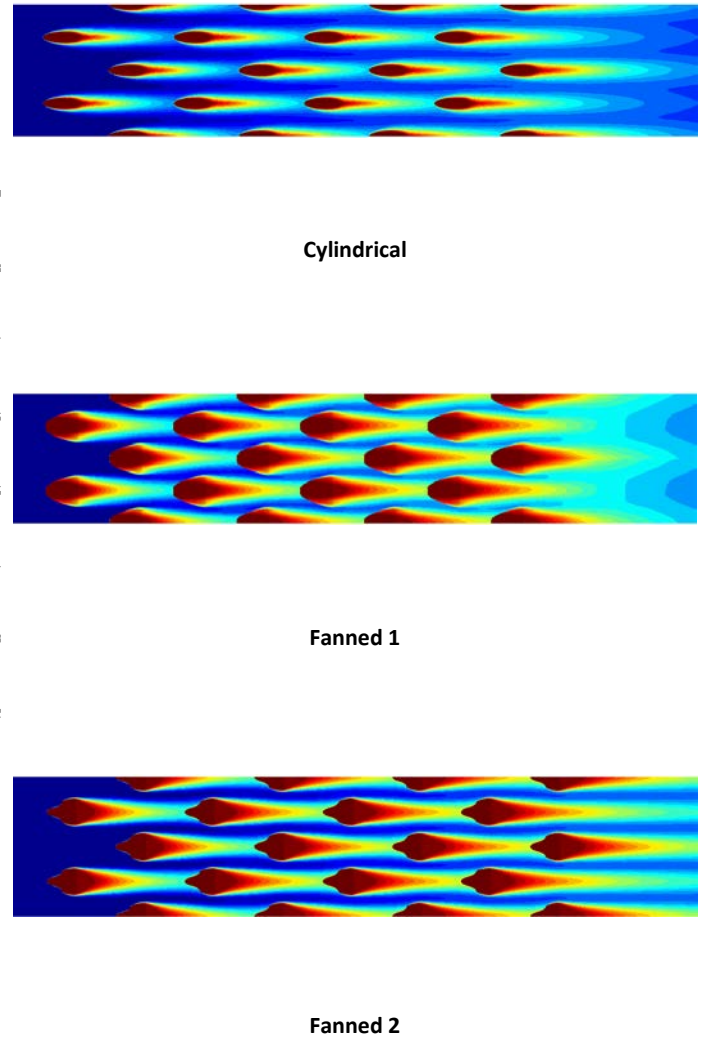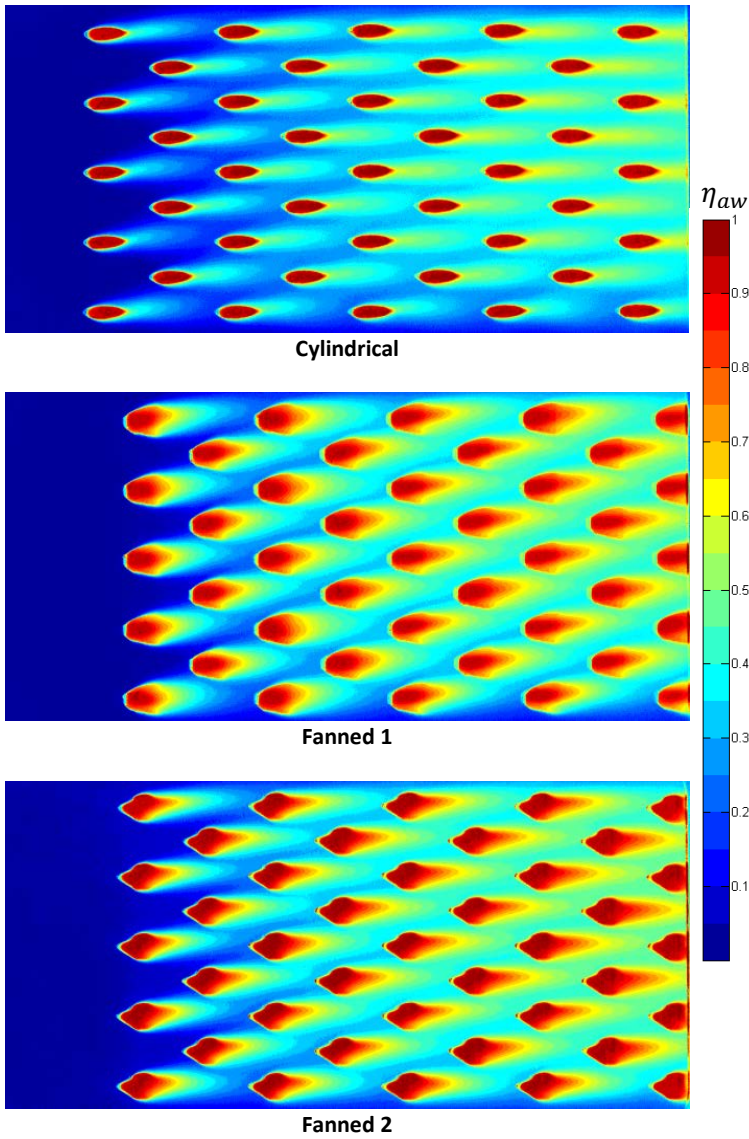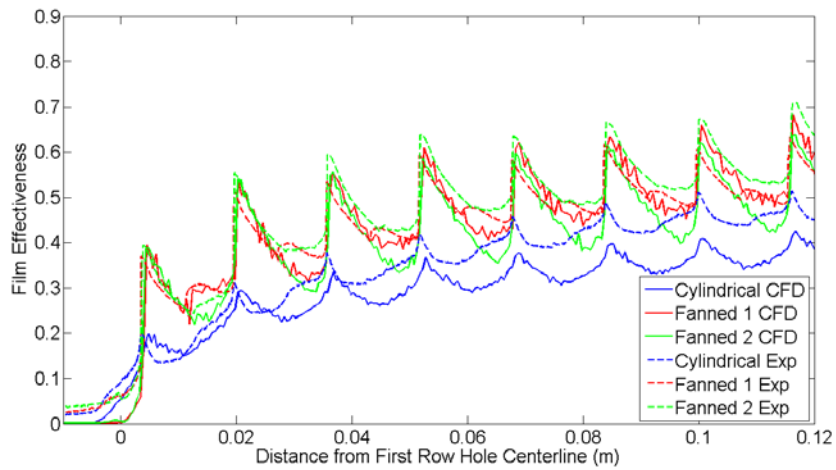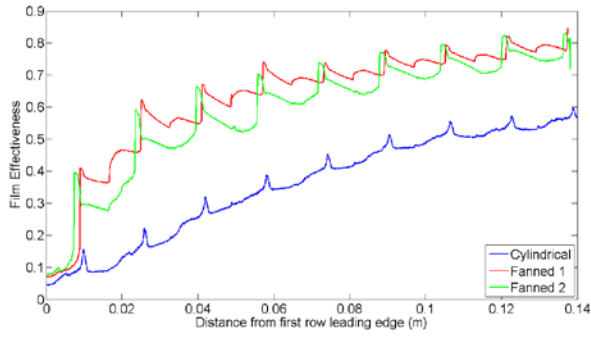**Figure 130 – Spanwise Average Film Effectiveness at M~3.8**

Cylindrical

Fanned 1

Fanned 2

Figure 131 - PSP Measurements Film Effectiveness Surface Maps for M~0.8

Cylindrical

Fanned 1

Fanned 2

Figure 132 - Computational Film Effectiveness Surface Maps for M~0.8

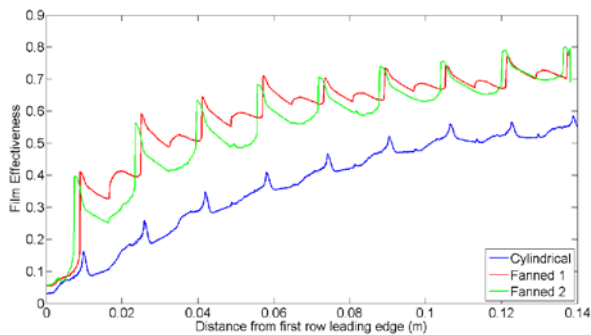**Figure 133 – Spanwise Average Film Effectiveness at M~0.8**

M~3.8
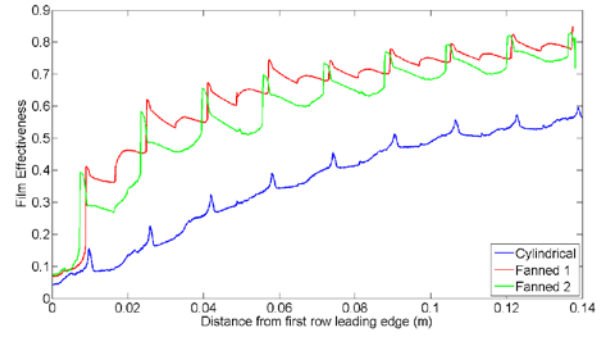
M~3.2
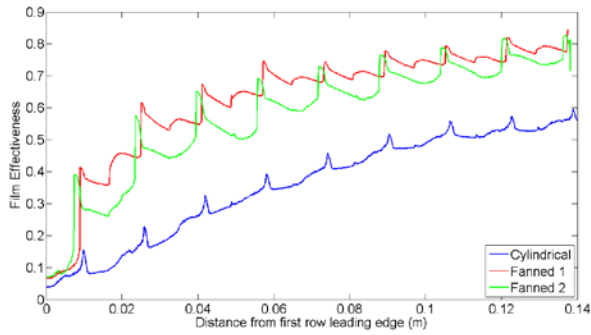
M~2.6
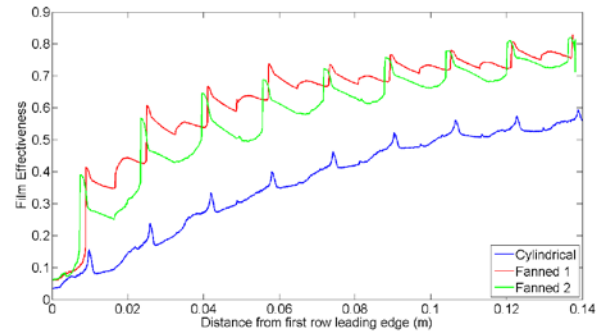
M~2.1

M~1.5
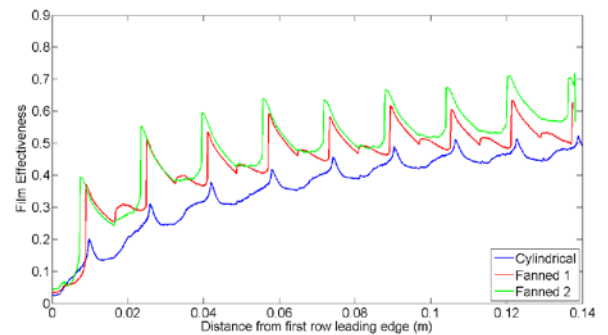
M~0.8

Figure 134 - Spanwise Averaged Film Effectiveness PSP Measurements